APPROVAL SHEET

Title of Dissertation: Interactions of Radiation with Aerosols and Clouds in a Three-Dimensional Atmosphere: Implications for Aerosol and Cloud Remote Sensing

Name of Candidate: Chamara P.N. Rajapakshe
Doctor of Philosophy, 2020

Dissertation and Abstract Approved: Zhibo Zhang
Professor Zhibo Zhang
Associate Professor
Department of Physics

Date Approved: 07/22/2020

ABSTRACT

Title of dissertation: INTERACTIONS OF RADIATION WITH AEROSOLS AND CLOUDS IN A THREE-DIMENSIONAL ATMOSPHERE: IMPLICATIONS FOR AEROSOL AND CLOUD REMOTE SENSING

Chamara P.N. Rajapakshe, Ph.D., 2020

Dissertation directed by: Professor Zhibo Zhang
Department of Physics

The global measurements of the properties of clouds, aerosols, and aerosol-cloud interactions are primarily based on satellite remote sensing. Thus, the retrieval artifacts associated with the remote sensing techniques have significant implications in our understanding of the properties of clouds, aerosols, and their influence on the weather and climate. For the sake of computational efficiency, the passive remote sensing techniques often assume the atmosphere as a collection of horizontally homogeneous, radiatively isolated columns. When the realistic atmosphere deviates from these assumptions, the retrieval technique is susceptible to the biases that are often referred to as "3D effects". To study the 3D effects in the aerosol and cloud property retrievals, ideally, it is required to compare the retrieved-properties with the underlying physical properties. Such comparisons are problematic to achieve based on the observational data. In this work, we simulate both 3D and 1D radiative transfer in the large-eddy simulation cloud fields (LES-cloud fields) and artificially

synthesize the "satellite data products" to perform a comprehensive study on the 3D radiative effects of cloud property retrievals.

This thesis is organized as follows: A brief introduction of two popular cloud remote sensing techniques, one based on spectral radiometric observations and the other on polarimetric observations of cloud reflectance, is provided in Chapter 1. The aerosol and cloud remote sensing simulator based on the LES model and radiative transfer models are described in Chapter 2. In Chapter 3, we present a study of the potential interactions between the seasonal above cloud smoke and the underlying stratocumulus cloud in the southeast Atlantic region based on space-borne lidar observations. In Chapter 4, we investigate the impacts of the 3D radiative effects on the so-called bi-spectral method for remote sensing of cloud optical thickness and effective radius. In particular, we present a novel framework based on two-dimensional Taylor expansion that provides a more comprehensive understanding of the convoluted impacts of 3D radiative effects on the simultaneous COT and CER retrievals. In Chapter 5, we present a study of the 3D radiative effects on the CER and CEV retrievals based on the multi-angular polarimetric observations. Several important 3D radiative effects, such as the parallax effect, and their impacts on the polarimetric retrievals are identified and the underlying physics illustrated. Finally, in Chapter 6, we explore a novel method to identify the 3D radiative effect in the operational cloud remote sensing algorithms based on the combination of bi-spectral and polarimetric observations. The results from this study are expected to improve our understanding of the uncertainties caused by 3D effects in the satellite remote sensing products and also useful for the planning of future satellite missions.

INTERACTIONS OF RADIATION WITH AEROSOLS AND CLOUDS IN A THREE-DIMENSIONAL ATMOSPHERE : IMPLICATIONS FOR AEROSOL AND CLOUD REMOTE SENSING

by

Chamara P.N. Rajapakshe

Dissertation submitted to the Faculty of the Graduate School of the
University of Maryland, Baltimore County in partial fulfillment
of the requirements for the degree of
Doctor of Philosophy
2020

Advisory Committee:
Professor Zhibo Zhang, Chair/Adviser
Professor Vanderlei Martins
Professor Pengwang Zhai
Professor Jianwu Wang
Dr. Adriana Rocha Lima

Dedicated to my father

මගේ තාත්තාට පුදමි...

Acknowledgments

In the past five years, many people helped me to make this thesis possible, and because of them, my graduate experience has been one that I will cherish forever. First and foremost, I would like to thank my adviser, Professor Zhibo Zhang for providing me exceptional guidance and invaluable opportunities to work on challenging, extremely interesting projects. I have been lucky to start my research career with the guidance of such an extraordinary individual. I would also like to thank my committee members, Prof. Vanderlei Martins, Prof. Pengwang Zhai, Prof. Jianwu Wang, and Dr. Adriana Rocha Lima, not only for their extensive feedback on improving my research work but also for shaping my graduate student career to reach where I am today. I also owe my gratitude to the coauthors and collaborators of my journal publications and research work for their support and guidance.

I believe the knowledge is necessarily built upon generations of continuous teamwork. I would like to emphasize the research support that I received from Dr. Daniel Miller and Dr. Zhen Wang at the early stage of my work. I would also like to acknowledge the help and support received from the former members of the ACROS research group, Roy Prouty, Dr. Frank Werner, and Dr. Hua Song to name a few. In the past years, I have been blessed to be surrounded by talented and enthusiastic colleagues; Qianqian Song, Jianyu(Kevin) Zheng, Achala Denagamage, and the other fellow graduate students who have enriched my graduate student life in many ways. The memories of discussions, arguments, struggles, and most importantly your friendship that I will cherish forever.

I am indebted to my mother for her extraordinary courage and her keen understanding as an educator on preserving the creativity of a kid amid the competitiveness of the modern education system. I am grateful to my two brothers and two sisters for standing by me and pulling through against impossible odds at times.

Additionally, I would like to acknowledge the computational resources of the UMBC High-Performance Computing Facility which was another essential component of this work.

Finally, I thank my wife for supporting me throughout this endeavor. I am truly blessed to have you in my life.

Table of Contents

List of Tables

List of Figures

List of Abbreviations

SZA	Solar Zenith Angle
CER	Cloud Effective Radius
COT	Cloud Optical Thickness
RT	Radiative Transfer
CEV	Cloud Effective Variance
RICO	Rain In shallow Cumulus over the Ocean
SWIR	Shortwave Infrared
DYCOMS-II	the second Dynamics and Chemistry of Marine Stratocumulus
ATEX	Atlantic Trade wind EXperiment
LES	Large-Eddy Simulation
VNIR	Visible to near-infrared
MA	Multi-angular
CALIOP	Cloud-Aerosol Lidar with Orthogonal Polarization
VW	Vertically-weighted
ACA	Above-Cloud-Aerosols
LUT	Look-up-table
CATS	Cloud-Aerosol Transport System
MSCART	Multiple-Scaling-based Cloudy Atmospheric Radiative Transfer
MODIS	Moderate Resolution Spectro-radiometer
LWP	Liquid Water Path
IPA	Independent Pixel Approximation
SE	South-east
CALIPSO	Cloud-Aerosol Lidar and Infrared Pathfinder Satellite Observation
AOT	Aerosol Optical Thickness
PPA	Plane-Parallel Approximation
SAA	Solar Azimuth Angle
PSD	Particle Size Distribution
HARP	Hyper-angular Rainbow Polarimeter
VZA	Viewing Zenith Angle
PDF	Probability Density Function
IPCC	Intergovernmental Panel on Climate Change
ACROS	Aerosol, Cloud, Radiation-Observation and Simulation
SPFFT	Scattering Phase Function Forward Truncation
TDIS	Target Directional Importance Sampling
ACRS	Aerosol Cloud Retrieval Simulator
RSP	Research Scanning Polarimeter
POLDER	Polarization and Directionality of Earth Reflectance
IRE	Indirect Radiative Effect
DSD	Droplet Size Distributions
DRE	Direct Radiative Effect

NIR	Near-infrared
VIS	Visible
SDRE	Semi-direct Radiative Effect
RTE	Radiative Transfer Equation
MBL	Marine Boundary Layer
EM	Electromagnetic
CF	Cloud Fraction
NJK	Nakajima-King
SEVIRI	Spinning Enhanced Visible and Infrared Imager
OPAC	Optical Properties of Aerosols and Clouds
NASA	National Aeronautics and Space Administration
MSPI	Multiangle SpectroPolarimetric Imager
LWC	Liquid Water Content
JASO	July to October
ISS	International Space Station
DHARMA	Distributed Hydrodynamic-Aerosol-Radiation-Microphysics Application
CDF	Cumulative Density Function
AERONET	AErosol RObotic NETwork
TOA	Top Of the Atmosphere
SSA	Single Scattering Albedo
SIBYL	Selective, Iterated BoundarY Location
PACE	Plankton, Aerosol, Cloud, ocean Ecosystem
AOD	Aerosol Optical Depth

List of Variables

Θ_S	Scattering angle
μ	Cosine of viewing zenith angle
μ_0	Cosine of solar zenith angle
Ω	Solid angle
r_e, r_{eff}	Cloud effective radius
v_e, v_{eff}	Cloud effective variance
ρ_w	Density of water
τ	Optical thickness
n	Refractive index
n_r	Real part of the refractive index
n_i	Imaginary part of the refractive index
λ	Wavelength
R_λ	Reflectance at wavelength λ
k	Wave vector
β_e	Volume extinction coefficient
β_a	Volume absorption coefficient
β_s	Volume scattering coefficient
Q_e	Extinction efficiency
Q_a	Absorption efficiency
Q_s	Scattering efficiency
σ_e	Extinction cross-section
σ_a	Absorption cross-section
σ_s	Scattering cross-section
ω	Single Scattering Albedo
P_{ij}	Phase matrix elements
Q_1, Q_2, Q_3	First, second, and third quantiles

Chapter 1: Introduction

At any given time, on average about 60% of the sky is covered by clouds. In the visible region (0.4-0.7 μm), the Earth's view from the space is dominated by cloud fields. Among the various types of clouds, water clouds such as stratus, cumulus, and stratocumulus are generally located closer to the surface compared to the ice clouds. The radiative effects of low-level water clouds are more significant in the shortwave (SW, 0.4-0.7 μm) and near-infrared (0.7-4.0 μm) regions of the electromagnetic spectrum than in the longwave thermal infrared region (> 4 μm) (Cahalan et al., 1994). In contrast to the low-level clouds, cold high clouds usually have strong positive (warming) radiative effects in the thermal infrared region, although they may also have significant cooling effects in the shortwave. After averaging over all types of clouds over the globe, the SW cooling effects of low-level water clouds dominate over the warming effects of ice clouds, leading to a global annual mean net cloud radiative effects of about $-20 W/m^2$ (IPCC, 2013)(IPCC AR5 Chapter 7, Figure 7.7a-b). These strong radiative effects make clouds an important modulator of earth radiative energy balance (IPCC, 2013; Trenberth et al., 2009; Klein and Hartmann, 1993).

Aerosols are another atmospheric constituent that has a significant influence

on the earth's radiation budget. The sources of aerosols can be stemmed from a natural or anthropogenic source. These sources also can be classified as the emissions of primary particulate matter or secondary particulate matter derived from gaseous precursors. The radiative effects of aerosols can be categorized into three main categories: Direct Radiative Effect (DRE), Semi-direct Radiative Effect (SDRE), and Indirect Radiative Effect (IRE) (Rajapakshe et al., 2017). The DRE of aerosols occurs due to the direct interactions of aerosol with the incident shortwave and longwave radiation. Aerosols can also alter the thermodynamical structure of the atmosphere through radiative warming, which in turn influences the generation and evolution of clouds. This is known as the SDRE of aerosols. The indirect effects of aerosols occur when aerosols are activated as extra cloud condensation nuclei (CCN) and consequently modify the microphysical properties, precipitation efficiency, and lifetime of clouds (Johnson et al., 2004; Costantino and Bréon, 2013).

Figure (1.1) shows the contributions of the various anthropogenic radiative forcing drivers to the climate change. The best estimates of the globally averaged radiative forcing and corresponding uncertainties are shown in black points and error bars respectively. The level of confidence of each value is represented in the right-most column (VH very high, H high, M medium, L low, VL very low). A detailed description of this figure can be found in the Intergovernmental Panel on Climate Change 5^{th} assessment report (IPCC, 2013). It is well-known that the largest contribution ($1.68\ Wm^{-2}$) to the total anthropogenic radiative forcing is coming from CO_2. But a substantial amount of that CO_2 radiative forcing can be compensated by the uncertainty ($-1.33\ to\ -0.06\ Wm^{-2}$) associated with the

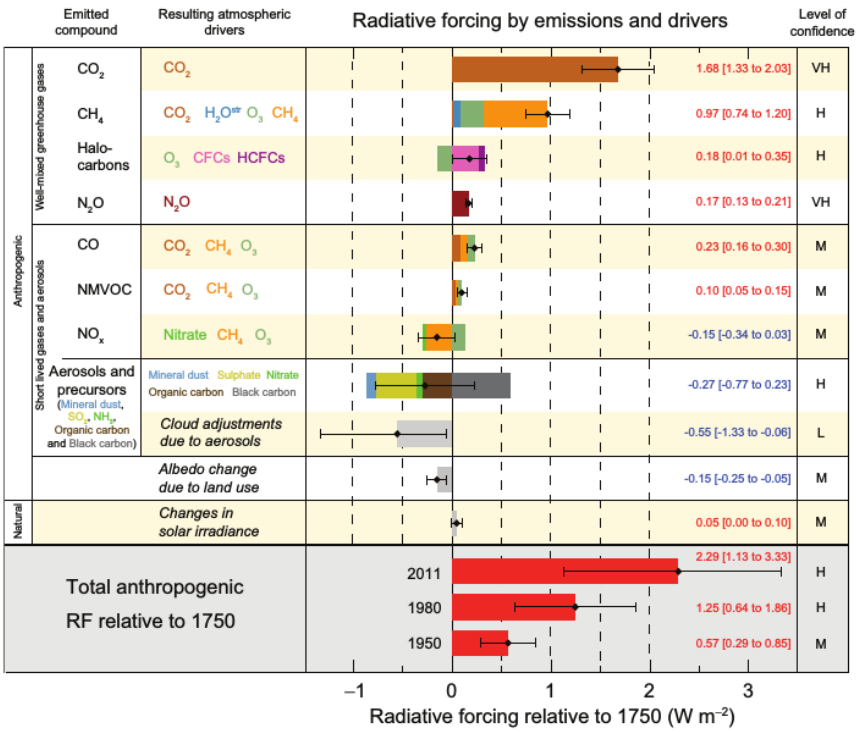

Figure 1.1: The radiative forcing estimates and corresponding aggregated uncertainties in 2011 relative to 1750 for the main drivers of climate change IPCC (2013).

radiative forcing of the "cloud adjustments due to aerosols" (i.e. IRE of aerosols). Therefore IRE of aerosols has been and will continue to be one of the vital fields of interest when it comes to quantification the anthropogenic climate forcing.

The global measurements of the properties of clouds, aerosols, and aerosol-cloud interactions are primarily based on satellite remote sensing. Thus the measurement artifacts associated with the remote sensing techniques have considerable implications for our understanding of the properties of aerosols, clouds, and aerosol-cloud interactions (Platnick et al., 2003). As an example, passive remote sensing techniques often treat the atmosphere as a collection of horizontally homogeneous columns (Plane-Parallel Approximation, PPA) and ignore the horizontal photon

transportation between the pixels (Independent Pixel Approximation, IPA). PPA and IPA approximations can affect Cloud Optical Thickness (COT) and Cloud Effective Radius (CER) retrievals which are two key parameters for understanding the radiative effects of clouds and the IRE of aerosols (Zhang et al., 2012; Marshak et al., 2006).

The current paradigm of aerosol and cloud remote sensing is to divide the whole sky into clear-sky (cloud-free) and cloudy-sky conditions. Aerosol property retrievals are only performed under cloud-free clear-sky conditions. However, recent satellite observations revealed that the aerosols often reside above the low-level clouds in many regions of the globe. The above-cloud aerosols raise a new challenge to aerosol and cloud remote sensing (Yu and Zhang, 2013). Compared to the cloud-free sky, aerosols located above the clouds absorb more solar radiation due to the high reflectance of the underlying clouds. In addition to the above-cloud aerosol condition, the radiation that scattered by cloud edges also can interact with the adjacent aerosols (Várnai and Marshak, 2009) which may have important implications for DRE and IRE studies of aerosols. Due to these complicated interactions, aerosol and cloud property retrievals such as aerosol optical depth (AOD), aerosol single scattering albedo, cloud effective radius (CER), cloud optical depth (COD) and cloud fraction are subjected to large uncertainties (Yu and Zhang, 2013; Meyer et al., 2013, 2015) which can consequently cause large uncertainties in the radiative forcing estimations. Besides, newly-launched NASAs Cloud-Aerosol Transport System (CATS) observations reveal that the bottom of the above-cloud aerosol (ACA) layer is much lower than previously estimated based on Cloud-Aerosol Lidar and In-

frared Pathfinder Satellite Observation (CALIPSO). Due to the proximity of the top aerosol base to the underlying cloud, aerosols might be more frequently entrained into the cloud and give rise to IRE of aerosols (Rajapakshe et al., 2017).

Compared to the cloud-free DRE of aerosols, the estimation of the cloudy sky DRE of aerosols has been a challenging task because as aforementioned the conventional passive remote sensing techniques are only performed in cloud-free regions (Yu and Zhang, 2013). Investigating the 3D radiative transfer (RT) effects on clouds (Várnai and Marshak, 2009) and ACA remote sensing (Meyer et al., 2015; Sayer et al., 2016) is an important and timely task that reduces the uncertainties associated with the aerosol and cloud property retrievals.

Miller et al. (2016) used a Large-Eddy Simulation (LES) cloud model coupled with 1D radiative transfer simulations to study the impact of cloud vertical structure on the bi-spectral cloud retrievals. Later, the study was extended to perform both bi-spectral and polarimetric cloud retrievals and two retrieval techniques were compared under 1D RT assumption (Miller et al., 2017). With the valuable insight that was gained from the aforementioned studies, especially about the impact of cloud vertical profile and horizontal inhomogeneities on the retrievals, this study further expands the 1D RT-based simulator setup to perform both 1D and 3D radiative transfer simulations. The main objective of this new study is to investigate how the different radiative transfer assumptions (1D and 3D) cause biases in the bi-spectral and polarimetric cloud property retrievals.

This chapter first provides some background information on the physical and optical properties of aerosols and clouds. Then the fundamentals of the focus-

ing remote sensing techniques are summarized. Chapter 2 describes our modified aerosol-cloud retrieval simulator setup. Chapter 3 presents an observational study on the above-cloud aerosol observations in the southeast Atlantic region (Rajapakshe et al., 2017). The most in-depth and comprehensive analyses of our study that has focused on the 3D radiative effects in the bi-spectral and polarimetric cloud retrievals are presented in Chapter 4 and 5 respectively. Finally, Chapter 6 presents the theoretical basis of a new technique to correct the large COT biases in the bi-spectral retrievals due to the 3D radiative effects (Rajapakshe and Zhang, 2020).

1.1 Background

1.1.1 Particle size distributions of clouds and aerosols

Cloud droplets and aerosols (or any other atmospheric particulate) exist in the nature as an ensemble of particles. Therefore the particle size distribution (PSD) functions are used to specify the number of particles per unit size interval per unit volume of such ensemble of particles. In theory, PSD could be any arbitrary function but in practice, some analytical distribution functions show better agreements with the *in situ* measurements and provide additional advantages in the practical remote sensing implementations. The modified Gamma distribution (Deirmendjian, 1964)(Equation 1.1) and another form of the Gamma distribution proposed by Hansen and Travis (1974) are commonly used to represent cloud PSDs. The bi-modal log-normal distribution function (Equation 1.10) is commonly used to represent aerosol size distributions (Dubovik et al., 2002; Omar et al., 2009).

If the cloud droplet radius is r, the modified gamma distribution $n(r)$ (Hansen and Travis, 1974) can be written as,

$$n(r) = \frac{dN(r)}{dr} = N_0 r^{(1-3v_e)/v_e} e^{\frac{-r}{r_e v_e}} \tag{1.1}$$

where N_0 is a normalization constant, r_e is the effective radius and v_e is the effective variance. In Equation (1.1), the product of r_e and v_e modifies the broadness of the tail of the distribution. Figure (1.2) shows the behavior of the modified gamma distribution for different combinations of r_e and v_e values. Clearly, for a given v_e the mode of the distribution decreases (becomes less monodisperse) as r_e increases.

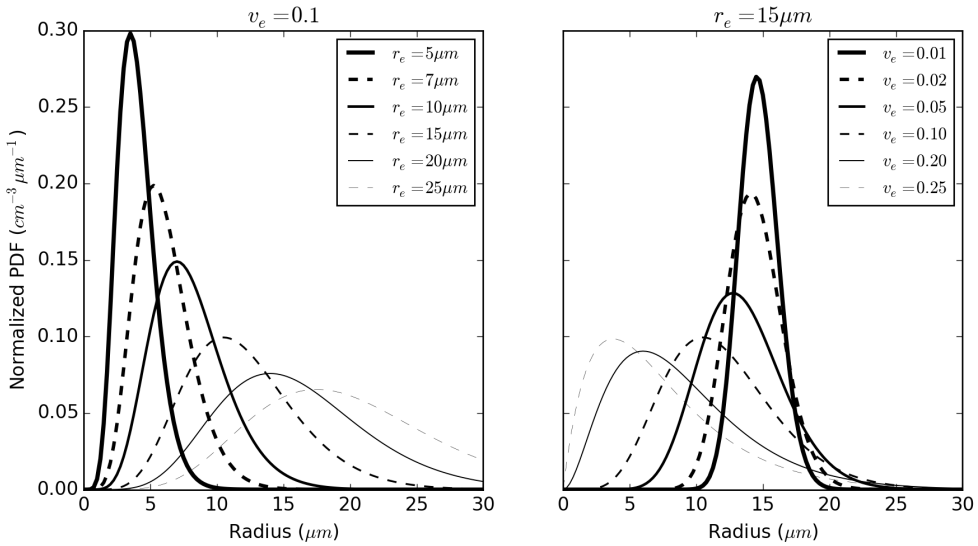

Figure 1.2: Modified gamma distribution (Hansen and Travis, 1974) for different combinations of r_e and v_e values.

In terms of radiation interactions, the average cross-section of the collection of particles is more important than the average radius. In terms of liquid water content (LWC), the volume is physically more meaningful. The advantage of using equation

(1.1) to represent the cloud droplet distributions is the relationships among r_e, v_e, and their various distribution moments (Equation (1.2)) can be used to get simple relationships between physical and optical properties.

$$\begin{aligned}
\langle r^1 \rangle &= r_e - 2r_e v_e = re(1 - 2v_e) \\
\langle r^2 \rangle &= r_e^2 (v_e - 1)(2v_e - 1) \\
\langle r^3 \rangle &= r_e^3 (v_e - 1)(2v_e - 1) \\
\langle r^4 \rangle &= r_e^4 (v_e - 1)(2v_e - 1)(v_e + 1)
\end{aligned} \tag{1.2}$$

We can write direct relationships to compute r_e and v_e from $n(r)$ (Hansen and Travis, 1974).

$$\begin{aligned}
r_e &= \frac{\langle r^3 \rangle}{\langle r^2 \rangle} = \frac{\int_0^\infty r^3 n(r) dr}{\int_0^\infty r^2 n(r) dr} \\
v_e &= \frac{\langle r^4 \rangle \langle r^2 \rangle}{\langle r^3 \rangle^2} - 1 = \frac{1}{r_e^2} \frac{\int_0^\infty (r - r_e)^2 r^2 n(r) dr}{\int_0^\infty r^2 n(r) dr}
\end{aligned} \tag{1.3}$$

Liquid water content (LWC) which gives the amount of liquid water per unit volume (in mass/volume) and the liquid water path (LWP) which measures the weight of the liquid water droplets in the atmosphere above a unit surface area (in mass/area) are two important quantities in many cloud physical processes.

$$\begin{aligned}
LWC &= \frac{\text{liquid water mass}}{volume} \\
LWP &= \frac{\text{liquid water mass}}{area}
\end{aligned} \tag{1.4}$$

By using Equation (1.2) the average LWC (in mass/volume) of a cloud can be obtained in terms of r_e and v_e as,

$$LWC = \rho_w \frac{4\pi}{3} \langle r^3 \rangle = \rho_w \frac{4\pi}{3} N_0 r_e^3 (v_e - 1)(2v_e - 1) \tag{1.5}$$

The relationship between cloud Liquid Water Path (LWP) and optical thickness can be written as,

$$LWP = C_{vp}\rho_w r_e \tau \tag{1.6}$$

where, C_{vp} is a coefficient that can be derived from the assumed vertical profile of the cloud. A comprehensive analysis on the impact of cloud vertical profile on LWP retrievals can be found in Miller et al. (2016).

From the remote sensing perspective, the mean cross-section that can interact with the incident radiation is more intuitive than the mean radius. By taking this into consideration, a meaningful quantity called "volume extinction coefficient" β_e can be defined by taking the the average extinction efficiency $Q_e(r)$ (see Section 1.1.3) weighted by cross-section πr^2 as follows,

$$\beta_e = \int_0^\infty Q_e(r)(\pi r^2)n(r)dr$$

For increasing size parameter (Equation 1.14), the Q_e approaches to an asymptotic maximum of two. In the visible wavelengths, the size parameter of the spherical cloud droplets is sufficiently large, thus for cloud particles $Q_e(r) \sim 2$ (Wendisch and Yang, 2012). Therefore for clouds,

$$\beta_e^{VIS} \simeq 2\pi \langle r^2 \rangle = N_0 r_e^2 (v_e - 1)(2v_e - 1) \tag{1.7}$$

Note that Equation (1.5) and (1.7) connect the distribution parameters r_e and v_e in Equation (1.1) with two important physical (LWC) and optical (volume extinction efficiency β_e) parameters respectively. Moreover, by considering the importance of the cross-section in radiation interaction, we can understand the physical interpretation of the effective radius r_e. We can define the "remote sensing perspective"

of droplet radius by weighting the actual physical radius r by $Q_e(r)$ and cross-section πr^2 as follows,

$$r_{rs} = \frac{\int_0^\infty Q_e(r)\pi r^2 r n(r) dr}{\int_0^\infty Q_e(r)\pi r^2 n(r) dr} \tag{1.8}$$

By substituting $Q_e(r) \sim 2$ (for cloud particles in visible wavelengths) into Equation 1.8 and comparing with Equation 1.3, we can see that the effective radius r_e is equivalent to the aforementioned "remote sensing perspective" of the droplet radius.

$$r_{rs} = \frac{\int_0^\infty Q_e(r)\pi r^2 r n(r) dr}{\int_0^\infty Q_e(r)\pi r^2 n(r) dr} = \frac{\langle r^3 \rangle}{\langle r^2 \rangle} = r_e \tag{1.9}$$

Therefore, the effective radius r_e can be considered as the "remote sensing perspective of cloud droplets". In summary, the parameters of modified gamma distribution as in Equation (1.1) can be used to obtain the physical and optical parameters like LWC (Equation (1.5)), LWP (Equation 1.6), volume extinction coefficient (Equation (1.7)), and effective radius (Equation (1.9))

Aerosol PSDs usually have polydispersity (shows two or more distinct modes). Therefore, a bimodal log-normal function (1.10) is the most appropriate PSD to represent an aerosol populations.

$$n(\ln r) = \frac{dN(r)}{d(\ln r)} = \sum_{i=1}^{2} \frac{N_i}{\sqrt{2\pi}\sigma_i} \exp\left[- \frac{(\ln r - \ln r_{m,i})^2}{2\sigma_i^2} \right] \tag{1.10}$$

where N_i is the particle number concentration of the i^{th} mode, $r_{m,i}$ is the median radius of the i^{th} mode and σ_i is the standard deviation of the i^{th} mode. By using Equation (1.10), following relations can be obtained to relate important physical

and optical parameters with the distribution parameters.

$$
\begin{aligned}
V_{total} &= \int_{-\infty}^{\infty} \frac{4\pi}{3} r^3 n(\ln r) d\ln r = \frac{4\pi}{3} \sum_{i=1}^{2} r_{m,i} \exp\left(\frac{9}{2}\sigma_i^2\right) \\
A_{total} &= \int_{-\infty}^{\infty} \pi r^2 n(\ln r) d\ln r = \pi \sum_{i=1}^{2} r_{m,i}^2 \exp\left(2\sigma_i^2\right)
\end{aligned}
\tag{1.11}
$$

where V_{total} is the total volume and A_{totoal} is the total cross-section of the aerosol population. When the physical quantity of interest for the aerosol population is mass, sometimes it is convenient to use the volume distribution function which can be used to understand the contributions of different particle sizes to the total mass. As mentioned earlier, the cross-section of the particle that interacts with the incident radiation is more important for remote sensing applications. Therefore, area distribution of the aerosol population is useful in some instances. The relations among number, cross-section and particle distributions are summarized in Equation (1.12).

$$
\begin{aligned}
n_{vol}(\ln r) &= \frac{dV}{d\ln r} = \frac{4\pi r^3}{3}\frac{dN}{d\ln r} = \frac{4\pi r^3}{3} n(\ln r) \\
n_{cs}(\ln r) &= \frac{d\acute{S}}{d\ln r} = \pi r^2 n(\ln r)
\end{aligned}
\tag{1.12}
$$

In AERONET-based aerosol characterization studies (Dubovik et al., 2002; Omar et al., 2003), the bimodal log-normal distribution is used to represent the particle volume distribution of aerosols . By using Equation (1.10) and (1.12), the particle volume distribution can be written as,

$$
n_{vol}(\ln r) = \frac{dV(r)}{d(\ln r)} = \sum_{i=1}^{2} \frac{V_i}{\sqrt{2\pi}\sigma_{V,i}} exp\left[- \frac{(\ln r - \ln r_{V,i})^2}{2\sigma_{V,i}^2} \right] \tag{1.13}
$$

Figure (1.3) shows the volume distributions for desert dust (a) and biomass burning aerosols (b) from the aerosol models that were developed using 8-year world-

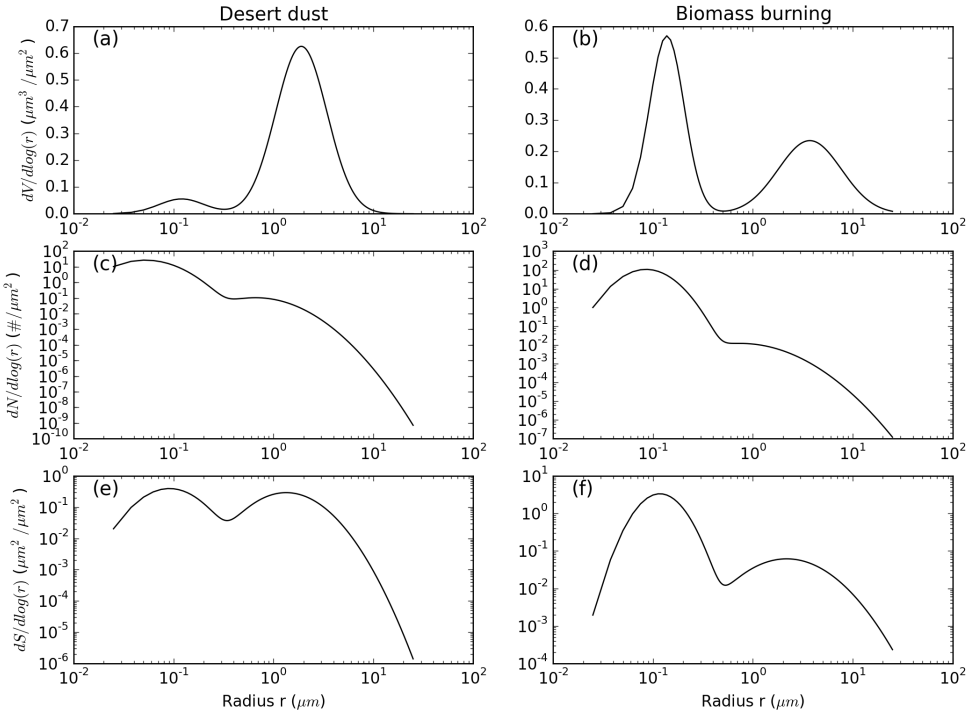

Figure 1.3: Particle volume distribution functions of desert dust (a) and biomass burning aerosols (b) from Dubovik et al. (2002) and corresponding particle size distribution functions (c, d) and cross-section distribution functions (e, f).

wide AERONET measurements (Dubovik et al., 2002). The desert dust volume distribution (Figure 1.3(a)) is based on the AERONET observations over Cape Verde and the biomass burning aerosol volume distribution (Figure 1.3(b)) is based on the observations from African savanna biomass burning. If we consider a unit volume of desert dust and biomass burning aerosols, for the desert dust case (Figure 1.3(a)), the coarser particles contribute more to the volume than the finer particles. But for the biomass burning aerosols (b), both modes contribute equally to the total volume. If the interested physical property is the cross-section which is more important

in terms of radiation interaction, the smaller particles contribute more to the total cross-section than the larger particles. Especially in the biomass burning aerosols' case, smaller particles show a substantial contribution to the total cross-section.

1.1.2 Refractive index

The index of refraction of a material is a key optical parameter which contains the information about how electromagnetic (EM) radiation propagate through that medium. In general, the refractive index (n) is a complex number ($n = n_r + n_c i$) where the real part (n_r) determines the phase velocity of the propagating wave and the imaginary part (n_i) determines the absorption associated with the propagation. Therefore, the refractive index plays a crucial role in determination of the single scattering properties of aerosol and clouds (discussed in Section 1.1.3).

The spectral dependence of the complex refractive index of water not only gives a colorful aesthetic appeal to the fascinating optical phenomena such as rainbow and glory, but also has important remote sensing implications. Figure (1.4) shows the spectral variation of the complex index of refraction of water (solid) and ice (dashed). A comprehensive characterization of the optical constants of water can be found in Hale and Querry (1973). From 0.4 μm to 1 μm spectral region, the n_r of pure water gradually decreases with the increasing wavelength which causes color dispersion. In contrast to n_r, the n_i of water is smaller in magnitude which corresponds to little absorption. Therefore in the visible wavelengths, the extinction of propagating light through clouds is dominated by the scattering. Thus the reflected

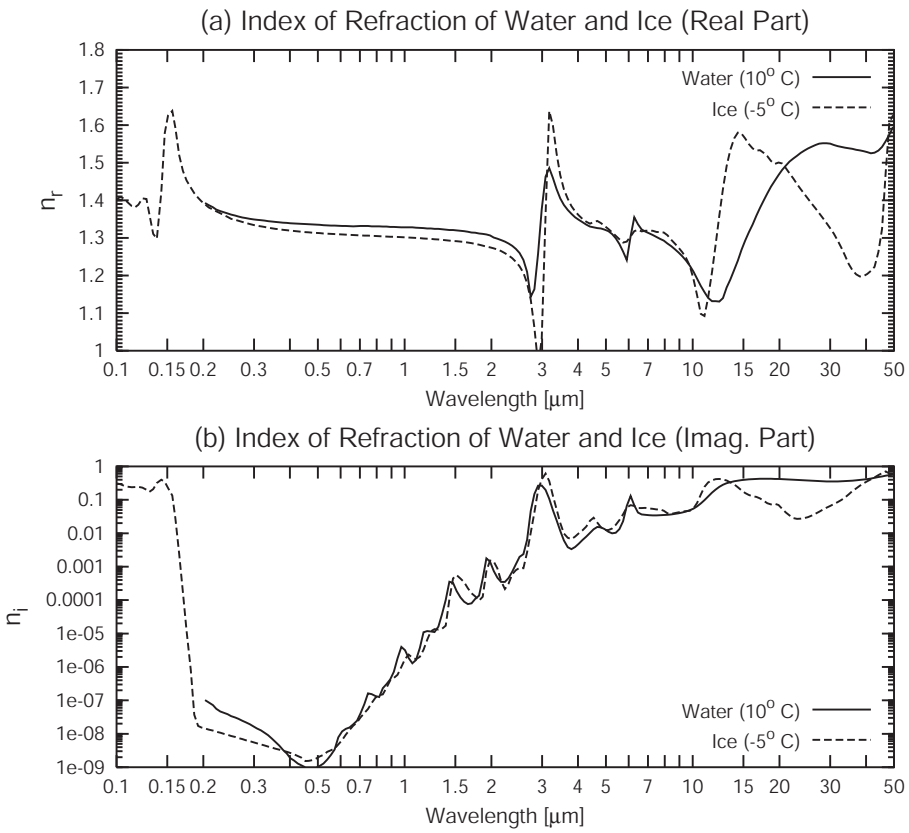

Figure 1.4: The spectral variation of the complex index of refraction of water (solid) and ice (dashed) (Petty, 2004).

visible light from clouds primarily contains the information about optical depth. The n_i of water has peaks near 1.5, 2.0 and 3.0 μm which explain the significant absorption that is associated with clouds. The reflected light at these wavelengths from clouds primarily contain the information about the droplet size (Nakajima and King, 1990). This mutually orthogonal sensitivity of the reflectance in non-absorbing and absorbing bands to the cloud optical depth and droplet size respectively has important remote sensing implications which are discussed in Section 1.2.

Unlike clouds, the complicated chemical composition of various types of aerosols makes the characterization of aerosol optical properties more challenging. Compared

to atmospheric gases or clouds, the high inhomogeneity and variability of aerosol populations add another level of complexity. Aerosols can be classified by the type of their sources of origination, as natural (desert dust, sea spray, volcanic ash, etc.) or anthropogenic (biomass-burning smoke, particles from fossil fuel combustion processes, etc.). These sources of originations also can be classified by the emissions of primary particulate matter(dust, volcanic ash, black carbon, etc.) or secondary particulate matter that derived from gaseous precursors (Sulphate, Nitrate).

Various attempts have been made to characterize the properties of aerosols. AERONET (AErosol RObotic NETwork) based studies like Dubovik et al. (2002) and Omar et al. (2003) characterize the physical and optical properties of aerosol to improve the satellite remote sensing algorithms. OPAC (Optical Properties of Aerosols and Clouds) is another such attempt that provides a software package which contains widely used microphysical and optical properties of six water clouds, three ice clouds, and 10 aerosol components (Hess et al., 1998). The OPAC can be used to get the optical properties of aerosols and water clouds (e.g. extinction coefficients, scattering coefficients, single scattering albedo and phase function) at 61 wavelengths between 0.25 and 40 μm. However, the size and the composition of hygroscopic aerosols change as the relative humidity increases. Thus the effective refractive index changes depending on the condensed water amount. The OPAC includes this effect by taking the volume weighted average of the refractive indices of the aerosol substance and water (Shettle and Fenn, 1979) and provides different sets of optical properties for eight different relative humidities.

1.1.3 Scattering properties of clouds and aerosols

In the scattering of radiation by the atmospheric particles, the size of the particles compared to the wavelength of the incident radiation plays a crucial role. The effect of particle size on scattering is often represented by a non-dimensional particle size parameter. For spherical particles, the size parameter x can be written as,

$$x = \frac{2\pi r}{\lambda} \tag{1.14}$$

where r is the radius and λ is the wavelength.

In general, the *Lorentz-Mie* solution to *Maxwell's equations* describes the scattering of electromagnetic radiation by a homogenous sphere. Depending on the value of size parameter x, we often identify different regimes of scattering such as *Rayleigh* ($x \ll 1$, e.g. scattering of visible light by molecules), Mie ($x \gtrsim 1$, e.g. scattering of visible light by clouds or aerosols) or geometric optics ($x >> 1$). By using Maxwell's equations for EM waves, an analytical solution for the single scattering properties of dielectric spheres with size parameter x was developed by Mie (Mie, 1908; Horvath, 2009). At the presence of an external electric field, dielectric spheres get polarized and become small electric dipoles. The strength of these dipoles (*polarizability*) depends on the *permittivity* (ϵ, SI unit: Farad per meter $[F/m]$) and the *permeability* (μ, SI unit: Newtons per Ampere squared $[N/A^2]$) of the material which can be characterized by the complex refractive index. From Mie theory, for a spherical dielectric particle of a given size parameter x, the scattering efficiency Q_s and the

extinction efficiency Q_e can be written as,

$$\begin{aligned} Q_s &= \frac{\sigma_s}{\pi r^2} = \frac{2}{x^2}\sum_{m=1}^{\infty}(2m+1)(|a_m|^2+)|b_m|^2) \\ Q_e &= \frac{\sigma_e}{\pi r^2} = \frac{2}{x^2}\sum_{m=1}^{\infty}(2m+1)Re(a_m+b_m) \end{aligned} \tag{1.15}$$

where σ_s is the scattering cross-section (in units of area) which represents the amount of incident energy scattered from the original direction, σ_e is the extinction cross-section which represents the amount of incident energy lost by both scattering and absorption, a_m and b_m are called the *Mie* scattering coefficients (functions of size parameter x and complex refractive index n) which can be calculated using recursion relations for the spherical Bessel functions. The absorption cross-section (σ_a) and efficiency (Q_a) can be found from the energy conservation principle.

$$\begin{aligned} \sigma_a &= \sigma_e - \sigma_s \\ Q_a &= Q_e - Q_s \end{aligned} \tag{1.16}$$

Based on Q_s and Q_e, the single scattering albedo (SSA) ω can be written as,

$$\omega = \frac{Q_s}{Q_e} \tag{1.17}$$

which represents the fraction of extinction due to scattering. Larger SSA implies significant scattering while smaller SSA indicates more absorption.

By representing the incident and scattered light in the form of Stokes vectors (see Section 1.1.4 Equation 1.31) $\vec{I_0}$ and $\vec{I}$ respectively, we can write,

$$\vec{I} = \frac{[S_{ij}(\Theta_s)]}{k^2 r^2}\vec{I_0} \tag{1.18}$$

where Θ_S is the scattering angle, $k(=2\pi/\lambda)$ is the wave vector, and $[S_{ij}(\Theta_S)]$ is the *scattering matrix* (*Muller matrix* for scattering by single particle) which describes

the relationship between the incident and scattered Stokes vectors. In remote sensing and also in atomic and nuclear physics, the angular distribution of scattered radiation energy is an important physical quantity which is also called *differential scattering cross-section*. The *Differential scattering cross-section* is symbolically denoted by $d\sigma_s/d\Omega$ which is *not* a derivative function of Ω but merely a symbolic representation where Ω is the solid angle. To conveniently represent the angular distribution of the scattered radiation energy, in remote sensing, the so-called *scattering phase function* is defined as follows,

$$p(\Omega) = \frac{4\pi}{\sigma_s k^2} \frac{d\sigma_s}{d\Omega} \tag{1.19}$$

By combining the concepts of *scattering matrix* and *scattering phase function*, it is also conventional to define the *phase matrix* $[P_{ij}(\Theta_S)]$ as,

$$[P_{ij}(\Theta_S)] = \frac{4\pi}{k^2 \sigma_s} [S_{ij}(\Theta_S)] \tag{1.20}$$

Phase matrix elements $P_{ij}(\Theta_S)$ represent the angular probability density functions (PDF) of scattered polarized light. In general, the scattering phase matrix contains 16 non-zeros elements. But for a single homogeneous spherical particle the scattering phase function reduces to 8 non-zero elements as follows,

$$[P_{ij}(\Theta_S)]^{sp} = \begin{bmatrix} P_{11}(\Theta_S) & P_{12}(\Theta_S) & 0 & 0 \\ P_{12}(\Theta_S) & P_{11}(\Theta_S) & 0 & 0 \\ 0 & 0 & P_{33}(\Theta_S) & P_{34}(\Theta_S) \\ 0 & 0 & -P_{34}(\Theta_S) & P_{33}(\Theta_S) \end{bmatrix} \tag{1.21}$$

Warren Wiscombe (Wiscombe, 1979) developed a code based on Mie theory which is widely used in the field to obtain aforementioned single-scattering prop-

erties (i.e. Q_s, Q_e, $[P_{ij}(\Theta_S)]^{sp}$, etc.) of a spherical particle by providing complex refractive index n and size parameter x. However, as mentioned in Section 1.1.1, both aerosols and clouds exists in nature as populations of particles with size variabilities. Therefore to represent the light scattering from clouds or aerosols we average the single scattering properties over the appropriate PSD and obtain the bulk scattering properties as follows,

$$\begin{aligned} \langle Q_s \rangle &= \frac{\int_0^\infty \pi r^2 \omega(r) Q_e(r) n(r) dr}{\int_0^\infty \pi r^2 n(r) dr} \\ \langle Q_e \rangle &= \frac{\int_0^\infty \pi r^2 Q_e(r) n(r) dr}{\int_0^\infty \pi r^2 n(r) dr} \\ [\langle P_{ij}(\Theta_S) \rangle] &= \frac{\int_0^\infty \pi r^2 \omega(r) Q_e(r) [P_{ij}(\Theta_S)] n(r) dr}{\int_0^\infty \pi r^2 \omega(r) Q_e(r) n(r) dr} \end{aligned} \tag{1.22}$$

Similarly, average scattering cross-section and average extinction cross-sections can be obtained as follows,

$$\begin{aligned} \langle \sigma_s \rangle &= \frac{\int_0^\infty \pi r^2 \omega(r) Q_e(r) n(r) dr}{\int_0^\infty n(r) dr} \\ \langle \sigma_e \rangle &= \frac{\int_0^\infty \pi r^2 Q_e(r) n(r) dr}{\int_0^\infty n(r) dr} \end{aligned} \tag{1.23}$$

By using $\langle Q_s \rangle$ and $\langle Q_e \rangle$ in Equation (1.22), we can define the *volume scattering coefficient* β_s and the *volume extinction coefficient* β_e as follows,

$$\begin{aligned} \beta_s &= \langle Q_s \rangle N_{tot} = \int_0^\infty \pi r^2 \omega(r) Q_e(r) n(r) dr \\ \beta_e &= \langle Q_e \rangle N_{tot} = \int_0^\infty \pi r^2 Q_e(r) n(r) dr \end{aligned} \tag{1.24}$$

It is useful to define the *optical thickness* $\Delta\tau$ which represents the amount of light removed from the incident EM wave when it travels from one point to another through the a medium. The $\Delta\tau$ can be written as follows,

$$\Delta\tau = \int_a^b \beta_e(s) ds \tag{1.25}$$

where s is the path length.

In the satellite remote sensing, the vertical optical thickness from the top-of-atmosphere (TOA) to a particular level is often define as the *optical depth*, which can be written as follows,

$$\tau(z) = \int_{TOA}^{z} \beta_e(s) ds \tag{1.26}$$

1.1.4 Radiative transfer of polarized light

Propagation of electromagnetic radiation through matter can be fundamentally explained by using the general form of the radiative transfer equation (RTE). If the monochromatic radiance I travels a distance ds through a medium, the general form of RTE can be written as,

$$\frac{dI(s,\acute{\Omega})}{k_m \rho ds} = -I(s,\acute{\Omega}) + J(s,\acute{\Omega}) \tag{1.27}$$

where J is the "source term" which includes the radiance added into the beam either from emission or scattering, k_m is the mass extinction cross-section (in area/mass), and ρ is the density of the material. By using the concept of volume extinction coefficient in Equation (1.24), we can write,

$$\beta_e = k\rho \tag{1.28}$$

From Equation (1.28) and (1.27), the general form of RTE can be written as,

$$\frac{dI(s,\acute{\Omega})}{\beta_e ds} = -I(s,\acute{\Omega}) + J(s,\acute{\Omega}) \tag{1.29}$$

In the absence of source term J, Equation (1.29) becomes the well-knows *Beer-Lambert* law. For a non-scattering medium in a local thermodynamic equilibrium,

the source term J becomes the *Planck function*, and consequently Equation (1.29) becomes the *Schwarzschild's equation*. This is the case for the transfer of thermal infrared radiation emitted from the Earth and the atmosphere. Other than the thermal emission, the light scattered through the medium itself also can become another "source term" for the propagating radiation. In fact, this scattered light from various types of atmospheric constituents such as molecules, cloud droplets, and aerosols not only give rise to many interesting optical phenomena (blue sky, rainbows, halos, etc.) but also provide an opportunity to remotely retrieve the information about the scattering medium.

The polarization state of scattered light contains additional information about the scattering medium than the total radiance alone. The complete polarization state of an EM wave can be represented by the *Stokes vector* which has four-elements referred to as the *Stokes parameters*. Fundamentally, the polarization state of an EM wave is described by the oscillation of the electric field vector and the phase difference between the two orthogonal decompositions of this vector into one parallel field E_l and one perpendicular field E_r to the scattering plane. By expressing E_l and E_r as complex oscillating functions as in Equation (1.30) where ω is the circular frequency, and $i = \sqrt{-1}$, we can write down the Stokes vector $\vec{I}$ as in Equation (1.31).

$$\begin{aligned} E_l &= a_l \exp\left[-i\left(\frac{2\pi}{\lambda}z - \omega t + \delta_l\right)\right] \\ E_r &= a_r \exp\left[-i\left(\frac{2\pi}{\lambda}z - \omega t + \delta_r\right)\right] \end{aligned} \tag{1.30}$$

$$\vec{I} = \begin{bmatrix} I \\ Q \\ U \\ V \end{bmatrix} = \begin{bmatrix} E_l E_l^* + E_r E_r^* = a_l^2 + a_r^2 \\ E_l E_l^* - E_r E_r^* = a_l^2 - a_r^2 \\ E_l E_r^* + E_r E_l^* = 2a_l a_r cos(\delta) \\ i(E_r E_l^* - E_l E_r^*) = 2a_l a_r sin(\delta) \end{bmatrix} \tag{1.31}$$

where the superscripts * denote the complex conjugate and $\delta = \delta_r - \delta_l$ is the phase difference between perpendicular (δ_r) and parallel (δ_l) fields. To exploit the polarization description of light in radiative transfer, we can replace the scalar monochromatic intensities I and J in Equation (1.29) by the vector intensities $\vec{I}$ and $\vec{J}$. Consequently, the general form of RTE for polarized light becomes,

$$\frac{d\vec{I}(s,\acute{\Omega})}{\beta_e ds} = -\vec{I}(s,\acute{\Omega}) + \vec{J}(s,\acute{\Omega}) \tag{1.32}$$

By introducing the optical thickness measured downwards from TOA as the vertical coordinates, the RTE for polarized light can be written as,

$$\begin{aligned} \mu\frac{d\vec{I}(\tau,\mu,\phi)}{d\tau} &= \vec{I}(\tau,\mu,\phi) - \vec{J}(\tau,\mu,\phi) \\ \vec{J}(\tau,\mu,\phi) &= \frac{\langle\omega\rangle}{4\pi}\int_0^{2\pi}\int_{-1}^{1} L(\pi - i_2)P(\Theta_S)L(-i_1)I(\tau,\mu^{'},\phi^{'})d\mu^{'}d\phi^{'} \end{aligned} \tag{1.33}$$

where L is the *rotation matrix* of the Stokes parameters , i_1 and i_2 are rotational angles (Liou, 2002).

1.2 Remote sensing techniques

1.2.1 The bispectral retrieval technique

Among many satellite-based cloud remote sensing techniques, the so-called bispectral solar reflective method is a widely used method to simultaneously infer

the cloud optical thickness (COT) and cloud droplet effective radius (CER) from satellite observation of cloud reflectance (Nakajima and King, 1990). This method uses cloud reflectance measurements from a pair of spectral bands. One is in the visible or near-infrared **(VIS/NIR)** spectral region (e.g., $0.64\mu m$ or $0.86\mu m$) where water absorption is negligible and therefore cloud reflection generally increases with COT. The other measurement is usually in the shortwave infrared (SWIR) spectral region (e.g., $2.1\mu m$ or $3.7\mu m$), where water droplets are moderately absorptive and cloud reflectance generally decreases with increasing r_e for optically thick clouds. This technique is widely used in the earth-observing satellites such as Moderate Resolution Spectro-radiometer (MODIS, (Platnick et al., 2003)) and Spinning Enhanced Visible and Infrared Imager (SEVIRI, (Roebeling et al., 2006)).

For a given solar viewing geometry (μ, μ_0, ϕ) Figure (1.5) shows the relationships between one water non-absorbing wavelength ($0.75\mu m$) and water absorbing wavelength ($2.16\mu m$) for various values of cloud optical thickness (τ) and effective radii (r_e). The VNIR band (Visible to Near Infrared) $0.75\mu m$ has a low absorption, thus dominated by multiple scattering which in turn provides sensitivity to τ. Therefore in Figure (1.5), for a given r_e, VNIR reflectance is primarily a function of τ. In the SWIR (Short Wave Infrared) band $2.16\mu m$, cloud droplets are moderately absorptive, thus sensitive to r_e. This nature is depicted from the vertical dashed lines in Figure (1.5). However, stronger absorption restricts the microphysics retrieval only to the uppermost part of the cloud. A simultaneous observation from the two bands corresponds to a point in the LUT (look-up-table) space in Figure (1.5). The circles that are shown in Figure (1.5) are such observations from a marine

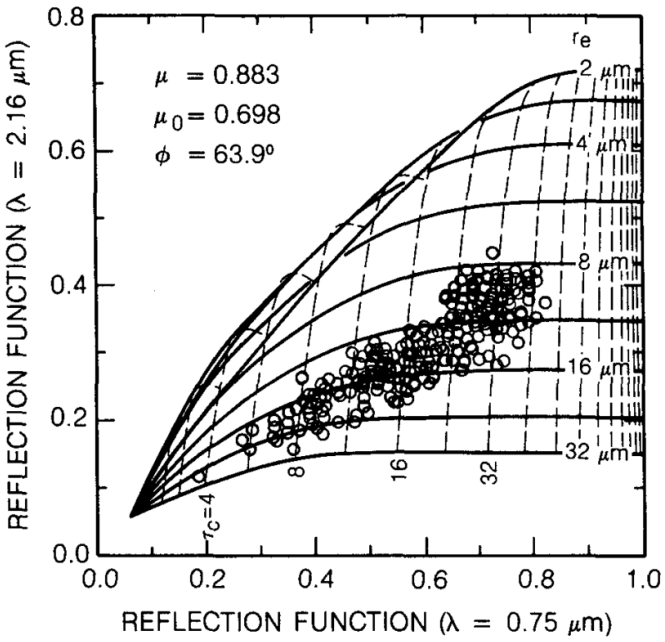

Figure 1.5: Theoretical relationships between one water non-absorbing wavelength $0.75\mu m$ and water absorbing wavelength $2.16\mu m$ for various values of cloud optical thicknesses and effective radii. Circles are observed reflectances from a marine stratocumulus cloud (Nakajima and King, 1990). The "Reflection Function" is the total reflectance of the indicated wavelength.

stratocumulus cloud. Based on these observed reflectances, a two-dimensional inverse interpolation method can be implemented to retrieve r_e and τ simultaneously. However, in smaller optical depths the retrieval uncertainty increases as the orthogonal behavior of the isolines become less significant. Moreover, this non-linearity in the LUT has implications in the cloud retrievals with high inhomogeneity in the pixel level (Zhang et al., 2012, 2016a).

1.2.2 The polarimetric retrieval technique

The bispectral method relies on the total reflectance (I) from the cloud field. The polarized reflectance (Q) from a cloud field which was first quantitatively measured from a spaceborne instrument POLDER (Polarization and Directionality of Earth Reflectance, (Deschamps et al., 1994)) shows a color dispersive supernumerary bow feature over the cloud for scattering angle 150 to 160 degrees as wavelength varies. The directional signature of the polarized reflectance Q can be exploited to retrieve both r_e and v_e of the underlying cloud's PSD (Bréon and Goloub, 1998; Bréon and Doutriaux-boucher, 2005). The directional signature of polarized light has potential applications in aerosol, cloud and plankton remote sensing which caused to emerge several airborne polarimeters such as Airborne Multiangle Spectro-Polarimetric Imager (AirMSPI, (Diner et al., 2013)) and Air-HARP(Hyperangular Rainbow Polarimeter, (Martins et al., 2017)) and space-borne missions such as HARP and PACE (Werdell, 2017).

Since the singly-scattered radiation is the major contribution to the polarized reflectance, its measurement is directly related to the polarized phase function $P_{12}(\Theta_S)$. Consider a monochromatic incident flux F_o upon a homogeneous cloud layer of τ^* optical thickness at μ_o incident cosine. The single scattering contribution

to TOA reflectance can be written as,

$$
\begin{aligned}
I[\tau = 0, \mu, \phi] &= \int_0^{\tau^*} J[\tau^{'}, \mu, \phi] e^{\tau^{'}/\mu} d\tau/\mu \\
&= \int_0^{\tau^*} \frac{\omega F_o}{4\pi} P[\Theta_s(\mu, \phi, \mu_o, \phi_o)] e^{\tau^{'}/\mu_o} e^{\tau^{'}/\mu} d\tau/\mu \\
&= \frac{\omega F_o}{4\pi} P[\Theta_s(\mu, \phi, \mu_o, \phi_o)] \int_0^{\tau^*} e^{-\frac{\mu+\mu_o}{\mu\mu_o}\tau^{'}} d\tau/\mu \\
&= \frac{\omega \mu_o F_o}{4\pi(\mu + \mu_o)} P[\Theta_s(\mu, \phi, \mu_o, \phi_o)] \left[1 - e^{-\frac{\mu+\mu_o}{\mu\mu_o}\tau^*}\right]
\end{aligned}
$$

When, $\omega = 1, e^{-\frac{\mu+\mu_o}{\mu\mu_o}\tau^*} \simeq 0$, the singly-scattered polarized reflectance can be written as,

$$
R_p = \frac{\pi Q[\tau = 0, \mu, \phi]}{\mu_o F_o} = \frac{P_{12}[\Theta_s(\mu, \phi, \mu_o, \phi_o)]}{4(\mu + \mu_o)}
$$

Therefore, we can obtain a relationship between polarized phase function P_{12} and the singly-scattered polarized reflectance as follows,

$$
R_p^* = 4(\mu + \mu_o) R_p[\Theta_s(\mu, \phi, \mu_o, \phi_o)] = P_{12}[\Theta_s(\mu, \phi, \mu_o, \phi_o)] \tag{1.34}
$$

Figure (1.6) shows $P_{12}(\Theta_S)$ for different cloud droplet size distributions (DSD) which are characterized by different r_e and v_e values. In Figure 1.6(b), as v_e increases the magnitude of the supernumerary bow (around 152^o) decreases and the amplitudes of the oscillations eventually smoothing out as v_e further increases. It is important to note this behavior because as v_e increases (ie. as DSD bocomes less mono-disperse) the pattern of $P_{12}(\Theta_S)$ becomes less significant and consequently retrievals become less sensitive to r_e and v_e. As r_e increases in Figure 1.6(c) the supernumerary bow features become narrower and shift towards smaller scattering angles. Figure 1.6(a) shows the $P_{12}(\Theta_S)$ for three wavelengths. Though the

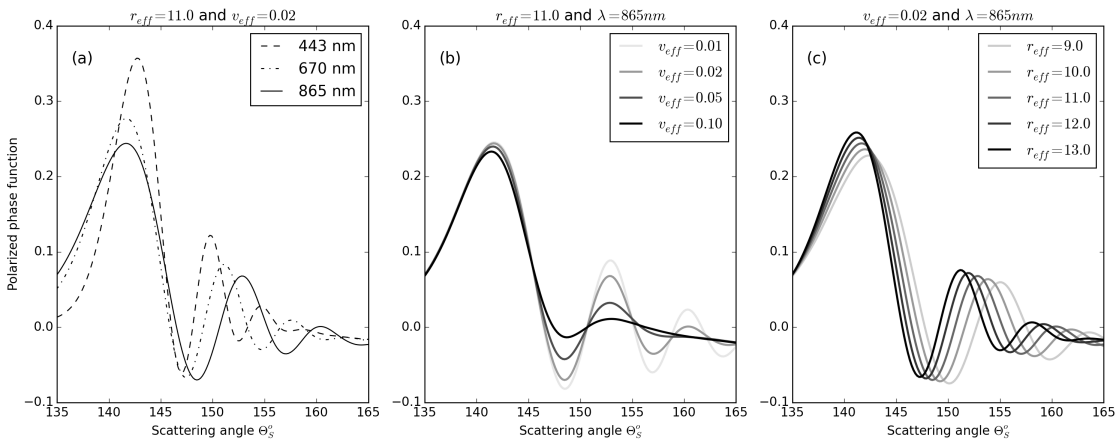

Figure 1.6: Polarized phase function $P_{12}(\Theta_S)$ as a function of scattering angles for different wavelengths (a), v_e values (b) and r_e values.

pattern of the function is the same, the peak position of the supernumerary bow shifts as wavelength decreases which cause cloudbow type color dispersion around the supernumerary bow that is observable in POLDER images of polarized light.

A parametric curve fitting retrieval technique (Alexandrov et al., 2012) can be implemented to match the angular pattern of the polarized reflectance with a library of $P_{12}(\Theta_S)$ curves of varying r_e and v_e in order to retrieve appropriate r_e and v_e values. The τ retrievals can not be directly obtained via the polarimetric technique. But with known r_e, v_e, and conjunction with bispectral retrieval technique (Section 1.2.1) we can develop a hybrid technique to retrieve r_e, v_e and τ simultaneously.

Chapter 2: Aerosol-cloud retrieval simulator

In this study, we extended the Aerosol-Cloud Retrieval Simulator setup (hereafter referred to as ACRS) of ACROS (Aerosol, Cloud, Radiation-Observation and Simulation) research group at UMBC which was only coupled with 1D radiative transfer simulations (Miller et al., 2016, 2017) to perform both radiometric and polarimetric 3D radiative transfer. ACRS takes simulated cloud and aerosol properties as inputs to drive MSCART (Multiple-Scaling-based Cloudy Atmospheric Radiative Transfer) (Wang et al., 2017a) 3D Monte Carlo Radiative Transfer code. The simulated reflectances obtained with MSCART are then used to retrieve the aerosol and cloud properties. To study the influences of the 3D radiative effects, we compared the retrieved properties with the input physical and optical properties to the simulations.

2.1 3D Monte-Carlo radiative transfer simulations

Compared to the other radiative transfer simulation methods, Monte-Carlo method has more flexibility hence requires fewer simplifications. This allows us to handle realistic atmosphere consisting of three-dimensionally optical/microphysical properties and complicated geometries associated with remote sensing. Moreover, a

Monte-Carlo simulation can be decomposed into intermediate steps to study the impacts from different scattering orders (Mayer, 2009). However, additional flexibility costs a considerable amount of computational power, especially when the considering medium has a highly forward-peaked phase function such as cloud droplets or ice crystals. In such cases, relatively less-important scattering events contribute more to the radiance which requires more sampling to reduce the noise. Most MC RT codes employs some type of variance reduction such as Scattering Phase Function Forward Truncation (SPFFT) technique and Target Directional Importance Sampling (TDIS) technique to tackle the forward-peaked phase function in order to accelerate the convergence rate(Hu et al., 2000; Nakajima and Asano, 1977; Wiscombe, 1977). In SPFFT, the sharp forward peak of the phase function is truncated for each order of scattering adaptively. In TDIS, the extinction coefficients of the optically thin regions are increased in each order of scattering which could increase the collision chance in those regions with low sampling chance(Wang et al., 2011). The Multiple-Scaling-based Cloudy Atmospheric Radiative Transfer (MSCART, (Wang et al., 2017a,b)) model that we use in our study combines both SPFFT technique and TDIS technique to increase the efficiency.

2.2 1D simplified cloud fields

In this study, to understand the basic physics behind the horizontal photon transfer and their impacts on the reflectances and retrieval, simplified hypothetical 1D cloud fields have been used. Among them, the simplest 1D cloud field is called

the "step cloud" which has an optically thick region surrounded by two adjacent optical thin regions as shown in Figure 2.1. Although the step cloud field is useful to get a simple and intuitive understanding on the physics of photon propagation, it is far from the actual clouds. In addition to the step cloud case, the well-known bounded cascade model has been used as the second simplified cloud model. Both of these models are used in Chapter 6 to explain the 3D RT effects in the bi-spectral and polarimetric retrievals (Section 6.3) before introducing a new method to detect and correct strong positive COT biases in the bi-spectral retrievals.

2.2.1 Step cloud

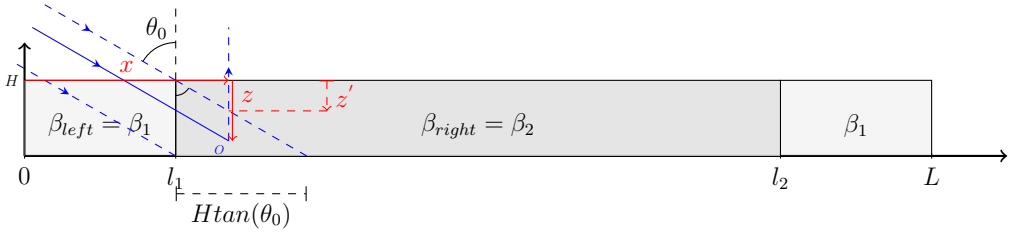

Figure 2.1: Illustration of the hypothetical step cloud. The specific step cloud case that is used in this section has following features. $H = 1km$, $l_1 = 2km$, $l_2 = 10km$, $\beta_1 = 0.1km^{-1}$ and $\beta_2 = 10km^{-1}$. The darker and lighter regions correspond to the optically thick and thin regions respectively.

Figure 2.1 illustrates a step cloud which has a homogeneous optically thin regions from 0 to l_1 and l_2 to L and an optically thick region with a step-wise rise and drop at l_1 and l_2 respectively. We can use this step cloud model to derive a theoretical expression for the observed reflectance at each point of the TOA to understand the

impact of the horizontal photon transfer. A simple analytical solution can be derived to obtain the single scattering 3D reflectance ($I_{SS}(x)$) for nadir viewing geometry as shown in Equation 2.1. The solution simply becomes solving a geometrical problem which allows to characterize the variability of the reflectance by the value of $z^{'}$ as defined in Equation 2.3. This type of single scattering solution would be more useful in explaining 3D polarized reflectance because they are strongly dominated by single scattering. The analytical solution to the single scattering 3D polarized reflectance ($Q_{SS}(x)$) of unpolarized incident light for nadir viewing geometry can be obtained by replacing $P_{11}(\Theta_S)$ with $P_{12}(\Theta_S)$.

In the expression in Equation 2.1, the singly-scattered reflectance at each point x is a function of $z^{'}$ which is defined in Equation 2.3. In Equation 2.3, $z^{'}$ is a function of horizontal coordinate x only when $l_1 < x < l_1 + Htan(\Theta_0)$ or $l_2 < x < l_2 + Htan(\Theta_0)$. Therefore the singly-scattered horizontal photon transportation only affects the edges extending $Htan(\theta_o)$ distance into the optically thick cloud region from $x = l_1$ and a same distance outward to optically thin region from $x = l_2$. The variability of the reflectance is characterized by $z^{'}(x, \theta_0)$.

$$\frac{4\pi I_{SS}(x)}{F_0 \beta_{right} \omega_{right} P_{11}(\Theta_S)} = \frac{1}{\beta_{right} C_1}\left[1 - e^{-\beta_{right} C_1 z^{'}}\right] + \frac{e^{-(\beta_{right}-\beta_{left})\frac{z^{'}}{\mu_0}}}{C_2}\left[e^{-C_2 z^{'}} - e^{-HC_2}\right] \tag{2.1}$$

ω_{right} is the single scattering albedo (correspond to β_{right}) of the middle part of the step cloud in Figure 2.1. The *left* and *right* subscripts indicate the region to the left

and right side from $x = l_1$.

$$\begin{aligned} C1 &= \frac{1}{\mu_0} + \frac{1}{\mu_v} \\ C2 &= \frac{\beta_{left}}{\mu_0} + \frac{\beta_{right}}{\mu_v} \end{aligned} \tag{2.2}$$

$$z^{'} = \begin{cases} H, & \text{if } 0 < x < l_1 \\ \frac{x-l_1}{tan(\theta_0)}, & \text{if } l_1 < x < l_1 + Htan(\theta_0) \\ H, & \text{if } l_1 + Htan(\theta_0) < x < l_2 \\ \frac{x-l_2}{tan(\theta_0)}, & \text{if } l_2 < x < l_2 + Htan(\theta_0) \\ H, & \text{if } l_2 + Htan(\theta_0) < x < L \end{cases} \tag{2.3}$$

$$\beta_{left} = \begin{cases} \beta_1, & \text{if } 0 < x < l_1 + Htan(\theta_0) \\ \beta_2, & \text{if } l_1 + Htan(\theta_0) < x < l_2 + Htan(\theta_0) \\ \beta_1, & \text{if } l_2 + Htan(\theta_0) < x < L \end{cases} \tag{2.4}$$

$$\beta_{right} = \begin{cases} \beta_1, & \text{if } 0 < x < l_1 \\ \beta_2, & \text{if } l_1 < x < l_2 + Htan(\theta_0) \\ \beta_1, & \text{if } l_2 + Htan(\theta_0) < x < L \end{cases} \tag{2.5}$$

$$\begin{aligned} \mu_0 &= cos(\theta_0) \\ \mu_v &= cos(\theta_v) = 1 \end{aligned} \tag{2.6}$$

2.2.2 Fractal cloud

Though the step cloud case is very useful to demonstrate and understand certain physical principles, it is too simple from realistic cloud fields. Hence we will use a well-known fractal cloud generation model, the bounded cascade model (Cahalan et al., 1994) to generate our second hypothetical 1D cloud field which is hereafter referred as the fractal cloud for short.

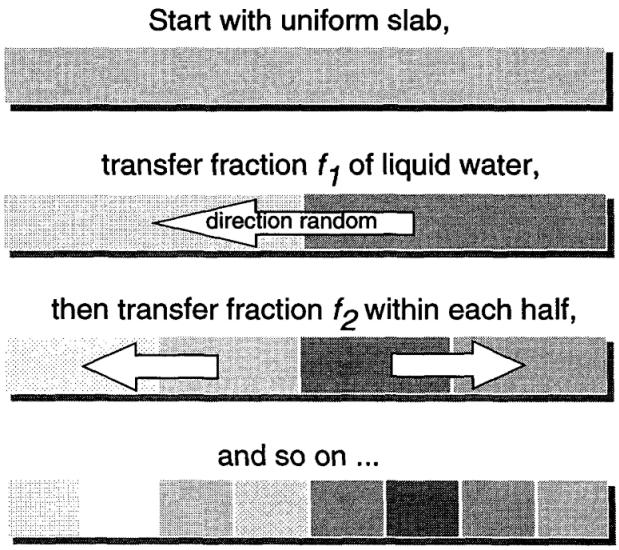

Figure 2.2: Schematic of bounded cascade model (Cahalan et al., 1994) which uses a two-parameter multiplicative recurrent process that allows simulating the realistic horizontal spatial distribution of the cloud liquid water path (LWP) when the mean LWP is known.

The bounded cascade model is a two-parameter multiplicative recurrent process that allows simulating the realistic spatial distribution of the cloud LWP when the mean LWP is known (Davis and Marshak, 2010; Marshak et al., 1994). The

modeling process starts with a uniform plane-parallel cloud slab with a constant mean LWP as shown in Figure 2.2. This initial cloud slab has a finite geometrical thickness vertically (z) and along one horizontal direction (x). The cloud is infinite along the other horizontal direction (y). The recursive procedure proceeds as follows: divide the uniform slab into two halves from the middle of the x dimension, and transfer f_0 fraction of water mass from one side to the other chosen randomly with equal probability. Subsequently, each of the new halves is treated as two separate slabs and sub-divided into two new halves. A fraction f_1 of water is transfer among adjacent halves with chosen randomly with equal probability. This process continues multiple times to produce fractal-like LWP variation along the x dimension.

2.3 LES cloud fields

Simplified 1D cloud fields e.g., step cloud and fractal cloud models are helpful to develop a fundamental understanding of the 3D RT effects. To mimic the real clouds in nature, more sophisticated cloud fields from LES models have been used, namely the simulated cloud fields from DHARMA Large-Eddy Simulation (LES) model (Ackerman et al., 2004; Zhang et al., 2012; Miller et al., 2016). DHARMA model provides detailed bin microphysics based on basic physical relationships to describe droplet activation, condensation, collision-coalescence, and sedimentation. Four LES scenes that cover different optical and microphysical properties have been used in this study. The LWP of each selected LES scene are shown in Figure 2.3.

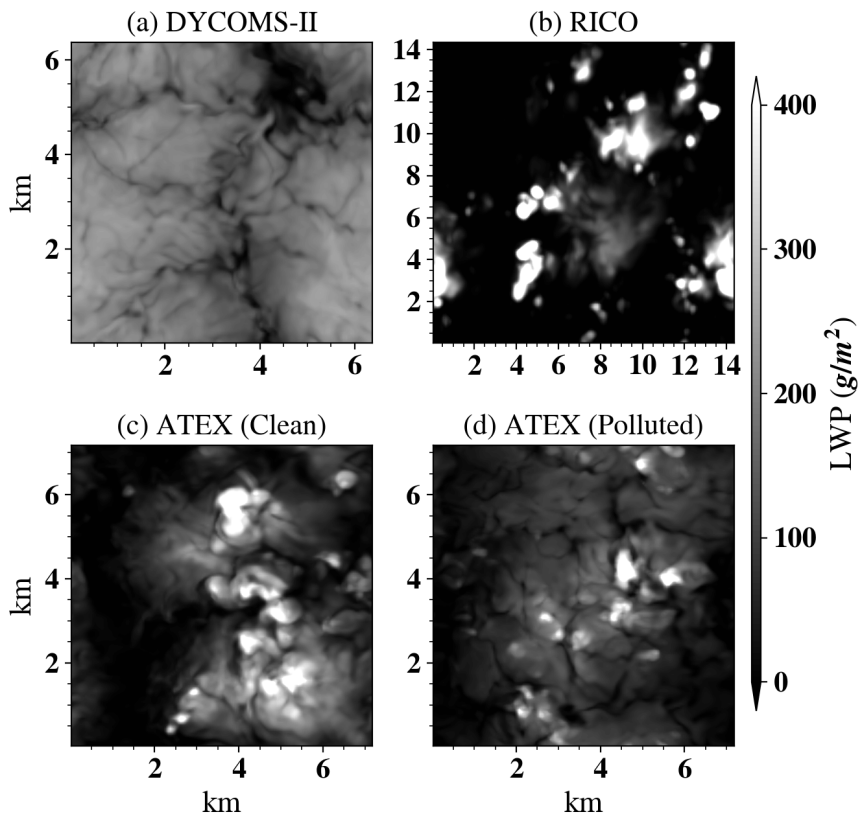

Figure 2.3: Liquid water path of (a) DYCOMS-II (Stevens et al., 2003) (b) RICO (Rauber et al., 2007), (c) ATEX-clean, and (d) ATEX-polluted (Stevens et al., 2001) LES scenes from DHARMA LES model (Ackerman et al., 2004)

.

Cloud properties and LES domain specification of each case are summarized in Table 2.1.

The first LES case in Figure 2.3 (a) is based on the idealized conditions observed during the research flight of Second Dynamics and Chemistry of Marine Stratocumulus project (hereafter referred to as DYCOMS-II,(Stevens et al., 2003)). The DYCOMS-II case (Figure 2.3 (a)) has the largest cloud fraction (100% overcast

Table 2.1: Summary of cloud properties and domain specifications for selected LES cloud cases. Cloud mask definition is based on the simulated 1D total reflectance at 0.860 μm wavelength ($R^{1D}_{I,0.860\mu m} > 0.02$). Cloud properties are from the vertically-weighted pseudo retrievals (Section 2.4). SZA=40^o, VZA=0. The columns from left to right are case name, cloud fraction, mean LWP [g/m^2], mean COT, standard deviation of COT, mean CER, mean CEV, horizontal grid unit [m], vertical grid unit [m], number of grids and domain size respectively.

case	CF	mean(LWP)	mean(τ)	std(τ)	mean(r_e)	mean(v_e)	dxdy	dz	Num. of grids	Domain size
DY	99.72	165.98	17.92	6.25	15.73	0.06	50	varies	128x128x96	6.4x6.4x1.5
RC	41.23	58.05	3.27	8.96	28.29	0.25	100	40	144x144x100	14.3x14.3x4
AC	91.29	86.26	7.44	8.00	17.00	0.15	50	varies	144x144x200	7.1x7.1x3
AP	97.77	73.63	17.22	14.75	7.31	0.13	50	varies	144x144x200	7.1x7.1x3

cloud domain) among all four selected cases and has relatively minimal microphysical variability. It represents the usual properties of marine stratocumulus clouds. The second case (Figure 2.3 (b)) is referred to as the "RICO" case (Rain In shallow Cumulus over the Ocean (Rauber et al., 2007)) which has predominant cloud-free regions (mean cloud fraction $\sim 41\%$) compared to the other three cases with drastic optical and microphysical variability which is challenging in 3D radiative transfer simulations. These two cases have been used throughout the study to test and investigate two extreme scenarios in cloud remote sensing.

ATEX-clean (Figure 2.3 (c)) and ATEX-polluted (Figure 2.3 (d)) cases are based on an idealized case study from the Atlantic Trade wind Experiment (ATEX, Stevens et al. (2001)) with different aerosol loadings. ATEX cases represent the

scattered cumulus / broken stratocumulus regime.

2.4 Vertically weighted pseudo retrievals

An LES domain contains detailed information about the vertical profile of each column. To assess different retrieval approaches relative to the LES cloud properties, we derived reference cloud properties based on the vertical weighting method which was introduced by Platnick (2000) and adopted in many later studies (Alexandrov et al., 2012; Zhang et al., 2017; Miller et al., 2017). When μ_o and μ are the cosines of the solar and viewing zenith angles, an analytical vertical weighting function for optical thickness τ can be approximated as follows,

$$\begin{aligned} w(\tau) &= c\tau^b e^{-a\tau\left(\frac{1}{\mu}+\frac{1}{\mu_o}\right)} \\ c &= 1/\int_0^{\tau_{tot}} w(\tau)d\tau \end{aligned} \tag{2.7}$$

where 'a' and 'b' are strictly positive parameters which scale the multiple scattering effects (Zhang et al., 2017; Miller et al., 2017). 'a' parameterizes the optical thickness for the multiple scattering ($0 < a \leq 1$, $a = 1$ for single scattering) and 'b' determines the peak of the vertical weighting function which corresponds to the penetration depth. c is a constant which normalizes the weighting function to the total optical thickness. Figure 2.4 shows an example of vertically-weighted cloud properties for each LES scene in Figure 2.3 assuming $a = 1$ and $b = 0$.

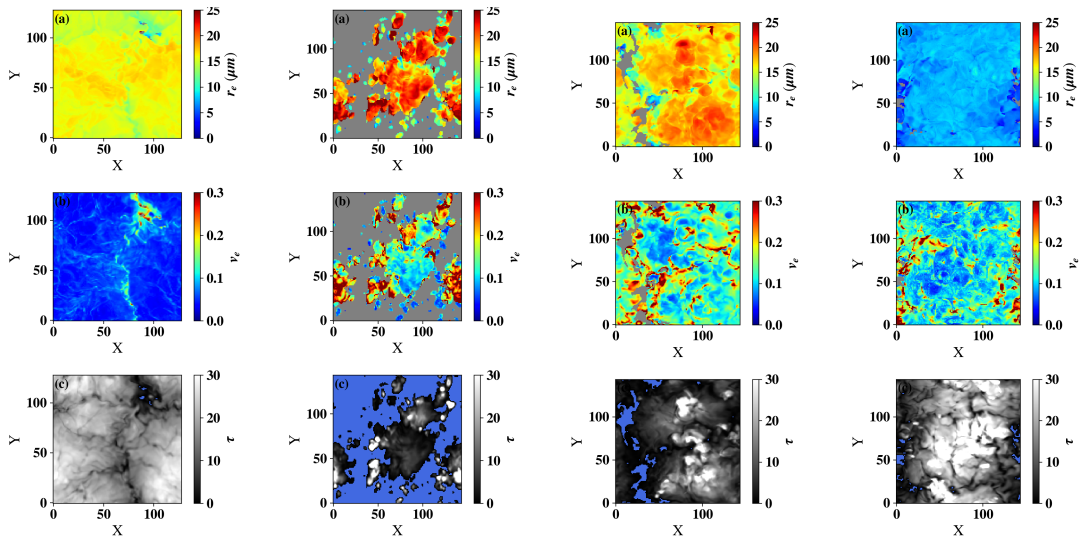

(i) DYCOMS-II (ii) RICO (iii) ATEX(clean) (iv) ATEX(polluted)

Figure 2.4: Vertically-weighted retrievals for (i) DYCOMS-II, (ii) RICO, (iii) ATEX-clean, and (iv) ATEX-polluted cases. (a), (b), and (c) panels of each column are vertically-weighted Cloue Effective Radius (CER [μm]), Cloud Effective Variance (CEV), and Cloud Optical Thickness (COT). (SZA=40^o, VZA=0^o)

2.5 Cloud masks

Several cloud mask definitions have been used throughout the study. Among them, the simplest definition is based on the vertically-weighted COT retrievals which select $COT > 0.1$ pixels as "cloudy" pixels (hereafter referred to as VW-COT cloud mask). The VW-COT cloud masks of each LES scene for all solar zenith angles that have been used throughout this study are shown in Figure 2.5. Since the polarimetric retrievals are based on the multi-angular measurements, they are susceptible to the parallax effects. In order to identify and avoid such biases due to the parallax effect at the cloud edges, we use a cloud mask that only labels a cloudy

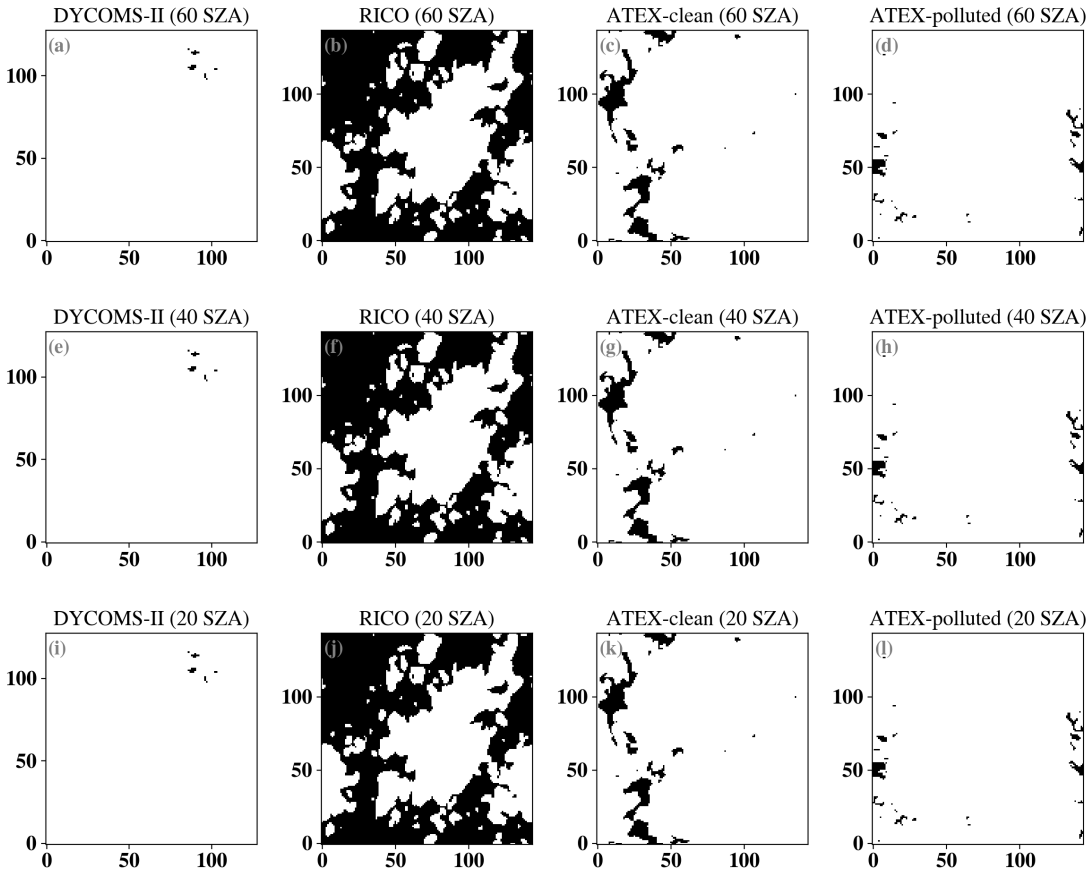

Figure 2.5: Cloud mask based on vertically-weighted COT threshold (VW-COT) in the native resolution. Pixels where $\tau > 0.1$ are being considered as clouds and are shown in white.

pixel if the total reflectance at 0.860 μm is greater than 0.02 for a complete cloud-bow scattering angle range of $135^o < \Theta_S < 165^o$ (Section 5.4.1.1). Since the multi-angular reflectances have been used to determine the cloudy and cloud-free pixels, we referred to this cloud mask as the multi-angular cloud mask (MA cloud mask for short). The MA cloud masks for each LES scene and observational geometry are shown in Figure 2.6. The characteristic angular pattern of the polarized phase function $P_{12}(\Theta_S)$ in the cloud bow region dissipates as CEV increases, hence the

polarimetric retrieval technique fundamentally unable to retrieve cloud drop size distributions with large CEV values. In order to analyze the influence of 3D radiative transfer effects in the polarimetric retrievals, often we use the MA cloud mask with a filter to ignore $CEV > 0.2$ values based on the 1D polarimetric retrievals because polarimetric retrieval technique loses its sensitivity as CEV increases (Section 1.2) . Figure 2.7 shows the MA cloud mask with $CEV > 0.2$ filter (hereafter referred to as MA-fil cloud mask for short) for each LES case.

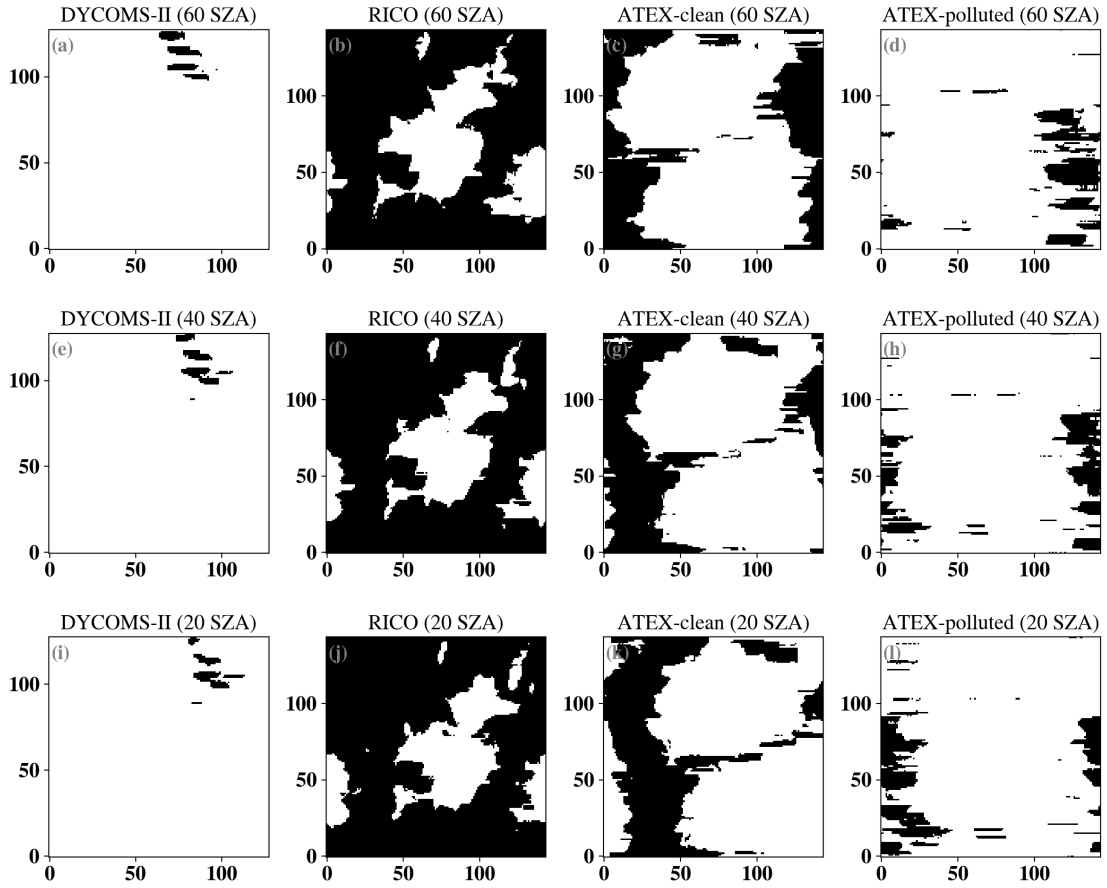

Figure 2.6: Multi-angular (MA) cloud mask in the native resolution. "Cloudy pixels" are the pixels that have total reflectance at 0.860 μm greater than 0.02 ($R_I^{1D,0.860\mu m} > 0.02$) along all directions corresponding to a scattering angle (Θ) greater than 135^o and less than 165^o. Cloudy pixels are shown in white.

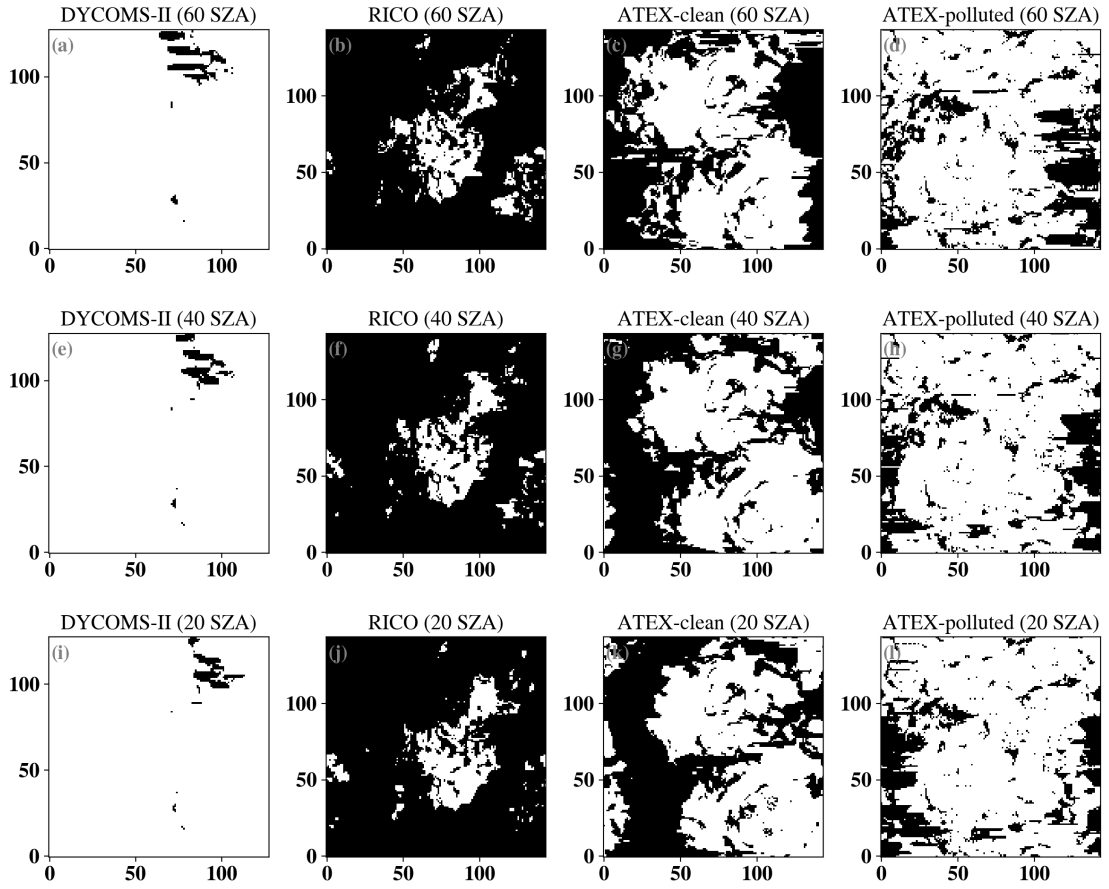

Figure 2.7: MA cloud mask with $CEV < 0.2$ filter (MA-fil cloud mask) in the native resolution. In addition to MA cloud mask, only the pixels that have polarimetric CEV less than 0.2 have been considered as "cloud pixels". Cloudy pixels are shown in white.

Chapter 3: Above-cloud aerosols

The main content of this chapter is adapted from the published prior work of the author (Rajapakshe et al., 2017).

3.1 Introduction

Every year from about June to October over the southeast (SE) Atlantic, the prevailing easterly winds in the free troposphere often transport the smoke and pollution aerosols from the African continent to the west, over the ocean where extensive marine boundary layer (MBL) clouds persist for most of the year (Adebiyi and Zuidema, 2016). This leads to a nearpersistent seasonal biomass burning aerosol layer over MBL clouds in SE Atlantic (Devasthale and Thomas, 2011; Zhang et al., 2016a)

As summarized in Yu and Zhang (2013) instruments onboard NASA's ATrain satellite constellation provide valuable observations of the aerosol layer and underlying clouds. In particular, the lidar on the spaceborne mission CALIPSO provides unique observations of the vertical distribution of the aerosol layer that have been widely used to characterize the aerosol layer above cloud over SE Atlantic Chand et al. (2009); Devasthale and Thomas (2011); Meyer et al. (2013) and assess its

impacts on the radiation budget Chand et al. (2009); Zhang et al. (2016a).

The seasonally transported south-east (SE) Atlantic aerosol layer can influence the regional radiative energy budget through the direct radiative effect (DRE) (Chand et al., 2009; Zhang et al., 2016a). The absorption by aerosol layer can also influence the thermodynamical structure of lower atmosphere and in turn change cloud field, which is known as the semidirect effect (Johnson et al., 2004; Wilcox, 2010; Sakaeda et al., 2011; Wilcox, 2012). The sign and magnitude of the semidirect effect are strongly dependent on the vertical distribution of aerosol with respect to the underlying clouds (Johnson et al., 2004). In addition to DRE and semidirect effect, the aerosol particles could be entrained into the clouds and activated as cloud condensation nuclei, giving rise to the socalled aerosol indirect effects (Costantino and Bréon, 2010, 2013; Painemal et al., 2014). Intuitively, the closer the bottom of the aerosol layer gets to the top of underlying cloud, the more likely the aerosol particles are entrained into the cloud. Previous studies have used the 532 nm observations from the CALIPSO lidar to estimate the distance from the aerosol layer bottom to the cloud top (referred to hereafter as AB2CT distance for short). Costantino and Bréon (2010) show that 84% of the time the AB2CT distance in SE Atlantic is larger than 250 m. Devasthale and Thomas (2011)found that in 0^o to 30^oS region, 90-95% of abovecloudaerosol cases have an AB2CT distance greater than 100 m. Yu et al. (2012) derived the average AB2CT of 1700 m over a 2 year period in SE Atlantic. These analyses based on CloudAerosol Lidar with Orthogonal Polarization (CALIOP) 532 nm observations seem to indicate that the seasonal aerosol layer in SE Atlantic is well separated from the underlying clouds,

and thus, the aerosol indirect effects may be secondary in comparison to the aerosol direct and semidirect effects (e.g. Sakaeda et al. (2011)).

It is known that the CALIOP 532 nm based layer detection often misses the lowest boundary of a thick aerosol layer, thereby biasing the bottom of the aerosol layer too high. This may be especially problematic for daytime observations Meyer et al. (2013). Recently, several novel remote sensing techniques have been developed to retrieve the AOD (aerosol optical depth) of abovecloudabsorbing aerosol layers from passive sensors (e.g. Waquet et al. (2009); Torres et al. (2011); Meyer et al. (2015)). In addition, an alternative lidar method has been developed for CALIOP, utilizing signals from the underlying cloud instead of the attenuated backscatter profile (Liu et al., 2015). When compared with the retrievals from passive sensors and the alternative CALIOP algorithm, the operational 532 nm CALIOP AOD retrievals are systematically biased low by 26% on average (Liu et al., 2015) and can be up to a factor of 5 lower (Jethva et al., 2014). A likely explanation for this bias is that the strong aerosol attenuation at 532 nm by the upper portion of the aerosol layer together with the small backscatter cross section of the aerosol particles substantially weakens the attenuated backscatter signal from the lower part of the aerosol layer to a level under the detection threshold of CALIOP (Torres et al., 2011; Jethva et al., 2014; Liu et al., 2015). This laser attenuation issue leads to an overestimation of the aerosol layer bottom height (too high), an underestimation of the physical thickness of the aerosol layer (too thin), and thereby an underestimation of AOD (too small).

In this study, we seek to shed new light on the vertical distribution of the SE

Atlantic absorbing aerosol layer with respect to the underlying clouds using observations from NASA's CloudAerosol Transport System (CATS) mission. Because of instrument and algorithm differences, CATS ACA retrieval suffers much less from the laser saturationinduced bias than CALIOP 532 nm algorithm. We do a comparative analysis of CATS and CALIOP retrievals in the SE Atlantic region for two recent biomass burning seasons (2015 and 2016). As shown in the latter (Figure 3.5), the CATS 1064 nm observations suggest that the bottom of the ACA layer is much lower, and therefore closer to underlying cloud top, than previously estimated based on CALIOP 532 nm observations. Our results are important for future studies of the microphysical indirect, as well as the semidirect, effects of ACA on underlying clouds.

3.2 Data

The occurrence frequency of abovecloudaerosol in the SE Atlantic (20^oW to 20^oE; 30^oS to 10^oN) is highest during JulytoOctober (JASO) with the peak during August-September (Zhang et al., 2016a) . In this study, we focus on the two biomass burning seasons (JASO) of 2015 and 2016 so that we can directly compare CALIPSO and CATS (Figure 3.1).

3.2.1 CALIOP

The lidar instrument onboard the CALIPSO mission, which has an orbital height of ∼700 km, is the CloudAerosol Lidar with Orthogonal Polarization (CALIOP).

CALIOP directly measures the rangeresolved total (particulate plus molecular) attenuated backscatter signal at two wavelengths, 532 nm and 1064 nm, using analog detection. In addition to the total attenuated backscatter, CALIOP also measures two orthogonal polarized components of the 532 nm backscatter signal (Winker et al., 2009). The accuracy of the CALIOP Level2 (L2) data products (aerosol type, particulate backscatter and extinction coefficient, optical depth) is dependent on the accurate detection of cloud and aerosol layers.

Uniform cloud and aerosol layer detection and cloudaerosol discrimination (CAD) techniques are challenging due to the complexity of atmospheric scenes encountered. The current version of CALIOP Selective, Iterated Boundary Location (SIBYL) algorithm uses the 532 nm total attenuated backscattered signals to determine boundaries of cloud and aerosol layers, with a typical vertical resolution of 30 m. The SIBYL scheme detects atmospheric features by iteratively comparing horizontally averaged CALIOP 532 nm total attenuated backscatter profiles at multiple horizontal resolutions. The CALIOP CAD algorithm is a multidimensional probability distribution function (PDF) technique based on statistical differences of several cloud and aerosol properties (e.g., layer-integrated 532 nm attenuated backscatter and layerintegrated backscatter color ratio). Previous studies have shown that the SIBYL and CAD algorithms perform well for cirrus clouds and several aerosol types (McGill et al., 2015; Yorks et al., 2015).

3.2.2 CATS

CATS is an elastic backscatter lidar employing photon counting detection and two highrepetition rate lasers that operate at 532 and 1064 nm (McGill et al., 2015) that has been operating on the International Space Station (ISS) since February 2015. The ISS orbit, which is at an altitude of ∼415 km and a 51^o inclination, allows CATS to observe locations at different local times each overpass (∼60 days to complete full diurnal cycle) with roughly a 3 day repeat cycle.

The CATS layer detection algorithm is a thresholdbased layer detection method that is nearly identical to the CALIOPSIBYL technique with four distinct differences, namely, the use of 60 m vertical resolution, a single horizontal spatial resolution (5 km), the use of the 1064 nm wavelength rather than 532 nm, and a technique to identify clouds embedded within aerosol layers (Yorks et al., 2015). The CATS L2 Operational (L2O) CAD algorithm is a multidimensional PDF technique like the CALIOP one (Yorks et al., 2015) but uses the layerintegrated attenuated backscatter at 1064 nm and other variables such as layer midtemperature and layer thickness instead of the layerintegrated backscatter color ratio due to the unreliable 532 nm data in Mode 7.2. The use of a single horizontal spatial resolution in the CATS algorithm misses optically thin cirrus clouds and aerosols during the daytime in the CATS L2O Version 105 data products, though it performs well during nighttime observations. Future versions of CATS L2O data products will include layer detection at 60 km, but since Version 105 is used in this study, CATS daytime data were excluded.

For abovecloud aerosol (ACA), the more relevant difference between the algorithms is the preferred wavelength for atmospheric layer detection. The current CALIOPSIBYL primarily uses 532 nm because it has higher signaltonoise ratios and lower Minimum Detectable Backscatter (MDB,weakest aerosol backscatter coefficient that can be detected) than the CALIOP 1064 nm data resulting in more accurate uniform cloud and aerosol layer detection. The CATS layer detection algorithm uses the 1064 nm attenuated scattering ratio because the CATS 532 nm data in Mode 7.2 are extremely noisy and the 1064 nm MDB is orders of magnitude lower (Yorks et al., 2015). For ACA detection specifically, the 1064 nm wavelength is preferred over the 532 nm wavelength for layer detection. The aerosol signal at 1064 nm has 16 times less molecular contamination compared to 532 nm. As discussed in Section 3.1, the 532 nm backscatter signal may be insensitive to the entire vertical extent of absorbing aerosol layers. Because aerosol extinction is usually smaller at 1064 nm than 532 nm, and the CATS 1064 nm backscatter signal is very robust, the vertical extent of absorbing aerosol layers is fully captured from CATS 1064 nm backscatter profiles. It is worth mentioning that the current CATS operational algorithm uses $AB2CT < 360m$ as the threshold to detect the clouds embedded within aerosol layers (CEAL). When $AB2CT < 360$, the ACA and the cloud below are merged and identified a CEAL case.

The detectability of the aerosol layer base using 532 and 1064 nm is demonstrated in Figure 3.1. CATS and CALIPSO passed over the same ACA layer over the SE Atlantic on 6 August 2016, although the differing orbits of the ISS and CALIPSO mean that the two curtains do not align exactly. There is a 0.1-1.0 km gap between

cloud top and aerosol base in the attenuated total backscatter and vertical feature mask based on CALIOP 532 nm data. In contrast, CATS 1064 nm observation finds the aerosol plume to extend all the way to the cloud top, which is also confirmed by the CALIOP 1064 nm attenuated backscatter observation. The example clearly demonstrates the advantage of 1064 nm over 532 nm based layer detection technique for identifying the bottom of thick smoke layers. Although CALIOP also has the 1064 nm observation, it has not yet been utilized in the current operational algorithm. Note that the differences between CALIOP and CATS observations shown below are mainly due to the use of different wavelength (i.e., 532 nm versus 1064 nm) for layer detection. At the moment of writing, the CALIPSO operational product team is planning to make more use of the 1064 nm observations in their operational layer detection algorithm, which could significantly improve its retrievals for thick aerosol layers like the example in Figure 3.1.

3.3 Results

We have used the following criteria to identify ACA columns in both CALIOP and CATS layer products: (1) the cloud layer product identifies liquid phase cloud at the top layer of the profile, (2) the aerosol layer product identifies at least one layer of aerosol in the profile, and (3) the base height of at least one aerosol layer is higher than the top of the highest cloud layer. In the SE Atlantic region, most ACA cases are simple, with only one aerosol layer on top of singlelayer MBL clouds. After the identification of ACA columns, we compute the AB2CT by calculating the

difference between the minimum aerosol base height which is greater than maximum cloud top height and the maximum cloud top height. For CALIOP, we derived the ACA and cloud statistics for both daytime and nighttime conditions (though daytime and nighttime statistics are computed separately). The CATS results are only for nighttime since its aerosol retrieval does not perform well during daytime at the fixed 5 km horizontal resolution as discussed above.

Figures 3.2(a-c) show the multiyear (2015-2016) SE Atlantic JASO Cloud Fraction (CF), defined as $CF = N_{cloudy}/N_{total}$ in $2^o \times 2^o$ grid boxes where N_{cloudy} is the number of cloudy columns and N_{total} is the number of total columns. Because we are interested in aerosol above lowlevel MBL clouds, ACA occurrence frequency (ACA_F) is shown in Figures 3.2(d-f) which is defined as $ACA_F = N_{ACA}/N_{cloudy}$ where N_{ACA} is the number of ACA columns. Among the three data sets, CATS nighttime observations identify the highest ACA occurrence frequency, with domain averaged ACA_F around 0.24. CALIOP daytime observations have the lowest ACA occurrence frequency, with domainaveraged ACA_F only around 0.17. The CALIOP nighttime observations are comparable to the CATS nighttime observations (domain average $ACA_F \sim 0.23$). Some differences between the three data sets may have physical explanations. For example, CALIOP observes a larger CF during nighttime than during daytime, which is likely a result of the strong cloud diurnal cycle in the SE Atlantic region (Min and Zhang, 2014). The other differences may stem from algorithm and instrument differences. For example, the lower ACA_F using daytime CALIOP might be an artifact due to the impact of background solar noise on the lidar retrieval Liu et al. (2015).

Overall, the results in Figure 3.2 suggest that despite some minor differences, CALIOP and CATS observe similar geographical patterns of ACA in the SE Atlantic. We now focus on the vertical distribution of aerosol and cloud from the two instruments. Figure 3.3 shows the 2 year (2015-2016) mean aerosol layer base height (Figure 3.3 , top row), cloud layer top height (Figure 3.3 , middle row), and AB2CT distance (Figure 3.3 , bottom row) of ACA over the SE Atlantic region during JASO from CALIOP and CATS. While the magnitudes differ, cloud top heights from all three data sets show a similar pattern, lowest off the coast of Namibia (near 20^oS and 10^oE) and gradually increasing along the northwest direction to about 2 km around 5^oS and 15^oW. In contrast to the similarity of cloud top height, the mean ACA base height from the three data sets show significant differences. ACA base height from daytime CALIOP observations is much higher than nighttime CALIOP, which is in turn higher than nighttime CATS. As a result, the AB2CT distance from nighttime CATS is below 500 m in most of the SE Atlantic region, suggesting that the aerosol layer extends close to the cloud top. On the other hand, a clear separation between aerosol base and cloud top during both daytime and nighttime is implied by the CALIOP data, a likely result of the above mentioned CALIOP ACA layer detection issues.

We analyzed the AB2CT distances from the three observations further in Figure 3.4. Here we show the cumulative density function of the AB2CT distance for the samplingmasked ACA cases of Figure 3.3. According to CATS nighttime 1064 nm observations (red curve), about 60% of ACA cases are identified as CEAL (i.e., $AB2CT < 360m$), in contrast to only 15% and 6% occurrence of such cases

in CALIOP 532 nm nighttime (blue curve) and daytime (green curve) observations, respectively. Moreover, 82% and 64% of ACA cases have $AB2CT > 1km$ according to the daytime and nighttime CALIOP 532 nm observations, respectively, in contrast to 22% according to CATS observations.

Figure 3.5 shows meridionally averaged daytime (Figure 3.5 (a)) and nighttime CALIOP (Figure 3.5 (b)) 532 nm, and nighttime CATS 1064 nm (Figure 3.5 (c)) observations of ACA top (dashed red line) and bottom (solid red line) height, cloud top height (blue line), and the fraction of ACA cases with $AB2CT < 360m$ (black line). Also shown are one standard deviation variability for ACA top (red error bars), ACA base (light red shades), and cloud top (light blue shades). All three observations show nearly the same top of aerosol layer, just below 4 km. The cloud top heights are also similar in all three observations, rising from 1 km near the coast westward to about 1.5-2.0 km at 19 W. Daytime CALIOP observes slightly higher cloud top height (domain average 1.39 km) compared to nighttime (domain average 1.33 km). Among all three data sets, the CATS detects the highest cloud top height (domain average 1.60 km). In contrast to aerosol top and cloud top heights, ACA base heights are substantially different among the three data sets. The CALIOP nighttime product (Figure 3.5 (b)) gives domainaveraged ACA base height at 2.63 km; daytime CALIPSO retrievals (Figure 3.5 (a)) are even higher. Nighttime CATS 1064 nm (Figure 3.5 (c)), however, observes a significantly lower ACA domainaveraged base height around 2 km.

Even after considering one standard deviation variability, there is still a clear separation between the ACA base and cloud top in both the daytime (Figure 3.5 (a))

and nighttime. As can be seen in Figure 3.5 (b), this is confirmed by the small values of the fraction of $AB2CT < 360m$ throughout the domain for the CALIOP retrievals. With CATS (Figure 3.5 (c)), however, there is clear evidence that the ACA base and cloud top are in much closer proximity than is implied by CALIOP 532 nm observation, as the fraction of $AB2CT < 360m$ is mostly around 60%.

3.4 Summary and Discussion

The microphysical indirect effects of the seasonally transported aerosols in the SE Atlantic are often overlooked in the literature. This is partly because CALIOP's 532 nm based operational layer detection algorithm often detects the aerosol layer bottom too high and thereby suggests that the abovecloud aerosol layer is well separated from the underlying clouds. The CATS mission (launched in January of 2015) provides a new data set of the vertical distribution of aerosol and clouds. Several instrument and algorithm advantages of CATS, chiefly among which is the primary use of 1064 nm for layer detection, allow it to better identify the full vertical extend of the SE Atlantic ACA layer than CALIOP 532 nm product. We have compared the current CATS and CALIPSO products during JASO of 2015 and 2016 over the SE Atlantic. The CF, ACA_F, and cloud top geographical patterns from the two instruments agree well. However, CATS 1064 nm observes the ACA layer bottom height much lower and much closer to the underlying cloud top than CALIOP 532 nm does. According to CATS, about 60% of the ACA cases have an $AB2CT < 360m$, in contrast to the 15% and 6% based on CALIOP nighttime and

daytime 532 nm observations, respectively.

Our study provides direct evidence that spacebased lidar layer detection at 1064 nm is more representative of the true ACA scene compared to 532 nm. More importantly, our study suggests that the occurrence of aerosol entrainment into clouds might be much more frequent than previously thought based on CALIOP 532 nm observations. This implies that the microphysical indirect effects could be an important mechanism through which the transported aerosol influences the clouds and radiation in SE Atlantic region (Lu et al., 2018). Finally, an accurate measurement of the vertical distribution of aerosols would also help us better understand the semidirect effects of smoke aerosols.

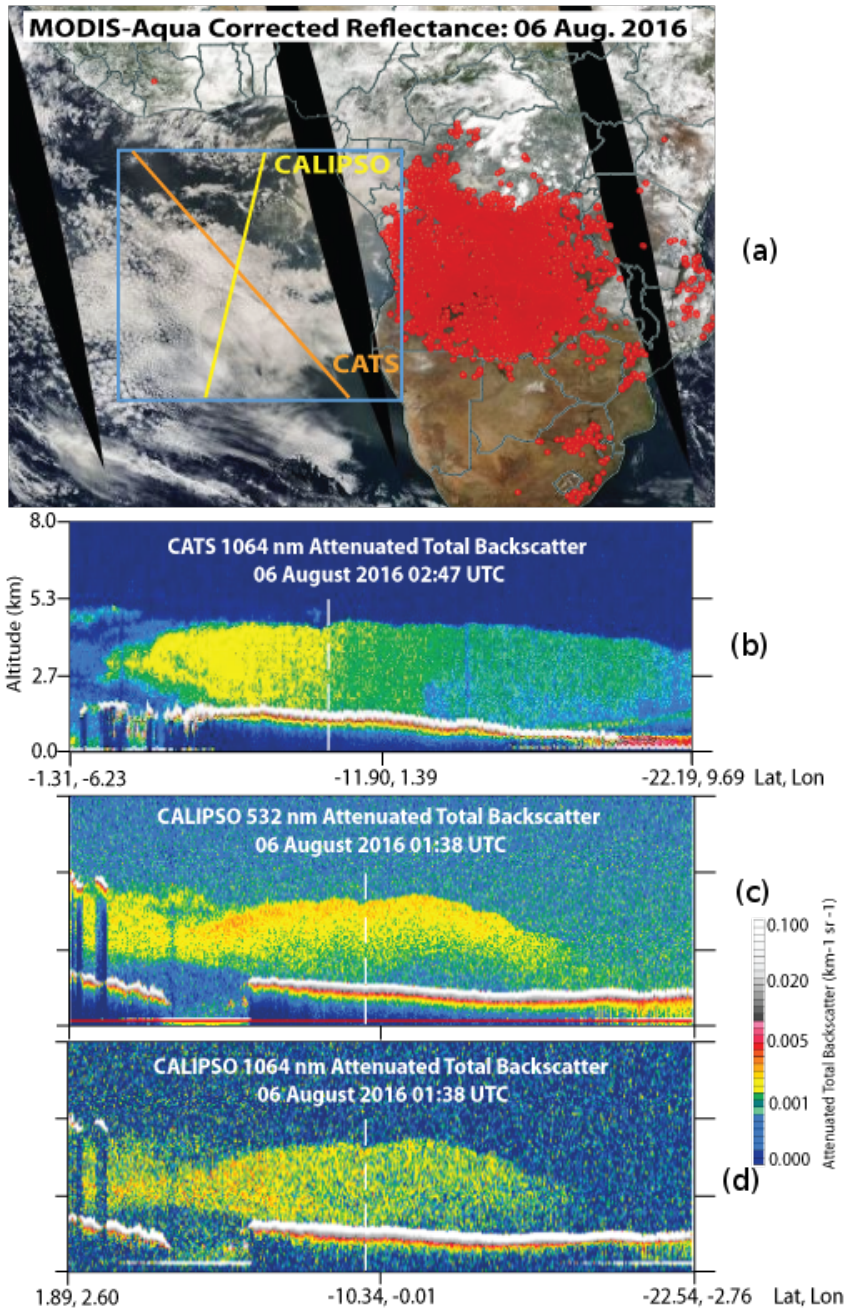

Figure 3.1: (a) A smoke above MBL cloud event on 6 August 2016. The red dots in the African Continent are fire events. Attenuated total backscatter layer-integrated backscatter color ratio of (b) CATS 1064nm, (c) CALIOP 532nm, (c) and CALIOP 1064 nm.The dashed lines correspond to the point where the CAT and CALIPSO tracks overlap with each other (Rajapakshe et al., 2017).

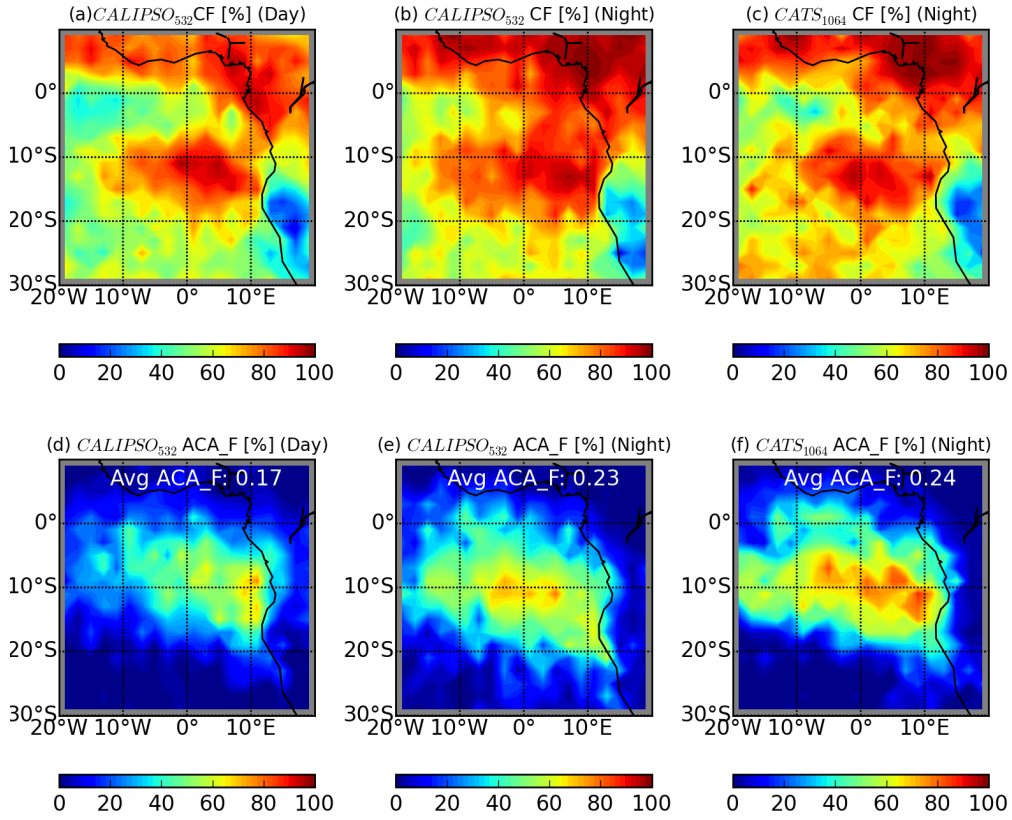

Figure 3.2: Multiyear (2015-2016) seasonal mean (July to October) cloud fraction CF (%) in the SE Atlantic region based on (a) CALIOP daytime, (b) CALIOP nighttime, and (c) CATS nighttime observation. The seasonal mean ACA (ACA_F [%]) occurrence frequency from (d) CALIOP daytime, (e) CALIOP nighttime, and (f) CATS nighttime observations (Rajapakshe et al., 2017).

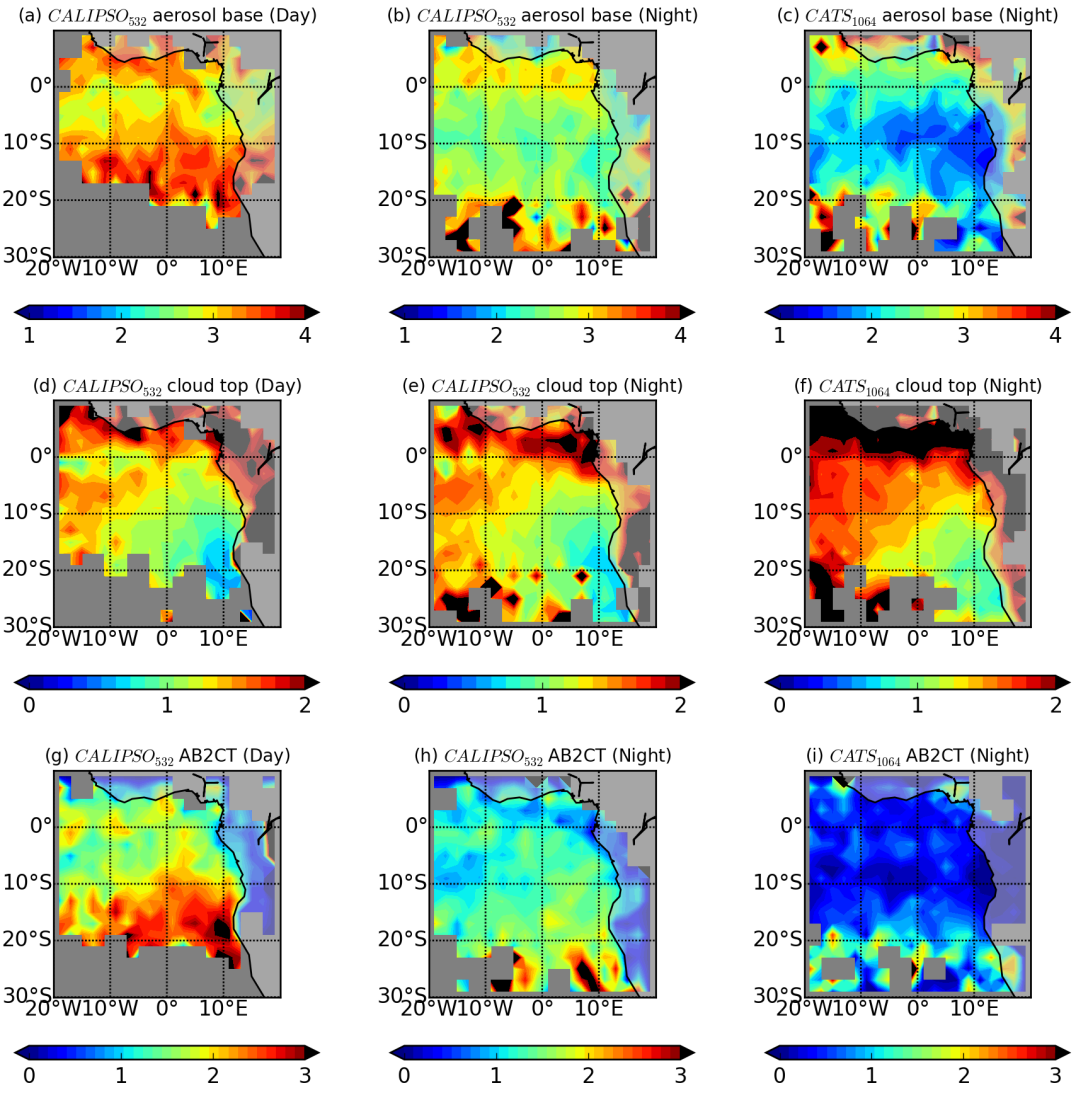

Figure 3.3: Multiyear (2015-2016) (top row) seasonal mean aerosol layer base height [km], (middle row) cloud layer top height [km], and (bottom row) aerosol base to cloud top (AB2CT[km]) distance of ACA over the SE Atlantic region during JASO from CALIOP and CATS (Rajapakshe et al., 2017).

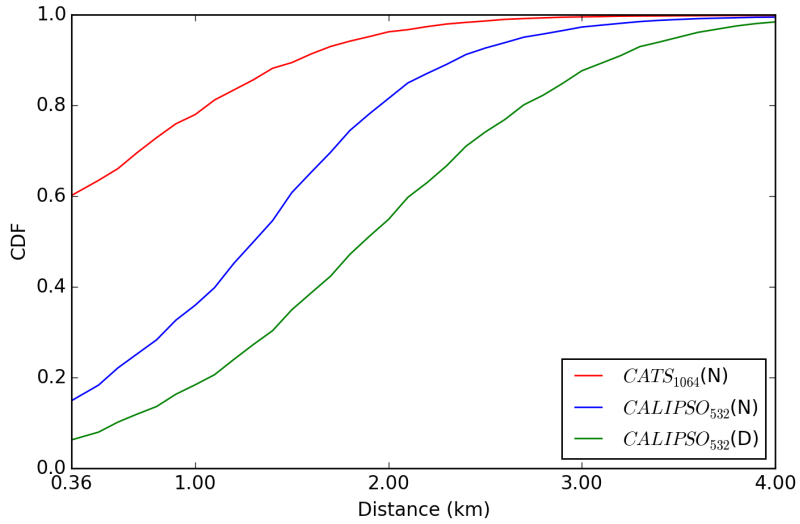

Figure 3.4: Cumulative probability distribution function (CDF) of the distance between aerosol layer bottom and cloud top (AB2CT distance) of the ACA observations in Figure 3.3(d-f). (Rajapakshe et al., 2017).

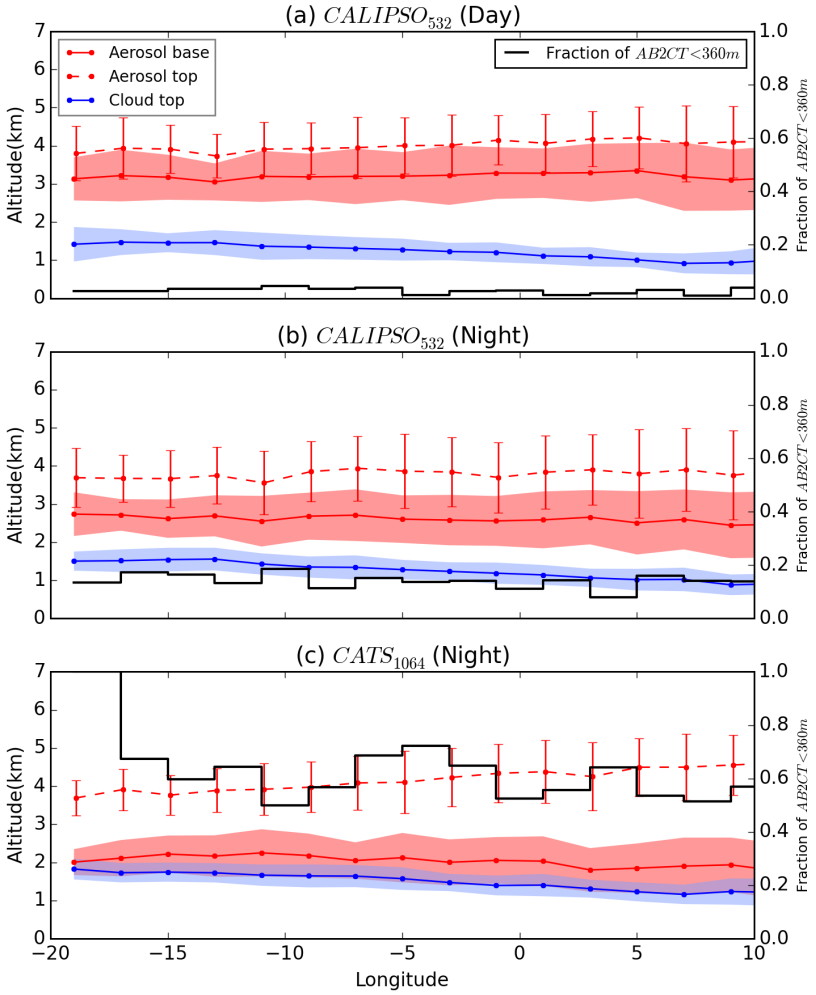

Figure 3.5: Meridionally averaged aerosol bottom (solid red line), top (dashed red line), and cloud top (solid blue line) heights, with fraction of AB2CT < 360 m (black line), for the SE Atlantic region during JASO 2015-2016. One standard deviation variability for each is denoted by the red error bars for aerosol top height, and by the red and blue shaded regions for the aerosol bottom and cloud top heights, respectively (Rajapakshe et al., 2017).

Chapter 4: 3D radiative transfer effects in bi-spectral retrievals

4.1 Overview

The bi-spectral cloud property retrievals (aka Nakajima-King retrievals or also referred to 'NJK' in this text) use a pair of reflectances. One from a spectral band with little water absorption and, another from a band with significant absorption. This is used to retrieve cloud optical thickness (COT) and cloud effective radius (CER) simultaneously (Nakajima and King, 1990). This method is widely used in space and airborne sensors including MODIS (Platnick et al., 2003) and SEVIRI (Roebeling et al., 2006) and have greatly improved our understanding of the global cloud properties. For the sake of computational efficiency, the bi-spectral retrieval technique uses a pre-computed library of reflectances as a function of tabulated cloud microphysical and optical properties. This so-called LUT is then used in the operational algorithm to infer cloud properties from observed reflectances. An important point to note is that these pre-computed libraries are based on 1D RT theory instead of realistic 3D RT. The 1D RT is based on two main assumptions. (1) Plane Parallel Approximation (PPA) that assumes the cloud fields are vertically and horizontally homogeneous, (2) Independent Pixel Approximation (IPA) which assumes that a particular pixel is seperated and independent from its neighboring

pixels. When real clouds have significant 3D structures, the retrieved cloud properties tend to deviate from these assumptions hence are called to be influenced by "3D radiative effects". These 3D RT effects are the main scope of this study. If a particular pixel appears to reflect more radiation under realistic 3D RT than 1D RT, such pixels are called "illuminated" pixels while if the 3D reflectance is smaller than its 1D counterpart, such pixels are called "shadowed" pixels. In other words, this definition is based on the results of the 3D effects, not the mechanism or underlying physics. The implications of the realistic 3D spatial dependence of the cloud properties and the 3D radiative transfer on the bi-spectral retrievals have been extensively studied in literature (Marshak and Davis, 2005; Loeb and Davies, 1996; Davis et al., 1997; Oreopoulos and Davies, 1998; Várnai and Marshak, 2002; Marshak et al., 2006; Zhang et al., 2012; Miller et al., 2017). Moreover, efforts have been taken towards minimizing the biases in the bi-spectral retrievals due to the 3D RT effects(Várnai and Marshak, 2002; Rajapakshe and Zhang, 2020). This chapter mainly focuses on certain assumptions that have been frequently used in the literature related to the 3D effects of bi-spectral retrievals but have not been investigated in detail.

Section 4.2 uses 1D RT simulations to demonstrate the functionality of the aerosol-cloud retrieval simulator (ACRS) setup that has been used in this study. Section 4.3 summarizes the main key understanding of the 3D RT of the bi-spectral retrievals emphasizing the assumptions that we are going to test. Section 4.4 presents the bi-spectral retrievals under 3D radiative transfer from ACRS. And the last two sections discuss the solar zenith angle and the horizontal resolution dependence of the 3D RT effects in the bi-spectral retrievals.

4.2 Bi-spectral retrievals under 1D rdiative transfer

In this section, we use the aerosol-cloud retrieval simulator (ACRS) setup to synthesize bi-spectral cloud retrievals equivalent to satellite (or airborne) observations but based on 1D RT. First, we use MSCART to simulate 1D RT in the cloud domain and synthesize radiance fields equivalent to observations and then we use those radiances to implement the bi-spectral retrievals and "retrieve" COT and CER.

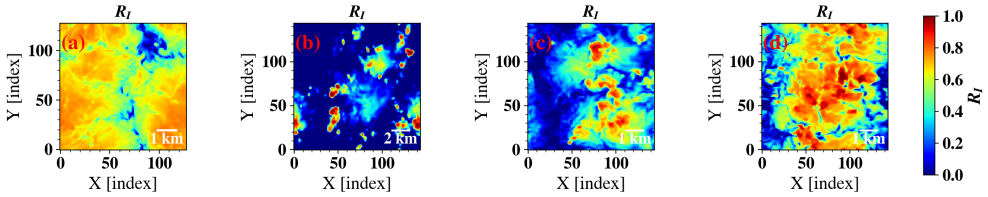

Figure 4.1: Simulated 1D total reflectances ($\pi I/\mu_0/F_0$) from MSCART for (a) DYCOMS-II, (b) RICO, (c) ATEX-clean, and (d) ATEX-polluted cases in 0.860 μm. X and Y axes are pixel indices. The Sun is to the left at $SZA = 40^o$

Figure 4.1 shows the simulated reflectances from MSCART 1D radiative transfer simulations for 0.860 μm wavelength ($R_I^{1D,\lambda} = \frac{\pi I}{\mu_0 F_0}$ for $\lambda = 0.860\ \mu m$). The Sun is to the left side of the domain at $SAA = 0^o$. The same $SAA(= 0^o)$ has been used throughout the study unless specifically mentioned otherwise. In this particular case, SZA set to be 40-degrees. The native-resolution $R_I^{1D,\lambda}$ for $\lambda = 0.860\ \mu m$ simulations from MSCART for DYCOMS-II, RICO, ATEX-clean, and ATEX-polluted LES cases are shown in panel (a), (b), (c), and (d) respectively.

Two reflectance measurements from the same cloud-target, one from a non-

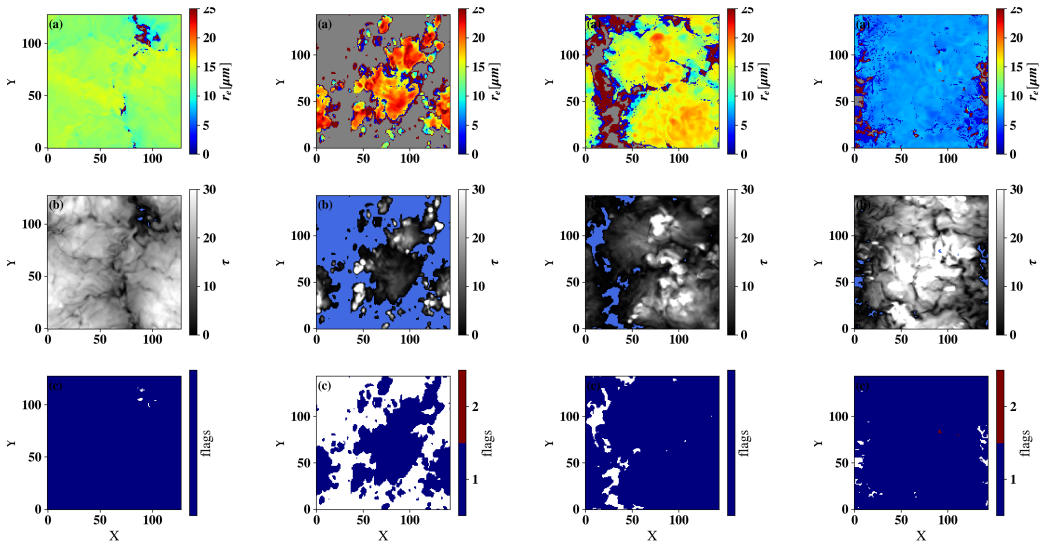

(i) DYCOMS-II (ii) RICO (iii) ATEX(clean) (iv) ATEX(polluted)

Figure 4.2: Bi-spectral retrievals at the native resolution for each LES case based on 1D RT. Panel (a),(b) and (c) of each column are CER ($r_e^{NJK,1D}$), COT($\tau^{NJK,1D}$) and retrieval quality flags. The Sun is to the left at $SZA = 40^o$. The VW-COT cloud mask (see Section 2.5) has been used. Flag 1 and 2 "successful retrieval" and "outside the lookup table" respectively.

absorbing VNIR band and the other from a moderately absorbing SWIR band are required to perform bi-spectral retrievals. Figure 4.1 shows the simulated radiance fields for VNIR band (0.860 μm). After simulating the SWIR (2.13μm) reflectances using MSCART, the bi-spectral retrieval technique is implemented. Each column of Figure 4.2 corresponds to the bi-spectral retrievals of CER (a-panels) and COT (b-panels) of each LES case. The Sun is to the left side of the domain (SAA=0^o) with SZA=40^o. VW-COT cloud mask has been applied to mask the columns with vertically-weighted COT retrievals smaller than 0.1. The c-panels of each column

corresponds to the retrieval quality flag where '1' and '2' indicate a "successful retrieval" and a "retrieval outside the look-up-table" respectively. Except for a single pixel in the RICO case and a couple of pixels in the ATEX-polluted case, all the other pixels are indicated as "successful retrievals". However, these flags are merely an indication that the observed reflectances are within the range of look-up-table (LUT) which do not necessarily imply physically accurate retrievals. For example, at the optically thin cloud edges, we can see unreasonable fluctuations of CER retrievals between very large and small values that do not exist in the corresponding vertically-weighted retrievals in Figure 2.4. This phenomenon is more frequent in RICO (Figure 4.2 (ii)(a)) and ATEX-clean (Figure 4.2 (iii)(a)) cases where predominant cloud-free regions exist. These unreasonable fluctuations of CER retrievals are associated with very small VNIR and SWIR reflectances where the constant COT and CER contours of the LUT-grid are not orthogonal (black solid and dashed lines respectively in Figure 1.5). Hence a slight difference in either VNIR or SWIR reflectance in these small reflectances could cause a drastic difference in the retrieved-CER.

Figure 4.3 compares the bi-spectral retrievals ($r_e^{NJK,1D}$, $\tau^{NJK,1D}$) with the corresponding vertically-weighted retrievals (r_e^{vw}, τ^{vw}) for (i) DYCOMS-II, and (ii) RICO case at $SZA = 40^o$ under 1D RT. In general, CER ($r_e^{NJK,1D} - r_e^{vw}$ in the a-panels of Figure 4.3) has a negative bias while the COT ($\tau^{NJK,1D} - \tau^{vw}$ in the c-panels of Figure 4.3) has a slightly positive bias. In the joint-histograms of $r_e^{NJK,1D}$ vs. r_e^{vw} (b-panels of Figure 4.3), a clear negative bias exists which is more prominent in the DYCOMS-II case (Figure 4.3 (i)(b)). However, in Chapter 5, the po-

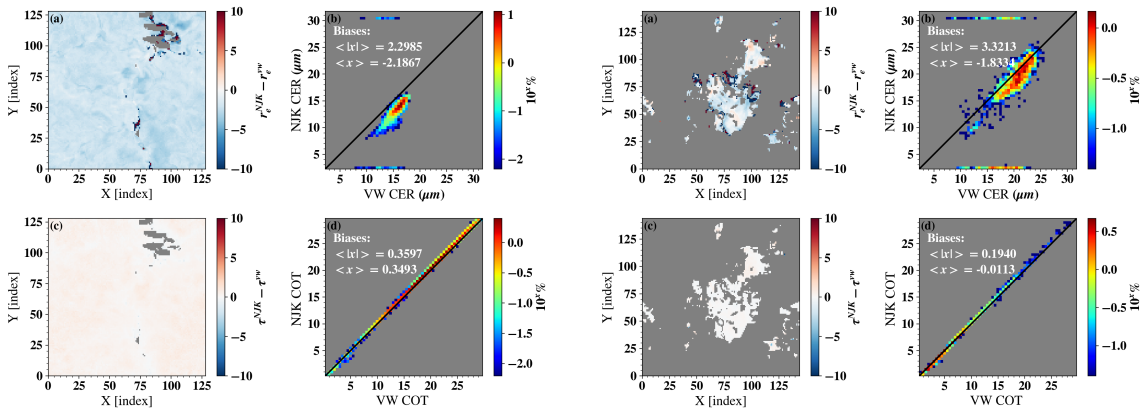

(i) DYCOMS-II (ii) RICO

Figure 4.3: Comparisons of bi-spectral retrievals (r_e^{NJK}, τ^{NJK}) with the vertically-weighted retrievals (r_e^{vw}, τ^{vw}) for (i) DYCOMS-II and (ii) RICO cases at $SZA = 40^o$ under 1D radiative transfer. Color bar of the joint histograms is the percentage of counts on a logarithmic scale. $< x >$ and $< |x| >$ are the mean bias and mean absolute bias respectively (see Appendix A for bias-statistic definitions). The Sun is to the left side of the domain. CEV-fil cloud mask (see Section2.5) has been used.

larimetric retrievals show a better correlation with the vertically-weighted retrievals (Figure 5.5(ii)(b)) than the $r_e^{NJK,1D}$ vs. r_e^{vw} correlation in Figure 4.3 (i)(b). This is because we choose parameters of the vertical weighting function (in Section 2.4, a=1, and b=0 in Equation 2.7) to comply with the single scattering approximation which is more appropriate to polarized reflectance rather than the total reflectance which has significant multiple scattering effects. Miller et al. (2017) computes 'a' and 'b' parameters of the vertical weighting function (Equation 2.7) for each band and observation geometry following Platnick (2000) and get much closer correlation with the vertically-weighted retrievals and the bi-spectral retrievals. More absorbing

bands have larger 'a' values since strong absorption limits the transmission into the cloud while 'b' value depends on the geometry and less absorptive bands tend to have large b values since photon travel deeper into the cloud via multiple scattering before getting absorbed. Therefore, this significant CER bias between the bi-spectral and vertically-weighted retrievals are due to the selections of 'a' and 'b' parameters to resemble the singly-scattered photons. Miller et al. (2017); Miller (2017); Miller et al. (2016) have performed a comprehensive analysis that assesses the 1D bi-spectral retrievals against the vertically-weighted retrievals and the influence of cloud vertical profile in the bi-spectral retrievals. Therefore, instead of using vertically-weighted retrievals as the reference, this chapter will use 1D RT simulation-based retrievals ($r_e^{NJK,1D}, \tau^{NJK,1D}$) as the reference cloud properties. The retrievals based on 3D RT are compared directly against their 1D counterparts to understand 3D RT effects.

4.3 A new framework for understanding the impact of 3D effects

Many studies have been focused on investigating various retrieval biases in the bi-spectral retrievals due to the 3D RT effects (Marshak and Davis, 2005). For oblique solar geometries, the sun-lit sides of the clouds appear brighter and corresponding retrieved-COT tend to have large values. Such COT biases in the satellite cloud observations have been investigated in detail (Várnai and Marshak, 2001, 2002; Loeb and Davies, 1996; Marshak et al., 1995). Even though the early studies on COT biases usually assumed constant CER and overlooked the CER-retrieval biases due to the 3D RT, a series of later studies such as Marshak et al.

(2006); Zhang and Platnick (2011); Zhang et al. (2012); Miller et al. (2016) have been investigated the biases in cloud microphysics retrievals due to the different aspects of 3D RT effects. However, increasing usage of high-resolution observations and aerosol indirect effect studies in complement with the availability of more computational power encourage us to perform further investigations on 3D effects in the bi-spectral retrievals.

The 3D nature of radiative transfer exists regardless of the instrument specification or the underlying retrieval technique. Hence the biases in the retrievals can be either due to the violation of PPA at the spatial scales below the footprint of the measurement (unresolved 3D variability) or due to the violation IPA at the spatial scales larger than the footprint of the reflectance measurement (resolved 3D variability). Even though both unresolved and resolved 3D variabilities appear as same CER or COT biases at the retrievals-end, the radiative effects due to the unresolved and resolved 3D variabilities are usually separated in 3D RT effect investigations (Marshak et al., 2006). As CER increases, SWIR reflectance (R_{SWIR}) decreases following a convex ($f'' > 0$) functional relationship. Hence ignoring sub-pixel variability (ie. unresolved 3D variability) underestimates the underlying CER retrievals. VNIR reflectance (R_{VNIR}) vs. COT relationship follows a concave functional relationship ($f'' < 0$). Thus averaging the reflectances in unresolved spatial scales to a large-scale footprint also underestimates the COT retrieval. In summary ignoring sub-pixel variabilities underestimates both COT and CER retrievals (Marshak et al., 2006).

Marshak et al. (2006) also shows that, if ΔR_{SWIR}^{3D-1D} ($R_{SWIR}^{3D} - R_{SWIR}^{1D}$) of all the

pixels due to the resolved 3D variability follows a Gaussian distribution about zero (i.e. illuminating and shadowing effects of the reflectances statistically cancel-out from each other), due to the non-linearity of the functional relationship between R_{SWIR} and CER, the shadowing effects dominate in the CER retrievals, i.e.,

$$\Delta r_e^{ill.} < \Delta r_e^{shad.} \tag{4.1}$$

By following a similar argument, if ΔR_{VNIR}^{3D-1D} has a Gaussian distribution about zero, the non-linearity of the R_{VNIR} vs COT relationship makes illuminating effect domination in the COT retrievals, i.e.,

$$\Delta \tau^{ill.} > \Delta \tau^{shad.} \tag{4.2}$$

Even though the underlying mathematical reasoning is sound, two key assumptions behind Equation 4.1 and 4.2: (1) assuming ΔR^{3D-1D} distribution as a Gaussian distribution about zero (2) assuming CER and COT retrievals are independent from each other are not valid. We will illustrate this last point in Section 4.3.1.

While the classical study of Marshak et al. (2006) had shed an illuminating light on the impacts of the 3D effect on the COT and CER retrievals based on the bi-spectral method, it has an important limitation. That is, the retrieval of COT and CER are considered to be completely separated and independent from each other. As pointed out in several previous studies, in particular Zhang et al. (2016b), the COT and CER retrievals are actually convoluted with each other because the LUT used in the bi-spectral method is nonlinear. To illustrate the nonlinear effect that ties the COT and CER retrieval together, we first extend the COT and CER,

both a function of R_{VNIR} and R_{SWIR} , into Taylor series as follows,

$$\begin{aligned}\tau(R^{3D}_{VNIR}, R^{3D}_{SWIR}) =&\tau(R^{1D}_{VNIR} + \Delta R_{VNIR}, R^{1D}_{SWIR} + \Delta R_{SWIR}) \\ =&\tau(R^{1D}_{VNIR}, R^{1D}_{SWIR}) + \frac{\partial \tau}{\partial R_{VNIR}}\Delta R_{VNIR} + \\ &\frac{\partial \tau}{\partial R_{SWIR}}\Delta R_{SWIR} + O(\Delta R^2)\end{aligned} \tag{4.3}$$

$$\begin{aligned}r_e(R^{3D}_{VNIR}, R^{3D}_{SWIR}) =&r_e(R^{1D}_{VNIR} + \Delta R_{VNIR}, R^{3D}_{SWIR} + \Delta R_{SWIR}) \\ =&r_e(R^{1D}_{VNIR}, R^{1D}_{SWIR}) + \frac{\partial r_e}{\partial R_{VNIR}}\Delta R_{VNIR} + \\ &\frac{\partial r_e}{\partial R_{SWIR}}\Delta R_{SWIR} + O(\Delta R^2)\end{aligned} \tag{4.4}$$

where $\tau(R^{1D}_{VNIR}, R^{1D}_{SWIR})$ and $r_e(R^{1D}_{VNIR}, R^{1D}_{SWIR})$ are the COT and CER, respectively, based on the 1D radiative transfer simulation, while $\tau(R^{3D}_{VNIR}, R^{3D}_{SWIR})$ and $r_e(R^{3D}_{VNIR}, R^{3D}_{SWIR})$ are the conterparts based on the 3D RT simulations. Based on the above equation, we can write the differences between 3D and 1D retrievals, $\Delta\tau$ and Δr_e, as the following matrix product format,

$$\begin{bmatrix} \tau(R^{3D}_{VNIR}, R^{3D}_{SWIR}) - \tau(R^{1D}_{VNIR}, R^{1D}_{SWIR}) \\ r_e(R^{3D}_{VNIR}, R^{3D}_{SWIR}) - r_e(R^{1D}_{VNIR}, R^{1D}_{SWIR}) \end{bmatrix} = \begin{bmatrix} \Delta\tau \\ \Delta r_e \end{bmatrix} = \begin{bmatrix} \frac{\partial \tau}{\partial R_{VNIR}} & \frac{\partial \tau}{\partial R_{SWIR}} \\ \frac{\partial r_e}{\partial R_{VNIR}} & \frac{\partial r_e}{\partial R_{SWIR}} \end{bmatrix} \begin{bmatrix} \Delta R_{VNIR} \\ \Delta R_{SWIR} \end{bmatrix} \tag{4.5}$$

where $\Delta R_{VNIR} = R^{3D}_{VNIR} - R^{1D}_{VNIR}$ and $\Delta R_{SWIR} = R^{3D}_{SWIR} - R^{1D}_{SWIR}$ are the differences in cloud reflectances in the VNIR and SWIR bands, respectively, due to the 3D radiative transfer. Equation 4.5 decomposes the impact of 3D effects on the COT and CER retrievals based on the bispectral method into two parts: (1) the magnitude of the subpixel reflectance variance and covariance specified by the

vector ($\Delta R_{VNIR}, \Delta R_{SWIR}$) and (2) the derivative matrix of the LUT with respect to R_{VNIR} and R_{SWIR} (referred to as "matrix of first derivatives"). Given the LUT, the matrix of first derivatives can be easily derived from straightforward numerical differentiation. An example of such a derived-matrix based on the LUT for 0.86 μm reflectance (R_{VNIR}) and 2.13 μm reflectance (R_{SWIR}) at $SZA = 60^o$ and nadir-viewing is shown in Figure 4.4. The values of the first derivatives ($a_{i,j}$) for the grids of LUT are indicated by the color bar. Note that the sign of $\Delta\tau$ and Δr_e is determined by both the first derivatives and the cloud reflectance perturbation due to the 3D RT, i.e., (ΔR_{VNIR},ΔR_{SWIR}).

It is clear from Equation 4.5 that the COT and CER retievals are influeced not only by the reflectance perturbation in the primary band (i.e., ΔR_{VNIR} for $\Delta\tau$ and ΔR_{SWIR} for Δr_e) but also by the perturbation of the secondary band (i.e. ΔR_{VNIR} for Δr_e and ΔR_{SWIR} for $\Delta\tau$).

It is important to note that Marshak et al. (2006) only considered the impact of the primary band by assuming that the COT and CER retrievals are separated and independent. In the context of Equation 4.5, their study only considers the impact of diagonal elements of the first derivative matrix and ignores the effects due to the off-diagonal element.

Our study in this section is built upon the previous studies, in particular, Marshak et al. (2006) and Zhang et al. (2016b). In comparison with Marshak et al. (2006), our study is based on the Equation 4.5 which provides a more comprehensive perspective of how 3D effects influence the simultaneous retrievals of COT and CER. Different from Zhang et al. (2016b) that focuses on the sub-pixel inhomogeneity and

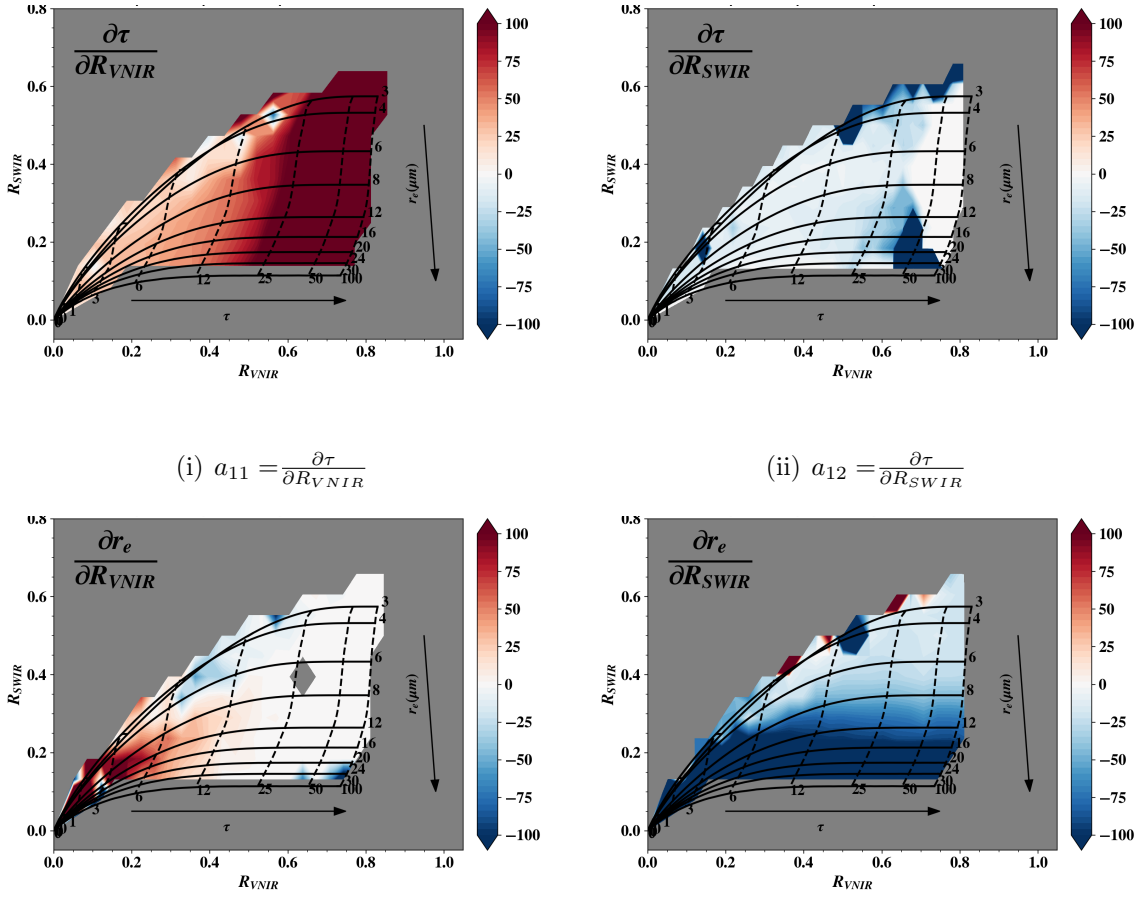

(i) $a_{11} = \frac{\partial \tau}{\partial R_{VNIR}}$ (ii) $a_{12} = \frac{\partial \tau}{\partial R_{SWIR}}$

(iii) $a_{21} = \frac{\partial r_e}{\partial R_{VNIR}}$ (iv) $a_{22} = \frac{\partial r_e}{\partial R_{SWIR}}$

Figure 4.4: The partial derivatives of τ and r_e with respect to $R_{VNIR,0.860\mu m}$ and $R_{SWIR,2.13\mu m}$ at SZA, VZA and SAA at 60^o, 0 and 0 respectively ("Matrix of first derivatives", Equation 4.5)

the consequential PPHB, here we focuses on the bias caused by the 3D radiative transfer and IPA assumption.

4.3.1 3D Radiative transfer simulations of the total reflectance

If the 3D reflectance of a particular pixel is greater than its 1D counter part, that pixel is considered as an "illuminated" pixel. On the other hand, if the 3D

RT-based reflectance is smaller than corresponding 1D RT-based reflectance, that pixels is considered as a "shadowed" pixel. Previous studies assume that ΔR^{3D-1D} of both VNIR and SWIR bands follow a Gaussian distribution about zero and CER and COT retrievals are independent from each other (i.e. $\frac{\partial \tau}{\partial R_{SWIR}}$and $\frac{\partial r_e}{\partial R_{VNIR}}$in Equation 4.5 are zero). If this assumptions are correct, the shadowing effects in the CER-biases ($\Delta r_e^{shad.}$), and the illuminating effects in the COT-biases ($\Delta \tau^{ill.}$) dominate in the bi-spectral retrievals due to the unresolved 3D effect variability. Figure 4.1 shows the radiance fields from 1D RT simulations. In order to investigate ΔR^{3D-1D} distributions, we need to perform 3D RT simulations for the LES cases.

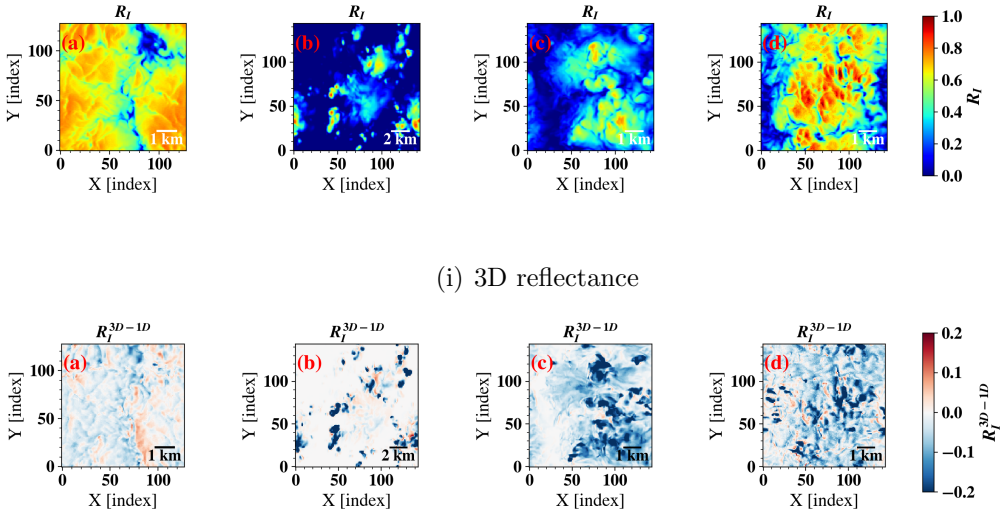

(i) 3D reflectance

(ii) Reflectance bias

Figure 4.5: Simulated 3D total reflectances ($\pi I/\mu_0/F_0$) from MSCART (i) and reflectance bias ($R_I^{3D} - R_I^{1D}$) (ii) for (a) DYCOMS-II, (b) RICO, (c) ATEX-clean, and (d) ATEX-polluted cases in 0.860 μm. The Sun is to the left at $SZA = 40^o$

Figure 4.5 shows the simulated 3D reflectance fields(i) and 3D and 1D reflectance biases (ii) of (a) DYCOMS-II, (b) RICO, (c) ATEX-clean, and (d) ATEX-

polluted cases from the MSCART RT model at 0.860 μm wavelength in the native resolution. The Sun is to the left side of the domain at SZA=40^o. In general, as shown in Figure 4.5 (ii), large biases exist where strong spatial gradients of R_I exist (e.g. Figure 4.1 (c) [X=70,Y=120]). Interestingly, there are negative biases in Figure 4.5 (ii)(b-c) (i.e. $\Delta R^{3D-1D} < 0$ shadowing effects) even though some of these cloud structures facing towards the sun. This reduction of R^{3D} at the optically thick cumulus cloud structures are likely due to the photon leaking from the sides. Note that in this example, a moderate SZA(=40) has been used. For more oblique solar geometries, the classic illuminating and shadowing effects (i.e. illuminating effect at the sun-lit side while the shadowing effects at the opposite side) more significant than moderate or high solar geometries.

Illuminating and shadowing effects in the radiance fields can occur due to many reasons. Directly facing towards the sun or facing opposite direction to the sun is not the only reason behind 3D variability in the radiance fields. Photon leaking from the cloud sides also could cause "shadowing effects" while the cloud facing directly towards the sun. However, from the retrieval's perspective, the more primitive question would be whether the illuminating effect or the shadowing effect will be the most statistically significant effect for a given scene. In other words, whether ΔR^{3D-1D} follows a Gaussian distribution about zero or skewed to negative (shadowing) or positive (illuminating) direction.

Figure 4.6 shows the PDF (probability density function) and CDF (cumulative density function) of ΔR^{3D-1D} for DYCOMS-II (a,b) and RICO (c,d) cases at $SZA = 40^o$. In Figure 4.6 (a), the PDF of $\Delta R^{3D-1D}_{I,SWIR}$ is more closely following a

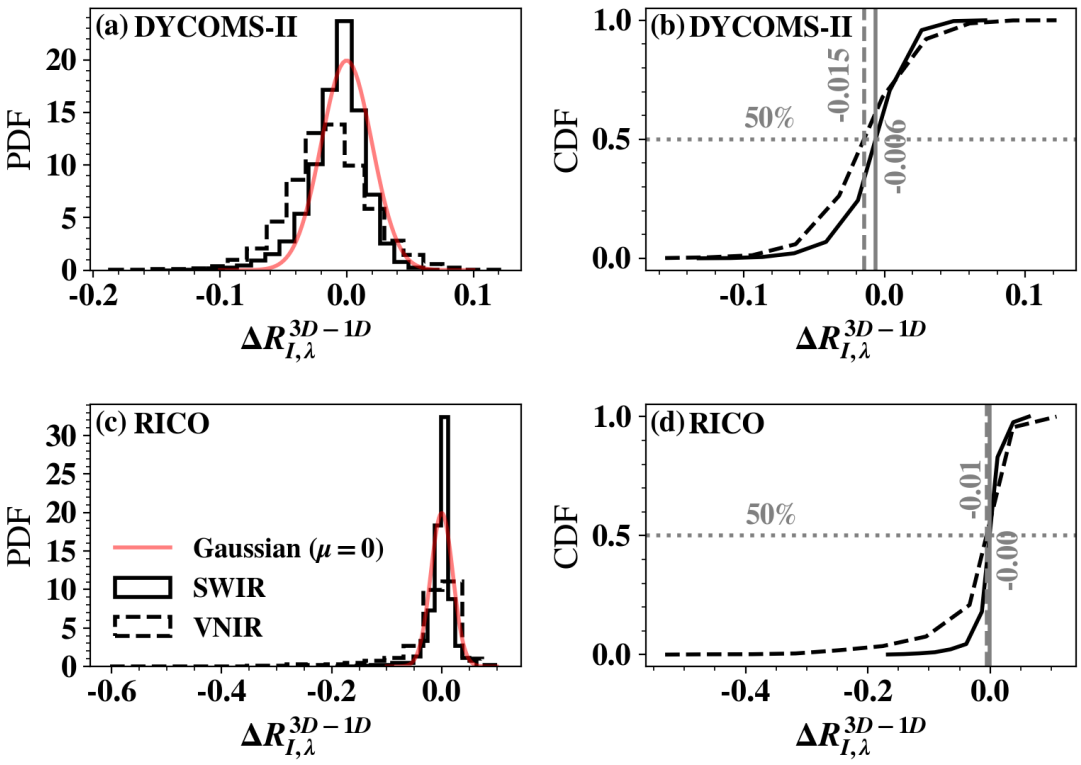

Figure 4.6: Distribution of $\Delta R_{I,\lambda}^{3D-1D}(R_{I,\lambda}^{3D} - R_{I,\lambda}^{1D})$ for DYCOMS-II (a,b) and RICO (c,d) case in the native-resolution at $SZA = 40^o$ for VNIR (dashed) and SWIR (solid) wavelengths. MA-fil cloud mask has been used.

Gaussian distribution about zero than $\Delta R_{I,VNIR}^{3D-1D}$. A relatively long negative tail exists in the VNIR-PDF than the SWIR-PDF in Figure 4.6 (a) which indicates strong shadowing effects are more frequent in the VNIR band than the SWIR band. The CDFs in Figure 4.6 (b) confirm this argument by having -0.015 50-percentile for the VNIR band and -0.006 50-percentile for the SWIR band. Moreover the absolute values of the first ($|Q_1|$) and third ($|Q_3|$) quantiles of $\Delta R_{I,VNIR}^{3D-1D}$ are ~ 0.03 and 0.005 respectively for the VNIR band which indicate more strong shadowing effects exist than the illuminating effects (i.e. $|Q_1| > |Q_3|$ implies frequent strong

shadowing effects than illuminating effects). $|Q1/Q3|$ ratio also can be used to check whether the extreme biases are dominated by illuminating or shadowing effects. In the DYCOMS-II case, the VNIR band $|Q1/Q3| = 6.4$ while SWIR band $|Q1/Q3| = 3.0$. In all the LES cases, at the native resolution $|Q1/Q3| > 0$ which indicates frequent strong shadowing effects than the illuminating effects. This phenomenon is prominent in the VNIR band than the SWIR band which likely due to the strong absorption in the SWIR band. Less-absorbing VNIR photons can cause more horizontal photon transfer via multiple scattering to increase the unresolved 3D variability at the fine resolutions.

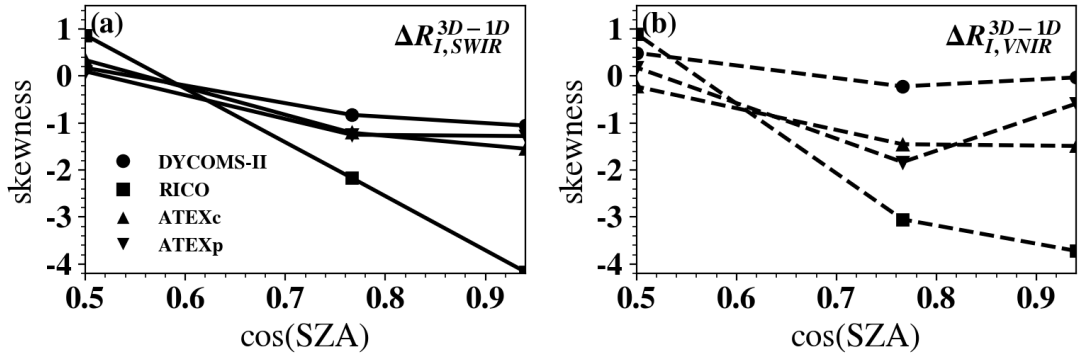

Figure 4.7: The skewness of ΔR^{3D-1D} distribution as SZA varies in the native resolution. MA-fil cloud mask has been used.

To get a better understanding of the general shape of the ΔR^{3D-1D}distribution of all LES cases, Figure 4.7 plots the skewness (see Appendix A, Equation A.2 for definition) of the distribution as SZA varies for all LES cases at the native resolution. For small SZAs , ΔR^{3D-1D}distribution is negatively skewed. The mean value of $\Delta R^{3D-1D}$for all the LES cases are negative values close to zero. The negative skewness with a negative mean close to zero indicates that the more weight of

the ΔR^{3D-1D}distribution is in the shadowing (negative) part. If ΔR^{3D-1D}_{SWIR}follows a Gaussian distribution about zero, shadowing effects dominate in the CER retrievals as indicated in the inequality in Equation 4.1 . However, Equation 4.1 only consider $\frac{\partial r_e}{\partial R_{SWIR}}$element in the first derivative matrix in Equation 4.5 and ignores the $\frac{\partial r_e}{\partial R_{VNIR}}$. That is, Equation 4.1 approximate $\Delta r_e \approxeq \frac{\partial r_e}{\partial R_{SWIR}} \Delta R_{SWIR}$, but in reality $\Delta r_e = \frac{\partial r_e}{\partial R_{VNIR}} \Delta R_{VNIR} + \frac{\partial r_e}{\partial R_{SWIR}} \Delta R_{SWIR}$ from Equation 4.5. In Figure 4.4(iii), $\frac{\partial r_e}{\partial R_{VNIR}}$is mostly zero for larger COTs, but for optically thin clouds, $\frac{\partial r_e}{\partial R_{VNIR}} > 0$. Therefore, for large COTs, $\Delta r_e \approxeq \frac{\partial r_e}{\partial R_{SWIR}} \Delta R_{SWIR}$ approximation is reasonable thus Equation 4.1 would be valid when ΔR^{3D-1D}-distribution has an ideal Gaussian shape (Gaussian distribution with $\mu = 0$) but for smaller COTs it is not necessarily true. When ΔR^{3D-1D}_{SWIR}deviates from Gaussian distribution about zero to have more weight at the shadowing side, following a similar argument based on the Equation 4.5, we can see Equation 4.1 still be valid with even stronger shadowing effect dominance in the CER retrievals for optically thick clouds, but not for optically thin clouds.

The inequality in Equations 4.2 indicates that the illuminating effects become more significant in the COT biases if the ΔR^{3D-1D}_{VNIR}follows a Gaussian distribution about zero and COT retrievals are independent from CER (i.e. $\frac{\partial \tau}{\partial R_{SWIR}} \approxeq 0$). However, when the ΔR^{3D-1D}_{VNIR}distribution has more weight in the shadowing side, this inequality 4.2 will not be necessarily valid anymore. The dominant shadowing effects would cause more negative biases in the COT retrievals instead of the positive biases as indicated in Equation 4.2 . In summary, for large SZAs, ΔR^{3D-1D}more closely follows a Gaussian distribution about the zero. Thus, the Equation 4.1 and 4.2 valid

for large SZAs (We can observe this phenomenon in Figure 4.9(a). Strong COT and CER biases exist due to the dominant illuminating effect in the COT retrievals and the shadowing effects in the CER retrievals respectively).

So far we discussed about the ΔR^{3D-1D}distributions at the native resolution. Other than the RICO case that has 100 m native resolution, all the other LES cases have 50 m native resolution. Figure 4.8 shows the variation of the skewness of ΔR^{3D-1D}distribution as the horizontal resolution increases. In general, as the horizontal resolution increases, all ΔR^{3D-1D}distributions become more symmetric around the mean hence get closer to a Gaussian distribution about zero. Therefore, in coarse resolutions, assuming ΔR^{3D-1D}distribution as Gaussian distribution about zero would be a more reasonable approximation than in the fine resolutions. Consequently, when the resolution gets coarser, the CER and COT 3D RT biases would tend to follow the inequalities in Equation 4.1 and Equation 4.2 respectively if the dominant biases come from the diagonal-terms in Equation 4.5.

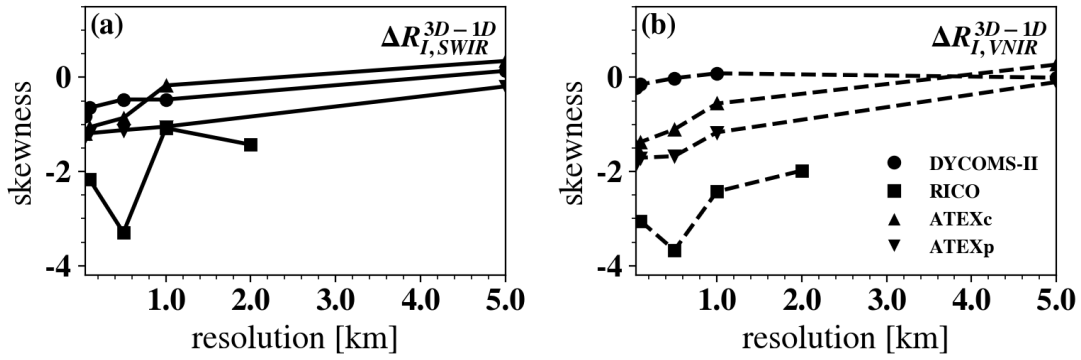

Figure 4.8: The skewness of ΔR^{3D-1D} distribution as horizontal spatial resolution varies at $SZA = 40^o$. MA-fil cloud mask has been used.

In summary, if the resolved 3D variability of the radiance follows a Gaus-

sian distribution about the zero, and the CER and COT retrievals are independent from each other (i.e. off-diagonal terms of Equation 4.5 are zero), the shadowing effects dominate in the CER retrieval biases (Equation 4.1) and the illuminating effects dominate in the COT retrieval biases (Equation 4.2). Even though the ΔR^{3D-1D}distribution follows a Gaussian distribution about zero in coarse resolutions where the resolved 3D variability is minimal, as the resolution becomes finer, the resolved 3D variability increases (because smaller footprints likely cause more IPA violations) and the shape of ΔR^{3D-1D}distribution deviates from the Gaussian shape about the zero. In the fine resolutions, ΔR^{3D-1D}distribution becomes a negatively skewed distribution with a negative mean value close to zero. Hence more weight of ΔR^{3D-1D}distribution is in the shadowing side. Consequently, this skewness of ΔR^{3D-1D}distribution towards causing more shadowing effects in finer resolution would cause more positive biasses in CER-retrievals (agrees with Equation 4.1) and more negative biases in the COT retrievals (does not agree with Equation 4.2) if $\frac{\partial r_e}{\partial R_{VNIR}}$and $\frac{\partial \tau}{\partial R_{SWIR}}$terms in Equation 4.5 are negligible. However, it is also important to note that, for optically thicker clouds, illuminating effects can cause stronger COT biases than the illuminating effects in the optically thin clouds, because R_{VNIR} vs COT relationship is an asymptotically increasing function (in the Nakajima-King LUT space, the constant COT lines become closer to each other as VNIR reflectance increases). In this section, we discussed mainly the biases in the reflectances, and then their consequences on the retrievals. Section 4.4 investigates how these 3D RT effects in the radiance fields influenced the underlying cloud property retrievals in detail.

4.4 Bi-spectral retrievals under 3D radiative transfer

In general, ΔR^{3D-1D}-distribution has a Gaussian shape centered to zero. However as the resolution increases (in fine resolutions) or the SZA decreases, the shape of the distribution deviates from the original Gaussian shape, and more weight of the distribution tend to be centered in the shadowing part. In this section we discuss how these radiance biases influence the underlying CER and COT retrievals. Since we are going to assess the influence of 3D RT for different radiative and physical quantities (e.g. CER, COT, R_{SWIR}, R_{VNIR}), it is convenient to define a common "3D effect impact factor" as follows,

$$f_P = \frac{P_{3D} - P_{1D}}{P_{1D}} \tag{4.6}$$

where $P = COT$, CER, R_{SWIR}, R_{VNIR}, etc.

Figure 4.9 compares different f_P quantities with each other for the DYCOMS-II case at $SZA = 60^o$. CEV-fil cloud mask has been used. Figure 4.9 (d) is the joint-histogram of $f_{R_{SWIR}}$vs. $f_{R_{VNIR}}$. Both $f_{R_{SWIR}}$and $f_{R_{VNIR}}$, in general, follow a Gaussian distribution about the zero, yet $|f_{R_{SWIR}}|$ frequently have slightly larger values than $|f_{R_{VNIR}}|$ as $|f|$ increases. That is, $f_{R_{SWIR}}$distribution has a large variability than $f_{R_{VNIR}}$distribution even though in the Figure 4.6(a) and (c), the ΔR^{3D-1D}_{VNIR}-distribution has a large spread than ΔR^{3D-1D}_{SWIR}distribution (Note that $SZA = 40^o$ in Figure 4.6. But the same argument is valid for $SZA = 60^o$ case too). This is because the SWIR band is more absorptive thus, in general, the R_{SWIR} tends to have smaller values compared to the R_{VNIR}. Therefore, the denominator of Equa-

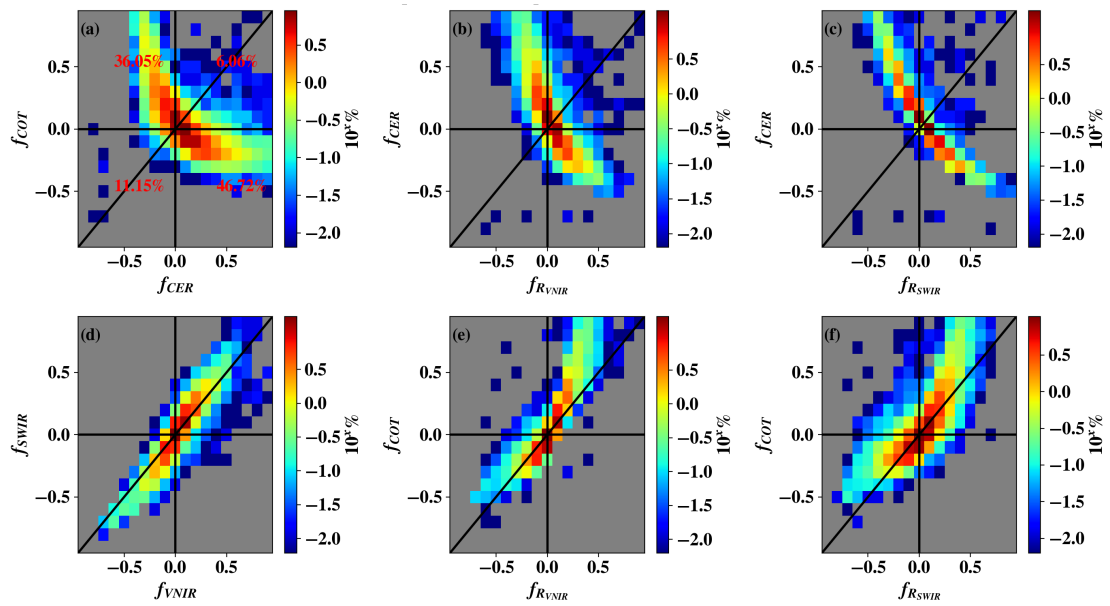

Figure 4.9: 3D effect impact factor (f_P, Equation 4.6) comparisons for DYCOMS-II case at $SZA = 60^o$. CEV-fil cloud mask has been used. Colorbar of the joint histograms is the percentage of counts on a logarithmic scale.

tion 4.6 becomes smaller and consequently causes large $f_{R_{SWIR}}$values relative to the $f_{R_{VNIR}}$values.

The interesting question is how these impacts on the radiances influence the COT and CER retrievals. Figure 4.9 (a) shows f_{COT} vs. f_{CER} for the DYCOMS-II case at $SZA = 60^o$. A vast majority of strong 3D effects in the COT retrievals with $|f_{COT}| > 0.5$ are due to the illuminating effects. A negligible amount of pixels have $f_{COT} < -0.5$, which indicates illuminating effects dominate in the strong COT biases as in Equation 4.2. The strong CER biases that have $|f_{CER}| > 0.5$ are dominated by shadowing effects that agree with Equation 4.1. Thus, for the DYCOMS-II case, 4.2 and 4.1 inequalities are reasonable for large 3D effects impact factors of both COT

and CER retrievals.

To be compliance with the assumptions of Marshak et al. (2006), we can assume the off-diagonal elements ($\frac{\partial \tau}{\partial R_{SWIR}}$and $\frac{\partial r_e}{\partial R_{VNIR}}$) of Equation 4.5 are zero and the ΔR^{3D-1D}-distribution as an ideal Gaussian distribution about the zero. Then the positive $\Delta R^{3D-1D}_{VNIR}$and ΔR^{3D-1D}_{SWIR}values should give positive COT-biases (because $\frac{\partial \tau}{\partial R_{VNIR}} > 0$ as in Figure 4.4) and negative CER-biases (because $\frac{\partial r_e}{\partial R_{SWIR}} < 0$ as in Figure 4.4) respectively which correspond to the second quadrant of Figure 4.9 (a). Due to the same reason (i.e. $\frac{\partial \tau}{\partial R_{VNIR}} > 0$ and $\frac{\partial r_e}{\partial R_{SWIR}} < 0$), when $\Delta R^{3D-1D}_{SWIR}$and $\Delta R^{3D-1D}_{VNIR}$are negative, the COT and CER biases should be negative and positive respectively which correspond to the fourth quadrant of Figure 4.9 . Since the COT contours in the LUT-space get closer as R_{VNIR} increases ($\frac{\partial^2 \tau}{\partial^2 R_{VNIR}} > 0$), the COT biases due to the illuminating effects are stronger than the COT biases due to the shadowing effects (i.e. $\Delta\tau^{ill.} > \Delta\tau^{shad.}$ as in Equation 4.2). We can observe this phenomenon in Figure 4.9 (e) where shows the joint-histogram of f_{COT} vs. $f_{R_{VNIR}}$. The illuminating effects of the VNIR reflectance ($f_{R_{VNIR}} > 0$) cause strong positive biases in the COT retrievals (i.e. large f_{COT} values) relative to the shadowing effects ($f_{R_{VNIR}} < 0$). As R_{SWIR} decreases, the CER contour lines of the LUT-space get closer ($\frac{\partial r_e}{\partial R_{SWIR}}$), hence the CER biases due to the shadowing effects should be stronger than the CER biases due to the illuminating effects(i.e. $\Delta r_e^{shad.} > \Delta r_e^{ill.}$ as in Equation 4.1). Figure 4.9 (c) shows the joint-histogram of f_{CER} vs. $f_{R_{SWIR}}$. We can see in Figure 4.9 (c), in contrast to the illuminating effects, even a small shadowing effect (slightly negative $f_{R_{SWIR}}$value) can cause large bias in CER (large increment in f_{CER}). For the DYCOMS-II case 83% of cloudy-pixel are in quadrant I

and II, where the Equation 4.2 and 4.2 are a reasonable approximation to understand the COT and CER biases.

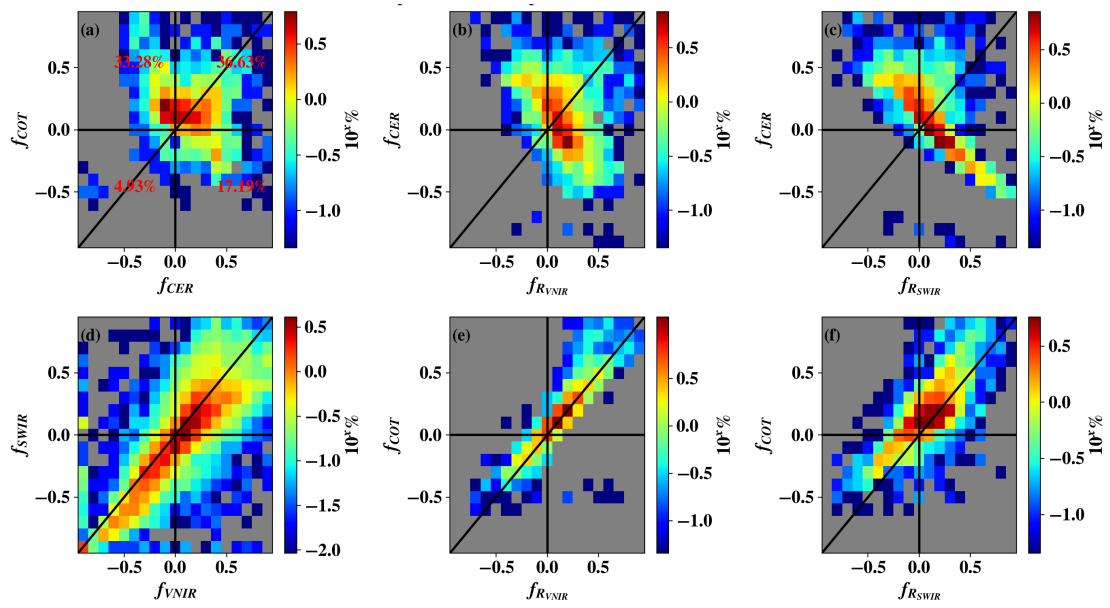

Figure 4.10: 3D effect impact factor (f_P, Equation 4.6) comparisons for RICO case at $SZA = 60^o$. CEV-fil cloud mask has been used. Colorbar of the joint histograms is the percentage of counts on a logarithmic scale.

The DYCOMS-II case is an overcast cloud scene with minimal microphysical and optical variabilities compared to the other LES cases. The dominant trends of COT and CER biases (for 83% of pixels) that we discussed so far based on Figure 4.9 can be explained from 4.1 and 4.2 inequalities. Figure 4.10 shows the correlations among the f_P quantities for the RICO case at $SZA = 60^o$. The CEV-fil cloud mask has been used. Compared to the DYCOMS-II case (in Figure 4.9 (c)) which has strong f_{CER} values for slightly negative $f_{R_{VNIR}}$values, Figure 4.10 (c) does not have such frequent high f_{CER} values. The ΔR^{3D-1D}_{SWIR}-distribution of the

RICO case has a positive mean and positive skewness hence more weight is in the illuminating part with possible strong illuminating effects in contrast to the DYCOMS-II case that has a ΔR_{SWIR}^{3D-1D}-distribution closer to an ideal Gaussian shape (Gaussian shape with $\mu = 0$). Thus, the DYCOMS-II case which has ΔR_{SWIR}^{3D-1D}-distribution closer to a Gaussian distribution has large f_{CER} values that tend to agree with Equation 4.1, while in the RICO case does not have such values likely because the ΔR_{SWIR}^{3D-1D}-distribution is skewed to illuminating side.

In contrast to the DYCOMS-II case (Figure 4.9) where most of the COT and CER retrieval-biases tend to be in Quadrant-II and IV, in the RICO case (Figure 4.10), more than 1/3 of pixels are in Quadrant-I where the both COT and CER retrieval biases are positive. If we assume the off-diagonal elements of Equation 4.5 are negligible, since $\frac{\partial \tau}{\partial R_{VNIR}} > 0$ and $\frac{\partial r_e}{\partial R_{SWIR}} < 0$, the only possibility of having both positive COT and CER retrieval biases is from $\Delta R_{VNIR}^{3D-1D} > 0$ and $\Delta R_{SWIR}^{3D-1D} < 0$ values respectively. In Figure 4.10 (d), there exist such values (in Quadrant-IV) but they do not necessarily correspond to the values in the Quadrant-I of Figure 4.10 (a). Therefore, Figure 4.11 (a) shows the correlation between ΔR_{VNIR}^{3D-1D}vs. $\Delta R_{SWIR}^{3D-1D}$of the $\sim$36% of pixels that have both positive COT and CER retrieval biases correspond to the Quadrant-I of Figure 4.10 (a). Among that 36% of pixels, only a 5% has $\Delta R_{VNIR}^{3D-1D} > 0$ and $\Delta R_{SWIR}^{3D-1D} < 0$, thus neglecting the off-diagonal terms of Equation 4.5 can not explain $\sim$ 30% of biased-pixels in the RICO case (Note that, to avoid confusion, all the indicated percentages are relative to the total cloudy-pixels of the whole domain). Among the 36% of pixels that have positive COT and CER biases, the majority of pixels (19%) have $\Delta R_{VNIR}^{3D-1D} > 0$ and $\Delta R_{SWIR}^{3D-1D} > 0$. Figure 4.11 (b)

further analyses those 19% of pixels. The x-axis of Figure 4.11 (b) is the CER bias ($\Delta r_e = r_e(R^{3D}_{VNIR}, R^{3D}_{SWIR}) - r_e(R^{1D}_{VNIR}, R^{1D}_{SWIR})$) computed from the retrieval simulator. The y-axis shows the $\frac{\partial r_e}{\partial R_{SWIR}} \Delta R^{3D-1D}_{SWIR}$ term of Equation 4.5 by neglecting the $\frac{\partial r_e}{\partial R_{VNIR}} \Delta R^{3D-1D}_{VNIR}$term. The a_{21} ($\frac{\partial r_e}{\partial R_{VNIR}}$) and a_{22} ($\frac{\partial r_e}{\partial R_{SWIR}}$) terms are computed based on the LUT correspond to the considering geometry ($SZA = 60^o$,$SAA = 0^o$, and $VZA = 0^o$) and shown in Figure 4.4. As shown in Figure 4.11 (b), if we only consider $\frac{\partial r_e}{\partial R_{SWIR}} \Delta R^{3D-1D}_{SWIR}$term, the computed-CER retrievals by no means agree with the simulated Δr_e. The computed CER biases based on the LUT have negative values while the simulated-Δr_e has positive values. However, if we include the contributions from $\frac{\partial r_e}{\partial R_{VNIR}} \Delta R^{3D-1D}_{VNIR}$, (in Figure 4.11 (c)), the correlation between the computed CER biases (i.e. $\frac{\partial r_e}{\partial R_{VNIR}} \Delta R^{3D-1D}_{VNIR} + \frac{\partial r_e}{\partial R_{SWIR}} \Delta R^{3D-1D}_{SWIR}$) and simulated-$\Delta r_e$ becomes more reasonable than the Figure 4.11 (b). We can see including both terms gives a reasonable sign for the computed-CER biases in many cases (i.e. many points tend to have in Quadrant-I of Figure 4.11 (c)). The points still do not get the sign of the simulated-Δr_e accurately, either have very small Δr_e values or small $\Delta R^{3D-1D}_{VNIR}$where fine resolution LUT tables are required to accurately compute a_{21} and a_{22} terms which we left for future studies.

In summary, if the resolved 3D variability of the radiance (ΔR^{3D-1D}) follows a Gaussian distribution about the zero, and the COT and CER retrievals are independent of each other (i.e. the off-diagonal elements of Equation 4.5 are negligible), the shadowing effects dominate in the CER retrieval biases (Equation 4.1) and the illuminating effects dominate in the COT retrieval biases (Equation 4.2). For large SZAs (Figure 4.7) and coarse resolutions (Figure 4.8) ΔR^{3D-1D}-distribution more

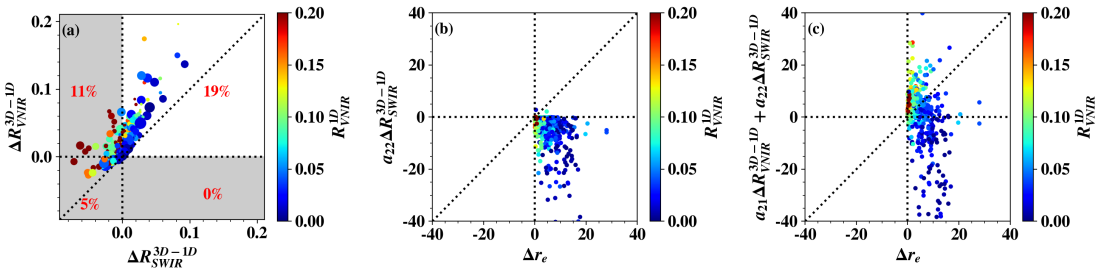

Figure 4.11: (a) VNIR vs. SWIR reflectance bias correlation (ΔR^{3D-1D}_{VNIR}vs. ΔR^{3D-1D}_{SWIR}) for the pixels with $f_{CER} > 0$ and $f_{COT} > 0$ (36% of cloudy-pixels) in Figure 4.10(a) for the RICO case at $SZA = 60^o$. Colors of the points represent the magnitude of R^{1D}_{VNIR}. Large points indicate the high CER biases. (b) $\frac{\partial r_e}{\partial R_{SWIR}}\Delta R^{3D-1D}_{SWIR}$vs. Δr_e^{3D-1D} (the difference between 1D and 3D CER retrievals) and, (c) ($\frac{\partial r_e}{\partial R_{VNIR}}\Delta R^{3D-1D}_{VNIR} + \frac{\partial r_e}{\partial R_{SWIR}}\Delta R^{3D-1D}_{SWIR}$) vs. Δr_e^{3D-1D} of the pixels in the Quadrant-I of panel (a) (19% of cloudy-pixels of the RICO case) .

close to an ideal Gaussian distribution (a Gaussian distribution with $\mu = 0$) than for small SZAs and fine resolutions. Even the ΔR^{3D-1D}-distribution closely follows a Gaussian distribution about zero, only a subset of pixels follow 4.1 and 4.2 because assuming CER and COT retrievals independent from each other only accurate when the COT and CER contour lines of the LUT are orthogonal. Hence for overcast clouds with minimal microphysical variabilities as in the DYCOMS-II case, a majority of pixels tend to follow Equation 4.2 and 4.1 at larger SZAs and coarse resolution where the ΔR^{3D-1D}-distribution tend to have closer to a Gaussian distribution about the zero. However, to fully understand the biases due to the 3D effects in the bi-spectral retrievals, especially when the cloud scene is dominated by scattered cumulus clouds with many thin cloud edges (such as in the RICO

case), the contributions from all four-elements in the "matrix of first derivatives" (Equation 4.5) have to be considered.

The 3D radiative effects are usually classified into two groups of unresolved 3D variability. The 3D RT effects in smaller scales than the measurement footprint and the resolved 3D variability effects of larger scales than the measurement footprint. Due to the non-linear functional dependence of R_{VNIR} vs. COT and R_{SWIR} vs. CER, ignoring unresolved variability (averaging over subpixels) cause negative biases in both COT and CER retrievals. If the resolved 3D variability ΔR^{3D-1D}has a Gaussian distribution about the zero, and the COT and CER retrievals are independent of each other, (i.e., the off-diagonal elements of Equation 4.5 are negligible), the shadowing effects dominate in the CER retrievals (Equation 4.1) and the illuminating effects dominate in the COT retrievals (Equation 4.2). In general, for large SZAs and coarse resolutions, ΔR^{3D-1D}more close to a Gaussian distribution about zeros than the small SZAs and fine resolutions. When ΔR^{3D-1D}-distribution has an ideal Gaussian shape (Gaussian distribution with $\mu = 0$), a subset of pixels tends to follow 4.1 and 4.2 inequalities. When the retrievals are based on the non-orthogonal region of the LUT-space where the off-diagonal elements of the matrix of first derivatives (Equation 4.5) are significant, the 4.1 and 4.2-inequalities do not necessarily true. This section summarizes the bi-spectral retrievals of all four LES cases under 3D RT mainly emphasizing when the results agree with the theoretical understanding and when they do not agree.

Figure 4.12 shows the bi-spectral retrievals of (i) DYCOMS-II, (ii) RICO, (iii) ATEX-clean, and (iv) ATEX-polluted cases similar to Figure 4.2 but based on 3D

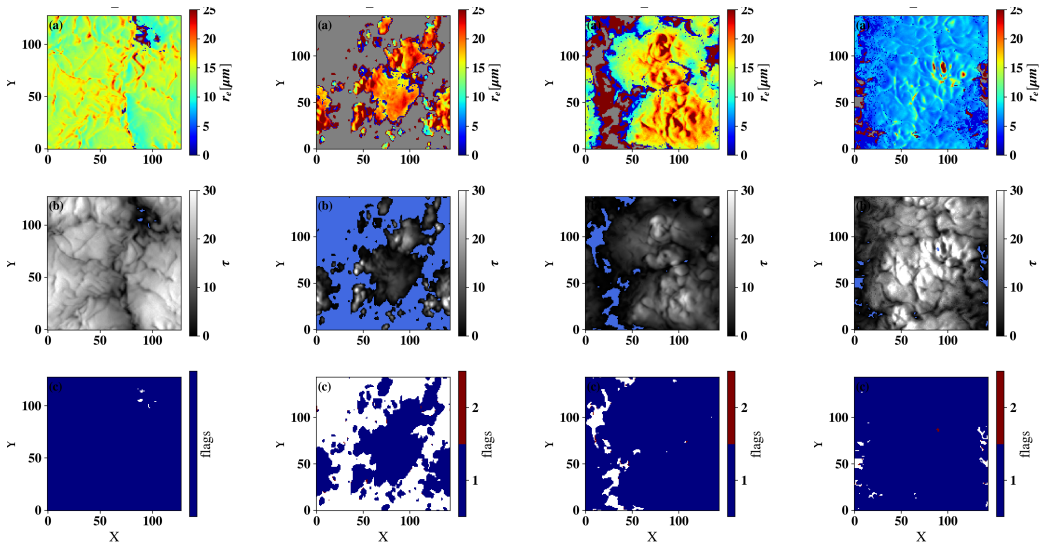

(i) DYCOMS-II (ii) RICO (iii) ATEX(clean) (iv) ATEX(polluted)

Figure 4.12: Bi-spectral retrievals at the native resolution for each LES case based on 3D RT. Panel (a),(b) and (c) of each column are CER ($r_e^{NJK,3D}$), COT($\tau^{NJK,3D}$) and retrieval quality flags. The Sun is to the left at $SZA = 40^o$. The VW-COT cloud mask (see Section 2.5) has been used. Flag 1 and 2 are "successful retrieval" and "outside the lookup table" respectively.

RT. The a and b-panels correspond to CER and COT retrievals respectively. The Sun is to the left side of the domain (SAA=0^o) with SZA=40^o. VW-COT cloud mask has been applied to mask the columns with vertically-weighted COT retrievals smaller than 0.1. The c-panels of each column correspond to the retrieval quality flag where '1' and '2' indicate a "successful retrieval" and a "retrieval outside the look-up-table" respectively. For the DYCOMS-II case, compared to Figure 4.2 (i)(a), the sides of the cloud that face away from the sun have larger $r_e^{3D,NJK}$ retrievals in Figure 4.12 (i)(a) which indicates the existence of classic shadowing effects. However,

Figure 4.12 is for a moderate SZA (SZA=40^o), thus the classic illuminating and shadowing effects (large 3D reflectance at the sun-lit side and small 3D reflectance at the other side respectively) are not frequent as in oblique solar geometries (e.g. SZA=60^o). It is important to note that facing the sun is not the only reason for illuminating effects or facing away from the sun for shadowing effects. For an example, the large $\tau_e^{1D,NJK}$ retrievals ($COT \sim 30$) in Figure 4.2 (iii)(b) has been significantly reduced ($COT < 30$) in the $\tau_e^{3D,NJK}$ retrievals in Figure 4.12 (iii)(b) despite the orientation relative to the Sun. That is, even the $\tau_e^{3D,NJK}$ of the sun-lit side is influenced by the shadowing effects which is likely due to the photon leaking from the sides. This phenomenon is more clearly visible in the RICO and ATEX cases than the DYCOMS-II case.

4.4.1 Solar zenith angle dependence

Solar geometry is a crucial factor when it comes to 3D RT effects. As discussed in Section 4.3, the shape of the ΔR^{3D-1D}-distribution (3D variability of the reflectance) changes as SZA varies. Moreover, the underlying LUT grid of the bi-spectral retrievals also varies hence the non-linearity of the cloud properties and the reflectances relationships also vary with SZA. This section further investigates solar zenith angle dependence of the 3D effects of the bi-spectral retrievals based on the selected four LES cases.

Figure 4.13 compares the bi-spectral retrievals based on 3D and 1D RT simulations for DYCOMS-II case at (i) SZA=20^o, (ii) SZA=40^o, and (iii) SZA=60^o. The

Sun is to the left side of the domain. MA-fil cloud mask has been used. For the DYCOMS-II case, ΔR^{3D-1D}-distribution becomes closer to an ideal Gaussian shape about the zero when SZA increases (skewness ~ 0 in Figure 4.7). For small SZAs, ΔR^{3D-1D}-distribution is negatively skewed with a negative mean value thus more weight is in the shadowing part of the distribution than the illuminating part. In Figure 4.13 (i)(d), the $\tau_e^{3D,NJK}$ retrievals frequently have negative biases compared to the $\tau_e^{1D,NJK}$ retrievals. The mean bias between the two retrievals is -0.8565. As SZA increases to 40^o, the positive COT biases become more frequent compared to SZA=20^o and consequently at SZA=60^o, the mean COT bias between 3D and 1D retrievals becomes 0.1967. For high sun, $\Delta R^{3D-1D}$is not an ideal Gaussian distribution about zero but skewed to have more shadowing effects which might likely cause shadowing effect dominance in the COT retrievals against 4.2 inequality. As SZA increases, ΔR^{3D-1D}becomes closer to the shape of an ideal Gaussian distribution about zero and illuminating effects in the reflectances cause strong postive COT retrieval biases than the shadowing effects of the same magnitude (agree with Equation 4.2), thus overall $\tau_e^{3D,NJK}$ becomes positively bias compared to $\tau_e^{1D,NJK}$.

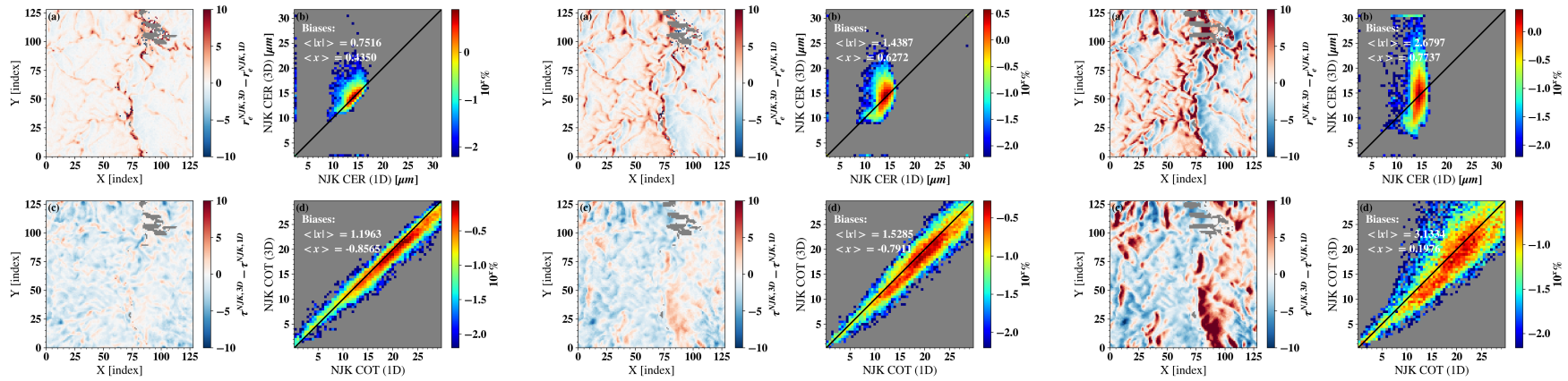

(i) $SZA = 20^o$ (ii) $SZA = 40^o$ (iii) $SZA = 60^o$

Figure 4.13: Comparisons of 3D vs 1D bi-spectral retrievals for DYCOMS-II case at (i) $SZA = 20^o$, (ii) $SZA = 40^o$ and (iii) $SZA = 60^o$ in the native resolution. Colorbar of the joint histograms is the percentage of counts on a logarithmic scale. $< x >$ and $< |x| >$ are the mean bias and mean absolute bias respectively (see Appendix A bias-statistic definitions). Sun is to the left side of the domain. MA-fil cloud mask has been used.

In the CER retrievals, at SZA=20^o (Figure 4.13 (i)(b)), most $r_e^{3D,NJK}$ retrievals agree with their $r_e^{1D,NJK}$ counterparts while the existing biases are dominated by shadowing effects ($r_e^{3D,NJK} > r_e^{1D,NJK}$). When SZA increases from 20^o to 40^o (in Figure 4.13 (ii)(b)), in general, the biases between $r_e^{3D,NJK}$ vs. $r_e^{1D,NJK}$ become more frequent especially the positive biases due to the shadowing effects than the negative biases due to the illuminating effects. When SZA increases from 20^o (Figure 4.13 (i)(b)) to 40^o (Figure 4.13 (ii)(b)), the mean bias increases from 0.4350 to 0.6272. So in general, CER retrievals tend to be consistent with Equation 4.1 perhaps because of the skewness of the ΔR^{3D-1D}-distribution complement to the inequality (Equation 4.1) by increasing the weight in the shadowing part of the distribution.

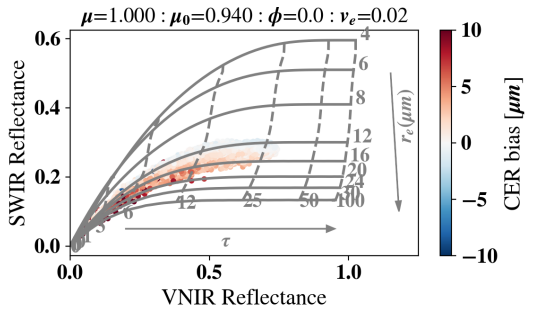

(i) CER bias at $SZA = 20^o$

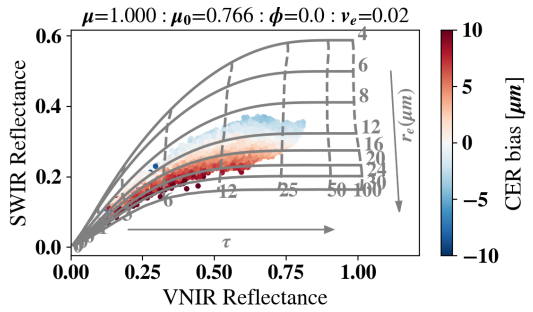

(ii) CER bias at $SZA = 40^o$

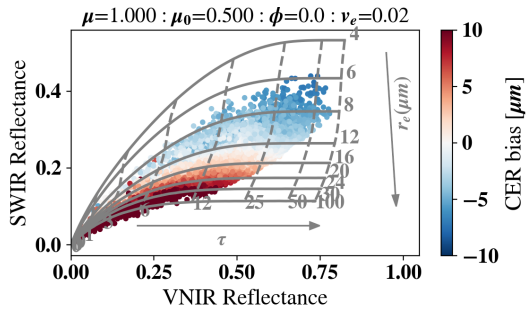

(iii) CER bias at $SZA = 60^o$

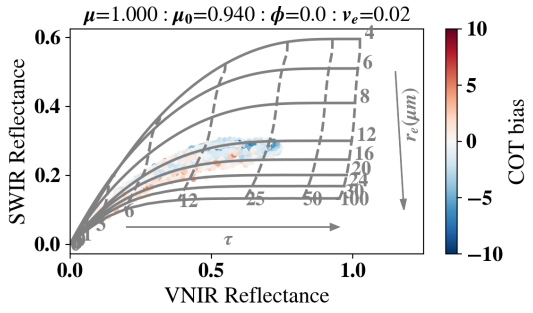

(iv) COT bias at $SZA = 20^o$

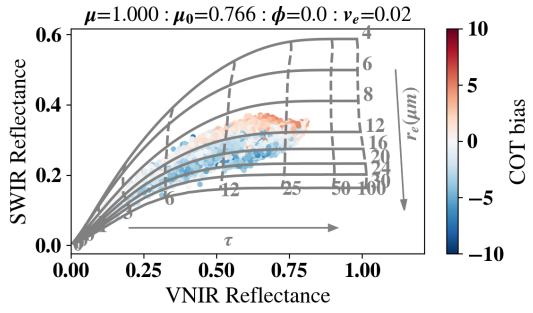

(v) COT bias at $SZA = 40^o$

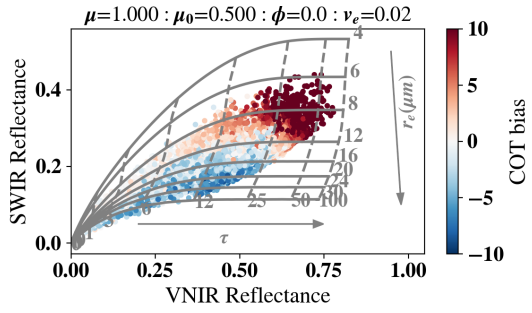

(vi) COT bias at $SZA = 60^o$

Figure 4.14: CER (i-iii for $SZA = 20^o$,40^o, and 60^o) and COT (iv-vi for $SZA = 20^o$, 40^o, and 60^o) biases overplayed on bi-spectral look-up-table space for DYCOMS-II case. The biases shown in (i), (ii), and (iii) correspond to a-panels Figure 4.13 (i), (ii), and (iii) respectively. The biases shown in (iv), (v), and (vi) correspond to c-panels in Figure 4.13 (i), (ii), and (iii) respectively. Sun is to the left side of the domain. MA-fil cloud mask has been used.

Figure 4.14 overlays the biases shown in Figure 4.13 on the corresponding Nakajima-King LUT-space for the DYCOMS-II case. Figure 4.14 (i-iii) correspond to the biases of $r_e^{3D,NJK}$ relative to $r_e^{1D,NJK}$ shown in the a-panels of Figure 4.13 (i-iii) for SZA= $20^o, 40^o$, and 60^o respectively. Figure 4.14 (iv-vi) correspond to the biases of $\tau_e^{3D,NJK}$ relative to $\tau_e^{1D,NJK}$ shown in the c-panels of Figure 4.13 (iv-vi) for SZA= $20^o, 40^o$, and 60^o respectively. The grey solid and dashed lines in Figure 4.14 are the constant CER and COT contours respectively. For optically thick clouds, the value of the CER-contour increases as the SWIR reflectance decreases (indicated by the downward arrow of each panel) while the value of the COT-contour increases as VNIR reflectance increases (indicated by the horizontal rightward arrow). It is also important to note that due to the non-linear behavior of the R_{VNIR} vs. COT function, the COT contour lines are closer to each other for large VNIR reflectances compared to the small reflectances. For optically thick clouds, due to the non-linearity between R_{SWIR} vs. CER relationship, the CER contour lines are closer to each other in the smaller SWIR reflectance region of the LUT. For optically thin clouds, COT and CER contour lines of the LUT are not orthogonal anymore and the CER contours are densely packed close to each other. In Figure 4.14 (i), the CER biases are mostly positive with minimal negative biases. In Figure 4.14 (ii) ($SZA = 40^o$), the CER biases between the 12 and 16 μm CER-contour lines are closer to zero. However when the SWIR reflectance decreases bellow the value correspond to the CER-16μm contour line, the bias between $r_e^{3D,NJK}$ and $r_e^{1D,NJK}$ increases. On the other hand, when the SWIR reflectance increases above CER-12μm contour line, the bias becomes negative. In Figure 4.14 (iii), these 3 groups are

more clearly observable. Between 12-16 μm contours, the CER-bias close to zero. When the SWIR reflectance increases greater than the corresponding value to the CER-12μm contour line, the CER bias becomes negative (bluish points) while the SWIR reflectance decreases bellow the value correspond to the CER-16μm contour line, the bias becomes positive (reddish points). The DYCOMS-II case has relatively constant microphysics in the range of 12-16μm (Figure 2.4(i)(a)). Thus the biases greater than 16 μm are likely due to the shadowing effects and the biases below 12 μm are likely due to the illuminating effects. In the region of the bluish points, the CER contours have more spread than the region of the reddish points, thus a particular -δR_{SWIR} bias in the SWIR reflectance can cause a stronger shadowing effect (positive CER bias) than an illuminating effect can do due to the same $+\delta R_{SWIR}$ (Equation 4.1).

Figure 4.15 summarizes the biases between the 3D RT-based bi-spectral retrievals and the 1D RT-based bi-spectral retrievals in the native resolution. Panel (a) and (b) are the mean ($\langle r_e^{3D} - r_e^{1D} \rangle$) and mean absolute biases ($\langle |r_e^{3D} - r_e^{1D}| \rangle$) of CER retrievals respectively. Panel (c) and (d) are the mean ($\langle \tau_e^{3D} - \tau_e^{1D} \rangle$) and mean absolute biases ($\langle |\tau_e^{3D} - \tau_e^{1D}| \rangle$) of the COT retrievals respectively. Except for the ATEX-polluted case at SZA=20^o, in Figure 4.15 the mean biases of the CER retrievals are greater than zero and less than ~ 1.6 for all LES cases and geometries. As discussed in Section 4.3, if the ΔR^{3D-1D}-distribution of the resolved 3D variability follows a Gaussian distribution with 0-mean and the off-diagonal elements of the matrix of first derivatives in Equation 4.5 are negligible, the shadowing effects dominate in the CER retrievals (Equation 4.1). For larger SZAs, all LES cases tend

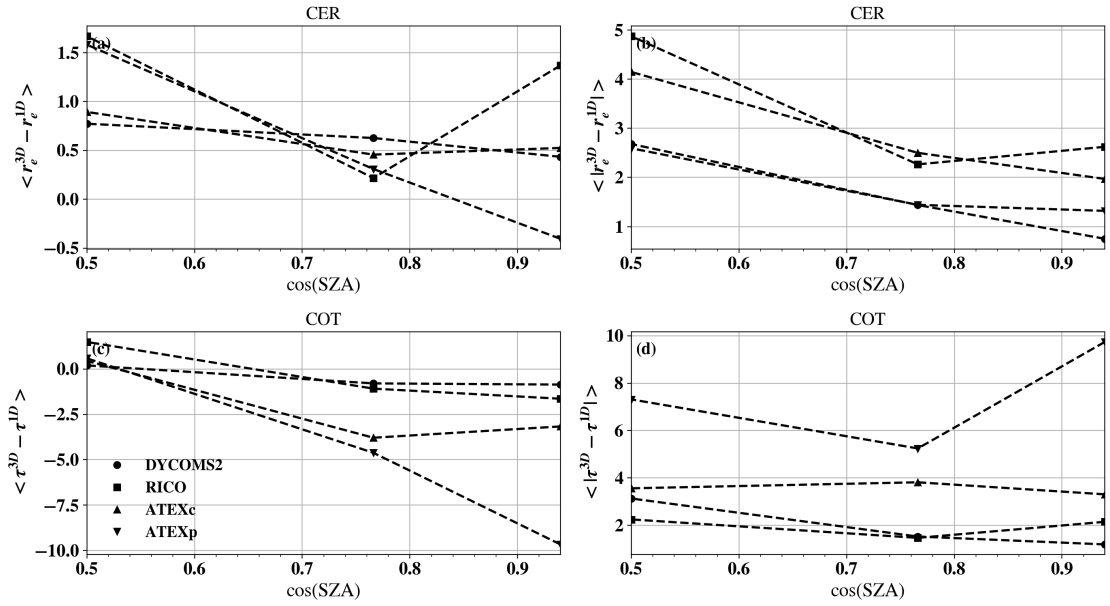

Figure 4.15: Mean bias ($\langle x \rangle$) and mean absolute bias ($\langle |x| \rangle$) (see Appendix A for definitions) between 3D and 1D RT-based bi-spectral retrievals in the native resolution. (a) and (b) are the mean and absolute mean CER biases as SZA varies. (c) and (d) are the mean and absolute mean COT biases as SZA varies. MA-fil cloud mask has been used.

to have ΔR^{3D-1D}-distribution closer to ideal Gaussian shape (Gaussian shape with $\mu = 0$). When the SZA becomes smaller, the ΔR^{3D-1D}tend to have a negatively-skewed distribution with a negative mean which in combine indicates more weight in the shadowing part ($\Delta R^{3D-1D} < 0$) than the illuminating part ($\Delta R^{3D-1D} > 0$). Therefore, for all SZAs, ΔR^{3D-1D}-distribution either has an ideal Gaussian shape or more weight in the shadowing part which both a complement to the inequality in Equation 4.1. In Figure 4.15 (b), the mean absolute bias between r_e^{3D} and r_e^{1D} gradually increases as SZA increases which indicates both illuminating and shad-

owing effects increases in all LES cases as SZA increases. The mean biases between the optical thickness retrievals in Figure 4.15 (c) are negative (shadowing effects) for all LES cases when SZA-40 and 20 in contrast to Equation 4.2 which indicates dominant illuminating effects. For smaller SZAs, ΔR^{3D-1D}-distribution has more weight in the shadowing part instead of the ideal Gaussian shape about zero (Section 4.3). So the dominant-negative biases perhaps due to that negative-skewness of the ΔR^{3D-1D}-distribution.

Chapter 5: 3D radiative transfer effects in polarimetric retrievals

5.1 Overview

In practice, the realistic 3D nature of the radiative transfer has to be replaced by the 1D radiative transfer assumption in many remote sensing applications mainly for the sake of computational efficiency. The 1D RT assumes that the cloud fields are vertically and horizontally homogeneous which is usually referred to as " Plane Parallel Approximation" (PPA). In addition to PPA, 1D RT assumes a particular pixel to be isolated from its neighboring pixels which is the so-called "Independent Pixel Approximation" (IPA). Although the PPA and IPA are practically useful in many situations, when the actual clouds deviate from these assumptions, the retrieved cloud properties show discrepancies known as 3D radiative effects (Marshak and Davis, 2005). The impact of 3D effects on the underlying retrievals is dependent on the solar geometry (Loeb and Davies, 1996), cloud inhomogeneity (Zhang et al., 2012; Marshak et al., 2006) and the spatial resolution (Davis et al., 1997; Oreopoulos and Davies, 1998). A large volume of studies have been performed to investigate the 3D radiative effects in bi-spectral retrievals (Várnai and Marshak, 2002, 2001; Marshak and Davis, 2005; Marshak et al., 2006; Zhang et al., 2012). However the 3D radiative effects in the polarimetric retrievals have not been extensively inves-

tigated probably because polarimetric cloud property retrievals are so far limited to POLDER (Deschamps et al., 1994) from space and a few airborne polarimeters such as RSP (Cairns et al., 1999; Alexandrov et al., 2012, 2020), AirMSPI (Diner et al., 2013) and AirHARP (Mcbride et al., 2019). However, ESAS (Earth Science and Applications from Space) decadal survey (NASEM, 2018) has prioritized the necessity of a multichannel-multiangle polarization imaging radiometer for future climate and air quality studies. Moreover, the forthcoming HARP CubeSat (Martins et al., 2018) demonstrations of the polarimetric cloud retrievals from space and PACE mission encourage to perform more simulation-based investigations towards understanding the influence of 3D radiative transfer on the polarimetric retrievals.

In addition to PPA and IPA, the polarimetric retrievals often assume polarized reflectance measurement mainly comes from the singly-scattered photons because multiple scattering tend to increase the depolarization. Therefore, relative to the bi-spectral retrievals which are based on the total reflectance that extensively includes the information from the multiply-scattered photons, polarimetric retrievals have been minimally affected by 3D RT effects (Rajapakshe and Zhang, 2020). However, the detailed-investigations on the 3D radiative effect of polarimetric retrievals are yet to be done. This chapter presents our effort to lay down the groundwork for understanding the 3D effects in polarimetric radiative transfer and retrievals. Section 5.2 starts with a brief discussion about the RT simulations of polarized reflectance from MSCART. Section 5.3 develops a basic understanding on the polarimetric retrievals based on 1D RT. Section 5.4 presents the observed 3D radiative effects in the polarimetric retrievals and the last three sections (Section 5.5, 5.6, and 5.7) discuss

the polarimetric retrievals under 3D RT explicitly focusing on the solar zenith angle dependence and the resolution dependence of the retrieval biases.

5.2 Radiative transfer simulations of the polarized reflectance

Similar to Chapter 4, we will use the LES-based retrieval simulator as main tool for our investigation of the 3D effects in polarimetric cloud observations and retrievals. Figure 5.1 shows the simulated reflectance from MSCART 1D radiative transfer simulations for the LES cases described in Section 2.3 ($R_Q^{1D,0.860\mu m} = \frac{\pi Q}{\mu_0 F_0}$). The Sun is to the left side of the domain with $SAA = 0^o$. To avoid confusion, the same $SAA = 0^o$ has been used throughout the study unless specifically mentioned otherwise. In this particular case, SZA set to be 40 degrees. Panel (a), (f), (k), and (p) are the native-resolution (Table 2.1) $R_Q^{1D,0.860\mu m}$ simulations from MSCART for DYCOMS-II, RICO, ATEX-clean, and ATEX-polluted LES cases respectively. The remaining panels of each row show the coarse-resolution images which are generated by computing the moving average of the native-resolution simulations with 2D square footprints that have different spatial resolutions. These coarse resolution images have been used to simulate the polarimetric observations with different spatial resolutions for study the 3D effects as the spatial resolution varies. (Section 4.2 discusses the purpose of using moving-averaged coarse-resolution images and their differences and similarities compared to the simple-average images). Over the cloud-free (or thin cloud) regions, a weak polarized signal can be observed relative to the optically thick regions. It is important to notice that, as the horizontal

resolution of the footprint increases, the magnitude of polarized reflectance appears to be decreased, especially when predominant cloud-free parts exist in the footprint. However, the polarimetric retrievals exploit the angular pattern of the polarized reflectance rather than the absolute magnitude. Thus, having smaller polarized reflectance along a particular direction does not necessarily indicate less-reliable retrievals.

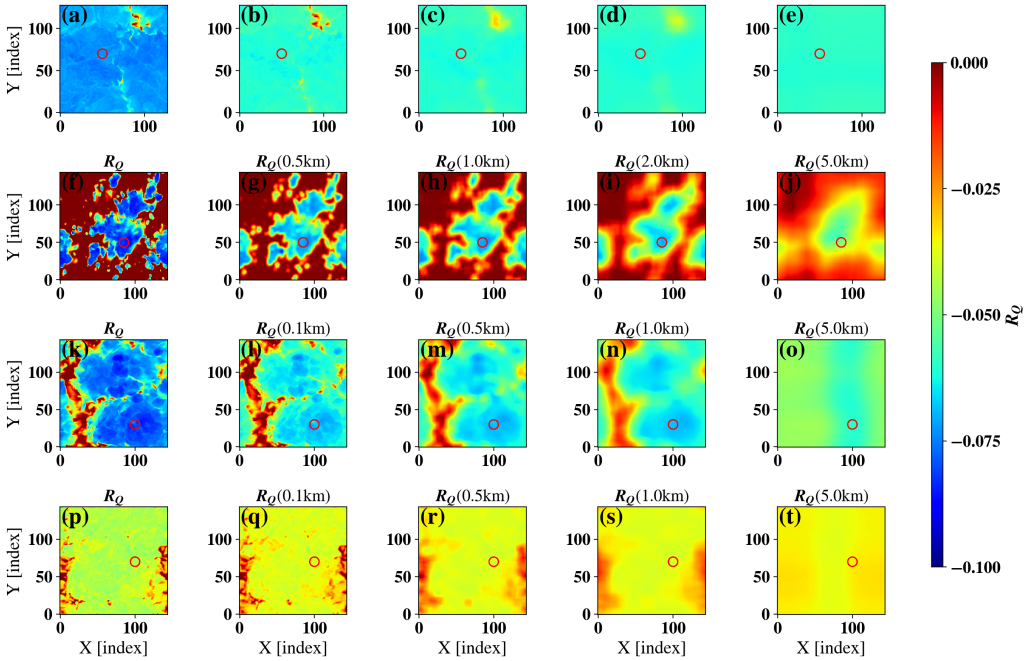

Figure 5.1: Panel (a),(f),(k), and (p) are the simulated 0.860 μm 1D polarized reflectances ($\pi Q/\mu_0/F_0$) of DYCOMS-II, RICO, ATEX-clean and ATEX-polluted cases respectively in the native resolution. Each coarse resolution image was produced by taking the moving average of a 2D square footprint on the native resolution image. The resolution of the footprint is indicated in the title of each panel. Sun is to the left at $SZA = 40^o$

We select a few points form the LES cases for more in-depth analysis. The

angular pattern of the geometrically corrected polarized reflectance $R_p^*(\Theta_S)$ (Equation 1.2.2) for points indicated by the red circles in Figure 5.1 are shown in Figure 5.2 for each LES case. If the domain is overcast like DYCOMS-II and ATEX-polluted cases, it is highly unlikely to contain cloud-free pixels inside the considering footprint. In such situations, the angular pattern of $R_p^*(\Theta_S)$ in the primary bow region is almost invariant for varying footprint size as shown in Figure 5.2 (a) and (d). If the domain contains a significant fraction of cloud-free regions as in the RICO case (Figure 2.5(f)), the angular pattern of $R_p^*(\Theta_S)$ has been significantly impacted as the resolution of the footprint increases, especially in the primary bow region (Figure 5.2(b)).

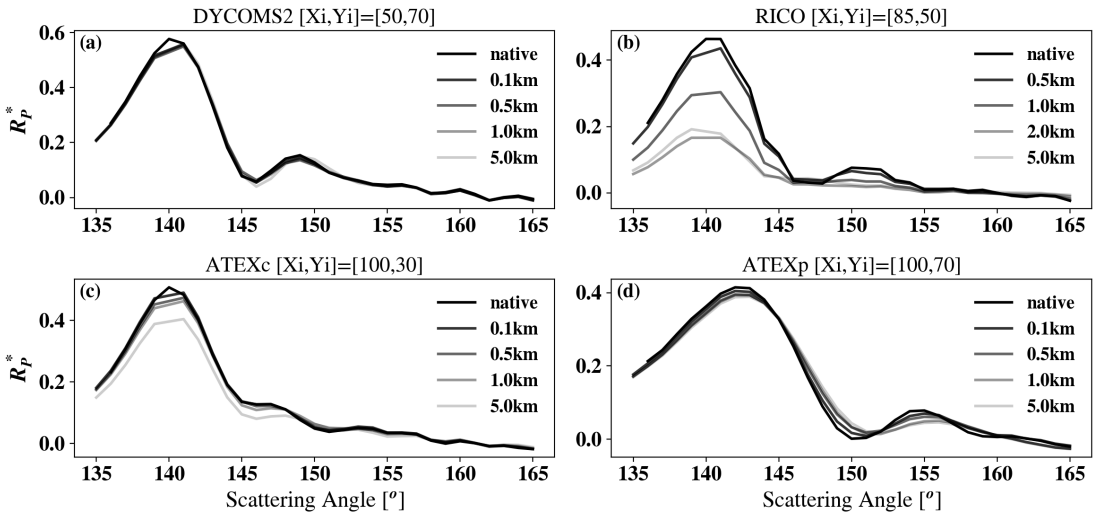

Figure 5.2: The angular pattern of the simulated 0.860 μm 1D polarized reflectance for the points indicated in Figure 5.1. The curves in (a),(b),(c) and (d) are corresponded to the red circles marked in 5.1 (a-e), (f-j), (k-o) and (p-t) for DYCOMS-II, RICO, ATEX-clean and ATEX-polluted cases respectively.

Figure 5.3 is the same figure as Figure 5.2 but from 3D radiative transfer simulations. In contrast to Figure 5.2(a), the angular features of $R_p^*(\Theta_S)$ in Figure 5.3(a) vary as footprint gets coarse, thus could have implications for underlying polarimetric retrievals. For an example, in Figure 5.3(a), the intensity of the supernumerary bow increases as the resolution of the footprint increases which would be interpreted as a CEV increase. This implies 1D and 3D radiative assumptions might lead us to different conclusions.

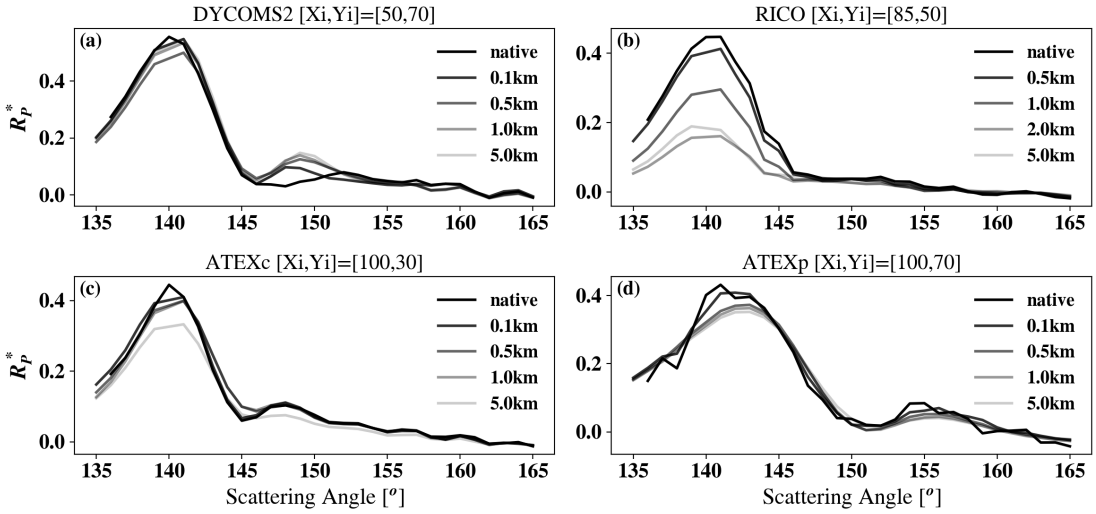

Figure 5.3: The angular pattern of the simulated 3D polarized reflectance for the points indicated in Figure 5.1. The curves in (a),(b),(c) and (d) are corresponded to the red circles marked in 5.1 (a-e), (f-j), (k-o) and (p-t) for DYCOMS-II, RICO, ATEX-clean and ATEX-polluted cases respectively.

From the retrieval technique's perspective, the variation of $R_p^*(\Theta_S)$ can be interpreted as cloud microphysics variability. Therefore, it is important to understand how far the other factors than the cloud microphysical variability can change the

angular features of $R_p^*(\Theta_S)$. For example, all the polarized reflectances that are shown in Section 5.2 are for 40^o solar zenith angle. Under 3D radiative transfer, different solar zenith angles might change $R_p^*(\Theta_S)$ differently. In addition to SZA, averaging over different horizontal footprints can also perturb the "true" angular features of $R_p^*(\Theta_S)$ correspond to the actual cloud microphysics. Both variability in $R_p^*(\Theta_S)$ due to the varying SZA and footprint resolution will be mixed with actual microphysical variability. Therefore, in practice, it is much easier to first investigate whether varying SZA and horizontal footprint could cause retrieval biases under 1D radiative transfer assumptions and later compare with the results under 3D radiative transfer.

5.3 Polarimetric retrievals under 1D radiative transfer

Polarimetric retrievals use the angular pattern of $R_p^*(\Theta_S)$ to retrieve CER and CEV. The angular features of $R_p^*(\Theta_S)$ is, on one hand, connected to the actual cloud microphysics, but on the other hand also influenced by both scattering geometry and the horizontal resolution of the footprint. Before investigating the 3D radiative transfer effects, this section investigates whether the 1D polarimetric retrievals are influenced by the solar zenith angle and horizontal resolution variability. The first and second rows of Figure 5.4 show the polarimetric CER ($r_e^{pol.,1D}$) and CEV ($v_e^{pol.,1D}$) retrievals of each LES case respectively. VW-COT cloud mask (the second row of Figure 2.5) has been applied to mask the columns with vertically-weighted COT less than 0.1. The third row shows the corresponding R^2 value of the under-

lying parametric curve-fitting. Significantly large $R^2(\gtrapprox 0.95)$ values indicate all the observed R_p^* patterns being converged to a particular P_{12} pattern in the library with sufficient accuracy. However large R^2 values can not necessarily indicate whether the retrieved values are physically reasonable or not. In contrast to observational studies that do not have a straight forward way to compare the retrieved properties with the actual physics, a simulation-based study can asses the underlying retrieval technique relative to more reasonable reference cloud properties.

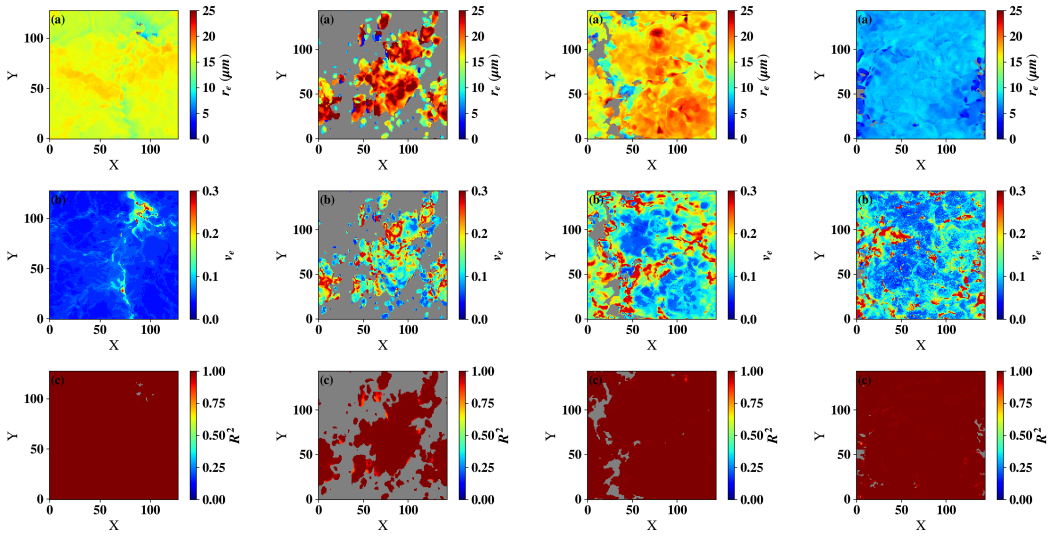

(i) DYCOMS-II (ii) RICO (iii) ATEX(clean) (iv) ATEX(polluted)

Figure 5.4: Polarimetric retrievals for each LES case in the native resolution based on 1D RT. Panel (a),(b) and (c) of each column are corresponded to CER, CEV and R^2 of the underlying parametric curve-fitting.(SZA=40^o, VW-COT cloud mask)

Figure 5.5(ii) compares the polarimetric retrievals ($r_e^{pol.,1D}$ and $v_e^{pol.,1D}$) of DYCOMS-II case (shown in Figure 5.4(i)) with the corresponding vertically-weighted retrievals (r_e^{vw} and v_e^{vw}). A strong correlation exists between $r_e^{pol.,1D}$ and r_e^{vw} with a domain mean absolute bias ($\langle|r_e^{pol.,1D} - r_e^{vw}|\rangle$) within fractions of micron. The

r-value of the $r_e^{pol.,1D}$ vs. r_e^{vw} correlations in this particular geometry (SZA=40^o) is 0.976. The ATEX-clean and polluted cases both have a high r-values 0.913 and 0.952 respectively for $r_e^{pol.,1D}$ vs. r_e^{vw} correlations. However, for the RICO case, r-value of the $r_e^{pol.,1D}$ vs. r_e^{vw} correlation is only 0.08, which is significantly lower than the other cases. Moreover the mean absolute bias between $r_e^{pol.,1D}$ and r_e^{vw} is more than 3 μm and a significant amount of pixels appears to have $r_e^{pol.,1D} = 30\mu m$ as depicted in Figure 5.6(ii)(b). The most obvious reason for this $r_e^{pol.,1D} = 30\mu m$ cluster is the 30 microns upper limit of the P_{12} library. All the $R_p^*(\Theta_S)$ patterns correspond to $CER > 30\mu m$ are being converged to the last bin of the library. Moreover, these large $r_e^{pol.,1D}$ in Figure 5.6(ii) (a) and (b) are mostly associated with $v_e^{pol.,1D} > 0.2$ retrievals. Since the supernumerary bow feature vanishes as CEV gets large (Figure 1.6), polarimetric retrieval technique does not sensitive to the size distributions with large CEV. Therefore, another cloud mask is used which filters $v_e^{pol,1D}$ greater than 0.2 (see Section 2.5 for detailed descriptions on cloud masks).

In the DYCOMS-II case, $v_e^{pol.,1D}$ vs. v_e^{vw} correlation shows a similar behavior as the $r_e^{pol.,1D}$ vs. r_e^{vw} correlation (Figure 5.5(ii)(d)). The mean absolute biases between $r_e^{pol.,1D}$ and r_e^{vw} retrievals are 0.006 with r-value 0.87 at $SZA = 40^o$. In the RICO case, the correlation between $v_e^{pol.,1D}$ and v_e^{vw} retrievals has 0.076 absolute bias with a low 0.297 r-value. However, if we use CEV-fil cloud mask (Figure 2.7(b)) that removes $v_e^{pol.,1D} > 0.2$ pixels, the mean absolute bias becomes 0.023 with a much higher 0.609 r-value. In contrast to the comparisons of CER retrievals for the RICO case in Figure 5.6(ii)(b), a significant fraction of polarimetric CEV retrievals in Figure 5.6(ii)(d) appears to have slight positive systematic bias with respect to

the vertically-weighted CEV retrievals. In native resolution retrievals, such a CEV systematic bias only exist in the RICO case.

5.3.1 Solar zenith angle dependence of the retrieval bias

Except for the biases due to the CEV greater than 0.2 PSDs, the polarimetric retrievals reasonably agree with the vertically-weighted retrievals under 1D radiative transfer assumption for moderate solar zenith angles ($SZA = 40^o$). In 3D radiative transfer, low solar geometries are favorable to horizontal photon transfer than the overhead sun. Before considering the retrievals under 3D radiative transfer, it is important to confirm whether the solar zenith angle variability could cause biases between 1D-polarimetric retrievals and vertically-weighted retrievals.

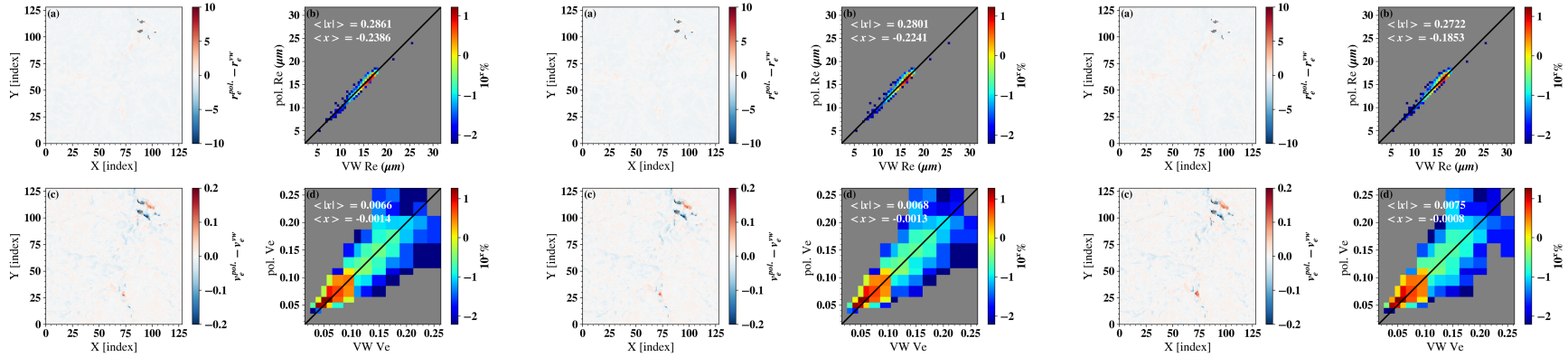

(i) $SZA = 20^o$ (ii) $SZA = 40^o$ (iii) $SZA = 60^o$

Figure 5.5: Comparisons of polarimetric retrievals against vertically-weighted pseudo retrievals for DYCOMS-II case at (i) $SZA = 20^o$, (ii) $SZA = 40^o$ and (iii) $SZA = 60^o$. Colorbar of the joint histograms is the percentage of counts on a logarithmic scale. $< x >$ and $< |x| >$ are the mean bias and mean absolute bias respectively. Sun is to the left side of the domain. VW-COT cloud mask have been used.

Figure 5.5 shows $r_e^{pol.,1D}$ vs. r_e^{vw} correlations for the DYCOMS-II case at (i) 20^o, (ii) 40^o and (iii) 60^o solar zenith angles. Figure 5.5(i)(a) is the difference between polarimetric ($r_e^{pol.,1D}$) and vertically-weighted (r_e^{vw}) CER retrievals for DYCOMS-II case at solar zenith angle 20 degrees. Panel (b) in Figure 5.5(i) is the joint histogram of $r_e^{pol.,1D}$ against r_e^{vw} for SZA=20^o. Panel (c) and (d) are the biases between polarimetric CEV retrievals ($v_e^{pol.,1D}$) with respect to the vertically-weighted CEV retrievals (v_e^{vw}) and the joint histogram of $v_e^{pol.,1D}$ against v_e^{vw} respectively. Figure 5.5 (ii) and (iii) are the same comparisons except for solar zenith angle 40 and 60 degrees respectively. Each corresponding panel of Figure 5.5(i), (ii) and (iii) do not show any prominent differences among each other. Table 5.1 summarizes the bias statistics computed for each case for varying SZA (Note that the computations in the table are based on CEV-fil cloud mask while the VW-COT cloud mask has been used in Figure 5.5. The difference due to the cloud mask is negligible for the DYCOMS-II case). For DYCOMS-II case, the mean absolute biases between $r_e^{pol.,1D}$ and r_e^{vw} are 0.28, 0.28, and 0.27 μm for SZA 20, 40 and 60 degrees respectively. The predicted gradients of the regression lines are 1.02, 1.03 and 1.04 for SZA 20, 40 and 60 degrees respectively. Thus, clearly, both CER and CEV polarimetric retrievals are closely correlated with the corresponding vertically weighted retrievals in the DYCOMS-II case regardless the SZA variation.

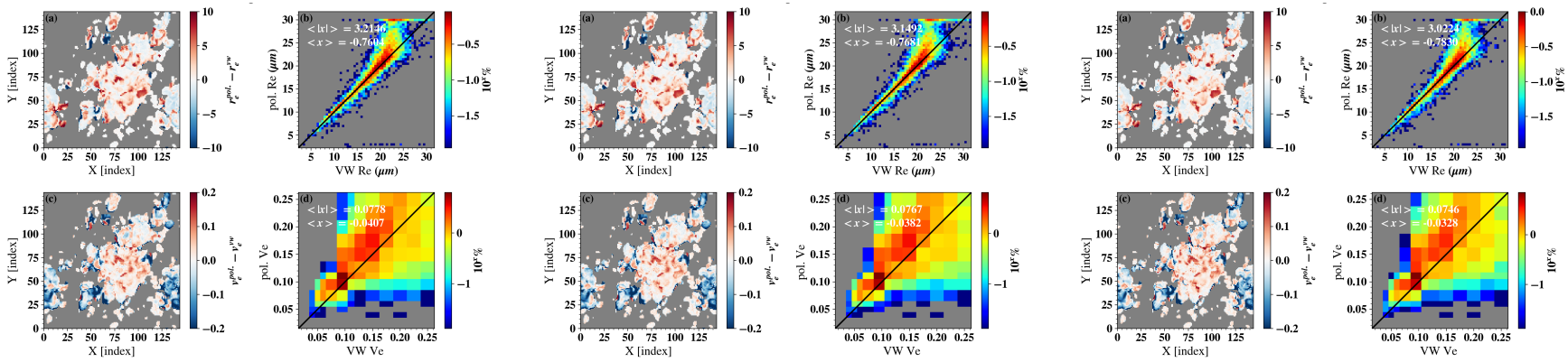

(i) $SZA = 20^o$ (ii) $SZA = 40^o$ (iii) $SZA = 60^o$

Figure 5.6: The comparisons of polarimetric retrievals against vertically-weighted pseudo retrievals for RICO case at (i) $SZA = 20^o$, (ii) $SZA = 40^o$ and (iii) $SZA = 60^o$ under 1D radiative transfer assumption. Colorbars of the joint histograms are the percentage of counts on a logarithmic scale. $< x >$ and $< |x| >$ are the mean bias and mean absolute bias respectively.

Among the four LES cases, RICO case has a broad DSD (large CEV) with considerable amount of large droplets. Figure 5.6 analyzes the CER and CEV biases between the polarimetric and vertically-weighted retrievals of the RICO case with VW-COT cloud mask (i.e. all the pixels with $\tau^{vw} > 0.1$ are included). The bias between $r_e^{pol.,1D}$ and r_e^{vw} has large values (3.21, 3.15, and 3.02 μm for SZA = 20, 40 and 60 degrees) for the RICO case in all geometries as depicted in Figure 5.6. In all the other cases, CER bias between the retrievals and the vertically-weighted properties are less than 1 μm for all the geometries compared to $> 3\mu$ in the RICO case. Similar to CER biases, the RICO case has the highest mean bias $\langle |v_e^{pol.,1D} - v_e^{pol.,vw}| \rangle$ (0.077, 0.076, and 0.074 for SZA = 20, 40, and 60 respectively) compared to the other cases ($\lesssim 0.03$). The biases with VW-COT cloud mask (which includes all the pixels that have COT greater than 0.1) provides a general picture of how well the ideal polarimetric retrievals under 1D RT agree with the corresponding reference cloud properties in different cloud regimes. However, for the DSDs with large CEV, the supernumerary bow features of the $R_p^*(\Theta_S)$ dissapears, thus the polarimetric retrievals are not reliable anymore. MA-fil cloud mask (Section 2.5) is used to ignore the pixels that have $r_e^{pol.,1D} > 0.2$ in addition to removing the pixels that have been influeced by the parallax effect (Section 2.5). Such a subset will be helpful to further investigate the biases due to the other effects than the $v_e^{pol.,1D} > 0.2$ and parallax effects. Even though using CEV-fil cloud mask does not impact the LES cases that have strongly mono-dispersed (large CEV) DSD with relatively small droplets (ex. DYCOMS-II and ATEX-polluted), it ignores considerable number of cloudy pixels when the cloud has large droplets with small CEVs (ex. RICO and ATEX-clean).

Even with the large biases that we discussed, in general, , behaviors of both $r_e^{pol.,1D}$ vs. r_e^{vw} and $v_e^{pol,1D}$ vs. v_e^{vw} correlations in Figure 5.5 and Figure 5.6 do not show significant variability as SZA varies for both DYCOMS-II and RICO cases. Knowing the existence of these biases under 1D RT assumption is helpful to eliminate them in the 3D effect analysis.

Table 5.1: Statistical quantities of the retrieval biases between 1D-polarimetric CER retrievals ($r_e^{pol.,1D}$) and vertically-weighted CER (r_e^{vw}) for varying solar zenith angle. μ and σ are the mean bias ($\langle r_e^{pol.,1D} - r_e^{vw} \rangle$) and standard deviation respectively. μ^* and σ^* are the mean absolute bias ($\langle |r_e^{pol.,1D} - r_e^{vw}| \rangle$) and standard deviation respectively. rms is the root-mean-square bias. β_1, β_0, $\beta_1^{std.}$ and r-value are the slope, intercept, variability of slope and the correlation coefficient of $r_e^{pol.,1D}$ vs. r_e^{vw} linear regression (Appendix A). CEV-fil cloud mask has been used.

case	SZA	μ	σ	μ^*	σ^*	rms	β_1	β_0	r value	$\beta_1^{std.}$
ATEXc	20	-0.27	1.02	0.53	0.91	1.05	0.93	1.07	0.83	0.01
ATEXc	40	-0.14	0.54	0.44	0.34	0.55	1.02	-0.57	0.96	0.00
ATEXc	60	-0.04	0.73	0.47	0.56	0.73	1.01	-0.19	0.95	0.00
ATEXp	20	-0.00	0.23	0.18	0.14	0.23	1.05	-0.41	0.95	0.00
ATEXp	40	0.00	0.25	0.19	0.16	0.25	1.05	-0.38	0.94	0.00
ATEXp	60	0.00	0.26	0.20	0.17	0.26	1.04	-0.29	0.95	0.00
DYCOMS2	20	-0.24	0.22	0.28	0.15	0.32	1.02	-0.60	0.97	0.00
DYCOMS2	40	-0.22	0.23	0.28	0.16	0.32	1.03	-0.68	0.97	0.00
DYCOMS2	60	-0.19	0.26	0.27	0.17	0.32	1.04	-0.80	0.97	0.00
RICO	20	0.59	1.53	1.10	1.22	1.64	1.25	-4.50	0.92	0.01
RICO	40	0.50	1.43	1.02	1.13	1.52	1.21	-3.56	0.93	0.01
RICO	60	-0.08	4.42	1.34	4.22	4.42	0.49	9.94	0.70	0.01

Table 5.1 shows the bias-statistics of $r_e^{pol.,1D}$ vs. r_e^{vw} comparisons in the native resolution as SZA varies . MA-fil cloud mask has been applied to filter the retrieval biases due to the parallax effect and $v_e^{pol.,1D} > 0.2$ retrievals. For the RICO case, in contrast to $\sim 3\mu m$ mean absolute bias as observed in Figure 5.6 (i)(b),(ii)(b) and (iii)(b) with VW-COT cloud mask, with MA-fil cloud mask, the mean absolute bias is $\sim 1\mu m$ for all SZAs. In addition to the RICO case, ATEX-clean case which also has a significant population of large droplets and large CEV values, also exhibits a same behavior. With the VW-COT mask, for the ATEX-clean case, the comparisons of $r_e^{pol.,1D}$ vs. r_e^{vw} have 0.71, 0.63, and 0.60 μm absolute CER mean biases for 20, 40, and 60 degrees SZAs respectively. Those values have been dropped to 0.53, 0.44 and 0.47 respectively in Table 5.1 where the CEV-fil cloud mask has been used.

Except in the RICO case, the mean absolute bias between $r_e^{pol.,1D}$ vs. r_e^{vw} is less than $1/2\mu m$. Moreover, the r-values of the linear regression between $r_e^{pol.,1D}$ vs. r_e^{vw} are larger than 0.9 for all cases in all geometries except DYCOMS-II at 20 SZA (0.83) and RICO at 60 SZA. In summary, under 1D RT assumption $r_e^{pol.,1D}$ reasonably agree with r_e^{vw} for all the cases without a significant variability due to the SZA variation. When the cloud consists of mono-disperse DSDs with small cloud droplets (ex. DYCOMS-II and ATEX-polluted case), $r_e^{pol.,1D}$ retrievals accurately represent the reference cloud microphysics. When the cloud has many large droplets with a broad DSD (ex. RICO and ATEX-clean), the polarimetric retrievals where $CEV > 0.2$ becomes less-reliable because supernumerary bow features in $P_{12}(\Theta_S)$ angular pattern vanishes as CEV increases.

5.3.2 Horizontal resolution dependence of the retrieval bias

In practice, usually, polarimetric cloud retrievals are performed within several hundred meters to 1km resolution from airborne sensors like RSP (Alexandrov et al., 2016) and airHARP (Mcbride et al., 2019). From space-borne sensors, the horizontal resolution of the polarimetric cloud retrievals could be even more than 100 kilometers. For an instance, even though POLDER has polarimetric measurements of $6km^2$ pixel-resolution, polarimetric cloud retrievals have been performed by averaging over $150km^2$ footprint to sample the complete cloud-bow scattering angle range (Bréon and Doutriaux-boucher, 2005). Hopefully, spaceborne polarimeters like HARP CubeSat and HARP2 will be able to perform retrievals within several km resolution (Mcbride et al., 2019). Therefore, understanding how the horizontal averaging cause biases in polarimetric retrievals will be helpful to better understand the future polarimetric cloud property retrievals. In this study, we expect to investigate the influence of horizontal resolution and SZA, specifically for 3D radiative transfer effects in polarimetric retrievals. Before we move on to 3D radiative transfer, this section investigates how the polarimetric retrievals comparable with underlying reference cloud microphysics under 1D RT assumption as the horizontal resolution varies.

All the LES cases other than the RICO case has 50 m native resolution. The native resolution of the RICO case is 100 m. Radiative transfer simulations are performed in the native resolution of each LES case using MSCART to obtain corresponding radiance fields. Figure 5.1 (a),(f),(k), and (p) are the simulated radiance

fields from MSCART in the native resolution for DYCOMS-II, RICO, ATEX-clean and ATEX-polluted cases respectively at $SZA = 40^o$. To obtain 0.1km-resolution radiance fields for DYCOMS-II, ATEX-clean, and ATEX-polluted cases, the moving average of a 100-by-100 meter footprint (equivalent to 2-by-2 pixel array) have been computed over the native-resolution image. Corresponding 0.1km-resolution radiance fields are shown in Figure 5.1 (b), (l) and (q). Similarly, the radiance fields equivalent to 0.5, 1.0, and 5.0 km resolutions are obtained by computing the moving average of 10-by-10, 20-by-20, and 100-by-100 pixel arrays on top of the native resolution radiance field respectively. In the RICO case, since the native resolution is different from the other three cases, 0.5, 1.0, 2.0, and 5.0 km coarse-resolution radiance fields are obtained by computing the moving average of 5-by-5, 10-by-10, 20-by-20, and 100-by-100 pixel arrays over the native-resolution radiance field respectively.

We note that the moving average leads to strong smoothing effects as a result of two adjacent pixels that are highly correlated because they are computed based on very similar populations of high-resolution pixels. In addition to the moving average, we have also performed a "simple" averaging based on the independent sampling of high-resolution pixels. Figure 5.7 shows the LES cases based on independent "simple" averaging. Clearly, the simple averaging reduces the number of pixels as the resolution becomes coarse. At 5km-resolution, each LES case has only 4 (1 in the RICO case) pixels. This makes the visualization very difficult, therefore, we choose to plot the results using the moving average. But in the statistical analysis we include the results from both moving and simple averages to ensure that the two

ways of obtaining coarse resolution observations lead to consistent results and the same conclusion.

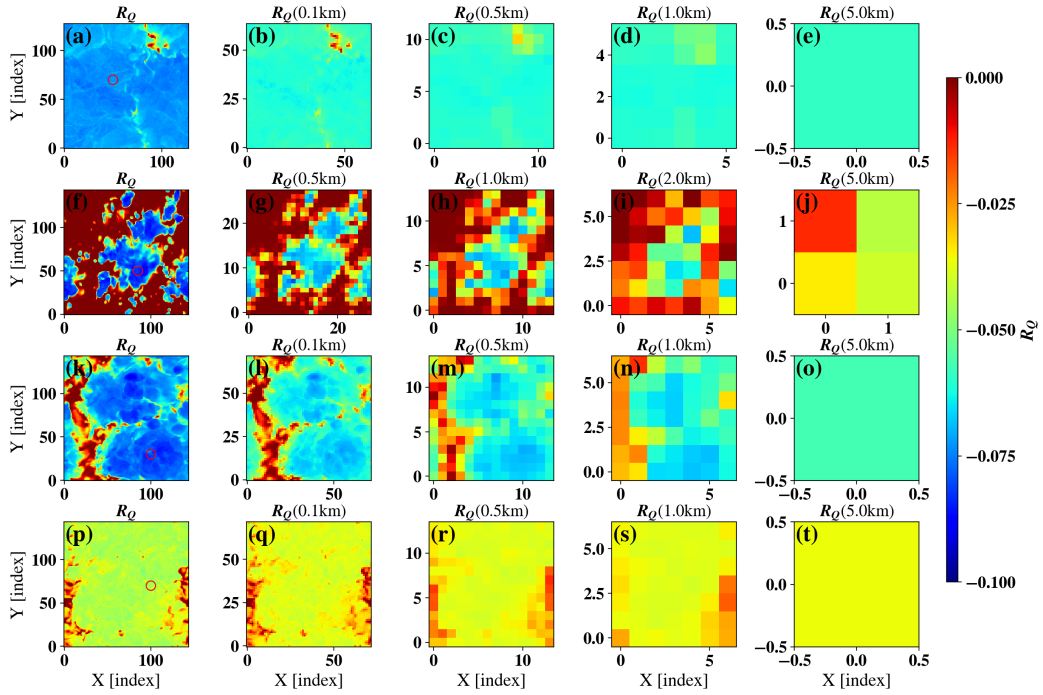

Figure 5.7: Simulated 0.860μm polarized reflectances from MSCART in the native resolution and corresponding coarse-resolution images. Panel (a),(f),(k), and (p) are the simulated 0.860 μm 1D polarized reflectances ($\pi Q/\mu_0/F_0$) of DYCOMS-II, RICO, ATEX-clean and ATEX-polluted cases respectively in the native resolution. Each coarse resolution image was produced by taking the simple average of a 2D square footprint on the native resolution image. The resolution of the footprint is indicated in the title of each panel. Sun is to the left at $SZA = 40^o$

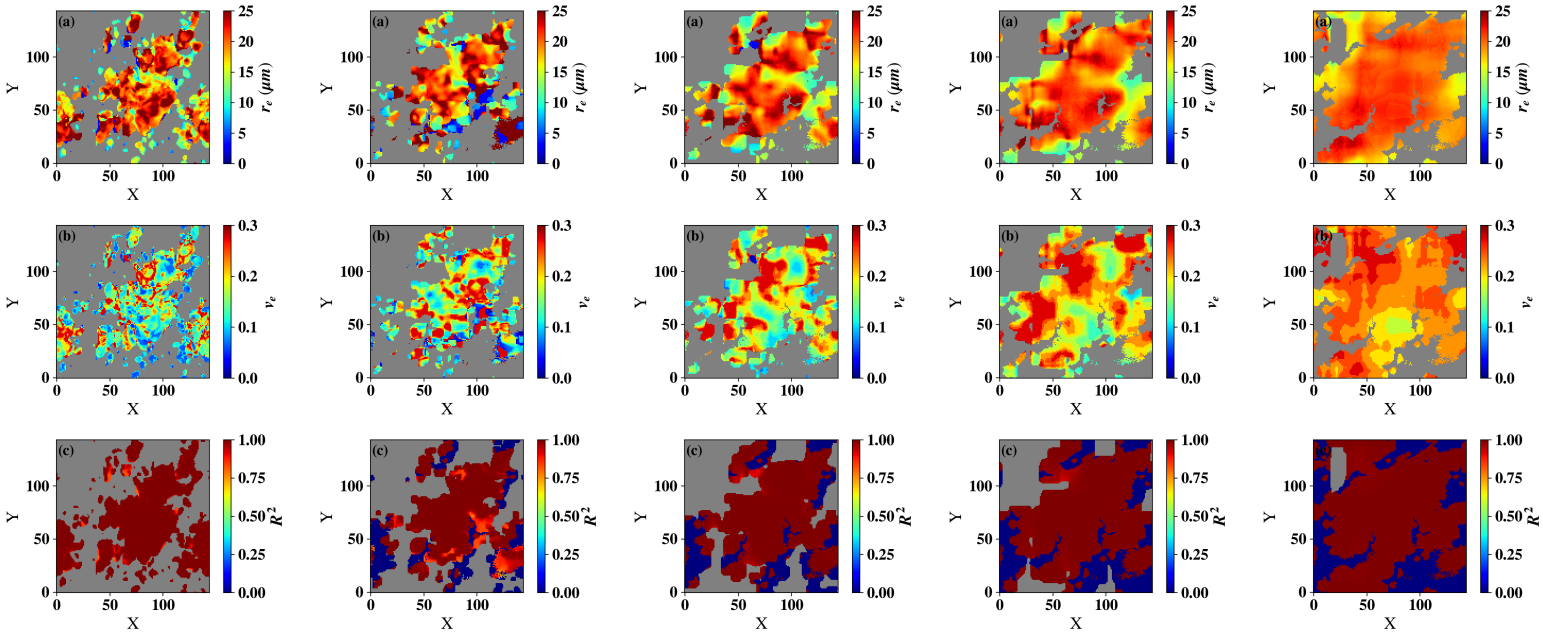

(i) Native (100m) (ii) 0.5km (iii) 1.0km (iv) 2.0km (v) 5km

Figure 5.8: Polarimetric retrievals of RICO case for different resolutions under 1D radiative transfer assumption. Panel (a),(b), and (c) of each column correspond to CER, CEV, and R^2 of the underlying parametric curve-fitting. (The Sun is to the left. SZA=60^o, VW-COT cloud mask has been used)

The a-panels in Figure 5.8 (i-v) show $r_e^{pol.,1D}$ in 0.1 (native), 0.5, 1.0, 2.0, and 5.0 km resolutions respectively. The b-panels in (i-v) are $v_e^{pol.,1D}$ for 0.1 (native), 0.5, 1.0, 2.0, and 5.0 km resolutions respectively. When implementing the polarimetric retrievals, each resolution radiance image has been treated as separate "satellite image". That is, for a particular resolution, all the retrievals, comparisons and computations are performed to mimic the realistic observational scenario.

The gray regions of the c-panels in Figure 5.8 (i-v) correspond to the pixels that have been omitted by the VW-COT cloud mask. It is important to note that the VW-COT cloud mask can be different for each resolution. The pixels of the considering resolution that have vertically-weighted COT smaller than 0.1 have been masked by the VW-COT cloud mask and hence shown in gray in the c-panels of Figure 5.8(i-v). The pixels that are shown in blue in the c-panels of Figure 5.8(i-v) indicate when the underlying curve-fitting of the polarimetric retrieval do not find a particular $P_{12}(\Theta_S)$ pattern in the library that has a reasonably large R^2 value. Therefore the gray-pixels in (a) and (b) panels of Figure 5.8(i-v) correspond to both blue (due to bad curve-fittings) and gray (cloud mask) pixels in each c-panel. However, it is important to emphasize that having reasonably large R^2 values does not necessarily indicate successful or physically reasonable polarimetric retrievals. Section 5.4 discusses the physical science basis of potential instances where the polarimetric retrievals could mathematically converge to physically unreasonable values.

When the polarized signal is averaged over a larger footprint, small-scale microphysical variation disappears and the retrievals become more horizontally homo-

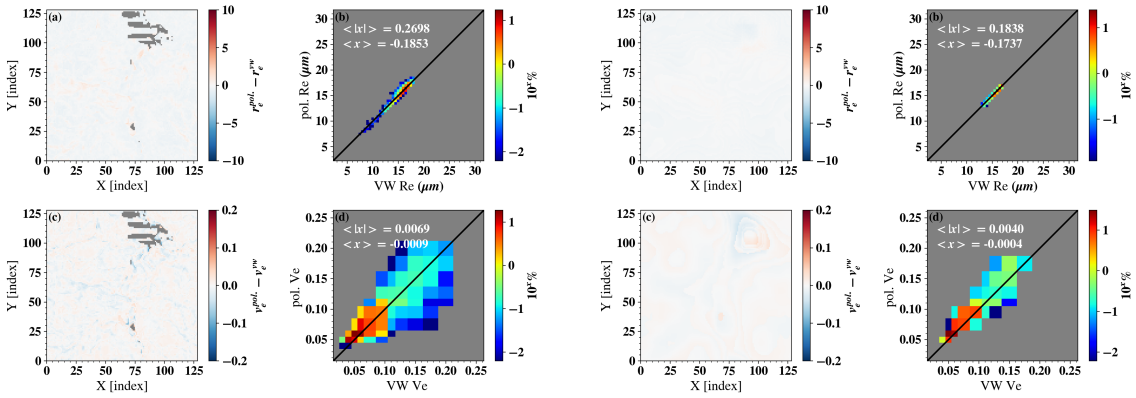

(i) Native resolution (50m) (ii) 1km resolution

Figure 5.9: Comparisons of polarimetric retrievals against vertically-weighted pseudo retrievals for DYCOMS-II case at $SZA = 60^o$ in (i) 50m resolution (native) and (ii) 1km resolution. The color bar of the joint histograms is the percentage of counts on a logarithmic scale. $< x >$ and $< |x| >$ are the mean bias and mean absolute bias respectively (refer to Appendix A for definitions).

geneous. This behavior can be observed in both $r_e^{pol.,1D}$ and $v_e^{pol.,1D}$ retrievals in Figure 5.8. As the horizontal resolution increases, the magnitude of $v_e^{pol.,1D}$ becomes larger than 0.2 in a large part of the domain. This has strong influence on the reliability of the polarimetric retrievals because the supernumerary bow features of $P_{12}(\Theta_S)$ disappears when CEV becomes large (Figure 1.6).

In addition to the retrieval failures due to the $CEV > 0.2$ PSDs, in realistic 3D RT, the parallax effect also causes biases in the polarimetric retrievals which is discussed in detail in Section 5.4.1. MA-fil cloud mask is introduced (Section 2.5) to filter the pixels that have been influenced by large CEV-values and the parallax effect at the cloud edges to investigate the unknown biases due to the 3D effects. In this

section, we temporarily ignore the 3D nature of radiative transfer and assume 1D RT assumption to investigate how the varying horizontal resolution of the footprint influences the polarimetric retrievals of cloud properties. Figure 5.9 (i) and (ii) compares polarimetric and vertically-weighted retrievals of the DYCOMS-II case at 50m (native) and 1km resolutions respectively at $SZA = 60^o$. In Figure 5.9(i)(b) we can see that the mean absolute bias between $r_e^{pol.,1D}$ and r_e^{vw} is low as ~ 0.269 in 50m resolution and further reduces as horizontal resolution increases to 1km in Figure 5.9(ii)(b). The CEV retrieval biases also have similar behavior as shown in the d-panels of Figure 5.9(i) and (ii), which is low in general and further reduces as the horizontal resolution of the footprint increases from 50m to 1km.

DYCOMS-II case has horizontally homogeneous cloud microphysics compared to the other LES cases. Figure 5.10 summarizes the variation of mean bias and mean absolute bias of polarimetric retrievals relative to the vertically-weighted cloud properties as the horizontal resolution of the footprint varies. Underlying RT simulations are from 1D RT simulations at $SZA = 40^o$. MA-fil cloud mask is used to filter the retrievals that have been influenced by the parallax effect and $v_e^{pol.,1D} > 0.2$ retrievals. Panel (a) shows the variation of the mean CER bias between polarimetric and vertically-weighted retrievals as the horizontal resolution increases from the native resolution to 5km. The mean CER bias between the retrievals and the vertically-weighted properties under 1D RT assumption only varies in fractions of microns as the resolution varies. Except the RICO case, mean absolute bias between $r_e^{pol.,1D}$ vs. r_e^{vw} of all the other LES cases (Figure 5.10(b)) are less than 1 μm. When the resolution varies from 50 m to 1.0 km, the mean absolute bias gradually

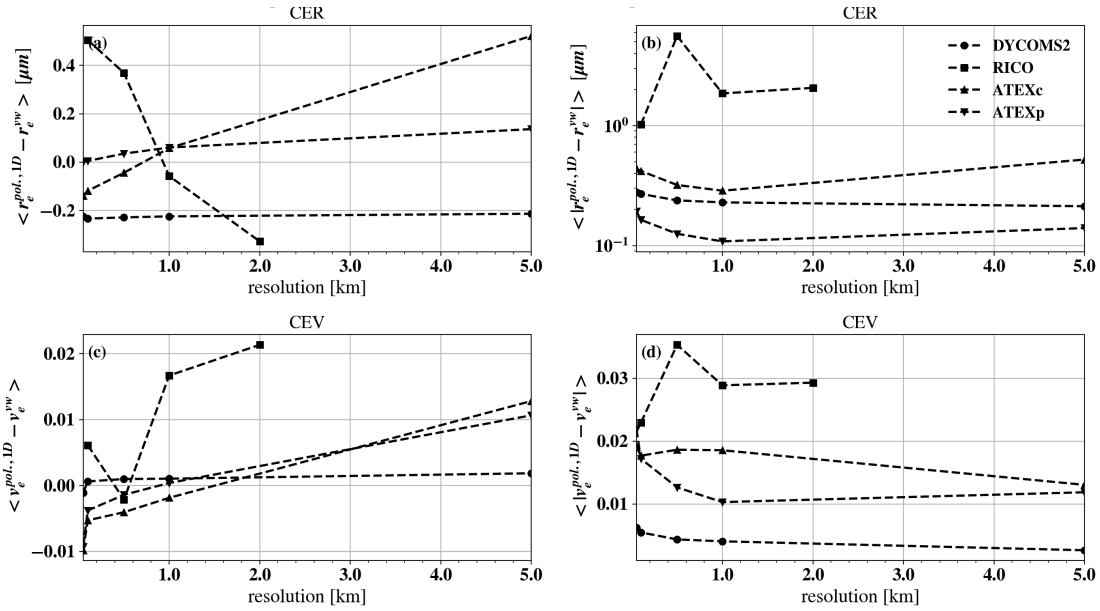

Figure 5.10: Mean bias ($\langle r_e^{pol.,1D} - r_e^{vw} \rangle$) and mean absolute bias ($\langle |r_e^{pol.,1D} - r_e^{vw}| \rangle$) of CER retrievals vs. horizontal resolution are shown in panel (a) and (b) respectively. Panel (c) and (d) are the mean bias ($\langle v_e^{pol.,1D} - v_e^{vw} \rangle$) and mean absolute bias ($\langle |v_e^{pol.,1D} - v_e^{vw}| \rangle$) of CEV retrievals vs. horizontal resolution of the footprint. $SZA = 40^o$. MA-fil cloud mask (Section 2.5) have been used.

decreases. This could be a result of smoothing the fine microphysical variabilities in the domain due to the horizontal averaging.

In Figure 5.10, the RICO case does not show any results for the resolutions greater than 2.0 km. In those resolutions, all the pixels either have $v_e^{pol.,1D} > 0.2$ retrievals, or have been influenced by the parallax effects at the cloud edges. The influence of parallax effects that happen at the cloud edges is discussed in Section 5.4.1. In general, polarimetric retrievals become less reliable when the footprint of the polarized signal has predominantly covered by cloud-free regions. In other words,

polarimetric retrievals become less reliable when the scene is dominated by broken cloud fields. In the RICO case, when the footprint becomes large, the polarized signal has been averaged over more broken cloud fields. Hence, as the horizontal resolution increases, the difference between $r_e^{pol.,1D}$ and r_e^{vw} increases, and eventually, all the retrievals have been filtered due to the unreliable retrievals that cause by either $v_e^{pol.,1D} > 0.2$ retrievals or parallax effect at the cloud edges.

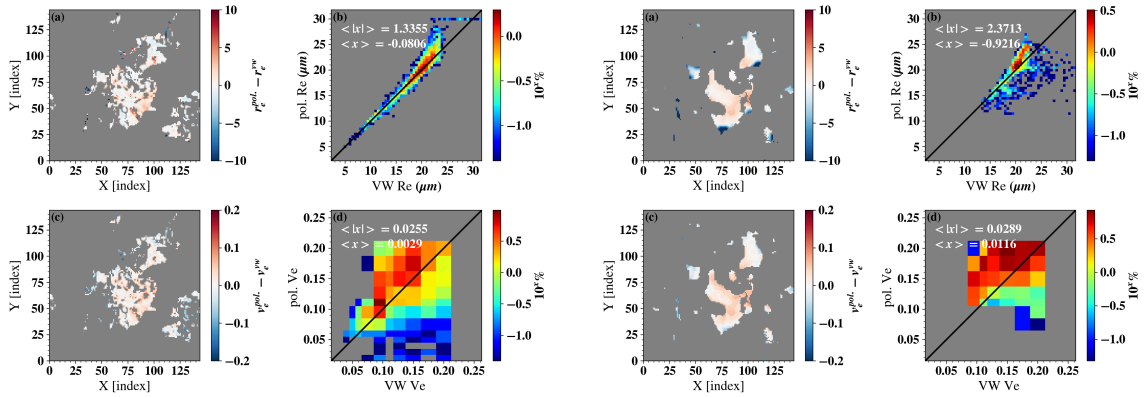

(i) Native resolution (100m) (ii) 1km resolution

Figure 5.11: Comparisons of the polarimetric retrievals against the vertically-weighted pseudo retrievals of the RICO case at $SZA = 60^o$ under 1D radiative transfer assumption for (i) native resolution and (ii) 1km resolution. MA-fil cloud mask has been used. Colorbar of the joint histograms is the percentage of counts on a logarithmic scale. $< x >$ and $< |x| >$ are the mean bias and mean absolute bias respectively (see Appendix A for bias-statistic definitions). The Sun is to the left side of the domain.

Figure 5.11 (i) compares the polarimetric and vertically-weighted retrievals for the RICO case at the native resolution after masking the values based on MA-fil

cloud mask. The retrievals correspond to high $v_e^{pol.,1D}(> 0.2)$ values that appear in Figure 5.8(i)(b) with VW-COT cloud mask are filtered, and remaining more reliable $r_e^{pol.,1D}$ and $v_e^{pol.,1D}$ results are compared with the corresponding vertically-weighted retrievals in Figure 5.11 (i) (b) and (d) respectively. Unlike the other cases, even after filtering the biases due to the $v_e^{pol.,1D} > 0.2$ and the parallax effects at the cloud edges, the RICO case has more than $1\mu m$ absolute CER bias between the polarimetric and vertically-weighted CER retrievals under 1D RT assumption. Similarly, CEV retrievals of the RICO case has the highest bias of 0.0255 compared to 0.006, 0.018, 0.022 mean absolute biases for DYCOMS-II, ATEXc, and ATEXp. As the resolution increases from 100m (native) to 1km, mean absolute bias between two CER retrievals for RICO case increases from 1.33 μm (Figure 5.11 (i)(b)) to 2.37 μm (Figure 5.11(ii)(b)). The mean absolute bias of CEV also increases as resolution increases from native to 1km resolution. In summary, the different behavior in the RICO case compared to the other cases potentially due to the existence of the predominant cloud-free region of the considering footprint.

Unless the domain consists with broken clouds that contain "holes" inside the footprint like in the RICO case, under 1D RT assumption, the polarimetric retrievals agree with the corresponding vertically-weighted retrievals with the mean absolute bias of CER less than 1 micron and the mean absolute bias of CEV less than 0.025. In the majority of cases that we discussed in this section, the polarimetric retrievals under 1D RT assumption reasonably agree with the vertically-weighted retrievals. Section 5.6 and 5.7 summarizes how the polarimetric retrievals under 3D radiative transfer comparable with respect to the vertically-weighted retrievals. Before that,

the next section (Section 5.4) discusses three main effects that we can observe in the polarimetric retrievals due to the 3D nature of radiative transfer that has been ignored by the 1D RT assumption.

5.4 3D radiative transfer effects

Compared to the numerous studies that have investigated the 3D radiative effects of the bi-spectral retrievals (Várnai and Marshak, 2002, 2001; Marshak and Davis, 2005; Marshak et al., 2006; Zhang et al., 2012), the 3D radiative effects of the polarimetric retrievals have been poorly investigated. Since the main contribution to the polarmetric reflectance comes from the singly-scattered photons, it is generally considered that the polarimetric retrievals have been minimally affected by the multiple scattering. Therefore, unlike bi-spectral retrieval that relies on the total reflectance where the multiple scattering plays a crucial role, polarimetric retrievals are usually assumed to be minimally influenced by 3D RT effects. However, these assumptions are not sufficiently tested in the literature. This section presents potential 3D RT effects that can cause biases in the polarimetric retrievals and explains the physical science basis of those biases.

5.4.1 Parallax effect at the cloud edges

Two reflectance measurements registered to a single-pixel but with different viewing angles have different lines of sights, hence effectively looking at different regions of the cloud. This is known as the "parallax effect" in cloud remote sens-

ing. The bi-spectral retrievals are based on a pair of total reflectance measurements that have been measured from the same viewing geometry. Therefore the VNIR and SWIR reflectance pair that used in the bi-spectral retrievals have the same line of sight, despite the possibility of retrieved cloud properties belong to different regions of the cloud than the registered pixel. In other words, even though the bi-spectral retrievals can be influenced by the parallax effect, they do not use measurements from different lines of sight to obtain a particular pair of CER and COT retrievals. In contrast to the bi-spectral retrievals, polarimetric retrievals depend on the multi-angular measurements. Therefore, a single pair of CER and CEV polarimetric retrieval requires the measurements from different viewing angles, hence from different lines of sight. However, no comprehensive investigations have done to assess and understand the potential uncertainties in the polarimetric retrievals due to the parallax effects. The objective of this section is to fill this gap.

Figure 5.12 compares the 1D-polarimetric and vertically-weighted retrievals of the RICO case at $SZA = 60^o$ and $SZA = 20^o$. COT-VW cloud mask has been imposed to include all the pixels that have vertically-weighted COT greater than 0.1. The b-panels of Figure 5.12(i) and (ii) are the joint histograms of $r_e^{pol.,1D}$ and r_e^{vw}. Strong positive and negative biases ($r_e^{pol.,1D} - r_e^{vw}$) exist in both $SZA = 20^o$ and $SZA = 60^o$ cases in panel (i)(b) and (ii)(b) respectively. Figure 5.12 (a) and (b) show the spatial locations of these strong positive and negative baiases for $SZA = 60^o$ and $SZA = 40^o$ respectively. The Sun is to the left side of the domain. When $SZA = 60^o$ ((i)(a)), strong negative biases exist at the shadowing edges (edges to the right) of the cloud. When $SZA = 20^o$ ((i)(b)), we can also observe strong negative biases

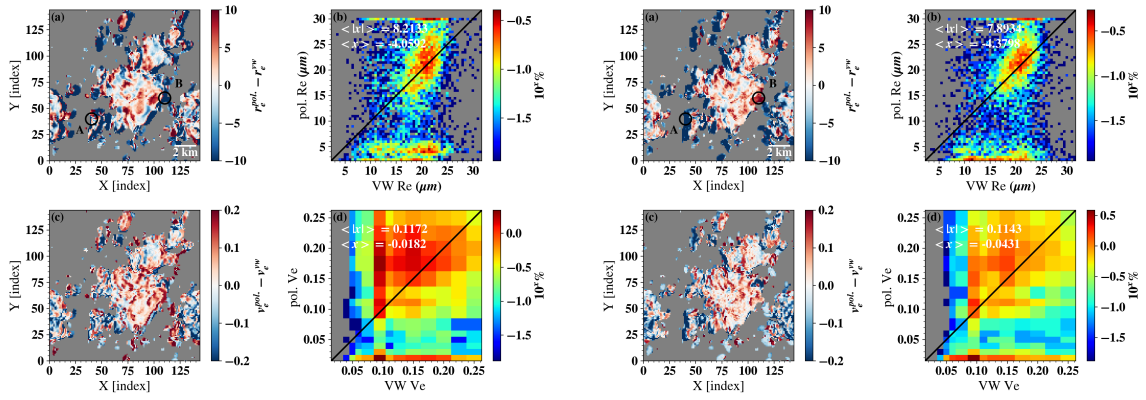

(i) SZA=60 (ii) SZA=20

Figure 5.12: Comparisons of the polarimetric retrievals against the vertically-weighted pseudo retrievals of the RICO case at (i) $SZA = 60^o$ and (ii) $SZA = 20^o$ under 1D radiative transfer assumption at the native resolution. Colorbar of the joint histograms is the percentage of counts on a logarithmic scale. $< x >$ and $< |x| >$ are the mean bias and mean absolute bias respectively. The Sun is to the left side of the domain. VW-COT cloud mask has been used to mask the cloud-free region.

but at the illuminating side. The positive biases also follow a similar spatial pattern depending on the solar geometry but less-significant compared to the negative biases. To illustrate how parallax effect can lead to strong polarimetric retrieval bias, we selected two cloud-edge points 'A' and 'B' with large and opposite bias. The vertical cross-sections along the y-axis of point 'A' and 'B' in Figure 5.12(i)(a) are shown in Figure 5.13(i) and Figure 5.14(i) respectively.

The green line in Figure 5.13(i) is the line of sight of the polarized reflectance correspond to the primary-bow ($\Theta_S \sim 140$) at point 'A' in Figure 5.12(i)(a) when

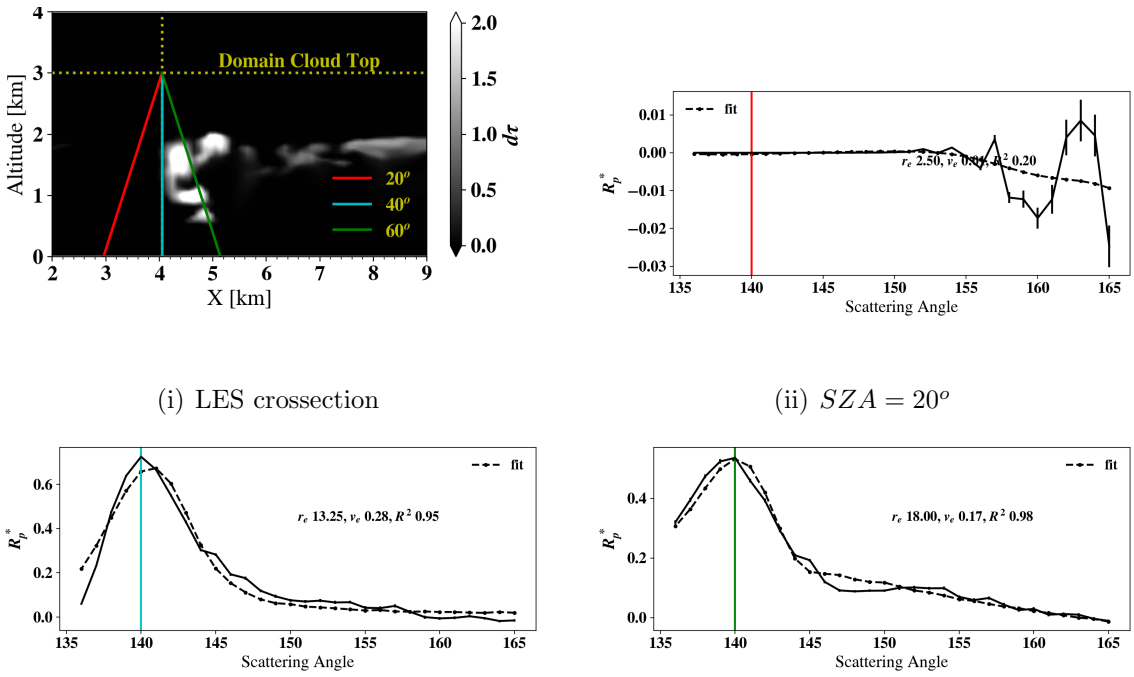

(i) LES crossection

(ii) $SZA = 20^o$

(iii) $SZA = 40^o$

(iv) $SZA = 60^o$

Figure 5.13: Point 'A'. Illustration of the parallax effect at the illuminating edge of the cloud using the RICO case. Panel (i) shows the vertical cross-section of the 3D LES domain correspond to the point 'A' in Figure 5.12(i)(a. The red, cyan and green lines in panel (i) correspond to the apparent primary-bow lines of sight at $SZA = 20^o$, $SZA = 40^o$, and $SZA = 60^o$ respectively. Panel (ii), (iii) and (iv) are the observed angular pattern of the geometrically-corrected polarized reflectance ($R_p^*(\Theta_S)$) correspond to red, cyan and green primary-bow lines of sight respectively.

$SZA = 60^o$. This green line intercepts with the non-zero COT part of the cloud. Therefore, when $SZA = 60^o$, the cloud-bow angular pattern ($R_p^*(\Theta_S)$) correspond to point 'A' in Figure 5.12(i)(a) has a clear primary bow feature as shown in Figure 5.13(iv). Existing the primary-bow feature in the cloud bow region confirms that the polarized reflectance has been measured from a cloud-target. The cyan

line in Figure 5.13(i) corresponds to the apparent primary-bow line of sight of the polarized reflectance measurement when $SZA = 40^o$. As shown in Figure 5.13(iii), the cloud-bow feature exists in $R_p^*(\Theta_S)$ in this case too which confirms that the polarized signal comes from a cloud. In contrast to both $SZA = 60^o$ and 40^o, when $SZA = 20^o$, the apparent cloud-bow line of sight (red line) in Figure 5.13(i) clearly goes through a cloud-free part and hence in Figure 5.13(ii), we can not observe the cloud-bow features in $R_p^*(\Theta_S)$. Therefore, the CER-retrieval correspond to the $R_p^*(\Theta_S)$ pattern in Figure 5.13(ii) is physically meaningless and exhibits a strong negative bias relative to the corresponding vertically-weighted retrievals as observed at point 'A' in Figure 5.12(ii).

The same phenomenon occurs at the shadowing edge-pixels like point 'B' of the cloud in Figure 5.12. The apparent primary-bow line of sight at $SZA = 60^o$ that goes through a cloud-free region (the green line in Figure 5.14(i)) gives physically unreasonable CER-retrievals which causes strong negative bias between $r_e^{pol.,3D}$ and r_e^{vw} (point B in Figure 5.12(i)(a)). In contrast to $SZA = 60^o$ case, at $SZA = 20^o$, the apparent primary-bow line of sight actually goes through the cloud (the red line in Figure 5.14(i)) and consequently gives cloud-bow features in $R_p^*(\Theta_S)$ as shown in Figure 5.14(ii). Therefore, the strong negative biases in point B (and similar pixels along the shadowing edge) in Figure 5.12(i)(a) at $SZA = 60^o$ do not exist in Figure 5.12(ii)(a) at $SZA = 20^o$.

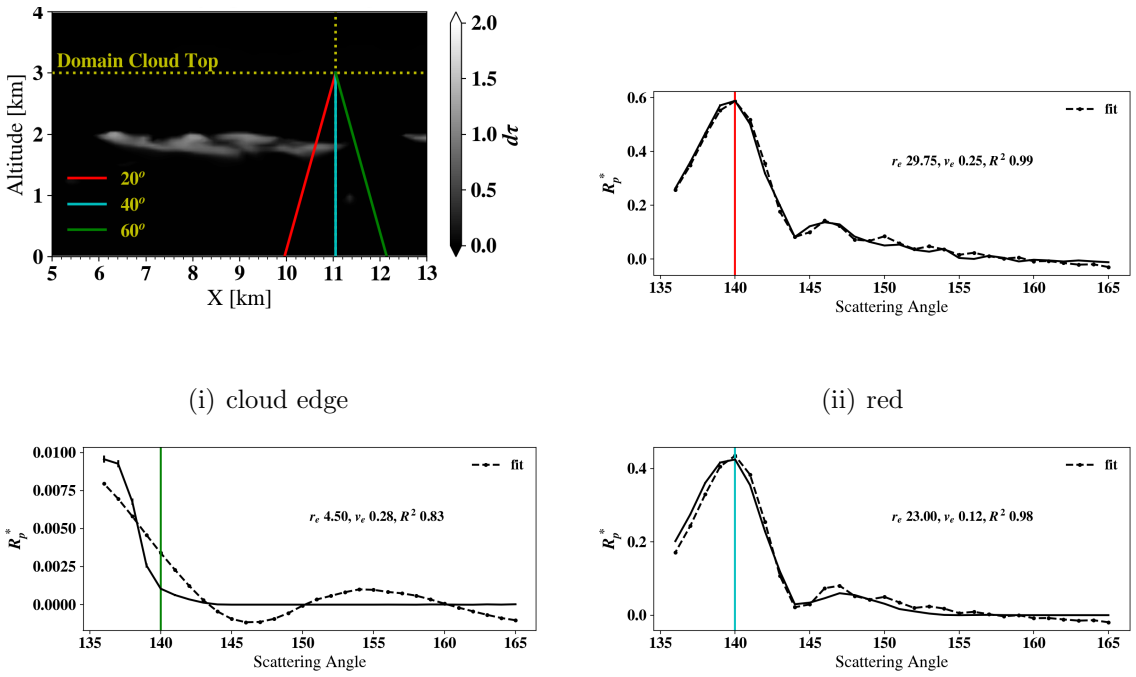

(i) cloud edge

(ii) red

(iii) blue

(iv) green

Figure 5.14: Point 'B'. Illustration of the parallax effect at the shadowing cloud edge. Panel (i) shows the vertical cross-section of the 3D LES domain correspond to the point 'B' indicated in Figure 5.12(i)(a) and (ii)(a). Red, cyan, and green lines in the panel (i) correspond to the apparent cloud-bow line of sight at $SZA = 20^o$, $SZA = 40^o$, and $SZA = 60^o$ respectively. Panel (ii), (iii) and (iv) are the observed angular pattern of the geometrically-corrected polarized reflectance ($R_p^*(\Theta_S)$) correspond to red, cyan and green lines respectively.

5.4.1.1 Multi-angular cloud mask

Since the polarimetric retrievals depend on multi-angular observations to retrieve a single CER-CEV pair, unavoidably, different angles that the polarized reflectance has been measured to obtain complete $R_p^*(\Theta_S)$ pattern always have dif-

ferent lines of sight. This is due to the "parallax effect" which could occur both at the cloud edges and in the middle of the cloud. It is practically impossible to completely eliminate the biases due to the parallax effect. However, at the cloud edges, when the apparent primary-bow line of sight orienting towards a cloud-free region, corresponding retrieved CER-CEV pair do not have a physical meaning. In order to identify and avoid such biases that occur due to the parallax effect at the cloud edges, we use a cloud mask that only labels a "cloudy pixel" if the total reflectance (at 0.860 μm) is greater than 0.02 for the complete cloud-bow scattering angle range($135 < \Theta_S < 165$). Since multi-angular reflectances have been used to determine the cloudy and cloud-free pixels, we referred to this cloud mask as the "multi-angular cloud mask" (MA cloud mask for short).

MA cloud mask misses a fraction of pixels that have been considered as "cloudy pixels" by the VW-COT cloud mask which simply use vertically-weighted COT threshold ($\tau^{vw} > 0.1 \Longrightarrow$ "cloudy pixel") to differentiate cloudy pixels from cloud-free pixels. Three different cloud masks that have been used throughout this study are discussed in Section 2.5. Figure 5.15 shows the MA cloud mask of each LES case for 1km-resolution. Since the MA cloud mask depends on the solar and viewing geometries, a different MA cloud mask have been computed for each SZA. For an example, the second column in Figure 5.15 is the MA cloud mask for the RICO case at 1k-resolution. The cloudy pixels are shown in white. Panel (b), (f) and (j) are for SZA 60^o, 40^o and 20^o respectively. For the overcast cloud scenes such as DYCOMS-II case, different geometries and resolutions do not cause any significant difference in the cloud mask in contrast to the broken cloud fields. The main objective of MA

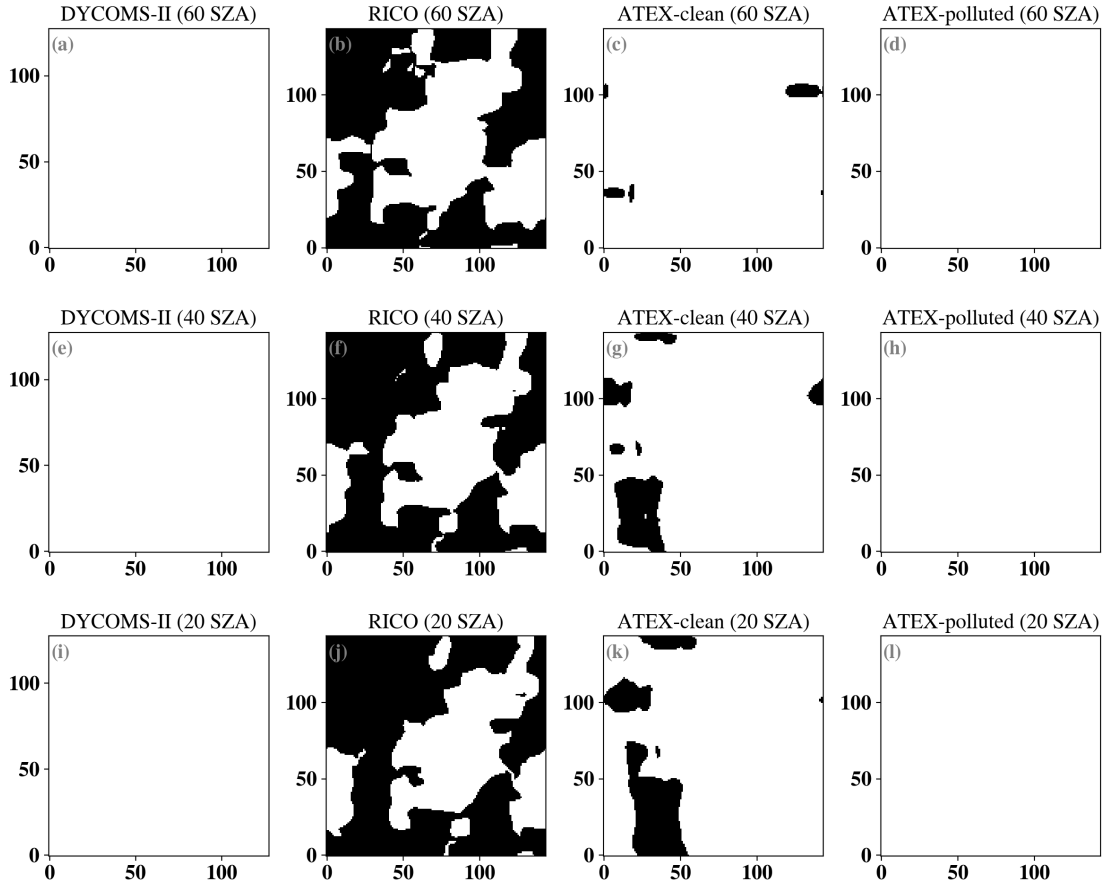

Figure 5.15: Multi-angular (MA) cloud mask for each LES-case at 1km resolution. Each column from left to right corresponds to DYCOMS-II, RICO, ATEX-polluted, and ATEX-clean LES cases. Each row is for 60, 40, and 20- degree solar zenith angles. The pixels that have VNIR total reflectance greater than 0.02 over the all cloud-bow scattering angle space ($135 < \Theta_S < 165$) have been considered as cloud and shown in white.

cloud mask is to mask the cloud edges where the polarimetric retrievals fail due to the parallax effects.

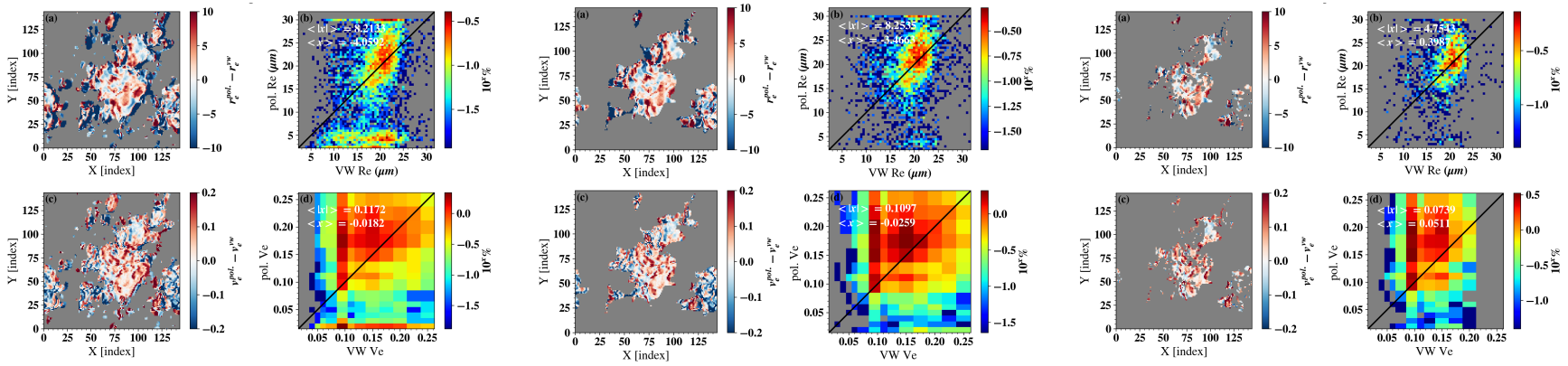

(i) VW-COT mask (ii) MA mask (iii) MA-fil mask

Figure 5.16: Comparisons of polarimetric retrievals versus the vertically-weighted retrievals by applying (i) VW-COT (ii) MA, and (iii) MA-fil cloud mask at the native resolution for $SZA = 60^o$. Colorbar of the joint histograms is the percentage of counts on a logarithmic scale. $< x >$ and $< |x| >$ are the mean bias and mean absolute bias respectively (see Appendix A.

Figure 5.16 uses the three different cloud masks ((i) VW-COT, (ii) MA and (iii) MA-fil) and compare polarimetric retrievals with the vertically-weighted retrievals for each scenario. The VW-COT cloud mask conservatively includes all the cloudy pixels while MA cloud mask can be used to filter out the biases due to the parallax effect at the cloud edges. Since the angular features of the cloud-bow region of the $P_{12}(\Theta_S)$ disappears as the CEV increases (Figuere 1.6), polarimetric retrievals also fail when $CEV > 0.2$. MA-fil combines MA cloud mask with a $CEV < 0.2$ filter to choose the polarimetric retrievals that are neither been influenced by parallax effects at the cloud edges and the $CEV > 0.2$ polarimetric retrievals.

5.4.2 Parallax effect in the middle of the cloud

When the radiance measurements have been made at a slant angle to the normal, the parallax effect always occurs and hard to avoid completely almost every practical situation. However, certain conditions reduce the influence of the parallax effect than the others. Primarily, when it is possible to accurately determine the cloud top, the biases due to the parallax effects can be significantly reduced. We can observe this scenario in the strati-formed cloud domains such as DYCOMS-II which has relatively minimum variability in the cloud-top altitude. Section 5.4.1 discusses how the polarimetric retrievals can be influenced by the parallax effect at the cloud edges under certain conditions. It is relatively easy to identify when the polarimetric retrievals fail at the cloud edges due to the parallax effects because the zero-polarized reflectance along the primary-bow line of sight clearly indicates

that the signal does not come from a cloud target, hence retrievals are physically unreasonable. However, when the same phenomenon (parallax effect) happens in the middle of the cloud, it is not easy to identify the pixels that have been influenced. This section discusses the possibility of happening the same scenario in the middle of the cloud with the aid of an example case.

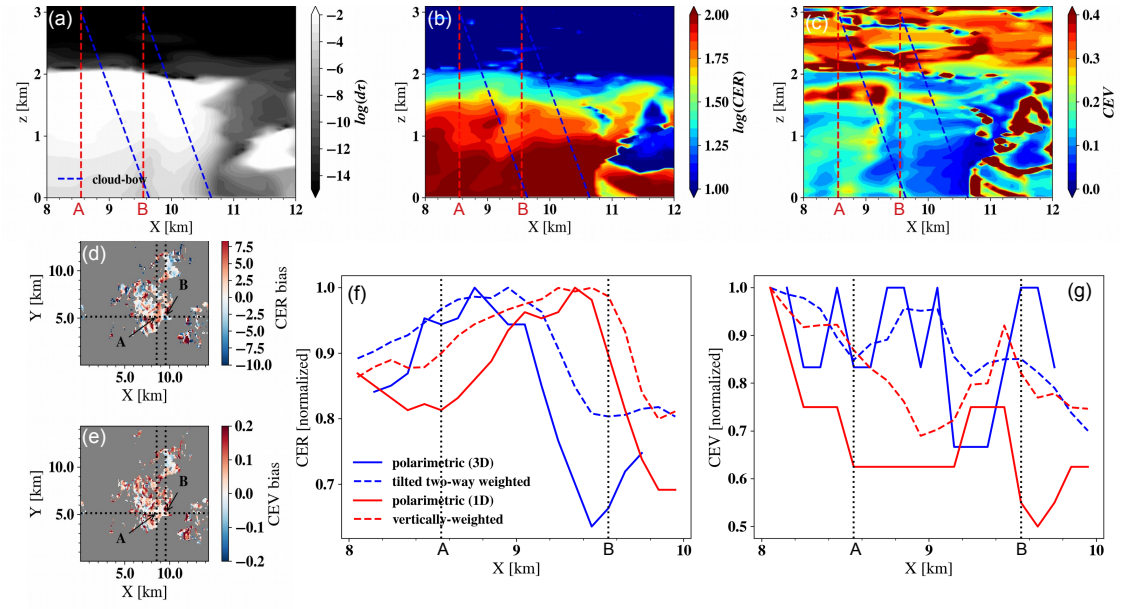

Figure 5.17: A case study to illustrate the parallax effect of the polarimetric retrievals in the middle of the cloud. Panel (d) and (e) are the difference between polarimetric and vertically-weighted CER and CEV retrievals respectively for RICO case after applying MA-fil cloud maks ($SZA = 60^o$, native resolution). The vertical cross-section of $d\tau$, CER, and CEV along the horizontal dotted-line in panel (d) and (e) are shown in panel (a), (b) and (c) respectively. Panel (f) and (g) show the spatial variation of the normalized CER and CEV retrievals respectively from X = 8 - 10 km.

The CER and CEV biases of polarimetric retrievals relative to the vertically-weighted retrievals for the RICO case are shown in Figure 5.17 (d) and (e) respectively. Relatively strong biases can be observed at point 'A' and 'B' in panel-d. Figure 5.17 (a) shows the vertical cross-sections of COT along $Y \sim 5km$ line from $X = 8-12km$ in Figure 5.17 (d). Similar vertical cross-sections of the CER and CEV profiles are shown in panel (b) and (c) respectively. The LES columns of x-locations correspond to the point 'A' and 'B' in Figure 5.17 (d) are shown in red dashed lines in panels a-c. The line-integral of the COT-weighted cloud microphysics along these red-lines are equivalent to the vertically-weighted retrievals. Figure 5.17 (f) and (g) show the variation of the normalized CER and CEV retrievals from $X = 8 - 10km$. The locations correspond to the point 'A' and 'B' are indicated by the black dotted lines. The values in Figure 5.17 (d) A-B correspond to the retrieved-CER differences between $r_e^{pol.,3D}$ (solid blue line) and r_e^{vw} (dashed red line) in panel-f. Note that the y-axis is not the absolute value of CER but an arbitrary unit that helps to focus on the variability of the retrieved value rather than the absolute value.

The geometry of the problem is crucial to understand the parallax effect. In Figure 5.17 , the sun is to the left side of the domain with a 60-degrees solar zenith angle. In this geometry, the apparent primary-bow line of sight corresponds to the retrievals indicated by point 'A' and 'B' are shown in blue dashed lines in panels a-c. If the primary information of the polarimetric retrievals comes from the cloud-bow scattering angles, under 3D radiative transfer, the cloud properties aggregated along the blue dashed lines (tilted two-way weighted retrievals) should better comparable with the 3D-polarimetric retrievals than the vertically-weighted

retrievals that compute the line integral of the cloud properties along the red dashed line. This is observable in panel-f. The variation of the 3D polarimetric retrievals (solid blue line) closely follows the variation of tilted two-way retrievals (dashed blue line) rather than the vertically-weighted retrievals (dashed red line). In contrast to the 3D-polarimetric retrievals, 1D retrievals are based on the RT simulations that assume the independent pixels. In 1D RT simulations, the photons are forcibly restricted to follow a vertical path. Therefore in Figure 5.17 (f), the retrievals that are based on the 1D RT (red solid line) closely correlated with the vertically-weighted retrievals (red dashed line) than the tilted two-way retrievals (blue dashed line).

Similar behavior can be observed in the CEV retrievals shown in Figure 5.17 (g). The polarimetric CEV retrievals based on 1D RT (solid red line) resembles vertically-weighted CEV (red dashed line) than the tilted two-way retrievals (blue dashed line), while the 3D polarimetric CEV-retrievals closely resembles the tilted two-way weighted CEV (blue dashed line) than the vertically-weighted CEV (red dashed line).

In summary, similar to the parallax effects at the cloud edges, the same phenomenon occurs in the inner region of the clouds which is relatively more difficult to identify. When the domain consists of scattered cumulus clouds with significant cloud top variability, there is a high chance to retrievals to be influenced by the parallax effect. Moreover, the geometry of the underlying observation is crucial in the parallax effect. If the primary-bow line of sight of the polarized reflectance measurements makes a large angle to nadir, such retrievals are more likely to be impacted by the parallax effects.

5.4.3 Angular shift of the cloud-bow pattern

Polarimetric retrievals rely upon the angular signature of the polarized reflectance. Specifically, CER retrievals depend on the exact angular pattern of $R_p^*(\Theta_S)$. When the parallax effect (or any other effect) shifts the angular pattern of the polarimetric retrievals, in theory, the corresponding bias of the retrieved-CER should be correlated with the underlying angular shift. This section investigates to what extent, the CER-retrieval biases are correlated with the angular shift of the observed polarized reflectance.

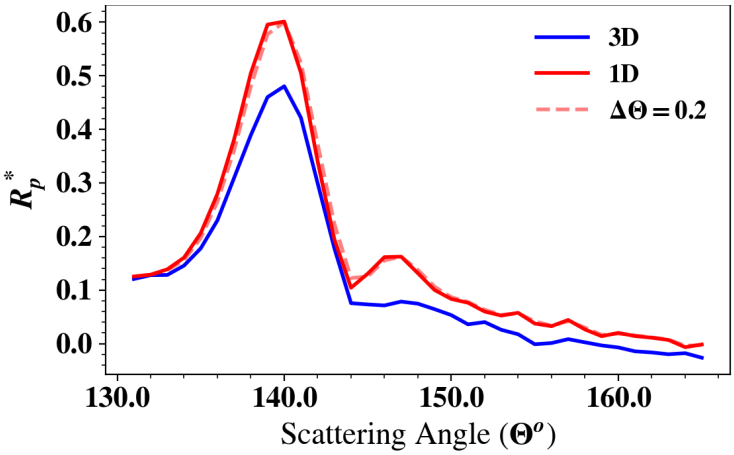

Figure 5.18: Shifting angular pattern of the 1D polarized reflectance $R_p^*(\Theta_S, 1D)$ (solid red curve) to be aligned with the angular pattern of the corresponding 3D polarized reflectance $R_p^*(\Theta_S, 3D)$ (solid blue curve) for an arbitrary pixel in the RICO case at native resolution. The Red dashed curve is the optimally correlated $R_p^*(\Theta_S, 1D)$ pattern with the corresponding $R_p^*(\Theta_S, 1D)$ which was obtained by shifting the 1D pattern (red solid line) over the angular space.

Figure 5.18 shows the angular pattern of the geometrically corrected polarized reflectance $R_p^*(\Theta_S)$ from a cloud target (an arbitrary pixel in the RICO case at native resolution) based on 1D and 3D RT in red and blue curves respectively. To obtain $R_p^*(\Theta_S + \Delta\Theta, 1D)$ pattern (dashed red curve) which is optimally correlated with $R_p^*(\Theta_S, 3D)$ (solid blue curve), the angular pattern of $R_p^*(\Theta_S, 1D)$ is shifted in 0.1 degrees steps to both left ($\Delta\Theta < 0$) and right ($\Delta\Theta > 0$) over the scattering angle space. In this example (Figure 5.18), $\Delta\Theta = 0.2$ means the angular pattern of polarized reflectance from 1D RT has been moved 0.2 degrees to the right to be aligned with the 3D results which implies under 3D radiative transfer, polarimetric CER retrieval is smaller than its 1D counterpart.

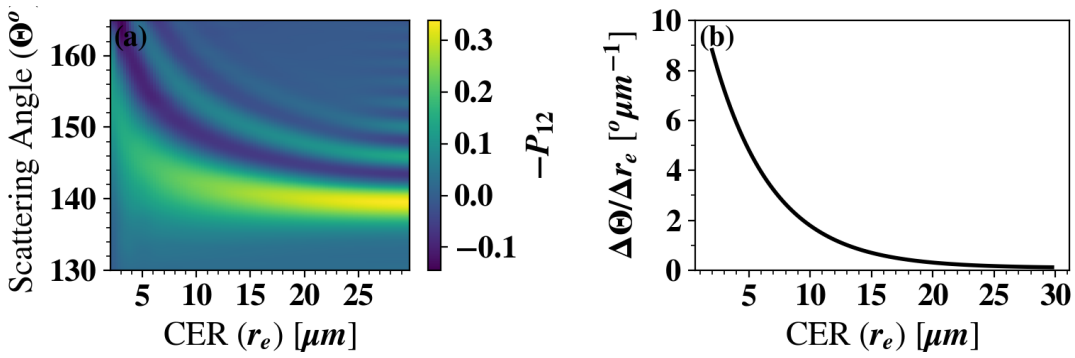

Figure 5.19: Angular shift ($\Delta\Theta$) of the polarized phase function ($P_{12}(\Theta_S)$) as cloud effective radius (CER) varies. (a) Angular pattern of $P_{12}(\Theta_S)$ for varying CER in the cloud bow scattering-angle range ($135^o < \Theta_S < 165^o$). (b) $\Delta\Theta/\Delta r_e$ vs. CER.

A theoretical relationship between $\Delta\Theta/\Delta r_e$ (phase shift per CER) vs. CER can be obtained from the pre-computed $P_{12}(\Theta_S)$ library. Figure 5.19 (a) shows $P_{12}(\Theta_S)$ for water clouds as CER varies for CEV=0.02. $P_{12}(\Theta_S)$ has more sharp

angular features for large CER values. As CER decreases, the angular pattern of $P_{12}(\Theta_S)$ becomes less significant and has a positive phase shift. That is the whole angular pattern of $P_{12}(\Theta_S)$ moves over the angular space towards increasing Θ_S direction as CER decreases. Figure 5.19 (b) shows $\Delta\Theta/\Delta r_e$ vs CER correspond to the $P_{12}(\Theta_S)$ patterns in Figure 5.19 (a). In the large cloud effective radius regime, $\Delta\Theta$ shift per 1 μm CER bias is smaller compared to small CER regime which has large $\Delta\Theta$ shift per $1\mu m$ CER bias.

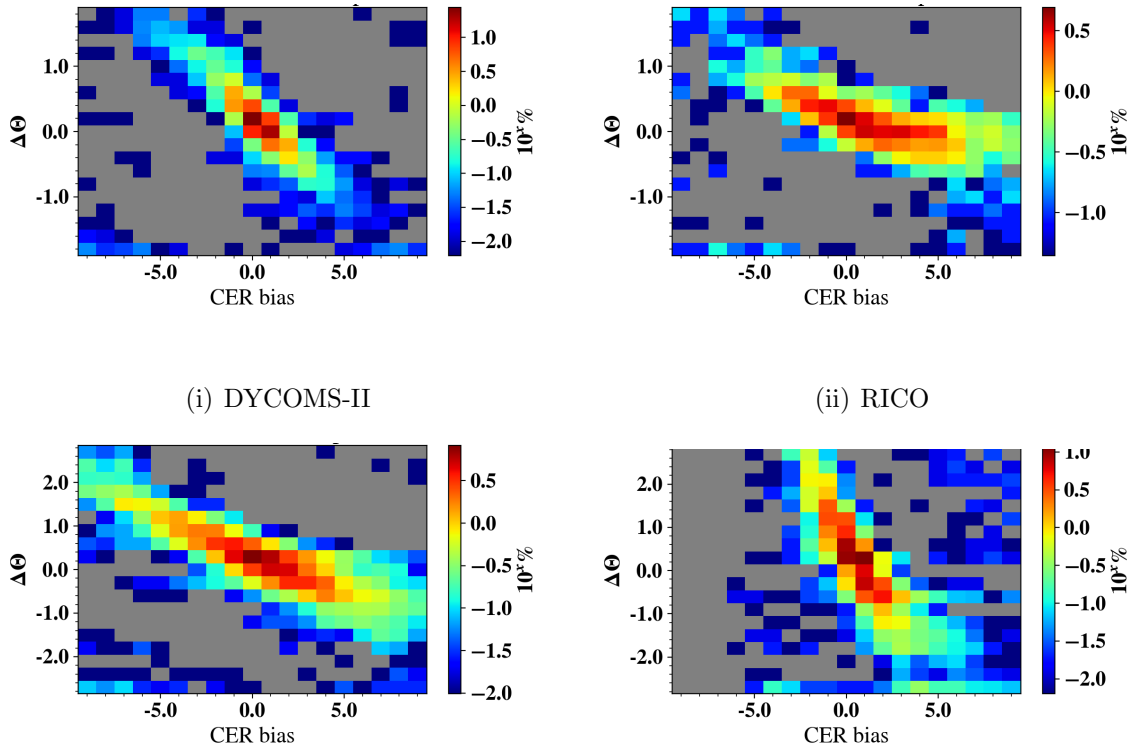

(i) DYCOMS-II

(ii) RICO

(iii) ATEX-clean

(iv) ATEX-polluted

Figure 5.20: Phase shift ($\Delta\Theta$) vs. CER-bias for (i) DYCOMS-II (ii) RICO, (iii) ATEX-clean, and (iv)ATEX-polluted cases respectively for $SZA = 60^o$.

Figure 5.20 shows $\Delta\Theta$ vs. CER bias for (i) DYCOMS-II, (ii) RICO, (iii) ATEX-clean, and (iv) ATEX-polluted LES cases for $SZA = 60^o$ after applying the

CEV-fil cloud mask. A clear negative correlation exists between $\Delta\Theta$ and CER bias in all LES cases. That is, after filtering the biases due to the large CEV-values and the parallax effects at the cloud edges, the remaining CER biases are likely stemmed from the angular shift of $P_{12}\Theta_S$ large CEV-values values. Moreover, the gradient of the regression line becomes steeper for the domains with relatively small CER (ATEX-polluted case) while the $\Delta\Theta/\Delta r_e$ becomes large for the domains with large CER (RICO). This observation is consistent with $\Delta\Theta/\Delta r_e$ vs. CER plot in Figure 5.19(b).

5.5 Polarimetric retrievals under 3D radiative transfer

Section 5.3 performed a closure study in order to understand the correlations between polarimetric retrievals and vertically-weighted retrievals under 1D radiative transfer. Unless the domain consists with broken cumulus clouds with many cloud-free regions such as in the RICO case, 1D polarmetric retrievals agrees with the corresponding vertically-weighted retrievals reasonably ($\langle|r_e^{pol.,1D} - r_e^{vw}|\rangle < 1\mu m$, $\langle|v_e^{pol.,1D} - v_e^{vw}|\rangle < 0.025$). This section investigates the biases between polarimetric retrievals under 3D radiative transfer ($r_e^{pol.,3D}$) with respect to the vertically-weighted retrievals (r_e^{vw}).

Figure 5.21 shows the polarimetric retrievals of (i) DYCOMS-II, (ii) RICO, (iii) ATEX-clean, and (iv) ATEX-polluted cases based on 3D radiative transfer. First two panels of each column are the CER ($r_e^{pol.,3D}$) and CEV ($v_e^{pol.,3D}$) retrievals. The pixels that have vertically-weighted COT less than 0.1 have been masked and

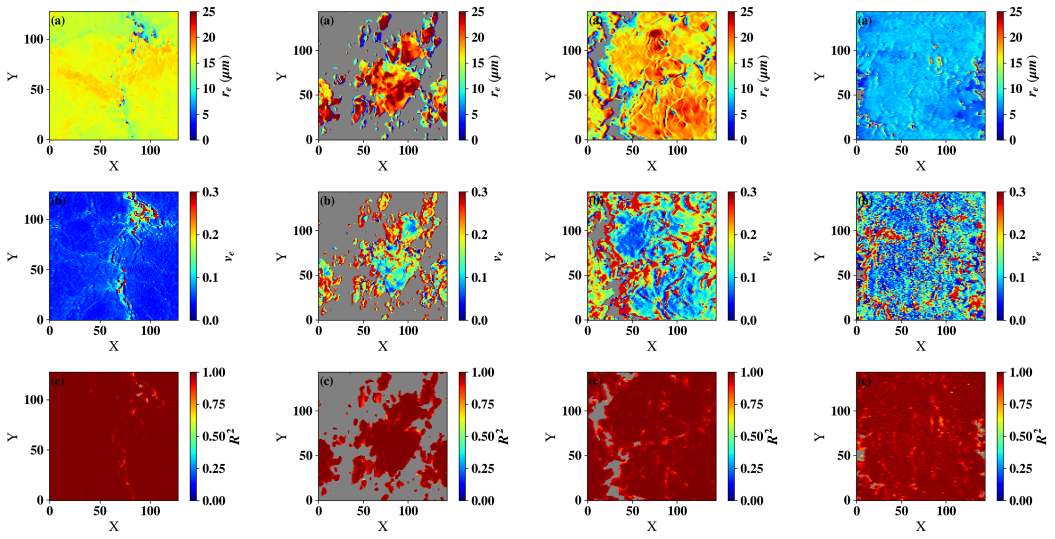

(i) DYCOMS-II (ii) RICO (iii) ATEX(clean) (iv) ATEX(polluted)

Figure 5.21: Polarimetric retrievals for each LES case in the native resolution based on 3D RT. Panel (a),(b), and (c) of each column correspond to CER, CEV, and R^2 of the underlying parametric curve-fitting. (Sun is to the left at SZA=40^o, VW-COT cloud mask have been used)

shown in gray by using the VW-COT cloud mask (the second row of Figure 2.5). The last row shows the corresponding R^2 value of the underlying parametric curve-fitting for each LES case. Significantly large $R^2(\gtrapprox 0.95)$ values indicate that the observed $R_p^*(\Theta_S)$ patterns have been converged to a particular $P_{12}(\Theta_S)$-pattern in the theoretically-computed library with a sufficient accuracy regardless the physical validity of the retrievals. Compared to the equivalent results from the 1D RT in the last row of Figure 5.4, the R^2 values of the 3D results in the last row of Figure 5.21 shows certain fine features. The R^2 values of the 3D results decrease at the cloud edges. Corresponding CEV retrievals of the relatively low R^2 values are associated with large CEV retrievals which is more visible in the ATEX-clean case. As CEV

increases, the supernumerary bow features of $P_{12}(\Theta_S)$ weaken (Figure 1.6), thus the polarimetric retrievals fails in the large CEV regime.

5.6 Solar zenith angle dependence

Section 5.4 discusses two scenarios where the parallax effect could influence the polarimetric retrievals. Among them, the prominent situation which appears to cause significant biases is the parallax effects that occur at the cloud edges. When the apparent primary-bow line of sight corresponds to the polarimetric measurement orienting away from the cloud towards the cloud-free region, the retrieved cloud properties become physically invalid. CEV-fil cloud mask remove such pixels that have been influenced by the parallax effect at the cloud edges in addition to the $v_e^{pol.,1D} > 0.2$ retrievals which also physically unreasonable.

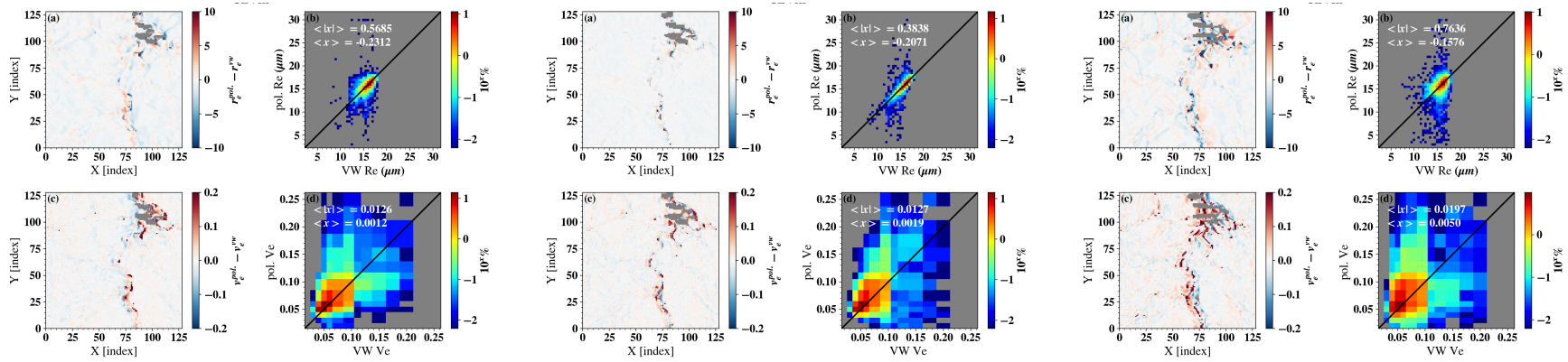

(i) $SZA = 20^o$ (ii) $SZA = 40^o$ (iii) $SZA = 60^o$

Figure 5.22: Comparisons of polarimetric retrievals against the vertically-weighted retrievals for DYCOMS-II case at (i) $SZA = 20^o$, (ii) $SZA = 40^o$ and (iii) $SZA = 60^o$ under 3D radiative transfer assumption. Colorbar of the joint histograms is the percentage of counts on a logarithmic scale. $< x >$ and $< |x| >$ are the mean bias and mean absolute bias respectively. Sun is to the left side of the domain. MA-fil cloud mask has been used.

After applying the CEV-fil cloud mask to remove the biases due to the parallax effect at the cloud edges and large CEV, Figure 5.22 compares 3D-polarimetric retrievals ($r_e^{pol.,3D}$ and $v_e^{pol.,3D}$) of the DYCOMS-II case with the vertically-weighted retrievals (r_e^{vw} and v_e^{vw}) for different SZAs. Similar to Figure 5.5 which performs equivalent comparisons based on 1D RT, a significant amount of pixels have strong one-to-one correlation between $r_e^{pol.,3D}$ and r_e^{vw} in the b-panels of Figure 5.22(i-iii). Even though substantially lower compared to the number of pixels that have one-to-one correlation, b-panels of Figure 5.22 indicates some pixels with the 3D-polarimetric retrievals have been significantly deviated from the one-to-one line. These deviations do not exist in Figure 5.5. Moreover, these $r_e^{pol.,3D}$ deviations appear to span over a longer range when SZA gets larger. The absolute bias between $r_e^{pol.,3D}$ and r_e^{vw} are 0.57, 0.38, and 0.76 μm for SZA = 20, 40, and 60 respectively while the similar quantities based on 1D RT are 0.28, 0.28, and 0.27 μm. The mean absolute bias of $v_e^{pol.,3D}$ with respect to v_e^{vw} are 0.0126, 0.0127, and 0.0197 for SZA = 20, 40, and 60 degrees respectively which are about 50% increment from the bias observed in the 1D counterparts (0.0066, 0.0068, and 0.0075 for SZA = 20, 40, and 60 degrees respectively).

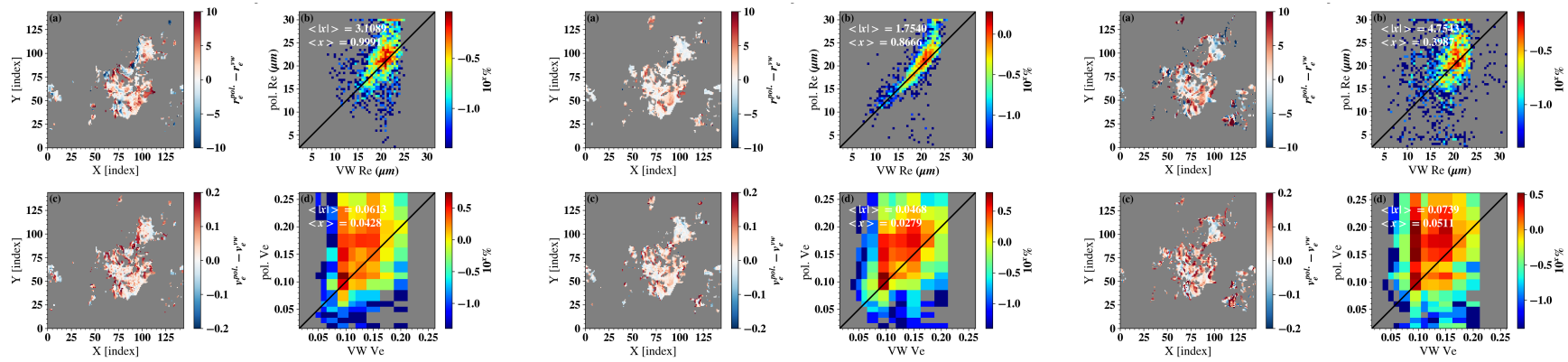

(i) $SZA = 20^o$ (ii) $SZA = 40^o$ (iii) $SZA = 60^o$

Figure 5.23: Comparisons of polarimetric retrievals against vertically-weighted pseudo retrievals for RICO case at (i) $SZA = 20^o$, (ii) $SZA = 40^o$ and (iii) $SZA = 60^o$ under 1D radiative transfer assumption. Colorbar of the joint histograms is the percentage of counts on a logarithmic scale. $< x >$ and $< |x| >$ are the mean bias and mean absolute bias respectively. Sun is to the left side of the domain. MA-fil cloud mask has been used.

RICO case is the most challenging case for the polarimetric retrievals among the four LES cases that have been used throughout this study. One reason for that is the scattered cumulus cloud fields can cause biases at the cloud edges due to the parallax effects more frequently than the stratocumulus cloud fields. In addition to the parallax effect, If we consider the vertically-weighted pseudo retrievals as reference cloud microphysics, RICO case has more $CEV > 0.2$ columns which are also challenging in the polarimetric retrievals because the angular pattern of $R_p^*(\Theta_S)$ gradually looses its supernumerary bow feature as CEV increases. After removing those two main biases due to the large CEV-values and the parallax effects at the cloud edges , Figure 5.23 compares the 3D-polarimetric retrievals and corresponding vertically-weighted retrievals for the RICO case at (i) $SZA = 20^o$, (ii) $SZA = 40^o$, and (iii) $SZA = 60^o$. The (a) and (c) panels are CER ($r_e^{pol.,3D} - r_e^{vw}$) and CEV ($v_e^{pol.,3D} - v_e^{vw}$) biases respectively for each SZA. The (b) and (c) panels are the joint histograms of the polarimetric and vertically-weighted retrievals. In the joint histograms (b-panels), the polarimetric CER retrievals more likely have deviated from the one-to-one regression line in both $SZA = 20^o$ and $SZA = 60^o$ cases compared to the $SZA = 40^o$ case. When $SZA = 60^o$, the apparent primary-bow line of sight of the polarimetric reflectance measurement (Figure 5.17(a) blue dashed line) makes 20-degree anti-clockwise angle with the -z direction. When $SZA = 40^o$ and 20^o, the apparent primary-bow lines of sight make 0^o and 20^o clockwise angles with the -z direction. If we assume the primary information of the polarimetric retrieval comes from the polarized reflectance measurement along the primary-bow line of sight, $SZA = 40^o$ is less likely to be impacted by the parallax effect while

$SZA = 20^o$ and $SZA = 60^o$ are equally susceptible to parallax effect due to the symmetry. Section 5.4.2 investigates this hypothesis further focussing on the strong positive and negative CER biases around (85,50) and (95,50) in Figure 5.23(iii)(a).

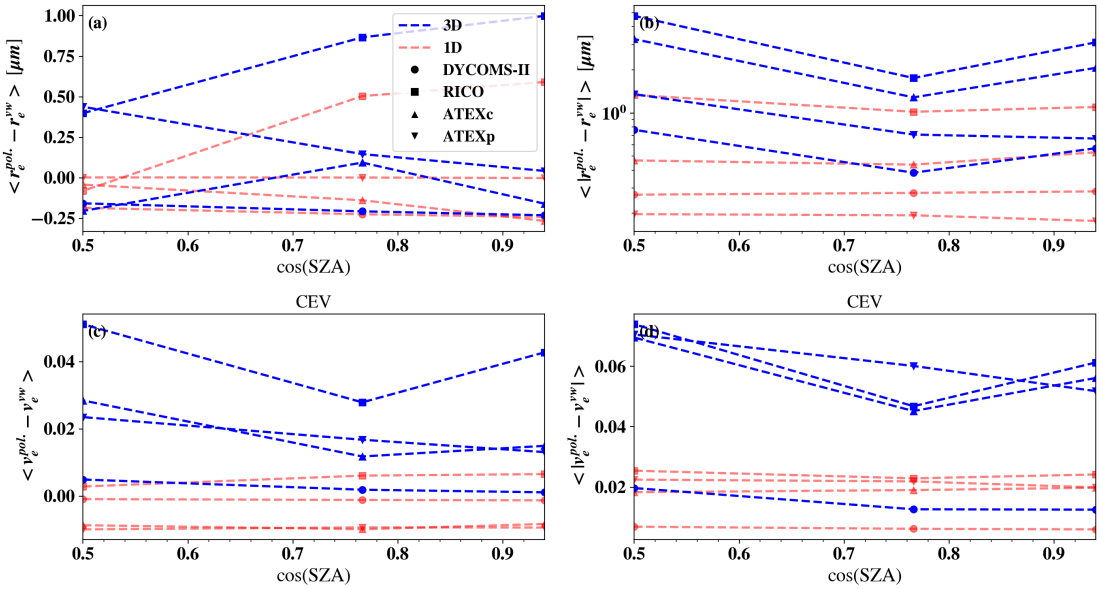

Figure 5.24: Mean bias ($\langle x \rangle$) and mean absolute bias ($\langle |x| \rangle$) (see Appendix A for definitions) of CER (a and b respectively) and CEV (c and d respectively) as SZA varies under 3D RT (in blue) and 1D RT assumption (in red) at the native resolution.

Figure 5.24 summarizes the mean and mean absolute biases between the polarimetric and vertically-weighted retrievals in the native resolution. Panel (a) and (b) are the mean and mean absolute biases of CER retrievals. Panel (c) and (d) are the mean and mean absolute biases of the CEV retrievals. The blue and red lines are based on 3D and 1D RT simulations respectively. After applying the CEV-fil cloud mask to ignore the pixels that have been influenced by the large CEV-values and the parallax effects at the cloud edges, both 3D and 1D mean biases are greater than -0.25 μm and less than 1 μm. The mean absolute biases of CER retrievals that are

shown in panel (b) give a better manifestation of the general behavior compared to the panel (a). For all LES cases, the mean absolute biases of 1D polarimetric CER retrievals do not show significant variation as SZA varies. The 3D absolute bias is always greater than its 1D counterpart. In Figure 5.24(b), the mean absolute biases of all four LES cases show a similar trend as SZA varies. When $SZA = 40^o$, the bias is minimum but increases when SZA decreases (to 20^o) and increases (to 60^o). The same trend can be observed in CEV mean absolute biases in Figure 5.24(d). This behavior is consistent with our understanding of the parallax effects in the middle of cloud (refer to Section 5.4.2). When $SZA = 40^o$, the line of sight of the primary-bow scattering direction ($\Theta_S \sim 140^o$) is exactly aligned with the nadir (Figure 5.17(a) red dashed line). Therefore, the vertically-weighted retrievals which obtain the weighted line-integral along the nadir agree well with the 3D-polarimetric retrievals at $SZA = 40^o$. When $SZA = 60^o$, the apparent primary-bow line of sight of the polarimetric reflectance measurement makes a 20-degree anti-clockwise angle with nadir (Figure 5.17(a) blue dashed line), while the same angle is 20^o clockwise when $SZA = 20$. Therefore, the apparent primary-bow directions are symmetric about the nadir when $SZA = 60^o$ and $SZA = 20^o$. Hence, compared to $SZA = 40^o$ (nadir apparent primary-bow) geometry which is minimally influenced by the parallax effects, $SZA = 60^o$ (apparent primary-bow is 20^o anti-clockwise from nadir) and $SZA = 20^o$ (apparent primary-bow is 20^o clockwise from nadir) geometries are equally influenced by the parallax effects due to the symmetry.

5.7 Horizontal resolution dependence

Figure 5.25 shows the polarimetric retrievals of the RICO case based on 3D RT as horizontal resolution varies. Panel (a) and (b) of each column are the CER and CEV retrievals respectively. The c-panels show the R^2 values of the underlying curve-fitting. The VW-COT (Section 2.5) cloud mask has been used and the sun is to the left with $SZA = 60^o$. The a-panels in Figure 5.25 (i-v) show $r_e^{pol.,3D}$ in 0.1 (native), 0.5, 1.0, 2.0, and 5.0 km resolutions respectively. The b-panels in Figure5.25(i-v) are $v_e^{pol.,3D}$ for 0.1 (native), 0.5, 1.0, 2.0, and 5.0 km-resolutions respectively. Figure 5.8 shows the same set of figures but based on 1D RT. In Figure 5.25(i)(a), shadowing edges of the cloud appear to have extremely low $r_e^{pol.,3D}$ values in contrast to the 1D results in Figure 5.8(i)(a). The magnitude of these small CER values in the a-panels of Figure 5.25 increases as the horizontal resolution of the footprint increases from 100m to 5km. These small CER retrievals at the shadowing edges cause strong negative biases relative to the vertically weighted retrievals as shown in Figure 5.12(i)(a). Such biases that occur at the cloud edges have been investigated in detail in Section 5.4.1 and likely due to the parallax effect that occurs at the cloud edge. At $SZA = 60^o$, the primary-bow line of sight of the polarized reflectance measurement is directed towards the cloud-free region, thus the retrieved polarimetric retrievals are physically unreasonable. Throughout this study, the MA cloud mask has been used to identify and filter the pixels that have been influenced by the parallax effect at the cloud edges (Section 5.4.1.1). As resolution increases, $v_e^{pol,3D}$ increases (b-panels of Figure 5.25(i-v)) and consequently the polarimetric

retrievals become unreliable because the supernumerary bow features of $P_{12}(\Theta_S)$ becomes less significant (Figure 1.2) as CEV increases. To identify and filter the pixels that have been influenced by both large CEV-values and the parallax effects at the cloud edges, the CEV-fil cloud mask (Section 2.5) has been used.

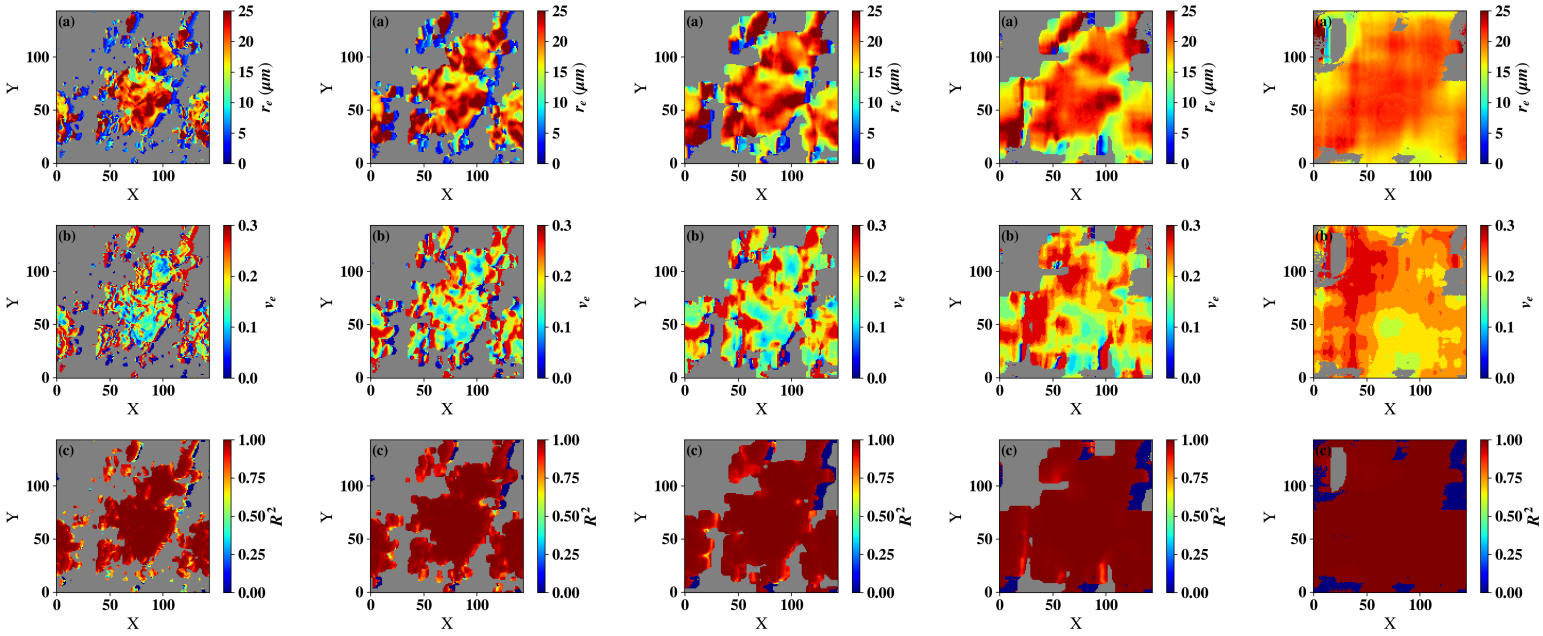

(i) Native (100m) (ii) 0.5km (iii) 1.0km (iv) 2.0km (v) 5km

Figure 5.25: Polarimetric retrievals of RICO case for different resolutions under 3D radiative transfer. Panel (a),(b), and (c) of each column correspond to CER, CEV, and R^2 of the underlying parametric curve-fitting. (The Sun is to the left. SZA=60^o, VW-COT cloud mask has been used)

Figure 5.26 summarizes the mean and mean absolute biases between the polarimetric and vertically-weighted retrievals at $SZA = 60^o$. Panel (a) and(b) are the mean and mean absolute biases of CER retrievals. Panel (c) and (d) are the mean and mean absolute biases of the CEV retrievals. The blue and red lines are based on 3D and 1D RT simulations respectively. The CEV-fil cloud has been used to ignore the pixels that are influenced by the large CEV-values and the parallax effects at the cloud edges. Except the RICO case, all the other LES cases have mean CER-bias (between $r_e^{pol.,3D}$ and r_e^{vw}) greater than -0.5 μm and less than $0.5\mu m$ without prominent resolution dependence. In contrast to the mean CER biases, mean CEV biases from 3D RT shows a clear resolution dependence. Starting from the largest value at the native resolution, in all the cases the CEV bias of $v_e^{pol.,3D}$ vs. v_e^{vw} gradually decreases as the resolution increases. The absolute mean biases in Figure 5.26 (b) and (d) also exhibits a similar trend. In general, 3D polarimetric retrievals have relatively higher biases than their 1D counterparts. The largest bias between the 3D-polarimetric and vertically-weighted results exist at the native resolution and gradually decreases as the resolution increases.

In Figure 5.26 , the coarse resolution results are based on the radiance images obtained by taking the moving average of the native resolution image. In Figure 5.27 , we compare the moving-average based coarse resolution results with the simple-average based coarse resolution results. The gray dashed lines in Figure 5.27 are the 3D polarimetric results using the moving-average coarse resolution images. Thus, the gray lines in Figure 5.27 are similar to the blue lines in Figure 5.26 . The 3D polarimetric retrievals based on the simple-averaging based coarse

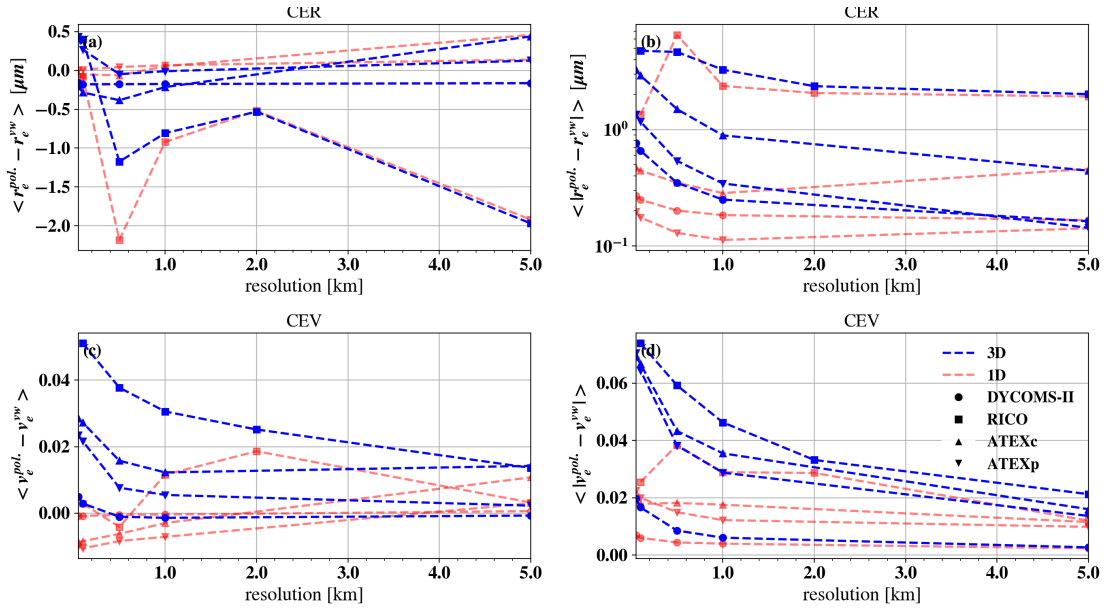

Figure 5.26: Mean bias ($\langle x \rangle$) and mean absolute bias ($\langle |x| \rangle$) (see Appendix A for definitions) of CER (a and b respectively) and CEV (c and d respectively) as the resolution of the footprint varies under 3D RT (in blue) and 1D RT assumption (in red) at $SZA = 60^o$.

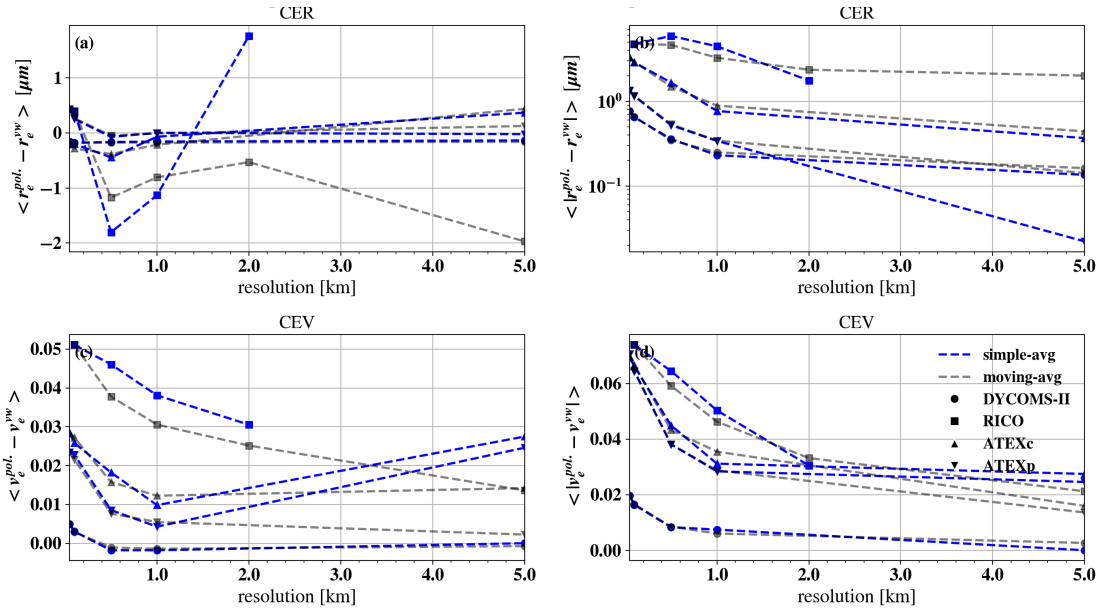

Figure 5.27: Mean bias ($\langle x \rangle$) and mean absolute bias ($\langle |x| \rangle$) (see Appendix A for definitions) of CER (a and b respectively) and CEV (c and d respectively) as the resolution of the footprint varies under 3D RT at $SZA = 60^o$ based on moving-averaged coarse resolution results (in gray lines which are similar to the blue lines in Figure 5.26) and simple-average coarse resolution results (in blue).

resolution images are shown in blue dashed lines in Figure 5.27 . In the majority of cases, different averaging techniques lead to similar results, especially as the resolution increases up to 1km. At the 5-km resolution, simple-average based results only have 4 pixels in DYCOMS-II and ATEX cases, and only 1 pixel in the RICO case which causes deviations from moving-average based results.

Chapter 6: Using polarimetric observations to detect and quantify the 3D RT effects in the bi-spectral retrievals

The content of this chapter is adapted from the published prior work of the author (Rajapakshe and Zhang, 2020).

6.1 Introduction

Clouds play an important role in the Earth systems. To better understand this role and simulate clouds in the numerical weather and climate models, it is requires observations of cloud properties from regional to global scales. Many satellite remote sensing techniques have been developed to meet this requirement. Of particular interest in this study is the cloud optical thickness (COT) retrievals from the passive satellite observations of cloud reflectance in the visible (VIS) or near-infrared (NIR) band. The COT is an important cloud parameter that largely determines the radiative effects of clouds. A widely used method for COT retrieval is simultaneously retrieving the COT with cloud effective radius (CER) based on a pair of observed cloud reflectances, one in VIS/NIR spectral region and the other in the water-absorbing shortwave infrared region (SWIR) (Nakajima and King, 1990). This so-called bi-spectral method has been adopted in several widely used operational cloud products,

such as MODIS (Moderate Resolution Imaging Spectroradiometer), VIIRS (Visible Infrared Imaging Radiometer Suite) and SEVIRI (Spinning Enhanced Visible and Infrared Imager) (Cao et al., 2014; Platnick et al., 2003; Roebeling et al., 2006). The retrievals that utilizes the multangular polarimetric observations for cloud microphysics retrievals is another widely used approach which exploits the angular pattern of the polarimetric cloud reflectances in the cloud bow scattering angles (Bréon and Goloub, 1998; Bréon and Doutriaux-boucher, 2005). This method not only provides retrievals of CER but also estimates the width of cloud droplet size distribution (i.e., cloud effective variance (CEV) of cloud top droplet size distribution). The polarimetric based cloud microphysics retrievals (polarimetric retrieval for short) have been used for the POLDER satellite mission, as well as several airborne polarimeters such as RSP (Research Scanning Polarimeter), airMSPI (Airborne Multiangle SpectroPolarimetric Imager) and airHARP (Airborne Hyper-Angular Rainbow Polarimeter) (Alexandrov et al., 2012; Diner et al., 2013; Martins et al., 2018).

Most operational passive satellite cloud remote sensing algorithms, including those mentioned above, are based on 1D Radiative Transfer (RT) theory, which makes two fundamental and important assumptions. The first assumption, often referred to as the plane-parallel approximation (PPA), assumes cloud fields within each cloudy pixel to be horizontally homogeneous. The second assumption is known as the independent pixel approximation (IPA) that assumes all pixels are independent of each other from the perspective of net photon transportation. In some situations, such as stratus clouds, these assumptions are not unreasonable. However, in many other circumstances, clouds have distinct 3D structures that deviate substantially

from the above two assumptions. In such cases, cloud radiative properties (e.g., reflectance and transmittance) determined by 3D RT would be different from those derived based on 1D RT theory. As a result, the operational passive remote sensing algorithms, which uses the 1D RT theory to interpret the observed cloud radiative properties, are subjected to significant biases and uncertainties. This is known as the 3D radiative transfer effect in passive cloud remote sensing. Hence, the 3D radiative effect is a fundamentally inherited challenge, not only in operational cloud property retrievals but also in various remote sensing applications other than the techniques that involve line-of-sight absorption and emission with little atmospheric scattering (Marshak et al., 2006; Marshak and Davis, 2005; Várnai and Davies, 1999).

The 3D RT effects in cloud property retrievals may have various adverse implications. For example, satellite retrievals are an important source of data for global cloud property observations, which are especially valuable for evaluating and improving global climate models. However, biases and uncertainties caused by the 3D effects can complicate the evaluation process and even mislead the conclusions (Kay et al., 2012; Seethala and Horváth, 2010). Furthermore, the studies on the aerosol indirect effects that use the observed relationship between the aerosol amount and cloud properties (Chang and Christopher, 2016; Kaufman et al., 2005; Rosenfeld and Feingold, 2003) could also be affected by the 3D radiative effects in passive cloud property retrievals (Marshak et al., 2006).

In the past, most research has focused on elucidating the physics behind the 3D RT effects and assessing the consequential impacts on the retrieved cloud properties, such as cloud optical thickness (Várnai and Davies, 1999; Loeb and Davies, 1996;

Marshak et al., 1995; Várnai and Marshak, 2001) and cloud effective radius (Zhang et al., 2012; Zhang and Platnick, 2011). Thanks to these studies, we now have a reasonable understanding of what conditions would favor the 3D RT effect (e.g., broken clouds under the low sun condition), which enables us to filter the satellite cloud property retrievals to reduce the impact of 3D radiative effect. For example, passive cloud property retrievals in the high-latitude regions are often disregarded all together in many model evaluation studies partly due to the concern of enhanced 3D RT effect under the low Sun conditions (e.g., Song et al. (2018); Takahashi et al. (2017); Zhang et al. (2019)). Obviously, such crude filtering causes a significant data loss. Pixel-level identification of 3D RT effect is certainly more ideal, but unfortunately it has been proven to be a highly challenging problem. Some studies attempted to use the sub-pixel inhomogeneity as an index for 3D RT effect (e.g., Zhang and Platnick (2011); Di Girolamo et al. (2010); Zhang et al. (2017)). The limitation of the sub-pixel inhomogeneity index is, it only can be used to identify the violation of the PPA but not IPA. As explained in Section 6.3, as well as many previous studies, the violation of IPA can lead to some strong 3D RT effects (e.g., illuminating and shadowing effect) and thereby cause large errors in retrieved COT and CER. Some attempts have been made to identify the 3D RT effects caused by the violation of the IPA. For example, Várnai and Marshak (2002) used the cloud top topography retrievals based on the infrared cloud observations that are minimally affected by the 3D RT effect to identify the pixels influenced by the illuminating and shadowing effects in the visible band. Their method clearly revealed that the COT retrievals influenced by the illuminating effects are statistically larger than those

influenced by the shadowing effect. Nevertheless, this method faces two limitations. First, although it can be useful to identify the pixels influenced by the 3D RT effect, it cannot be used to quantitively correct the COT retrieval bias. Second, the method involves rather complicated multi-pixel analysis which makes it difficult to implement as an operational algorithm. Lately, some attempts have been made to use the machine-learning techniques to retrieve the cloud properties based on the 3D, instead of the 1D RT theory. A common theme of these studies is to first develop a large collection of synthetic satellite cloud observations based on simulated cloud fields (e.g., from a large-eddy-simulation model) and 3D RT model. Then the simulated samples are used to train the machine-learning algorithm which will be in turn used to retrieve the cloud properties from the real observations. These methods are still at their infancy and their performance, especially applied to real data, need further studies.

In this study, we explore a new method based on the physical principles of RT and utilize the unique capability of multi-angular polarimetric cloud observation to both identify and correct the 3D radiative effect. In particular, our method, referred to as the maximum 1D reflectance method, is highly effective and efficient to detect the pixels influenced by strong illuminating effect. The outline of this paper, as follows. First, Section 6.2 provides a brief description about the hypothetical 1D cloud fields and the radiative transfer simulation model that have been used. Then, Section 6.3 uses one hypothetical cloud field to explain how the 3D RT effects appear at the cloud property retrievals. Thereafter, Section 6.4 introduces a quantity called 3D effect impact factor. After that, Section 6.5 explains our maximum 1D

reflectance mainly emphasizing the capability of detecting illuminating effects. Section 6.6 further explores the maximum 1D reflectance method towards correcting COT biases. Stepwise procedure of implementation is mentioned at the beginning of Section 6.5 by summarizing both Section 6.5 and 6.6. Section 6.7 discusses about potential observational implementation for future studies and Finally, Section 6.8 gives a summary and offers some concluding remarks.

6.2 Models

In this study, two hypothetical 1D cloud fields have been used. The first one is referred to "step cloud (Figure 6.1 (a)) which has a constant physical thickness of 1 km and an optically thick region (COT = 10.0) at the middle surrounded by two optically thin regions (COT = 0.1) at each edge. The cloud effective radius of the step cloud is assumed to be 10 m. Though the step cloud case is very useful to demonstrate and understand certain physical principles, it is too simple from realistic cloud fields. Hence we will use the well-known fractal cloud generation method, the bounded cascade model (Cahalan et al., 1994) to generate our second hypothetical 1D cloud field which is hereafter referred as the fractal cloud for short.

Figure 6.3 (a) shows the fractal cloud field simulated based on the bounded cascade model (Cahalan et al., 1994). This model uses a two-parameter multiplicative recurrent process that allows simulating the realistic horizontal spatial distribution of the cloud liquid water path (LWP) when the mean LWP is known (Davis and Marshak, 2010; Marshak et al., 1994). The modeling process starts with a uniform

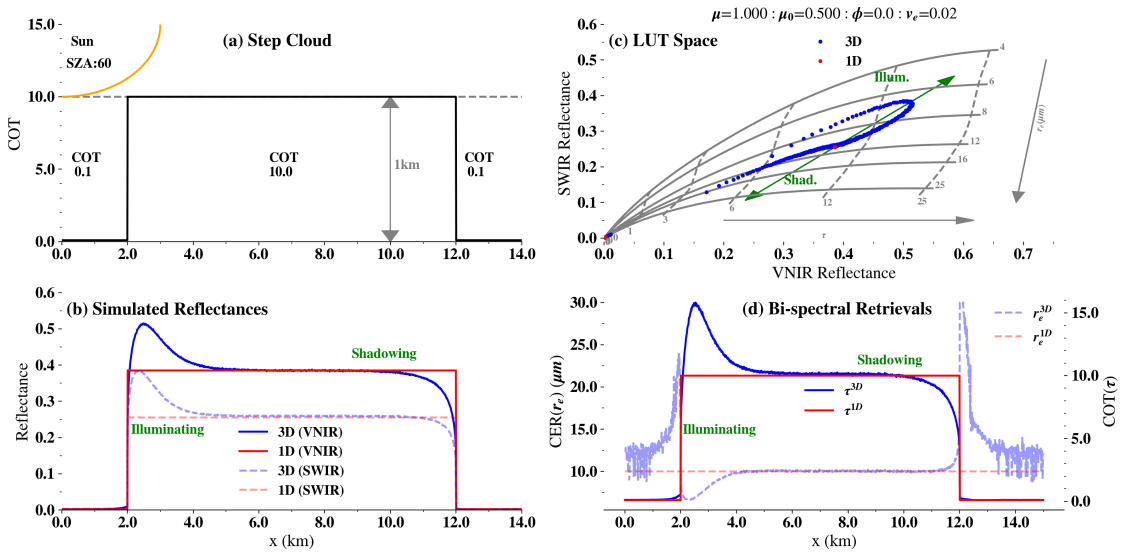

Figure 6.1: (a) An idealized 1D cloud field named the "step cloud". (b) Simulated 1D and 3D VNIR reflectances (solid red and blue respectively) and 1D and 3D SWIR reflectances (dashed red and blue respectively) for (a). (c) The illuminating and shadowing effects in (b) depicted in the bi-spectral LUT space ($SZA = 60^o$, $VZA = 0$, $CEV = 0.02$). (d) The cloud optical thickness and the cloud effective radius retrievals based on (c).

plane-parallel cloud slab with a constant mean LWP. This initial cloud slab has a finite geometrical thickness Δz and Δx, but infinite along the y direction. The recursive procedure proceeds as follows: Divide the uniform slab into two halves (i.e., $\Delta x/2$) at the middle of the x dimension, and then transfer f_0 fraction of water mass from one side to the other chosen randomly with equal probability. Subsequently, each of the new halves is treated as two separate slabs and sub-divide each into two halves and transfer f_1 fraction of water among adjacent halves again chosen randomly with equal probability. This process continues multiple times to produce

fractal-like LWP variation along the x dimension. The nth fractional mass is specified by

$$f_n = f_0 c^n \tag{6.1}$$

where scaling parameter c and the variance parameter f_0 are set to be $2^{-1/3}$ and 0.5, respectively, to follow LWP distribution characteristics of a stratocumulus cloud (Cahalan et al., 1994). The mean LWP of the cloud was set to be 90 g/m^2. The effective radius and effective variance are 12 μm and 0.05 respectively. The horizontal resolution, i.e., the final grid size, along the x-axis is 10 m. Periodical boundary conditions are used in RT simulations. Note that the Mie calculations for this study are computed using Wiscombe (Wiscombe, 1979) Mie code and the well-known modified gamma distribution (Hansen and Travis, 1974) is assumed as the droplet size distribution in the bulk optical property computations.

Both 3D and 1D radiative transfer simulations for this study were performed using the Multiple-Scaling-based Cloudy Atmospheric Radiative Transfer (MSCART) model (Emde et al., 2018; Wang et al., 2017a). When the medium has a highly forward-peaked scattering phase function such as in cloud droplets and ice crystals, the variance of the simulated radiances in a Monte-Carlo method increases dramatically which costs large amounts of photons and thereby computational time to reach sufficient accuracy. Many previous RT simulation models have used either the phase function forward truncation method or the target directional importance sampling technique for radiance variance reduction. In the phase function forward truncation method, the photons that are scattered into the highly forward-peak direction are

forcefully considered as not being scattered at all. Then to compensate the truncated forward-peak, the single scattering albedo and the optical thickness of the medium are adjusted (Hu et al., 2000; Wiscombe, 1977; Nakajima and Asano, 1977). The target directional importance sampling technique computes the probability that a photon will be scattered towards the sensor at each scattering event while tracing the photon path to improve the efficiency (Buras and Mayer, 2011) Different from these previous studies, MSCART uses a novel hybrid scattering-order dependent variance reduction method which combines the phase function forward truncation technique together with the target directional importance sampling technique at each scattering order to maintain the optimal balance between numerical efficiency and accuracy.

6.3 Illuminating and shadowing effects

As aforementioned, IPA is one among the two fundamental assumptions of the 1D RT theory. However, when the cloud field has significant horizontal variability, either optically or geometrically, the net horizontal transport of photon can lead to the violation of IPA and thereby 3D RT effects. The so-called illuminating and shadowing effects are classic examples of such 3D RT effects. Here, we use idealized "step-cloud example to illustrate 3D RT effects and their impacts on the bi-spectral retrievals of COT and CER. As shown in Figure 6.1 (a) the "step cloud case, If the cloud is illuminated from the left-hand side at solar zenith angle (SZA) = 60°, the resultant simulated reflectances for both VNIR (visible and near-infrared) and SWIR

(shortwave infrared) bands are shown in Figure 6.1(b). The solid and dashed red lines are VNIR and SWIR reflectances respectively based on 1D radiative transfer simulations. The solid and dashed blue lines are VNIR and SWIR reflectances respectively based on 3D radiative transfer simulations. (Note that, the same color convention, which is red for 1D and blue for 3D RT-based results, is adopted in all figures).

As a result of IPA, the simulated cloud reflectance based on the 1D RT theory is simply a step function that follows the variation of COT. Interestingly, the cloud reflectances simulated based on the 3D RT theory are quite different, especially at the transition regions (e.g., from thin to thick or from thick to thin). At the illuminating side (i.e., 24 km), the cloud reflectances simulated based on 3D RT theory (hereafter referred to as 3D cloud reflectance for short) are significantly larger compared to their 1D counterparts. This is known as the illuminating effect which is caused by the photon transfer from the optically thin region to the optically thick region due to the multiple scattering. In contrast, at the shadowing edge, (i.e., 1012 km) the photon leaking from optically thick region to optically thin region causes a significant drop in the 3D reflectances compared to the 1D reflectances which is called the shadowing effect. In general, at the illuminating side, both VNIR and SWIR reflectances increase due to 3D RT effects and both decrease at the shadowing side.

Figure 6.1(c) illustrates how these 3D RT effects influence the bi-spectral retrieval in Nakajima-King LUT (Look-up table) space (Nakajima and King, 1990). Since the 1D cloud reflectances are step functions, they simply reduce to two points

in the LUT space. One point corresponding to the thin part of the step cloud is located at the lower left corner close to the origin of the LUT. The other corresponding to the thick part is located at the center of the LUT with VNIR and SWIR reflectance around 0.39 and 0.25, respectively. In case of the illuminating effect, the 3D cloud reflectances are larger and therefore located to the upper right of the 1D cloud reflectances in the LUT space. As a result of the shadowing effect, the 3D cloud reflectances are smaller and therefore located to the lower left of the 1D cloud reflectances in the LUT space. Therefore, as shown in Figure 6.1(d), the illuminating effects cause positive biases in COT retrievals and negative biases in CER retrievals while the shadowing effects cause negative biases in COT and positive biases in the CER.

Figure 6.2 (a) shows the simulated VNIR polarized reflectance (i.e., $R_Q = \pi Q/(\mu_0 F_0)$ where Q is the second component of the reflected Stoke Vector, $\mu_0 F_0$ is the incident flux) for the step cloud case. The solid blue line is VNIR polarized reflectance from 3D RT simulations and the solid red line is VNIR polarized reflectance from 1D RT simulations. For the same band, polarized reflectance has sharp illuminating and shadowing effects compared to those in the total reflectances in Figure 6.1(b). It is important to note that, even though the magnitude of the polarized reflectance vary at the illuminating (x =2.11 km) and shadowing (x = 11.95 km) edges compared to the middle of the cloud (x = 6.01), as shown in Figure 6.2(b), the angular pattern remains mostly unchanged. Note that different from the bi-spectral CER retrievals which are based on the magnitudes of the total reflectances, the polarimetric CER retrievals rely upon the angular pattern of the

polarized reflectances. Hence the magnitude change in the polarized reflectance due to the 3D effects has a negligible influence on the underlying CER retrievals. This feature is evident in CER retrievals shown in Figure 6.2(a), where the polarimetric retrievals of CER (r_e^{pol}) from both 1D and 3D RT simulations (dotted red and dashed blue line respectively) are almost identical regardless the illuminating and shadowing effects. After further investigations, we exploit this interesting advantage of the polarimetric retrieval technique for our maximum 1D reflectance method in Section 6.5.

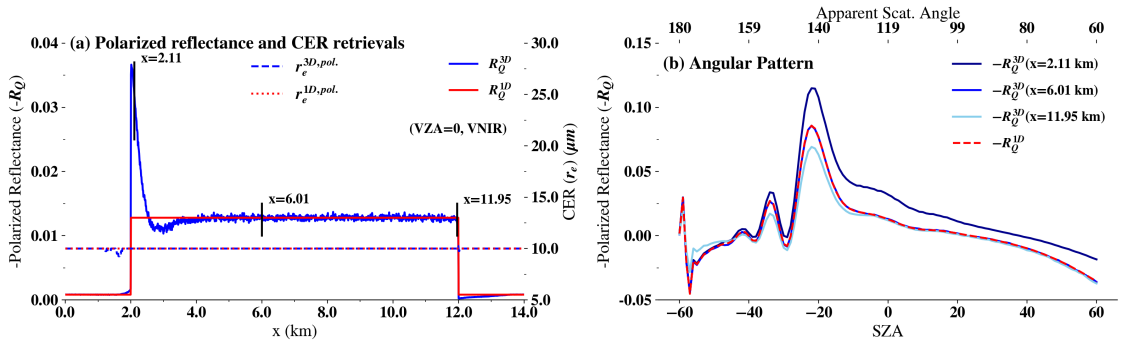

Figure 6.2: (a) Simulated polarized reflectances for the step cloud case in Figure 6.1(a) based on 3D and 1D RT simulations (blue and red solid lines respectively) at VZA = 0 for VNIR band. Corresponding polarimetric CER retrievals are shown in blue dashed and red dotted lines based on 3D and 1D RT-based polarized reflectance respectively. (b) Angular pattern of the polarized reflectance at the selected locations (x = 2.11, 6.01 and 11.95 km) in (a).

6.4 3D Effect impact factor

The step cloud case is useful for introducing main concepts and revealing the underlying physics, but it is too simple and ideal. To establish and test our method in more realistic conditions, in this section we will use the well-known fractal cloud field to further illustrate the illuminating and shadowing, and also to explain our maximum 1D reflectance method for 3D RT effect detection and correction.

Figure 6.3(b) shows 1D and 3D SWIR band (i.e., 2.13 μm) reflectances simulated using the MSCART model in red and blue respectively for the nadir viewing geometry. The Sun is to the left at SZA = 60°. One can see from the figure, whenever there is an abrupt variation in COT, e.g., around 11 km and 21 km, the illuminating and shadowing effects are clearly observable. To quantify how strong the 3D effect, we define a quantity called 3D effect impact factor as follows

$$f_{R_\lambda} = \frac{R_\lambda^{3D} - R_\lambda^{1D}}{R_\lambda^{1D}} \; ; \; \lambda = \text{SWIR,VNIR} \tag{6.2}$$

Where R_λ^{3D} and R_λ^{1D} are the 3D and 1D reflectance, respectively. The SWIR 3D effect impact factor ($f_{R_{SWIR}}$) derived based on the simulated SWIR reflectances (R_{SWIR}^{3D},R_{SWIR}^{1D}) of the fractal cloud case for SZA = 60° is shown in the black curve in Figure 6.3(c). Clearly, the positive 3D effect impact factors ($f_\lambda > 0$) indicate the illuminating effects while the negative values ($f_\lambda < 0$) indicate the shadowing effects. In other words, the sign and magnitude of the f_{R_λ} can be used to detect and quantify the illuminating and shadowing effects. Moreover, if the f_λ is known for a observed 3D cloud reflectance, Equation 6.2 can be used to obtain corresponding unbiased

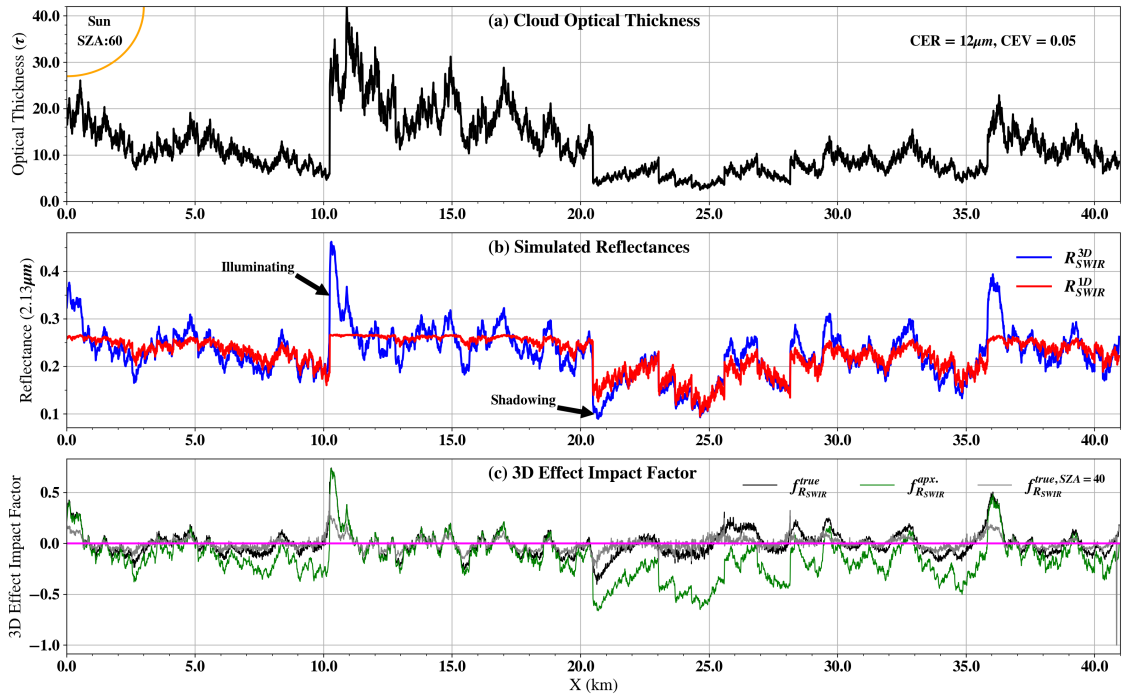

Figure 6.3: The cloud optical thickness variation of the fractal cloud generated from the bounded cascade model. The mean LWP, CER and CEV are $90g/m^2$, $12\mu m$ and 0.05 respectively. (b) The simulated SWIR reflectances from 1D (red) and 3D (blue) RT-based simulations at $SZA = 60^o$ and $VZA = 0^o$. (c) The actual (black) and approximated (green) 3D effect impact factors of the SWIR band. The grey line is the actual 3D effect impact factor of the SWIR band for $SZA = 40^o$.

R_λ^{1D} ($R_\lambda^{1D} = R_\lambda^{3D}/(1 + f_\lambda)$). The grey curve in Figure 6.3(c) is the 3D effect impact factor for SZA = 40°. While acknowledging the necessity of further investigations based on more realistic cloud fields in the future studies, here we can qualitatively observe that the strength of 3D effects (both illuminating and shadowing) decreases as SZA decreases.

6.5 Maximum 1D reflectance method to detect illuminating effect

As mentioned in the last section, the sign and the magnitude of the f_{R_λ} can be used to detect the 3D effect and assess its strength. Note that the observed cloud reflectance R_λ^{3D} is inherently a result of 3D radiative transfer. Therefore, the key problem is how to estimate the 1D cloud reflectance R_λ^{1D}. Unfortunately, it is an extremely challenging task to obtain the R_λ^{1D} for all pixels under all circumstances. And, it is not our objective. Instead, our method focuses on the pixels that are strongly influenced by the illuminating effect.

The step-by-step procedure for implementing the maximum 1D reflectance method to detect and correct strong illuminating effects as follows. Figure 6.6 shows the flowchart. The detection process is shown in solid lines and the correction process is shown in dashed lines. The detection and correction processes are explained in detail in Section 6.5 and Section 6.6 respectively.

1. Use the r_e^{pol} retrieved from the polarized reflectance as the true CER.

2. Select the corresponding SWIR-VNIR theoretical relationship ($g_{LUT}^{r_e=r_e^{pol}}$) for r_e^{pol} from the LUT and select a VNIR reflectance threshold (R_{VNIR}^*) such that the gradient of the SWIR-VNIR theoretical relationship $[\frac{dR_{SWIR}}{dR_{VNIR}}]r_e = r_e^{pol}$ is smaller than 0.01 (ideally approaches to zero). Subsequently obtain the maximum possible SWIR reflectance, $R_{SWIR}^{1D,max}(r_e^{pol})$ and assume $R_{SWIR}^{1D,max}$ as the R_{SWIR}^{1D} for all the observations that $R_{VNIR}^{3D} > R_{VNIR}^*$ (Eq. 3).

3. Use Equation 6.2 and 6.3 to get the 3D effect impact factor of the SWIR band,

$f^{apx}_{R_{SWIR}}$.

4. Assume both VNIR and SWIR 3D effect impact factors are approximately equal (Equation 6.4).

5. Use $f^{apx}_{R_{SWIR}}$ and $f^{apx}_{R_{VNIR}}$ to correct both SWIR and VNIR reflectances respectively for all the observations that $R^{3D}_{VNIR} > R^{*}_{VNIR}$ (By using, $R^{1D}_{\lambda} = R^{3D}_{\lambda}/(1 + f^{apx}_{R_{\lambda}})$).

6. Use the corrected reflectances to do bi-spectral retrievals.

We argue that, if the observed R^{3D}_{λ} for a target pixel is even larger than the maximum value of cloud reflectance that is allowed by the 1D RT theory, then this pixel must be influenced by the illuminating effect. The basic idea of our method can be readily appreciated from Figure 6.3(b). Focusing on the R^{1D}_{SWIR} (red line) in the figure, one can notice that no matter how optically thick the cloud is, the R^{1D}_{SWIR} never exceeds certain maximum value, i.e., around 0.27 in this case (see around $10 \sim 20$ km). This maximum value $R^{1D,max}_{SWIR}(r_e)$ is a result of the absorption of the SWIR band and it is mainly a function of CER (i.e., the larger the CER the smaller the $R^{1D,max}_{SWIR}$). Therefore, if the CER is known, then the maximum 1D reflectance can be estimated and used to detect the strong illuminating effect.

However, how to estimate the CER of the target cloud still remains as a challenge. As shown in the step cloud case as well as many previous studies, the CER retrieval from the bi-spectral method can be significantly biased due to the 3D effect and therefore cannot be used. This is where the polarimetric retrievals

becomes useful. As explained in Section 6.3 with the aid of Figure 6.2(b), although the magnitude of the polarimetric cloud reflectance is influenced by 3D effect, the angular features of the cloud bow remain unchanged. As a result, the retrieved CER from the multi-angular polarimetric observation is minimally affected by the 3D effects and, hence provides the basis to estimate the maximum 1D reflectance. In the rest of this section and the proceeding section, we will provide a step-by-step explanation of our method. The stepwise procedure is listed at the begining of this section and a flowchart for practical implementation is provided in Figure 6.6.

The first step of the maximum 1D reflectance method is to estimate the CER of the target cloud field. Figure 6.4 (a) shows the simulated polarized reflectances for the fractal cloud case in Figure 6.3 (a) based on 1D (solid red) and 3D (solid blue) RT simulations for the VNIR band at $VZA = 0$. We can clearly see the illuminating and shadowing effects near $x \sim 11$km and $x \sim 21$km respectively similar to the simulated total reflectance in Figure 6.3(b). Figure 6.4 (b) shows the CER retrievals from both bi-spectral (blue dashed line) and polarimetric (blue solid line) retrieval techniques based on 3D RT simulations (without applying any corrections). We can clearly see, even though the bi-spectral CER retrievals have strong biases due to the 3D RT effects, the polarimetric retrievals are mostly around 12 μm within fractions of a micron. Usually, in practice, the polarized reflectance has to be averaged over a coarser spatial domain to cover complete angular space of the cloud bow region in order to implement polarimetric retrieval technique. By taking this into consideration, if we use the domain averaged polarized reflectance to do the retrievals, we get $CER = 12.00$ μm, which is same as the assumed value

in the process of fractal cloud generation. In summary, since the polarimetric CER retrievals are minimally affected by 3D RT effects, we can use the retrieved r_e^{pol} based on the polarized reflectance to approximate the CER of the target cloud.

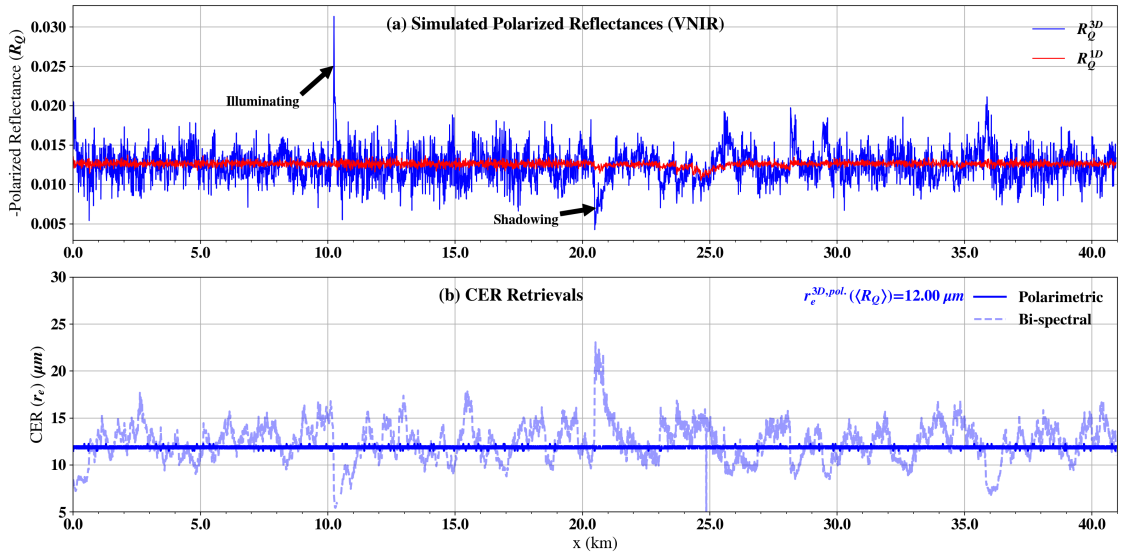

Figure 6.4: (a) Simulated 1D (solid red) and 3D (solid blue) polarized reflectances for the fractal cloud case in Figure 6.3(a). (b) CER retrievals from bi-spectral (dashed blue) and polarimetric (solid blue) retrieval techniques based on 3D RT simulations.

After obtaining the r_e^{pol} from the polarimetric observations, the next key step is to determine the maximum 1D reflectance ($R_{SWIR}^{1D,max}(r_e)$) correspond to the retrieved CER. Note again that, this is the maximum cloud reflectance in the SWIR band allowed by the 1D RT theory. Therefore, any observed cloud reflectance that is larger than this $R_{SWIR}^{1D,max}(r_e)$ is likely affected by the illuminating effect. Figure 6.5(a) shows the Nakajima-King (NK) LUT for $SZA = 60°$ and $VZA = 0°$, in which each solid and dashed isolines correspond to a constant CER ($g_{LUT}^{r_e=r_e^*}$) and a constant COT ($g_{LUT}^{\tau=\tau^*}$, respectively. For a given CER, as the cloud becomes optically thicker with

increasing COT, the SWIR reflectance first increases but eventually reaches to an asymptotic maximum value, i.e., $R_{SWIR}^{1D,max}(r_e)$. The determination of this saturated SWIR reflectance $R_{SWIR}^{1D,max}(r_e)$ from the observed quantities is not trivial and can be done as follows. Qualitatively, one can see in Figure 6.5 (a), for a given CER, R_{SWIR}^{1D} reaches $R_{SWIR}^{1D,max}$ when R_{VNIR}^{1D} becomes large enough. Therefore, when the CER is known from the polarimetric retrievals, $R_{SWIR}^{1D,max}$ can be deduced by using $g_{LUT}^{r_e=r_e^*}$ isoline from the appropriate LUT. To this end, we can define a SWIR-saturated VNIR reflectance threshold (R_{VNIR}^*) based on the slope of the constant CER curve, $[\frac{dR_{SWIR}}{dR_{VNIR}}]^{r_e=r_e^{pol}}$ such that the slope approaches to zero (i.e., R_{SWIR}^{1D} approaches to $R_{SWIR}^{1D,max}$) when $R_{VNIR}^{3D} > R_{VNIR}^*$. Figure 6.5(b) shows the gradients of the constant CER curves for three cloud effective radii. The green dashed line, black solid line, and magenta dashed line are for CER= 4.0, 12.0 and 25.0 μm, respectively. As CER increases the gradient of the constant CER curve reaches to zero faster (at a lower VNIR reflectance). Hence the VNIR filtering threshold (R_{VNIR}^*) would be smaller for larger CER (for a given geometry and CEV). In practice the threshold value R_{VNIR}^* can be precomputed based on the LUT. The underlying physics is simple: if the observed R_{VNIR}^{3D} is larger than R_{VNIR}^* then the cloud optical thickness is large enough to saturate the SWIR reflectance, hence the R_{SWIR}^{1D} should approach to $R_{SWIR}^{1D,max}$ i.e.,

$$R_{SWIR}^{1D} \approx R_{SWIR}^{1D,max}(r_e^{pol.})\ ;\ when\ R_{VNIR}^{3D} > R_{VNIR}^* \tag{6.3}$$

By substituting Equation 6.3 into Equation 6.2, we can obtain an approximate 3D effect impact factor $f_{SWIR}^{apx} = (R_{SWIR}^{3D} - R_{SWIR}^{1D,max})/R_{SWIR}^{1D,max}$. Evidently, a posi-

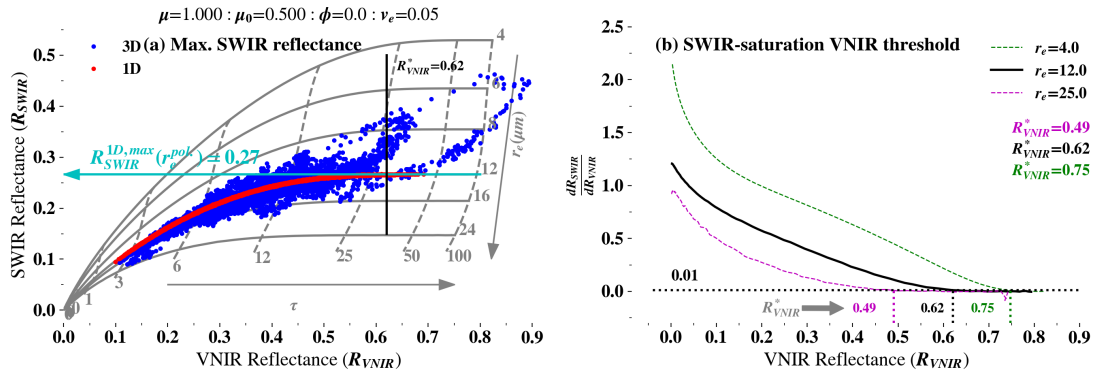

Figure 6.5: An illustration of implementing the maximum 1D reflectance method for the fractal cloud in Figure 6.3(a). (a) The theoretical relationships between VNIR and SWIR reflectances for various COT and CER (bi-spectral LUT space) are shown in grey for $SZA = 60^o$ and $VZA = 0^o$. The red and blue data points are based on 1D and 3D RT simulations respectively for the fractal cloud. Cyan arrow is the maximum possible SWIR reflectance for $CER = 12\mu m$. (b) The variations of the gradients of the constant CER curves for different cloud effective radii. The black horizontal line in (a) is the VNIR threshold based on the gradient of $CER = 12\mu m$ curve (black curve).

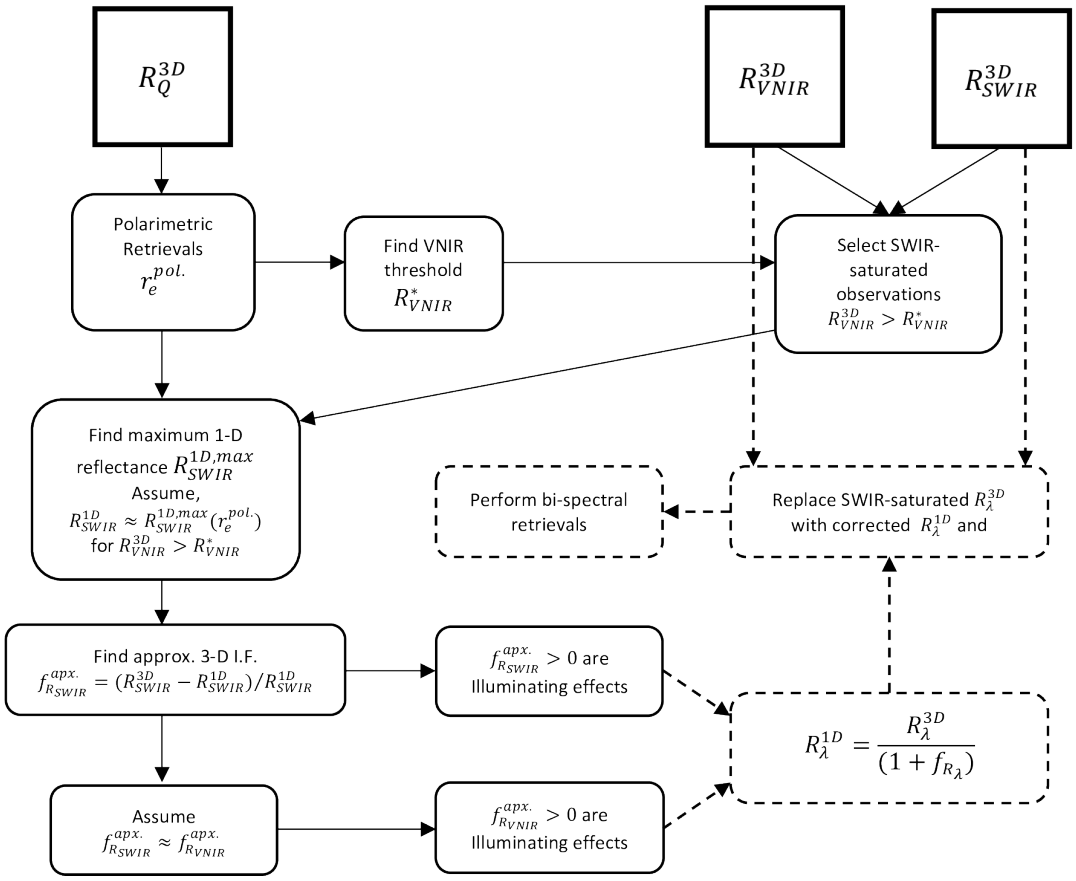

Figure 6.6: Flowchart for the practical implementation of the maximum 1D reflectance method. The detection procedure is shown in solid lines and the COT correction process is shown in dashed lines.

tive f^{apx}_{SWIR} indicates illuminating effect. In summary, on the basis of observed and retrieved quantities, i.e., r^{pol}_e , R^{3D}_{VNIR} and R^{3D}_{SWIR} we have developed an algorithm to detect the SWIR-saturated observations that are influenced by the illuminating effect. The performance of this detection algorithm for the fractal cloud case is shown in Figure 6.7. As shown in Figure 6.7(a), for the SWIR-saturated pixels (i.e., the pixels where $R^{3D}_{VNIR} > R^{*}_{VNIR}$), $f^{apx}_{R_{SWIR}}$ and the true 3D effect impact factor ($f^{true}_{R_{SWIR}}$) are almost identical with a correlation coefficient $R^2 \sim 1$, which indicates that our method works extremely well (100% sensitivity with 99.5% accuracy) for detecting the SWIR-saturated pixels (black circles) influenced by the illuminating effect. For comparison purpose, we loosen the requirement for $R^{3D}_{VNIR} > R^{*}_{VNIR}$ and compute the f^{apx}_{SWIR} for all pixels. As expected, $f^{apx}_{R_{SWIR}}$ is systematically smaller than $f^{true}_{R_{SWIR}}$ when considering all pixels. Nevertheless, it is interesting and important to note that when $f^{apx}_{R_{SWIR}}$ is positive the corresponding $f^{true}_{R_{SWIR}}$ is always positive, but the opposite is not true. In other words, a positive $f^{apx}_{R_{SWIR}}$ can be used as a conservative filter (43% sensitivity with 100% accuracy) for detecting the illuminating effect although it has a high missing rate.

So far, our detection algorithm has been focused the SWIR band. An important question remains to be addressed: Does it also work for the VNIR band? To address this question, we compare $f^{apx}_{R_{SWIR}}$ with $f^{true}_{R_{VNIR}}$ in Figure 6.7(b). It is encouraging to see that for 98% of SWIR-saturated pixels (i.e. the pixels where $R^{3D}_{VNIR} > R^{*}_{VNIR}$) (black circles), a positive $f^{apx}_{R_{SWIR}}$ corresponds to a positive $f^{true}_{R_{VNIR}}$. The false detection rate (i.e., a positive $f^{apx}_{R_{SWIR}}$ corresponding to a negative $f^{true}_{R_{VNIR}}$) is only 2%. Moreover, 97% of SWIR-saturated illuminating effects are sensitive to

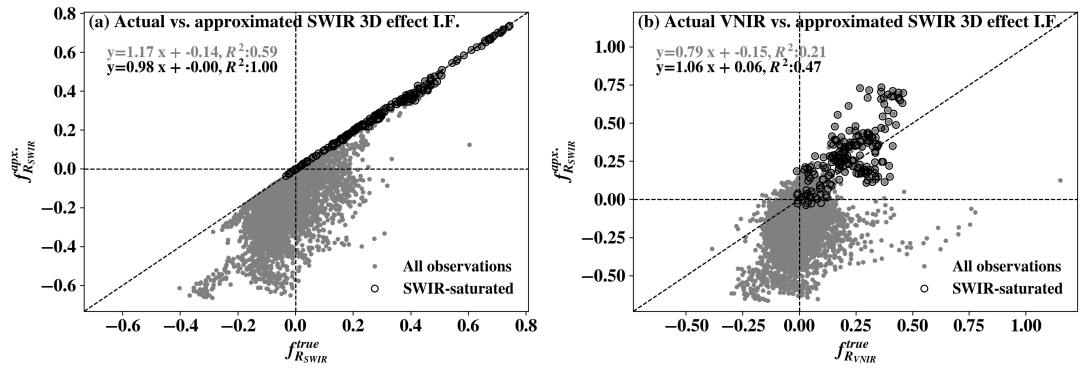

Figure 6.7: The correlation of the approximated 3D effect impact factor of SWIR vs. the actual 3D effect impact factors of the (a)VNIR and (b) SWIR bands for all (grey points) and SWIR-saturated (i.e. pixels such that) (black circles) pixels.

the detections. This result, together with the close correlation between $f^{apx}_{R_{SWIR}}$ and $f^{true}_{R_{SWIR}}$ in Figure 6.7(a), indicates that for pixels with $R^{3D}_{VNIR} > R^{*}_{VNIR}$ an illuminating effect in the SWIR band also implies an illuminating effect in the VNIR band, and they both can be detected using $f^{apx}_{R_{SWIR}}$. However, if we loosen the constraint on $R^{3D}_{VNIR} > R^{*}_{VNIR}$ (gray points in Figure 6.7 (b)), 21% of positive $f^{apx}_{R_{SWIR}}$ (i.e., indicative of illuminating effect) would correspond to a negative $f^{true}_{R_{VNIR}}$ (i.e., truly a shadowing effect). In other words, without screening out the SWIR-saturated observations, a simple filter of positive $f^{apx}_{R_{SWIR}}$ for all pixels can lead to 21% false detection. This result indicates that some pixels that influenced by the illuminating effect in the SWIR band (i.e., $R^{3D}_{SWIR} > R^{1D}_{SWIR}$) are influenced by the opposite shadowing effect in the VNIR band (i.e., $R^{3D}_{VNIR} < R^{1D}_{VNIR}$).

6.6 Explore the possibility of COT bias correction

In the rest of this section, we will try to go one step further and explore the possibility of correcting the COT retrieval bias in the identified pixels. For the reasons discussed in the last section, here we only focus on the SWIR-saturated pixels with $R^{3D}_{VNIR} > R^{*}_{VNIR}$. Assuming that the CER is already known from the polarimetric retrieval, the unbiased COT can be readily estimated from the LUT if the R^{1D}_{VNIR} is known. It follows from Equation 6.2 that $R^{1D}_{VNIR} = R^{3D}_{VNIR}/(1 + f_{R_{VNIR}})$. Therefore, the key problem is how to estimate the 3D effect impact factor for the VNIR band $f_{R_{VNIR}}$. Figure 6.7 (b) shows the correlation between the $f^{apx}_{R_{SWIR}}$ and the $f^{true}_{R_{VNIR}}$. As mentioned in the last section, even though the correlation between $f^{apx}_{R_{SWIR}}$ and $f^{true}_{R_{VNIR}}$ for SWIR-saturated observations (black circles) is sufficient to detect VNIR illuminating effects (97% sensitivity with 98% accuracy), $f^{apx}_{R_{SWIR}}$ is not perfectly accurate to approximate and $f^{true}_{R_{VNIR}}$ but follows the correct trend with $R^2 \sim 0.47$. While acknowledging the fact that further investigations are essential to get an accurate relationship between $f^{apx}_{R_{SWIR}}$ and $f^{true}_{R_{VNIR}}$, we approximate that the VNIR and SWIR 3D effect impact factors are equal to each other based on the trend in Figure 6.7(b) SWIR-saturated pixels (black circles), i.e.,

$$f_{R^{apx.}_{VNIR}} \approx f_{R^{apx.}_{SWIR}} \tag{6.4}$$

After the VNIR 3D effect impact factor has been approximated, we can correct SWIR-saturated 3D reflectances of the VNIR band (the pixels where $R^{3D}_{VNIR} > R^{*}_{VNIR}$) for 3D effects using Equation 6.2 ($R^{1D}_{VNIR} = R^{3D}_{VNIR}/(1 + f^{apx}_{R_{VNIR}})$).

Finally, both VNIR and SWIR corrected 3D reflectances can be provided as input reflectances to the bi-spectral retrievals to get the COT retrievals that are corrected for SWIR-saturated illumination effects.

Figure 6.8 summarizes the retrieved COT biases. The x-axis is the bias of the retrieved optical thickness relative to the unbiased retrievals (the retrievals based on 1D RT-based reflectances) and the y-axis is the probability density function (PDF). The grey line is the retrieved COT biases before the 3D correction. There are strong positive COT biases even greater than COT = 20 with a mean bias of 1.01. For demonstrational purpose, the dotted line in the figure shows the COT biases of the retrievals after implementing the 3D correction to all the observations without limiting to the SWIR-saturated observations. In other words, all grey points in Figure 6.7 (a) and (b) have been considered to do the corrections in Figure 6.8 dotted line. The strong COT biases greater than 20 are corrected but the mean bias becomes 1.81 which is 0.80 greater than the mean bias without any corrections. This is because both $f^{true}_{R_{SWIR}}$ vs. $f^{apx}_{R_{SWIR}}$ and $f^{true}_{R_{VNIR}}$ vs. $f^{apx}_{R_{SWIR}}$ relationships are only reasonable for the SWIR reflectances that have been saturated to reach to the asymptotic maximum ($R^{1D,max}_{SWIR}$). Therefore, in the maximum 1D reflectance method, we limit the corrections to the SWIR-saturated illuminated pixels (the pixels where $R^{3D}_{VNIR} > R^{*}_{VNIR}$). The black line in Figure 6.8 shows the retrieved COT biases after only correcting the 3D correction for SWIR-saturated observations. The strong illuminating effects of COT retrievals have been detected and corrected with a reasonable accuracy, but the remaining shadowing effects cause a negative bias which will be remained for future studies.

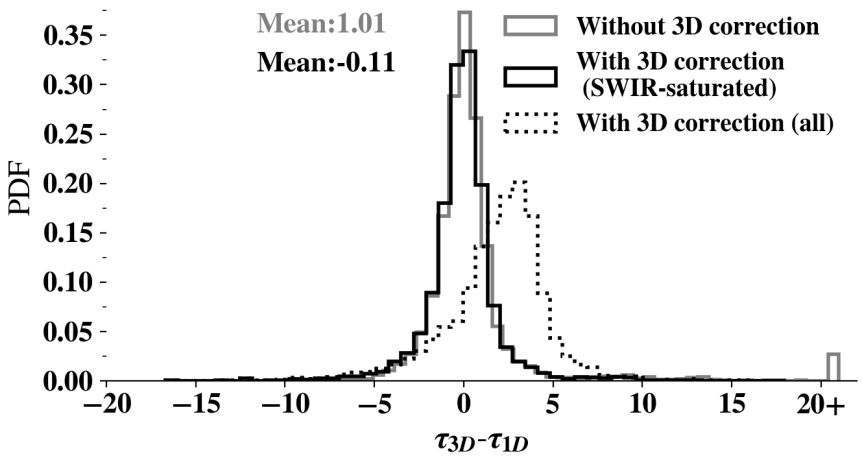

Figure 6.8: The summary of COT biases without (grey) and with (black) the 3D correction based on maximum 1D reflectance. The x-axis is the bias of retrieved optical thickness relative to the unbiased retrievals (the retrievals based on 1D RT-based reflectances) and the y-axis is the corresponding probability density function (PDF). Dotted line is the COT bias when the SWIR-saturated constrain has been removed.

6.7 Requirements on instrument

To implement the maximum 1D reflectance method in a realistic observational scenario, it is required both radiometric and multiangle polarimetric image of the same cloud target. Despite the gap occurred in the spaceborne polarimetric observations due to the failure of the Glory mission (Mishchenko et al., 2007), one of the primary instrument of it, Research Scanning Polarimeter (RSP) provides valuable field measurements of clouds that have been proven to be useful in many studies related to the cloud microphysical retrievals (Alexandrov et al., 2012, 2013; NASEM, 2018).

RSP measures both total and polarimetric reflectances in 9 spectral bands, 6 VNIR bands and 3 SWIR bands. More importantly it has exceptional angular resolution with 0.8-degree angular intervals within 60 degrees in both forward and backward directions (Alexandrov et al., 2012) which provide sufficient angular span and resolution to resolve the cloud bow features of the polarized reflectance while providing the radiometric image of the same cloud target. Hence RSP measurements will be a viable observational platform to further investigate the maximum 1D reflectance method.

Moreover, ESAS (Earth Science and Applications from Space) decadal survey (NASEM, 2018) has prioritized the necessity of a multichannel-multiangle polarization imaging radiometer for future climate and air quality studies which will be an encouragement for the further improvements of the maximum 1D reflectance method towards observational implementations.

6.8 Discussion and Conclusions

Many studies have been conducted to investigate the 3D RT effects in passive cloud property retrievals. However, relatively fewer attempts have been made to do pixel-level detections and corrections. From this study, we introduce a novel method called the maximum 1D reflectance method to detect and quantify the 3D RT effects in the bi-spectral cloud property retrievals. The main objective of this study is to explain the theoretical basis and investigate the feasibility of the detection and correction framework based on strictly hypothetical simulated 1D cloud fields. Rigorous investigations are yet to be done in the future based on more realistic cloud fields (e.g., synthetic cloud fields from large-eddy simulation) and observations (e.g., airborne RSP).

For a given CER, the SWIR reflectance reaches to an asymptotic physical maximum as COT increases. In the maximum 1D reflectance method, we use this asymptotic physical maximum limit of the SWIR reflectance as a proxy to 1D SWIR reflectance to detect the 3D RT effects. Furthermore, we explore the possibility of correcting cloud reflectances, and consequently the COT retrievals for 3D RT effects. Since the asymptotic maximum value where the SWIR reflectance saturates is chosen as the 1D reflectance, the corrections that have been made are only accurate for SWIR-saturated observations (pixels). Therefore, a VNIR filtering threshold (R^{*}_{VNIR}) is introduced to select SWIR-saturated observations and the corrections have only been applied to those cases where 3D-VNIR reflectance (R^{3D}_{VNIR}) is greater than the approximated VNIR reflectance (R^{*}_{VNIR}).

As shown in Figure 6.7(a) and (b) and explained in Section 6.5, the maximum 1D reflectance method is capable of detecting illuminating effects with a remarkable accuracy. For the SWIR-saturated pixels (the pixels where $R^{3D}_{VNIR} > R^{*}_{VNIR}$), maximum 1D reflectance method has a 100% sensitivity with a 99.5% accuracy for the illuminating effects in the SWIR band and a 97% sensitivity with a 98% accuracy for the illuminating effects in the VNIR band. This is because strong illuminating effects are usually associated with large reflectances which has a high likelihood to cause saturation in the SWIR band. In summary, the maximum 1D reflectance method can be used to detect illuminating effects in the SWIR-saturated observations. Although the method only sensitive to 43% and 31% of total illumination effects in the SWIR and VNIR bands respectively, it still has a 99% accuracy in the SWIR band and 79% accuracy in the VNIR band illumination effect detection. Hence, maximum 1D reflectance method could perform as a conservative filter to detect illuminating effects even without constraining to the SWIR-saturated observations, especially in the SWIR band.

Corresponding COT biases before and after implementing the maximum 1D reflectance method are summarized in Figure 6.8. In both with and without SWIR-saturation constraint (dotted and solid black lines respectively), the strong positive COT biases due to the illuminating effects have been corrected. However, R^{1D}_{SWIR} can be approximated by $R^{1D,max}_{SWIR}(r^{pol}_{e})$ only if the SWIR reflectance being saturated and reached to its asymptotic maximum. Hence, as shown in the dotted line, although the high COT biases have been corrected by the 3D corrections, the correction that have been applied to the observations where the SWIR reflectance has not been sat-

urated (i.e. $R^{3D}_{VNIR} < R^{*}_{VNIR}$) cause high mean bias. Therefore, in the maximum 1D reflectance method, we only apply the corrections to the SWIR-saturated pixels (i.e. $R^{3D}_{VNIR} > R^{*}_{VNIR}$ pixels). As shown in the solid black line in Figure 6.8, by applying correction only to the SWIR-saturated pixels, maximum 1D reflectance method can correct the high optical thickness biases in the bi-spectral COT retrievals.

In summary, we introduce a novel method to detect and quantify the 3D radiative effects in passive cloud property retrievals. In a realistic observational scenario, both polarimetric and radiometric images of the same cloud target will be needed to implement this method. This study only uses strictly hypothetical 1D cloud fields to explain the main concept and the theoretical basis of the maximum 1D reflectance method. Rigorous case studies base on more realistic simulated clouds fields and actual observations are yet to be done in the future.

Appendix A: Bias statistic definitions

If y_i and x_i are retrieved and reference cloud properties of the i^{th} pixel respectively, retrieval bias of the i^{th} pixel ϵ_i is defined as follows,

$$\epsilon_i = y_i - x_i \tag{A.1}$$

Subsequently, following statistics are defined.

$$\begin{aligned}
\text{Mean bias } (\mu) &= \frac{\sum \epsilon_i}{N} \\
\text{Std. } (\sigma) &= \sqrt{\frac{\sum(\epsilon_i - \mu)^2}{N}} \\
\text{Skewness} &= \frac{3(\mu - median)}{\sigma} \\
\text{Mean absolute bias } (\mu^*) &= \frac{\sum(|\epsilon_i|)}{N} \\
\text{Absolute std. } (\sigma^*) &= \sqrt{\frac{\sum(|\epsilon_i| - \mu^*)^2}{N}} \\
\text{root-mean-square (rms)} &= \sqrt{\frac{\epsilon_i^2}{N}}
\end{aligned} \tag{A.2}$$

When β_1 and β_0 are the coefficient of predicted regression line and $\beta_1^{std.}$ is the standard deviation of β_1, the form of predicted regression line can be written as follows,

$$y_i = f(x_i) = (\beta_1 \pm \beta_1^{std})x_i + \beta_0 \tag{A.3}$$

r-value (correlation coefficient) is computed as follows,

$$r_{xy} = \frac{\sum_{i=1}^{n}(x_i - \bar{x})(y_i - \bar{y})}{\sqrt{\sum_{i=1}^{n}(x_i - \bar{x})^2}\sqrt{\sum_{i=1}^{n}(y_i - \bar{y})^2}} \tag{A.4}$$

Bibliography

Ackerman, A. S., Kirkpatrick, M. P., Stevens, D. E., and Toon, O. B. (2004). The impact of humidity above stratiform clouds on indirect aerosol climate forcing. *Nature*, 432(7020):1014–1017.

Adebiyi, A. A. and Zuidema, P. (2016). The role of the southern African easterly jet in modifying the southeast Atlantic aerosol and cloud environments. *Quarterly Journal of the Royal Meteorological Society*, 142(697):1574–1589.

Alexandrov, M. D., Cairns, B., Emde, C., Ackerman, A. S., Ottaviani, M., and Wasilewski, A. P. (2016). Derivation of cumulus cloud dimensions and shape from the airborne measurements by the Research Scanning Polarimeter. *Remote Sensing of Environment*, 177:144–152.

Alexandrov, M. D., Cairns, B., Emde, C., Ackerman, A. S., and van Diedenhoven, B. (2012). Accuracy assessments of cloud droplet size retrievals from polarized reflectance measurements by the research scanning polarimeter. *Remote Sensing of Environment*, 125:92–111.

Alexandrov, M. D., Cairns, B., Mishchenko, M. I., Ackerman, A. S., and Emde, C. (2013). Characterization of cloud microphysical parameters using airborne measurements by the research scanning polarimeter. In *AIP Conference Proceedings*.

Alexandrov, M. D., Miller, D. J., Rajapakshe, C., Fridlind, A., van Diedenhoven, B., Cairns, B., Ackerman, A. S., and Zhang, Z. (2020). Vertical profiles of droplet size distributions derived from cloud-side observations by the research scanning polarimeter: Tests on simulated data. *Atmospheric Research*, 239.

Bréon, F. M. and Doutriaux-boucher, M. (2005). A Comparison of Cloud Droplet Radii Measured From Space. 43(8):1796–1805.

Bréon, F. M. and Goloub, P. (1998). Cloud droplet effective radius from spaceborne polarization measurements. 25(11):1879–1882.

Buras, R. and Mayer, B. (2011). Efficient unbiased variance reduction techniques for Monte Carlo simulations of radiative transfer in cloudy atmospheres: The solution. *Journal of Quantitative Spectroscopy and Radiative Transfer*, 112(3):434–447.

Cahalan, R. F., Ridgway, W., Wiscombe, W. J., Bell, T. L., and Snider, J. B. (1994). The albedo of fractal stratocumulus clouds.

Cairns, B., Russell, E. E., and Travis, L. D. (1999). Research Scanning Polarimeter: calibration and ground-based measurements. *Polarization: Measurement, Analysis, and Remote Sensing II*, 3754(October 1999):186–196.

Cao, C., De Luccia, F. J., Xiong, X., Wolfe, R., and Weng, F. (2014). Early on-orbit performance of the visible infrared imaging radiometer suite onboard the suomi national polar-orbiting partnership (S-NPP) satellite. *IEEE Transactions on Geoscience and Remote Sensing*, 52(2):1142–1156.

Chand, D., Wood, R., Anderson, T. L., Satheesh, S. K., and Charlson, R. J. (2009). Satellite-derived direct radiative effect of aerosols dependent on cloud cover. *Nature Geoscience*, 2(3):181–184.

Chang, I. and Christopher, S. A. (2016). Identifying Absorbing Aerosols above Clouds from the Spinning Enhanced Visible and Infrared Imager Coupled with NASA A-Train Multiple Sensors. *IEEE Transactions on Geoscience and Remote Sensing*, 54(6):3163–3173.

Costantino, L. and Bréon, F. M. (2010). Analysis of aerosol-cloud interaction from multi-sensor satellite observations. *Geophysical Research Letters*, 37(11):1–5.

Costantino, L. and Bréon, F. M. (2013). Aerosol indirect effect on warm clouds over South-East Atlantic, from co-located MODIS and CALIPSO observations. *Atmospheric Chemistry and Physics*, 13(1):69–88.

Davis, A., Marshak, A., Cahalan, R., and Wiscombe, W. (1997). The Landsat scale break in stratocumulus as a three-dimensional radiative transfer effect: Implications for cloud remote sensing. *Journal of the Atmospheric Sciences*.

Davis, A. B. and Marshak, A. (2010). Solar radiation transport in the cloudy atmosphere: A 3D perspective on observations and climate impacts. *Reports on Progress in Physics*, 73(2).

Deirmendjian, D. (1964). Scattering and Polarization Properties of Water Clouds and Hazes in the Visible and Infrared. *Applied Optics*, 3(2):187.

Deschamps, P. Y., Buriez, J. C., Bréon, F. M., Leroy, M., Podaire, A., Bricaud, A., and Sèze, G. (1994). The POLDER Mission: Instrument Characteristics and Scientific Objectives. *IEEE Transactions on Geoscience and Remote Sensing*, 32(3):598–615.

Devasthale, A. and Thomas, M. A. (2011). A global survey of aerosol-liquid water cloud overlap based on four years of CALIPSO-CALIOP data. *Atmospheric Chemistry and Physics*, 11(3):1143–1154.

Di Girolamo, L., Liang, L., and Platnick, S. (2010). A global view of one-dimensional solar radiative transfer through oceanic water clouds. *Geophysical Research Letters*, 37(18):1–5.

Diner, D. J., Xu, F., Garay, M. J., Martonchik, J. V., Rheingans, B. E., Geier, S., Davis, A., Hancock, B. R., Jovanovic, V. M., Bull, M. A., Capraro, K., Chipman, R. A., and McClain, S. C. (2013). The Airborne Multiangle SpectroPolarimetric Imager (AirMSPI): A new tool for aerosol and cloud remote sensing. *Atmospheric Measurement Techniques*, 6(8):2007–2025.

Dubovik, O., Holben, B. N., Eck, T. F., Smirnov, A., Kaufman, Y. J., King, M. D., Tanré, D., Slutsker, I., Sciences, G. E., and Directorate, E. S. (2002). Variability of Absorption and Optical Properties of Key Aerosol Types Observed in Worldwide Locations. *Journal of the Atmospheric Sciences*, 59(3):590–608.

Emde, C., Barlakas, V., Cornet, C., Evans, F., Wang, Z., Labonotte, L. C., Macke, A., Mayer, B., and Wendisch, M. (2018). IPRT polarized radiative transfer model intercomparison project Three-dimensional test cases (phase B). *Journal of Quantitative Spectroscopy and Radiative Transfer*, 209:19–44.

Hale, G. M. and Querry, M. R. (1973). Optical Constants of Water in the 200-nm to 200-μm Wavelength Region. *Applied Optics*, 12(3):555.

Hansen, J. E. and Travis, L. D. (1974). Light scattering in planetary atmospheres. *Space Science Reviews*, 16(4):527–610.

Hess, M., Koepke, P., and Schult, I. (1998). Optical Properties of Aerosols and Clouds: The Software Package OPAC. *Bulletin of the American Meteorological Society*, 79(5):831–844.

Horvath, H. (2009). Journal of Quantitative Spectroscopy & Radiative Transfer Gustav Mie and the scattering and absorption of light by particles : Historic developments and basics. 110:787–799.

Hu, Y. X., Wielicki, B., Lin, B., Gibson, G., Tsay, S. C., Stamnes, K., and Wong, T. (2000). δ -Fit: A fast and accurate treatment of particle scattering phase functions with weighted singular-value decomposition least-squares fitting. *Journal of Quantitative Spectroscopy and Radiative Transfer*, 65(4):681–690.

IPCC (2013). Working Group I Contribution to the IPCC Fifth Assessment Report, Climate Change 2013: The Physical Science Basis. *Ipcc*, AR5(March 2013):2014.

Jethva, H., Torres, O., Waquet, F., Chand, D., and Hu, Y. (2014). How do A-train sensors intercompare in the retrievalof above-cloud aerosol optical depth? A casestudy-based assessment. *Geophysical Research Letters*, pages 161–166.

Johnson, B. T., Shine, K. P., and Forster, P. M. (2004). The semi-direct aerosol effect: Impact of absorbing aerosols on marine stratocumulus. *Quarterly Journal of the Royal Meteorological Society*, 130(599):1407–1422.

Kaufman, Y. J., Koren, I., Remer, L. A., Rosenfeld, D., and Rudich, Y. (2005). The effect of smoke, dust, and pollution aerosol on shallow cloud development over the Atlantic Ocean. *Proceedings of the National Academy of Sciences*, 102(32):11207–11212.

Kay, J. E., Hillman, B. R., Klein, S. A., Zhang, Y., Medeiros, B., Pincus, R., Gettelman, A., Eaton, B., Boyle, J., Marchand, R., and Ackerman, T. P. (2012). Exposing global cloud biases in the Community Atmosphere Model (CAM) using satellite observations and their corresponding instrument simulators. *Journal of Climate*, 25(15):5190–5207.

Klein, S. A. and Hartmann, D. L. (1993). The seasonal cycle of low stratiform clouds.

Liou, K. N. (2002). *An Introduction to Atmospheric Radiation*, volume 84.

Liu, Z., Winker, D., Omar, A., Vaughan, M., Kar, J., Trepte, C., Hu, Y., and Schuster, G. (2015). Evaluation of CALIOP 532 nm aerosol optical depth over opaque water clouds. *Atmospheric Chemistry and Physics*, pages 1265–1288.

Loeb, N. G. and Davies, R. (1996). Observational evidence of plane parallel model biases: Apparent dependence of cloud optical depth on solar zenith angle. *Journal of Geophysical Research Atmospheres*, 101(D1):1621–1634.

Lu, Z., Liu, X., Zhang, Z., Zhao, C., Meyer, K., Rajapakshe, C., Wu, C., Yang, Z., and Penner, J. E. (2018). Biomass smoke from southern Africa can significantly enhance the brightness of stratocumulus over the southeastern Atlantic Ocean. *Proceedings of the National Academy of Sciences*, page 201713703.

Marshak, A. and Davis, A. (2005). *3D Radiative Transfer in Cloudy Atmospheres*.

Marshak, A., Davis, A., Cahalan, R., and Wiscombe, W. (1994). Bounded cascade models as nonstationary multifractals. *Physical Review E*, 49(1):55–69.

Marshak, A., Davis, A., Wiscombe, W. J., and Cahalan, R. F. (1995). Radiative smoothing in fractal clouds. *Journal of Geophysical Research*, 100(D12).

Marshak, A., Platnick, S., V??rnai, T., Wen, G., and Cahalan, R. F. (2006). Impact of three-dimensional radiative effects on satellite retrievals of cloud droplet sizes. *Journal of Geophysical Research Atmospheres*, 111(9):1–12.

Martins, J. V., Fernandez-Borda, R., McBride, B., Remer, L., and Barbosa, H. M. (2018). The harp hyperangular imaging polarimeter and the need for small satellite payloads with high science payoff for earth science remote sensing. *International Geoscience and Remote Sensing Symposium (IGARSS)*, 2018-July:6304–6307.

Martins, J. V., R., F.-B., McBride, B., Espinosa, R., and Remer, L. A. (2017). Combination between in-situ and remote sensing of tropospheric aerosols.

Mayer, B. (2009). Radiative transfer in the cloudy atmosphere. In *EPJ Web of Conferences*, volume 1, pages 75–99. EDP Sciences.

Mcbride, B. A., Martins, J. V., Barbosa, H. M. J., and Birmingham, W. (2019). Spatial distribution of cloud droplet size properties from Airborne Hyper-Angular Rainbow Polarimeter (AirHARP) measurements. (October):1–32.

McGill, M. J., Yorks, J. E., Scott, V. S., and Kupchock, Andrew W. Selmer, P. A. (2015). The Cloud-Aerosol Transport System (CATS): a technology demonstration on the International Space Station. *Proc.SPIE*, 9612.

Meyer, K., Platnick, S., Oreopoulos, L., and Lee, D. (2013). Estimating the direct radiative effect of absorbing aerosols overlying marine boundary layer clouds in the southeast Atlantic using MODIS and CALIOP. *Journal of Geophysical Research Atmospheres*, 118(10):4801–4815.

Meyer, K., Platnick, S., and Zhang, Z. (2015). Simultaneously inferring above-cloud absorbing aerosol optical thickness and underlying liquid phase cloud optical and microphysical properties using MODIS. *Journal of Geophysical Research Atmospheres*, 120(11):5524–5547.

Mie, G. (1908). contributions to the optics of diffuse media, especially colloid metal solutions. *Annalen der Physik*, 330(3):377–445.

Miller, D. J. (2017). *Satellite Simulator Studies of the Impact of Cloud Inhomogeneity on Passive Cloud Remote Sensing Retrievals*. Phd diss., University of Maryland Baltimore County.

Miller, D. J., Zhang, Z., Ackerman, A. S., Platnick, S., and Baum, B. A. (2016). The impact of cloud vertical profile on liquid water path retrieval based on the bispectral method: A theoretical study based on large-eddy simulations of shallow marine boundary layer clouds. *Journal of Geophysical Research: Atmospheres*, 121(8):4122–4141.

Miller, D. J., Zhang, Z., Platnick, S., Ackerman, A. S., Werner, F., Cornet, C., and Knobelspiesse, K. (2017). Comparisons of bispectral and polarimetric cloud microphysical retrievals using LES-Satellite retrieval simulator. *Atmospheric Measurement Techniques*, (September).

Min, M. and Zhang, Z. (2014). On the influence of cloud fraction diurnal cycle and sub-grid cloud optical thickness variability on all-sky direct aerosol radiative forcing. *Journal of Quantitative Spectroscopy and Radiative Transfer*, 142:25–36.

Mishchenko, M. I., Cairns, B., Kopp, G., Schueler, C. F., Fafaul, B. A., Hansen, J. E., Hooker, R. J., Itchkawich, T., Maring, H. B., and Travis, L. D. (2007). Accurate monitoring of terrestrial aerosol and total solar irradiance: Introducing the Glory mission. *Bulletin of the American Meteorological Society*.

Nakajima, T. and Asano, S. (1977). On the Peak Truncation Approximation of Phase Function for Radia-tive Transfer. *Science reports of the Tohoku University. Ser. 5, Geophysics*, 24(3):89–102.

Nakajima, T. and King (1990). Determination of the Optical Thickness and Effective Particle Radius of Clouds from Reflected Solar Radiation Measurements. Part I: Theory.

NASEM (2018). *Thriving on Our Changing Planet: A Decadal Strategy for Earth Observation from Space*. The National Academies Press, Washington, DC.

Omar, A., Winker, D., and Won, J. (2003). Aerosol models for the CALIPSO lidar inversion algorithms. *Proceedings of . . .*, 5240:1–12.

Omar, A., Winker, D. M., Kittaka, C., Vaughan, M. A., Liu, Z., Hu, Y., Trepte, C. R., Rogers, R. R., Ferrare, R. A., Lee, K.-P., Kuehn, R. E., and Hostetler, C. A. (2009). The CALIPSO Automated Aerosol Classification and Lidar Ratio Selection Algorithm. *Journal of Atmospheric and Oceanic Technology*, 26:1994–2014.

Oreopoulos, L. and Davies, R. (1998). Plane parallel albedo biases from satellite observations. Part I: dependence on resolution and other factors. *Journal of Climate*.

Painemal, D., Kato, S., and Minnis, P. (2014). Boundary layer regulation in the southeast Atlantic cloud microphysics. *Journal of Geophysical Research*, pages 288–302.

Petty, G. W. (2004). *A First Course in Atmospheric Radiation*. Sundog Publishing.

Platnick, S. (2000). Vertical photon transport in cloud remote sensing problems. *Journal of Geophysical Research Atmospheres*, 105(D18):22919–22935.

Platnick, S., King, M. D., Ackerman, S. A., Menzel, W. P., Baum, B. A., Riédi, J. C., and Frey, R. A. (2003). The MODIS Cloud Products : Algorithms and Examples From Terra. 41(2):459–473.

Rajapakshe, C. and Zhang, Z. (2020). Using polarimetric observations to detect and quantify the three-dimensional radiative transfer effects in passive satellite cloud property retrievals: theoretical framework and feasibility study. *Journal of Quantitative Spectroscopy and Radiative Transfer*, page 106920.

Rajapakshe, C., Zhang, Z., Yorks, J. E., Yu, H., Tan, Q., Meyer, K., Platnick, S., and Winker, D. M. (2017). Seasonally Transported Aerosol Layers over Southeast Atlantic are Closer to Underlying Clouds than Previously Reported. *Geophysical Research Letters*, (410).

Rauber, R. M., Stevens, B., Ochs III, H. T., Charles, K., Albrecht, B., Blyth, A., Fairall, C., Jensen, J., Lasher-Trapp, S., Mayol-Bracero, O., Vali, G., Anderson, J., Baker, B., Bandy, A., Burnet, E., Brenguier, J. L., Brewer, W., Brown, P., Chuang, P., Cotton, W., Girolamo, D., Geerts, B., Gerber, H., Goke, S., Gomes, L., Heikes, B., Hudson, J., Kollias, P., Lawson, R., Krueger, S., Lenschow, D., Nuijens, L., O'Sullivan, D., Rilling, R., Rogers, D., Siebesma, A., Snodgrass, E., Stith, J., Thornton, D., Tucker, S., Twohy, C., and Zuidema, P. (2007). RAIN IN SHALLOW CUMULUS OVER THE OCEAN The RICO Campaign. *Bulletin of the American Meteorological Society*, (December).

Roebeling, R. A., Feijt, A. J., and Stammes, P. (2006). Cloud property retrievals for climate monitoring: Implications of differences between Spinning Enhanced Visible and Infrared Imager (SEVIRI) on METEOSAT-8 and Advanced Very High Resolution Radiometer (AVHRR) on NOAA-17. *Journal of Geophysical Research Atmospheres*, 111(20):1–16.

Rosenfeld, D. and Feingold, G. (2003). Explanation of discrepancies among satellite observations of the aerosol indirect effects. *Geophysical Research Letters*, 30(14):1–4.

Sakaeda, N., Wood, R., and Rasch, P. J. (2011). Direct and semidirect aerosol effects of southern African biomass burning aerosol. *Journal of Geophysical Research Atmospheres*, 116(12):1–19.

Sayer, A. M., Hsu, N. C., Bettenhausen, C., Lee, J., Redemann, J., Schmid, B., and Shinozuka, Y. (2016). Extending Deep Blue aerosol retrieval coverage to cases of absorbing aerosols above clouds : Sensitivity analysis and first case studies. *Journal of Geophysical Research: Atmospheres*, pages 4830–4854.

Seethala, C. and Horváth, Á. (2010). Global assessment of AMSR-E and MODIS cloud liquid water path retrievals in warm oceanic clouds. *Journal of Geophysical Research Atmospheres*, 115(13):1–19.

Shettle, E. P. and Fenn, R. W. (1979). Models for the Aerosols of the Lower Atmosphere and the Effects of Humidity Variations on Their Optical Properties. *Environmental Research Papers*, 676(6):89.

Song, H., Zhang, Z., Ma, P. L., Ghan, S. J., and Wang, M. (2018). An evaluation of marine boundary layer cloud property simulations in the Community Atmosphere Model using satellite observations: Conventional subgrid parameterization versus CLUBB. *Journal of Climate*, 31(6):2299–2320.

Stevens, B., Ackerman, A. S., Albrecht, B. a., Brown, A. R., Chlond, A., Cuxart, J., Duynkerke, P. G., Lewellen, D. C., Macvean, M. K., Neggers, R. a. J., Sánchez, E., Siebesma, a. P., and Stevens, D. E. (2001). Simulations of Trade Wind Cumuli under a Strong Inversion. *Journal of the Atmospheric Sciences*, 58(14):1870–1891.

Stevens, B., Lenschow, D. H., Vali, G., Gerber, H., Bandy, A., Blomquist, B., Brenguier, J. L., Bretherton, C. S., Burnet, F., Campos, T., Chai, S., Faloona, I., Friesen, D., Haimov, S., Laursen, K., Lilly, D. K., Loehrer, S. M., Malinowski, S. P., Morley, B., Petters, M. D., Rogers, D. C., Russell, L., Savic-Jovcic, V., Snider, J. R., Straub, D., Szumowski, M. J., Takagi, H., Thornton, D. C., Tschudi, M., Twohy, C., Wetzel, M., and Van Zanten, M. C. (2003). Dynamics and Chemistry of Marine Stratocumulus - DYCOMS-II. *Bulletin of the American Meteorological Society*, 84(5):579–593+548.

Takahashi, H., Lebsock, M., Suzuki, K., Stephens, G., and Wang, M. (2017). An investigation of microphysics and subgrid-scale variability in warm-rain clouds using the A-train observations and a multiscale modeling framework. *Journal of Geophysical Research*, 122(14):7493–7504.

Torres, O., Jethva, H., and Bhartia, P. K. (2011). Retrieval of Aerosol Optical Depth above Clouds from OMI Observations: Sensitivity Analysis and Case Studies. *Journal of the Atmospheric Sciences*, 69:1037–1053.

Trenberth, K. E., Fasullo, J. T., and Kiehl, J. (2009). Earth's global energy budget. *Bulletin of the American Meteorological Society*, 90(3):311–323.

Várnai, T. and Davies, R. (1999). Effects of Cloud Heterogeneities on Shortwave Radiation: Comparison of Cloud-Top Variability and Internal Heterogeneity. *Journal of the Atmospheric Sciences*, 56(24):4206–4224.

Várnai, T. and Marshak, A. (2001). Statistical Analysis of the Uncertainties in Cloud Optical Depth Retrievals Caused by Three-Dimensional Radiative Effects. *Journal of the Atmospheric Sciences*, 58(12):1540–1548.

Várnai, T. and Marshak, A. (2002). Observations of Three-Dimensional Radiative Effects that Influence MODIS Cloud Optical Thickness Retrievals. *Journal of the Atmospheric Sciences*, 59(9):1607–1618.

Várnai, T. and Marshak, A. (2009). MODIS observations of enhanced clear sky reflectance near clouds. *Geophysical Research Letters*, 36(6):1–5.

Wang, Z., Cui, S., Yang, J., Gao, H., Liu, C., and Zhang, Z. (2017a). A novel hybrid scattering order-dependent variance reduction method for Monte Carlo simulations of radiative transfer in cloudy atmosphere. *Journal of Quantitative Spectroscopy and Radiative Transfer*, 189:283–302.

Wang, Z., Cui, S., Yang, J., Gao, H., Liu, C., and Zhang, Z. (2017b). A novel hybrid scattering order-dependent variance reduction method for Monte Carlo simulations of radiative transfer in cloudy atmosphere. *Journal of Quantitative Spectroscopy and Radiative Transfer*.

Wang, Z., Yang, S., Qiao, Y., Cui, S., and Zhao, Q. (2011). Multiple-scaling methods for Monte Carlo simulations of radiative transfer in cloudy atmosphere. *Journal of Quantitative Spectroscopy and Radiative Transfer*, 112(16):2619–2629.

Waquet, F., Riedi, J., Labonnote, L. C., Goloub, P., Cairns, B., Deuzé, J.-L., and Tanré, D. (2009). Aerosol Remote Sensing over Clouds Using A-Train Observations. *Journal of the Atmospheric Sciences*, 66:2468–2480.

Wendisch, M. and Yang, P. (2012). *Theory of Atmospheric Radiative Transfer: A Comprehensive Introduction, by Manfred Wendisch and Ping Yang*.

Werdell, J. (2017). NASA PACE- Home.

Wilcox, E. M. (2010). Stratocumulus cloud thickening beneath layers of absorbing smoke aerosol. *Atmospheric Chemistry and Physics*, 10(23):11769–11777.

Wilcox, E. M. (2012). Direct and semi-direct radiative forcing of smoke aerosols over clouds. *Atmospheric Chemistry and Physics*, 12(1):139–149.

Winker, D. M., Vaughan, M. A., Omar, A., Hu, Y., Powell, K. A., Liu, Z., Hunt, W. H., and Young, S. A. (2009). Overview of the CALIPSO mission and CALIOP data processing algorithms. *Journal of Atmospheric and Oceanic Technology*, 26(11):2310–2323.

Wiscombe, W. J. (1977). The Delta-M Method.

Wiscombe, W. J. (1979). Mie Scattering Calculations : Advances in Technique and Fast , Vector-Speed Computer Codes. *NCAR Tech, National Center for Atmospheric Research, Boulder, Colorado*.

Yorks, J. E., Mcgill, M. J., Palm, S. P., Hlavka, D. L., Selmer, P. A., Nowottnick, E. P., Vaughan, M. A., and Rodier, S. D. (2015). an Overview of the Cloud - Aerosol Transport System (Cats) Processing Algorithms and Data Products. 1:3–6.

Yu, H., Zhang, Y., Chin, M., Liu, Z., Omar, A., Remer, L. A., Yang, Y., Yuan, T., and Zhang, J. (2012). An integrated analysis of aerosol above clouds from A-Train multi-sensor measurements. *Remote Sensing of Environment*, 121:125–131.

Yu, H. and Zhang, Z. (2013). New Directions: Emerging satellite observations of above-cloud aerosols and direct radiative forcing.

Zhang, Y., Xie, S., Lin, W., Klein, S. A., Zelinka, M., Ma, P. L., Rasch, P. J., Qian, Y., Tang, Q., and Ma, H. Y. (2019). Evaluation of Clouds in Version 1 of the E3SM Atmosphere Model With Satellite Simulators. *Journal of Advances in Modeling Earth Systems*, pages 1253–1268.

Zhang, Z., Ackerman, A. S., Feingold, G., Platnick, S., Pincus, R., and Xue, H. (2012). Effects of cloud horizontal inhomogeneity and drizzle on remote sensing of cloud droplet effective radius: Case studies based on large-eddy simulations. *Journal of Geophysical Research Atmospheres*, 117(19):1–18.

Zhang, Z., Dong, X., Xi, B., Song, H., Ma, P. L., Ghan, S. J., Platnick, S., and Minnis, P. (2017). Intercomparisons of marine boundary layer cloud properties from the ARM CAP-MBL campaign and two MODIS cloud products. *Journal of Geophysical Research*, 122(4):2351–2365.

Zhang, Z., Meyer, K., Yu, H., Platnick, S., Colarco, P., Liu, Z., and Oreopoulos, L. (2016a). Shortwave direct radiative effects of above-cloud aerosols over global oceans derived from 8 years of CALIOP and MODIS observations. *Atmospheric Chemistry and Physics*, 16(5).

Zhang, Z. and Platnick, S. (2011). An assessment of differences between cloud effective particle radius retrievals for marine water clouds from three MODIS spectral bands. *Journal of Geophysical Research Atmospheres*, 116(20):1–19.

Zhang, Z., Werner, F., Cho, H., Wind, G., Platnick, S. E., Ackerman, A. S., Girolamo, L. D., Marshak, A., and Meyer, K. (2016b). A framework based on 2-D Taylor expansion for quantifying the impacts of subpixel reflectance variance and covariance on cloud optical thickness and effective radius retrievals based on the bispectral method. *Journal of Geophysical Research Atmospheres*, 121(12):7007–7025.